Multiple impinging jet arrays: an experimental study on flow and heat transfer

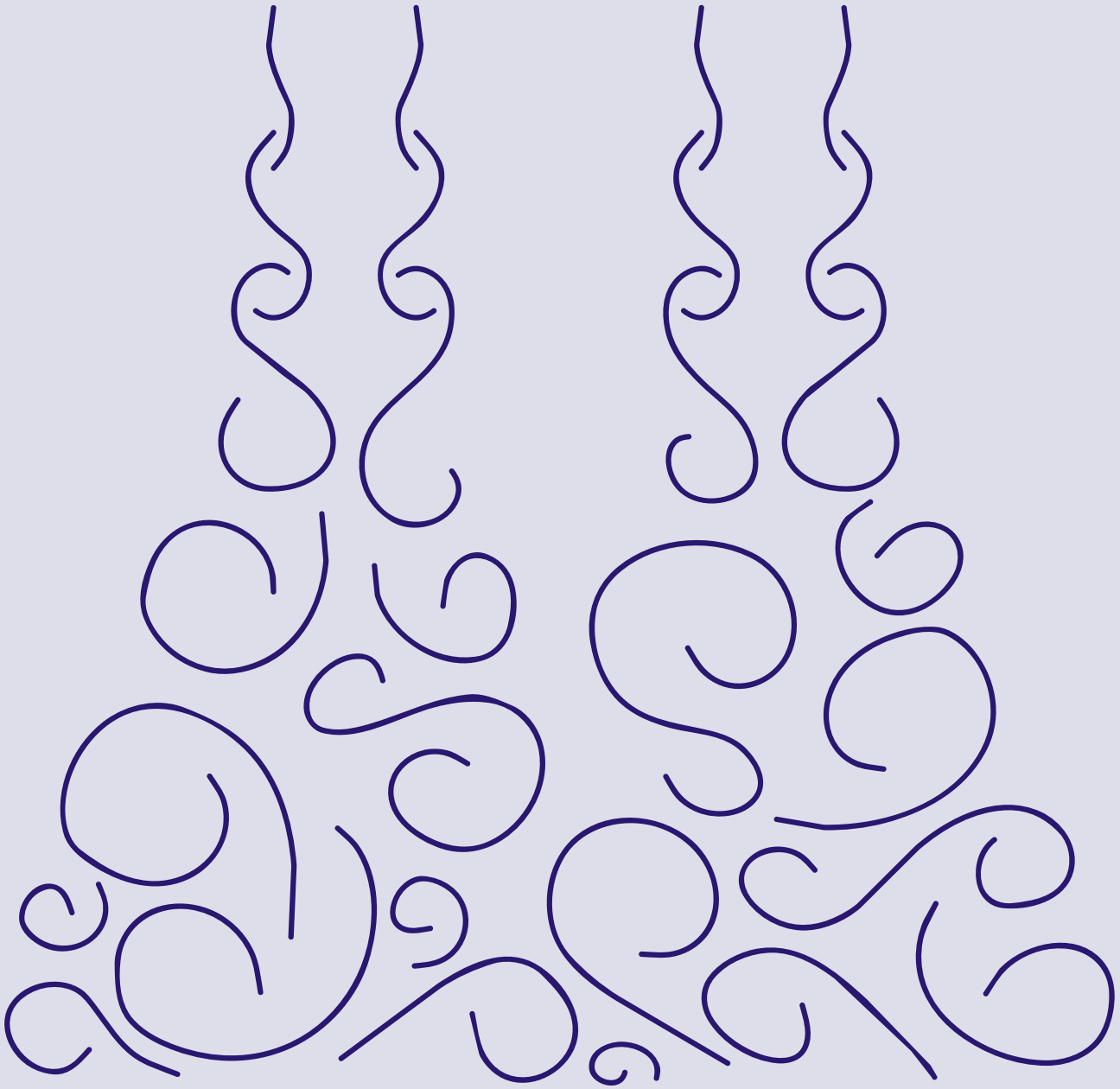

L.F.G. Geers

Multiple impinging jet arrays: an experimental study on flow and heat transfer

Multiple impinging jet arrays: an experimental study on flow and heat transfer

Proefschrift

ter verkrijging van de graad van doctor
aan de Technische Universiteit Delft,
op gezag van de Rector Magnificus prof. dr. ir. J. T. Fokkema,
voorzitter van het College voor Promoties,
in het openbaar te verdedigen op maandag 9 februari 2004 om 10:30 uur

door

Leonard Ferdinand Gerard Geers
scheikundig ingenieur
geboren te Tilburg.

Dit proefschrift is goedgekeurd door de promotor:
Prof. Dr. Dipl.-Ing. K. Hanjalić

Samenstelling promotiecommissie:

Rector Magnificus, voorzitter
Prof. Dr. Dipl.-Ing. K. Hanjalić, Technische Universiteit Delft, promotor
Prof. dr. ir. J. Westerweel, Technische Universiteit Delft
Prof. dr. R. F. Mudde, Technische Universiteit Delft
Prof. M. Yianneskis, King's College, London
Prof. dr. ir. Th. H. van der Meer, Universiteit Twente
Dr. ir. C. C. M. Rindt, Technische Universiteit Eindhoven
Dr. ir. M. J. Tummers, Technische Universiteit Delft

This research project was sponsored by The Technology Foundation (STW), TNO-TPD, and Rademaker - Den Boer BV.

ISBN 90 901 7774 4

Printed in the Netherlands

Voor Pa, Ma en Natasja

'The life of a scientist is one of vast periods of tranquility, punctuated by brief and sudden moments of drama and excitement.'

Prof. Ian Stewart – Does God play dice?

Contents

Chapter 1

Introduction

1.1 Background

Impinging jets are jets of fluid impinging on a surface that needs to be cooled or heated. Because of their high efficiency and their ability to provide high heat transfer rates, these jets are applied in a wide variety of rapid cooling and heating processes. Figure 1.1 presents a sketch of a jet issuing from a round pipe and impinging on a flat surface. Arrays of impinging jets are applied in, for instance, steel and glass quenching, textile drying, paper processing, baking. Figure 1.2 shows a schematic of another example: the internal cooling of turbine blades. Due to the high temperatures in gas turbines (1400–1500°C), the blades are subject to high stresses that can cause severe damage to the blades. While cooling of the mid-chord and trailing edge sections is being established by ribs and pin fins, respectively, the leading edge is cooled with swirling flow created

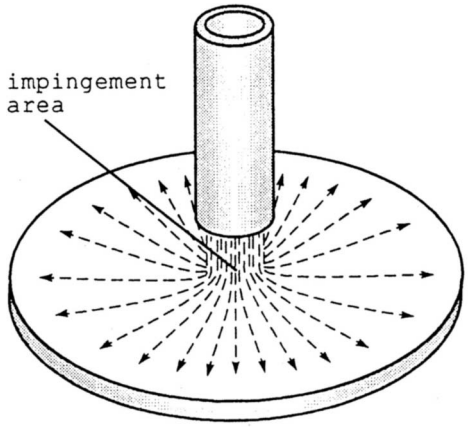

Figure 1.1: Jet issuing from a pipe and impinging on a flat surface (Peper et al., 1995).

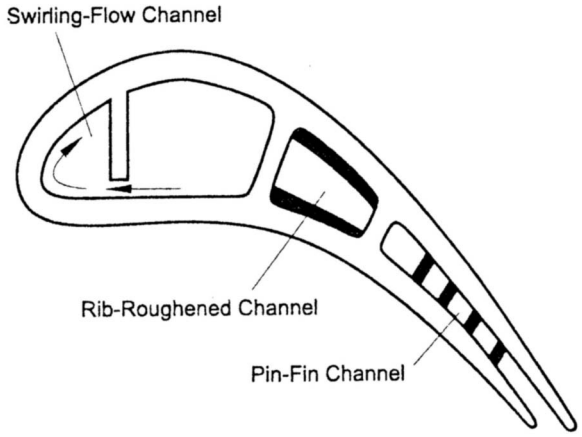

Figure 1.2: Internal cooling of a turbine blade with impinging jets (Hwang and Cheng, 1999).

by multiple side-entry jets that are placed tangential to the inner surface of the duct (Hwang and Cheng, 1999).

The design of industrial heat transfer equipment is currently based on empirical correlations derived from numerous experiments using a broad spectrum of different nozzle geometries to produce jets. Additionally, differences in experimental conditions such as turbulence in the jets, boundary conditions, and characteristic dimensions, and variable ranges add to the complexity of the problem to find generic correlations between geometrical and flow conditions on the one hand and heat transfer rates on the other. A detailed review of frequently used correlations is given by Viskanta (1993) for both single and multiple impinging jets. Martin (1977) has attempted to construct generic empirical correlations for a number of basic nozzle geometries on the basis of correlations published earlier by other researchers.

In order to achieve a suitable design of heat transfer equipment, both from an economic and a technical viewpoint, detailed knowledge of the dependence of the heat transfer rates on the external variables is required. The gas flow rate, the diameter of the nozzles, their spacing, and their distance to the product surface are the main variables, which can be chosen to solve a given heat or mass transfer problem. However, empirical correlations do not provide detailed knowledge, they are a mere tool for applying impinging jets within the variable range for which the correlation was derived. They cannot be used to optimize heat transfer processes or to design more efficient nozzles.

Realizing that the essence of heat transfer enhancement lies in adequate flow and turbulence fields, some recent works focused on measuring mean and fluctuating velocities aimed at providing more information about flow and turbulence structure. Kataoka (1990) provided an interesting pioneering discussion of eddy structure in a single jet, arguing that the large scale coherent structures, generated at the outer shear layer, play

the crucial role in the enhancement of impingement heat transfer. Cooper et al. (1993) reported on detailed measurements of the mean velocity and turbulence statistics in single impinging jet flows for two nozzle-to-plate distances using Hot Wire Anemometry (HWA) and Laser Doppler Anemometry (LDA). The measurements of Cooper et al. were performed using a well defined, fully developed turbulent pipe flow as an inlet condition and have served as reference for comparison of other experimental results, as well as for validating turbulence models for Computational Fluid Dynamics (CFD). More recently Nishino et al. (1996) performed 2D and 3D Particle Tracking Velocimetry (PTV) measurements in a single jet at two different Reynolds numbers. Next to mean features of the jet, they discuss the turbulence characteristics and the budgets for turbulent kinetic energy.

In contrast to single jets, very little is known about the flow and turbulence structure in multiple jet configurations. Here the additional factor is the interaction between neighboring jets, which — depending on their mutual distance — can have a dominant effect on heat transfer intensity, and especially on its distribution over the impingement surface. Most literature dealing with multiple jets report flow field data in jet arrays of custom-made nozzle arrangements, but only few results are available on the measurements of mean flow and turbulence characteristics. For instance, Barata (1996) conducted LDA measurements and numerical simulations in an arrangement of three jets and studied the effect of cross-flow on the jets below a V/STOL (Vertical/Short Take-Off and Landing) aircraft in ground proximity. Findlay et al. (1999) also investigated jets in a cross-flow, but their configuration consisted of a row of square nozzles. Finally, Matsumoto et al. (1999) examined the flow pattern and the heat transfer from an array of circular impinging jets. Although their geometry was a generic one, a square array of 5×5 round nozzles, they only studied the flow in a qualitative way. In the subsequent chapters a more extensive overview of impinging jet literature is presented.

1.2 Objectives

Knowing the interaction between turbulent structures in an impinging jet and impingement heat transfer, is the key to master control over the heat transfer and hence to be able to improve heat transfer efficiency and homogeneity. Therefore, the primary objective of the present investigation is to gain a better understanding of the interaction of the flow and the turbulence structure with the heat transfer in impinging jet arrays. It is attempted to identify coherent structures in the flow by using sophisticated experimental velocity measurement techniques like Particle Image Velocimetry (PIV) and Laser Doppler Anemometry (LDA), and structure identification methods such as Proper Orthogonal Decomposition (POD). Heat transfer measurements on the impingement surface are conducted with Liquid Crystal Thermography (LCT). In particular, the effect of geometrical parameters on the occurrence of coherent structures and on the heat transfer distribution is investigated. These geometrical parameters comprise the

nozzle-to-plate spacing, the distance between the nozzles (or pitch), and the shape of the nozzles. At the end, a comparison was made between the experiments reported here and simulations of the flow conducted by Thielen (2003).

1.3 Outline

Chapter 2 presents an introduction of turbulent flows in general and turbulent impinging jets in particular. Section 2.1 discusses the governing conservation laws in turbulent flow and heat transfer processes. Additionally, identification mechanisms are discussed for the isolation of turbulent structures, including a short explanation is given on the Proper Orthogonal Decomposition (POD). Section 2.2 summarizes features of impingement flow in both single impinging jets and multiple impinging jet arrays on the basis of currently available literature.

Chapter 3 is concerned with the three measurement techniques that were used to measure flow and heat transfer in impinging jets. Section 3.1 is a summary of the basic principles of Laser Doppler Anemometry (LDA). Section 3.2 presents the principles of Particle Image Velocimetry (PIV), followed by some advanced techniques for processing measured velocity distributions. Finally, Section 3.3 discusses Liquid Crystal Thermography (LCT), including an overview of the characteristics of thermochromic liquid crystals and image processing techniques needed for accurate temperature measurements with LCT.

All experimental rigs and measurement systems used are presented in Chapter 4. The chapter starts with a description of the single impinging jet in which both LDA and PIV measurements were done. Subsequently, the wind tunnel used for multiple impinging jet experiments is described, followed by a discussion of the PIV and LCT measurement systems, including the calibration procedure for the liquid crystals.

Chapter 5 starts with a discussion of the results of the LDA and PIV measurements in the single impinging jet in Section 5.1. Section 5.2 is split into three main parts. In Section 5.2.1 focuses on the the mean flow in the multiple impinging jet arrays. Next, Section 5.2.2 gives the results of the heat transfer measurements in the multiple impinging jet arrays, including the derivation of an empirical correlation for the heat transfer as a function of geometrical parameters and the flow velocity. Finally, Section 5.2.3 discusses the applicability of the structure identification techniques from Section 2.1 to PIV velocity fields in impinging jets. This is followed by a description of the flow structures that were found applying POD analysis to the measured velocity fields in multiple impinging jet arrays. Finally, a qualitative comparison is made between some experimental velocity fields and the results of numerical simulations that were done in a parallel research project by other researchers.

The general conclusions of the investigation are given in Chapter 6.

Chapter 2

Theoretical background and literature review

This chapter first presents a short summary of the governing conservation laws in turbulent flows and heat transfer. For a full description of these laws and their implications the reader is referred to Tennekes and Lumley (1972). Next, identification methods are discussed for isolating turbulent structures. These structures are known to play an important role in impinging jet heat transfer. Finally, a global overview is given of impinging jet flow and heat transfer on the basis of currently available literature.

2.1 Turbulent flows

2.1.1 Conservation laws

This section discusses the laws of conservation of mass, momentum, and energy that describe any flow. Throughout the section it is assumed that the fluid is Newtonian and that the density ρ is constant.

Mass is conserved if the divergence of the velocity field is equal to zero. This is also known as the continuity equation:

$$\frac{\partial u_i}{\partial x_i} = 0 \ , \tag{2.1}$$

where u_i is the velocity component in the x_i direction. Note that the Einstein summation convention for repeated indices applies here.

The Navier-Stokes equations represent the law of conservation of momentum:

$$\frac{\partial u_i}{\partial t} + u_j \frac{\partial u_i}{\partial x_j} = -\frac{1}{\rho}\frac{\partial p}{\partial x_i} + \nu \frac{\partial^2 u_i}{\partial x_j^2} + g_i \ , \tag{2.2}$$

where t is time, p is the pressure in the flow, ν is the kinematic viscosity of the fluid, and g_i is the gravity vector. The first term on the left-hand side represents the temporal change in momentum of a fluid element, and the second term is the advection term. On the right-hand side there is the contribution to the change of momentum by pressure gradients, viscous forces, and a body force in the form of gravity.

Together with boundary and initial conditions the Navier-Stokes equations and the continuity equation describe both laminar and turbulent flows. Unfortunately, there are no exact solutions of these equations in case of turbulent flows. The instantaneous velocity u_i and the instantaneous pressure p are random processes in the sense that their instantaneous values fluctuate in time and cannot be predicted. However, the velocity and pressure can be described in terms of probability. This leads to the introduction of mean values. Reynolds (1895) introduced the decomposition of the instantaneous turbulence quantities in a mean value and a fluctuating component:

$$u_i = \langle u_i \rangle + u_i' \ , \tag{2.3}$$

$$p = \langle p \rangle + p' \ , \tag{2.4}$$

where $\langle u_i \rangle$ is the ensemble mean value of u_i, u_i' is the fluctuating part of u_i, $\langle p \rangle$ is the ensemble mean pressure, and p' is the fluctuating part of the pressure. Substitution of the Reynolds decomposed Equation 2.3 into Equation 2.1 yields, after averaging:

$$\frac{\partial \langle u_i \rangle}{\partial x_i} = 0 \ . \tag{2.5}$$

When Equations 2.3 and 2.4 are substituted into Equation 2.2, and the resulting equation is ensemble averaged, the Reynolds-Averaged Navier Stokes (RANS) equations are found:

$$\frac{\partial \langle u_i \rangle}{\partial t} + \langle u_j \rangle \frac{\partial \langle u_i \rangle}{\partial x_j} = -\frac{1}{\rho}\frac{\partial \langle p \rangle}{\partial x_i} + \frac{\partial}{\partial x_j}\left(\nu \frac{\partial \langle u_i \rangle}{\partial x_j} - \langle u_i' u_j' \rangle \right) \ , \tag{2.6}$$

where the last term on the right-hand side, $\langle u_i' u_j' \rangle$, is the so-called Reynolds stress tensor, which has its origin in the non-linear convection term. This tensor is the turbulent equivalent of the laminar stress tensor, $\nu \, \partial u_i / \partial x_j$, describing the transfer of u_i momentum in direction x_j by molecular diffusion. In the turbulent stress tensor, fluctuating momentum u_i' is transfered in the x_j direction by means of velocity fluctuations u_j'. Mean transport of fluctuating momentum may change the momentum of the mean flow. The Reynolds stress tensor thus exchanges momentum between the turbulence and the mean flow.

The turbulent kinetic energy is an important quantity for turbulence research. It is defined as $k = \frac{1}{2}\langle u_i' u_i' \rangle$. A transport equation for k can be derived from the Navier-Stokes equation. First, Equation 2.2 is multiplied by u_i and all terms in the equation

are ensemble averaged. Then, the equation for conservation of the kinetic energy of the mean flow (see Tennekes and Lumley, 1972) is subtracted. The result is the k-equation:

$$\frac{\partial k}{\partial t} + \langle u_j \rangle \frac{\partial k}{\partial x_j} = P_k + T_k + \Pi_k + D_k - \varepsilon \ , \tag{2.7}$$

with

$$P_k = -\langle u_i' u_j' \rangle \frac{\partial \langle u_i \rangle}{\partial x_j} \ , \tag{2.8}$$

$$T_k + \Pi_k + D_k = \frac{\partial}{\partial x_j} \left(-\langle u_j' k' \rangle - \frac{1}{\rho} \langle p' u_j' \rangle + \nu \frac{\partial k}{\partial x_j} \right) \ , \tag{2.9}$$

$$\varepsilon = \nu \left\langle \frac{\partial u_i'}{\partial x_j} \frac{\partial u_i'}{\partial x_j} \right\rangle \ , \tag{2.10}$$

where P_k is the production of k, T_k is the transport of k by velocity fluctuations, Π_k is the transport of k by pressure fluctuations, D_k is the transport of k by diffusion, $k' = \frac{1}{2} u_i' u_i'$, and ε is the dissipation of k.

On the largest scales turbulent energy is produced (P_k) by deformation of the mean flow field. This energy is transferred to smaller scales through the mechanism of *vortex stretching* and it is dissipated (ε) on the smaller scales. Turbulent kinetic energy is mainly transported through the flow by velocity fluctuations (T_k) and pressure fluctuations (Π_k), because the diffusion transport (D_k) is usually very small, except near walls.

The law of conservation of energy is defined as:

$$\frac{\partial T}{\partial t} + u_j \frac{\partial T}{\partial x_j} = a \frac{\partial^2 T}{\partial x_j^2} \ , \tag{2.11}$$

where T is the temperature of the fluid and a is the heat diffusivity of the fluid. In this equation the contribution of the momentum dissipation to the thermal energy of the flow is neglected. The first term on the left-hand side is the change of the thermal energy of a fluid element in time, and the second term is the advection of heat. The term on the right-hand side represents the transfer of heat through diffusion. In this case, no thermal energy sources are considered.

Reynolds decomposition of the temperature, i.e. $T = \langle T \rangle + T'$, and of the velocity in Equation 2.11 results in:

$$\frac{\partial \langle T \rangle}{\partial t} + \langle u_j \rangle \frac{\partial \langle T \rangle}{\partial x_j} = \frac{\partial}{\partial x_j} \left(a \frac{\partial \langle T \rangle}{\partial x_j} - \langle u_j' T' \rangle \right) \ , \tag{2.12}$$

The extra term in Equations 2.12, $\langle u_j' T' \rangle$, is known as the turbulent heat flux. It is in analogy with the Reynolds shear stress in Equation 2.6.

2.1.2 Heat transfer

Heat transfer from solid boundaries to moving fluids can be described using Newton's law of cooling (e.g. Beek and Mutzall, 1975):

$$q'' = h(T_\infty - T_b) \ , \tag{2.13}$$

where q'' is the heat flux from the solid to the flow, h is the heat transfer coefficient, T_∞ is the temperature of the bulk of the fluid, and T_b is the temperature of the solid boundary. The temperature difference between the boundary and the bulk flow is the driving force of convective heat transfer.

The heat transfer coefficient, h, is often non-dimensionalized using the heat conductivity of the fluid λ and a length scale $\mathcal{D}$ which characterizes the geometry. This results in the Nusselt number:

$$\mathrm{Nu} = \frac{h\mathcal{D}}{\lambda} \ . \tag{2.14}$$

The Nusselt number is often a complex function of the geometry, the flow velocity, and the physical properties of the fluid. Usually, correlations are derived between the Nusselt number, the Reynolds number Re, the Prandtl number Pr, and a non-dimensional function of the geometry. The Reynolds number is defined as:

$$\mathrm{Re} = \frac{\mathcal{U}\mathcal{D}}{\nu} \ , \tag{2.15}$$

where $\mathcal{U}$ is a velocity scale that characterizes the flow. The Prandtl number is:

$$\mathrm{Pr} = \frac{\nu}{a} \ , \tag{2.16}$$

The Reynolds number and the Prandtl number appear in the non-dimensionalized form of the energy equation (Equation 2.11):

$$\frac{\partial T^*}{\partial t^*} + u_j^* \frac{\partial T^*}{\partial x_j^*} = \frac{1}{RePr} \frac{\partial T^*}{\partial {x_j^*}^2} \ . \tag{2.17}$$

The asterisk indicates non-dimensionalization using the bulk temperature of the fluid, the characteristic velocity scale $\mathcal{U}$ and the characteristic length scale $\mathcal{D}$, so that $T^* = T/T_\infty$, $t^* = t\mathcal{U}/\mathcal{D}$, $x_j^* = x_j/\mathcal{D}$, and $u_j^* = u_j/\mathcal{U}$.

A frequently used generic relationship between the non-dimensional quantities is the power law:

$$\mathrm{Nu} = \alpha_1 \, \mathrm{Re}^{\alpha_2} \, \mathrm{Pr}^{\alpha_3} \, f(geometry) \ , \tag{2.18}$$

where α_1, α_2, and α_3 are parameters that are dependent on the flow regime (turbulent, transitional, laminar), and the function f is geometry-dependent. This type of correlation provides an estimate of the heat transfer coefficient for a given flow geometry, and it can be used for scaling. However, it does not explain the mechanism by which heat transfer and flow interact.

2.1.3 Structure identification

Quasi-periodic, well organized and repeating eddy formations, known as *coherent structures* are known to play a major role in turbulence dynamics and in transporting momentum and species in turbulent flows. Proper identification of such structures and their morphology is a major prerequisite for understanding their role in transport mechanisms. Of special interest are those regions in turbulent flows, such as impingement, separation or reattachment regions, where the transport of scalars (heat and species) is markedly different from momentum transport, thus departing from the common Reynolds analogy. Strong coherent structures locally "trap" the fluid reducing the beneficial temperature or concentration difference and thus decreasing the heat or mass transfer, respectively. Therefore, adequate detection of these structures is of vital importance for the description of the flow and its effect on heat and mass transfer processes. In this section several methods for structure identification and their characteristics will be described.

Vorticity magnitude

An intuitive way of detecting eddies is to search for spiraling or closed path- or streamlines. However, vortices that move with a non-zero velocity in the frame of reference will not be detected using this method. In other words, the method is not Galilean invariant. This is one of two requirements for vortex identification mentioned by Jeong and Hussain (1995). To exclude potential flow regions, the second requirement states that a vortex core must have a net vorticity (hence, net circulation).

The magnitude of the vorticity vector, $\|\boldsymbol{\omega}\|$, is widely used to identify coherent structures.

$$\|\boldsymbol{\omega}\| = \left\{ \sum_{i=1}^{3} \left(\epsilon_{ijk} \frac{\partial u_k}{\partial x_j} \right)^2 \right\}^{1/2} , \tag{2.19}$$

where ϵ_{ijk} is the alternating unit tensor, x_j is the j^{th} coordinate, and u_k is the velocity component in the x_k direction. Although the use of $\|\boldsymbol{\omega}\|$ is successful in free shear flows, Jeong and Hussain show that it does not always produce satisfactory results in flows near obstacles or along walls. The vorticity magnitude is not only sensitive to the local swirling motion typical for a vortex but also to shear. So, when using the vorticity magnitude as an indication for turbulent structures, it is not easy to distinguish true vortices from background shear, when the shear is relatively high. A high value of the vorticity magnitude is a necessary but insufficient condition for detecting a vortex.

Second invariant of the velocity gradient tensor

The identification method on the basis of the second invariant of the velocity gradient tensor Q was originally proposed by Hunt et al. (1988). Q can be interpreted as a measure for the magnitude of rotation relative to strain. When Q is positive, rotation prevails over strain so that vortices can be identified as positive values of Q. Q is calculated from the symmetric ($\boldsymbol{S}$) and the anti-symmetric ($\boldsymbol{\Omega}$) parts of the velocity gradient tensor $\boldsymbol{\nabla v}$:

$$Q \equiv -\frac{1}{2}\frac{\partial u_i}{\partial x_j}\frac{\partial u_j}{\partial x_i} = \frac{1}{2}\left(\|\boldsymbol{\Omega}\|^2 - \|\boldsymbol{S}\|^2\right) \ , \tag{2.20}$$

where $\boldsymbol{S}$ and $\boldsymbol{\Omega}$ are defined as follows:

$$\boldsymbol{S} = \frac{1}{2}\left(\frac{\partial u_i}{\partial x_j} + \frac{\partial u_j}{\partial x_i}\right) \quad \rightarrow \quad \|\boldsymbol{S}\| = \sqrt{\mathrm{tr}(\boldsymbol{S}\boldsymbol{S}^{\boldsymbol{T}})} \ . \tag{2.21}$$

and

$$\boldsymbol{\Omega} = \frac{1}{2}\left(\frac{\partial u_i}{\partial x_j} - \frac{\partial u_j}{\partial x_i}\right) \quad \rightarrow \quad \|\boldsymbol{\Omega}\| = \sqrt{\mathrm{tr}(\boldsymbol{\Omega}\boldsymbol{\Omega}^{\boldsymbol{T}})} \ , \tag{2.22}$$

The advantage of Q over the vorticity magnitude as a quantitative vortex identifier is the fact that Q represents the local balance between shear strain rate and vorticity magnitude. Hence, Q is not affected by local shear, which is very important in the vicinity of walls. For example, in general a velocity gradient at a wall is defined by

$$\boldsymbol{\nabla v} = \begin{pmatrix} 0 & 0 & 0 \\ a & 0 & b \\ 0 & 0 & 0 \end{pmatrix} \ , \tag{2.23}$$

where the wall is assumed to be in the x, z-plane, and a and b are the wall normal gradients of the velocity components parallel to the wall. In this case $Q = 0$, while $\|\boldsymbol{\omega}\| = \sqrt{a^2 + b^2}$.

Kinematic vorticity number

An identifier similar to Q is the kinematic vorticity number N_k. This number is equal to the magnitude of the vorticity vector non-dimensionalized by the norm of the strain rate:

$$N_k \equiv \sqrt{\frac{\|\boldsymbol{\omega}\|^2}{2S_{ij}S_{ij}}} = \frac{\|\boldsymbol{\Omega}\|}{\|\boldsymbol{S}\|} = \sqrt{1 + \frac{2Q}{S_{ij}S_{ij}}} \ . \tag{2.24}$$

For example, $N_k \rightarrow \infty$ and $N_k = 0$ correspond to solid-body rotation and irrotational motion respectively, regardless of the vorticity magnitude. From Equation 2.24 it can be seen that a region with $N_k > 1$ is identical to that with $Q > 0$. For instance, in

the example of the velocity gradient near the wall mentioned above, $N_k = 1$. However, N_k does not discriminate between vortices with small and large vorticity as long as the quality of rotation is the same for both (Jeong and Hussain, 1995).

This is illustrated by the velocity gradient tensor in the center of a vortex in a shear layer:

$$\boldsymbol{\nabla v} = \begin{pmatrix} 0 & \frac{1}{2}\omega & 0 \\ s - \frac{1}{2}\omega & 0 & 0 \\ 0 & 0 & 0 \end{pmatrix} , \tag{2.25}$$

where s is the magnitude of the shear and ω is the magnitude of the vorticity in the vortex and $|\omega - s| > |s|$. In this case the kinematic vorticity number and the second invariant of the velocity gradient tensor are defined by

$$N_k = \frac{|\omega - s|}{|s|} , \tag{2.26}$$

and

$$Q = \frac{1}{4}(\omega - s)^2 - \frac{1}{4}s^2 . \tag{2.27}$$

N_k is determined by the ratio of ω and s, whereas Q is determined by the magnitudes of both quantities. If both the vorticity and the shear both become twice as strong, N_k will not change, but Q is multiplied by four.

Other methods based on the velocity gradient tensor

Identification of vortices on the basis of a negative second eigenvalue (λ_2) of $\boldsymbol{S}^2 + \boldsymbol{\Omega}^2$ forms a fourth identification method based on the velocity gradient tensor. Identification on the basis of the Q-definition may be incorrect when vortices are subjected to a strong external strain, whereas the λ_2-definition represents vortices correctly in this case. This method is superior to the Q-method described above. For details see Jeong and Hussain (1995).

Chong et al. (1990) describe the use of critical-point analysis for structure identification. A critical-point is a point in the flow field where all three velocity components are zero and the streamline slope is indeterminate. These points can be found by calculating the eigenvalues of the velocity gradient tensor. An eddy is characterized by one real eigenvalue and a pair of complex conjugate eigenvalues with a positive imaginary part. Critical-point analysis also correctly identifies vortices subjected to strain. It should be noted that the Q-method, the λ_2-method, and the critical point analysis are equivalent methods in planar flows (i.e. two-dimensional flows). Hence, the advantages of the λ_2-method and critical-point analysis over the Q-method only exist in three-dimensional flows.

Proper Orthogonal Decomposition

Dominant flow structures can be defined and extracted from turbulent flow fields on the basis of the proper orthogonal theorem of probability (Loève, 1955), as proposed by Lumley (1967). Proper orthogonal decomposition (POD) provides an optimal set of basis functions for an ensemble of data. It is optimal in the sense that it is the most efficient way of extracting the most energetic components of an infinite dimensional process with only a few modes (Holmes et al., 1996). When applied to experimental data, the POD can be viewed as a filtering device used to objectively eliminate the low energy motions of the flow that are obscuring the main energetic features of the flow (Gamard et al., 2002).

POD is based on a different approach than the above mentioned methods, because POD is not a vortex identifier and it acts on an ensemble of snapshots instead of only one. Below a short overview of the POD and its characteristics is given. A more complete analysis is given by Manhart and Wengle (1993).

Consider a turbulent flow field in which a domain V is defined where flow velocities are measured simultaneously. This is done at N_P locations over a sufficiently long period of time T at N_T time instants. The velocity vector $\boldsymbol{u}(\boldsymbol{x},t)$ comprises a space-time signal at discrete points in space and time and it is stored in the three-dimensional matrix $\boldsymbol{U}$ (Manhart and Wengle, 1993).

$$\boldsymbol{u}(\boldsymbol{x},t) \quad \rightarrow \quad \boldsymbol{U} = \begin{bmatrix} \boldsymbol{u}(\boldsymbol{x}_1,t_1) & \cdots & \boldsymbol{u}(\boldsymbol{x}_{N_P},t_1) \\ \vdots & \ddots & \vdots \\ \boldsymbol{u}(\boldsymbol{x}_1,t_{N_T}) & \cdots & \boldsymbol{u}(\boldsymbol{x}_{N_P},t_{N_T}) \end{bmatrix} \tag{2.28}$$

The velocity field can be expanded into an infinite series of orthogonal spatial basis functions $\boldsymbol{\varphi}^n(\boldsymbol{x})$ and uncorrelated coefficients $a^n(t)$, where n denotes the mode number. By considering only the modes comprising the most energetic components of the velocity signal, the series can be restricted to only N_M modes. In other words, N_M is the number of modes required to represent the flow field in a sufficiently accurate way, which is to be determined for each flow problem separately. Equation 2.29 displays the mathematical representation of the POD in continuous notation on the left and in matrix notation on the right. Both notations are presented for clarity.

$$\boldsymbol{u}(\boldsymbol{x},t) = \sum_{n=0}^{N_M-1} a^n(t)\boldsymbol{\varphi}^n(\boldsymbol{x}) \quad \rightarrow \quad \boldsymbol{U} = \boldsymbol{A}\boldsymbol{\Phi} \tag{2.29}$$

In matrix notation $a^n(t)$ and $\boldsymbol{\varphi}^n(\boldsymbol{x})$ are represented by $\boldsymbol{A}$ and $\boldsymbol{\Phi}$:

$$a^n(t) \quad \rightarrow \quad \boldsymbol{A} = \begin{bmatrix} a^0(t_1) & \cdots & a^{N_M-1}(t_1) \\ \vdots & \ddots & \vdots \\ a^0(t_{N_T}) & \cdots & a^{N_M-1}(t_{N_T}) \end{bmatrix} , \tag{2.30}$$

$$\boldsymbol{\varphi}^n(\boldsymbol{x}) \quad \rightarrow \quad \boldsymbol{\Phi} = \begin{bmatrix} \boldsymbol{\varphi}^0(\boldsymbol{x}_1) & \cdots & \boldsymbol{\varphi}^0(\boldsymbol{x}_{N_P}) \\ \vdots & \ddots & \vdots \\ \boldsymbol{\varphi}^{N_M-1}(\boldsymbol{x}_1) & \cdots & \boldsymbol{\varphi}^{N_M-1}(\boldsymbol{x}_{N_P}) \end{bmatrix} . \tag{2.31}$$

The temporal coefficients are uncorrelated, i.e. statistically orthogonal:

$$\frac{1}{T}\int_T a^m(t)a^n(t)\,dt = \lambda^n\delta_{mn} \quad \rightarrow \quad \frac{1}{N_T}\boldsymbol{A^T A} = \boldsymbol{\Lambda} , \tag{2.32}$$

where $\boldsymbol{A^T}$ is the transpose of $\boldsymbol{A}$, δ_{mn} is the Kronecker delta, and $\boldsymbol{\Lambda}$ is a diagonal matrix containing the eigenvalues λ^n which give the energy norm of the n^{th} mode.

The spatial modes are also orthogonal:

$$\iiint_V \boldsymbol{\varphi}^m(\boldsymbol{x}) \cdot \boldsymbol{\varphi}^n(\boldsymbol{x})\,d\boldsymbol{x} = \delta_{mn} \quad \rightarrow \quad \boldsymbol{\Phi G \Phi^T} = \boldsymbol{I} , \tag{2.33}$$

where $\boldsymbol{G}$ is a matrix resulting from the discretization of the spatial integral in Equation 2.33 and $\boldsymbol{I}$ is the identity matrix.

When POD is applied to experimental velocity fields consisting of instantaneous snapshots of the flow field that are uncorrelated in time, the temporal coefficients can be found by using the *method of snapshots* proposed by Sirovich (1987). Solving the eigenvalue problem in Equation 2.34 yields these coefficients and the eigenvalues of the modes.

$$\int_T C(t,t')a^n(t')\,dt' = \lambda^n a^n(t) \quad \rightarrow \quad \boldsymbol{CA} = \boldsymbol{A\Lambda} , \tag{2.34}$$

where $\boldsymbol{C}$ is the two-point temporal correlation tensor:

$$C(t,t') = \frac{1}{T}\iiint_V \boldsymbol{u}(\boldsymbol{x},t)\cdot\boldsymbol{u}(\boldsymbol{x},t')\,d\boldsymbol{x} \quad \rightarrow \quad \boldsymbol{C} = \frac{1}{N_T}\boldsymbol{UGU^T} . \tag{2.35}$$

The spatial basis function belonging to $a^n(t)$ can be found by solving:

$$\boldsymbol{\varphi}^n(\boldsymbol{x}) = \frac{1}{T\lambda^n}\int_T a^n(t)\boldsymbol{u}(\boldsymbol{x},t)\,dt \quad \rightarrow \quad \boldsymbol{\Phi} = \frac{1}{N_T}\boldsymbol{\Lambda^{-1}A^T U} . \tag{2.36}$$

The time dependent *spatial* energy of the flow field contained in the ensemble of snapshots, $E_V(t)$ is defined as

$$E_V(t) = \iiint_V \boldsymbol{u}(\boldsymbol{x},t) \cdot \boldsymbol{u}(\boldsymbol{x},t) d\boldsymbol{x} = \sum_{n=0}^{N_M-1} \left(a^n(t)\right)^2 \ . \tag{2.37}$$

The *total* energy of the flow field E_{tot} in the ensemble is the time mean of $E_V(t)$ and this is equal to the sum of all eigenvalues:

$$E_{tot} = \frac{1}{T}\int_T E_V(t)dt = \frac{1}{T}\int_T \sum_{n=0}^{N_M-1} \left(a^n(t)\right)^2 dt = \sum_{n=0}^{N_M-1} \lambda^n \ . \tag{2.38}$$

The time averaging integral can be replaced by an ensemble averaging sum if the snapshots are independent from each other. The eigenvalues λ^n represent the energy content of the structures of mode n, mode 0 being the ensemble averaged flow field. The energy of the fluctuations in the ensemble E_{fluct} can be calculated by summing the eigenvalues of mode 1 to mode $N_M - 1$. E_{fluct} is equal to the spatial integral of the sum of the Reynolds normal stresses:

$$E_{fluct} = \sum_{n=1}^{N_M-1} \lambda^n = \iiint_V \left(\langle u'^2\rangle + \langle v'^2\rangle + \langle w'^2\rangle\right) d\boldsymbol{x} = \iiint_V 2k \ d\boldsymbol{x} \ . \tag{2.39}$$

2.2 Impinging Jets

This section presents an overview of the current knowledge of the flow and heat transfer of both single impinging jets and multiple impinging jet arrays. First, the hydrodynamics of a single jet are described, followed by the flow features of multiple jet arrays. Next, single and multiple jet heat transfer is discussed. The dependencies of the Nusselt number on geometrical parameters and the Reynolds number are discussed on the basis of non-dimensional correlations.

2.2.1 Hydrodynamics of a single jet

Impinging jet structure

Figure 2.1 shows the flow of an impinging jet issuing from a nozzle in a flat plate. An impinging jet is commonly divided into three regions on the basis of the flow structure: the free jet region, the stagnation region, and the wall jet region. For high distances between the nozzle plate and the impingement plate, the free jet region has three zones:

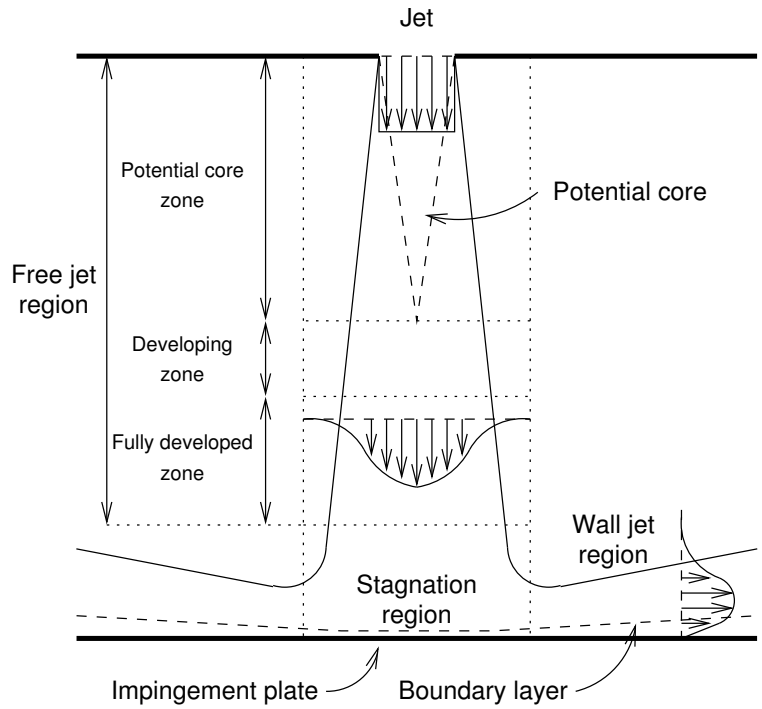

Figure 2.1: Flow configuration of a round impinging jet with regions of different flow regimes.

the potential core zone, the developing zone and the fully developed zone (Viskanta, 1993). These three zones are also shown in Figure 2.1.

Free jet region

In the free jet region, the shear-driven interaction of the exiting jet and the ambient produces entrainment of mass, momentum, and energy. The effects of this on the flow include the development of a non-uniform radial velocity profile within the jet, spreading of the jet, an increase of the total mass flow rate, and the modification of the jet temperature before it impinges upon the surface (only for jets with a temperature different from the ambient).

In the potential core the velocity remains constant and equal to the nozzle exit velocity. Due to growth of the shear layer surrounding the potential core, the core gradually decreases in width. The length of the potential core is dependent on the turbulence intensity at the nozzle exit and the initial velocity profile (Viskanta, 1993). Frequently reported values for the potential core length are between 4 and 6 nozzle diameters (see Livingood and Hrycak, 1973; Kataoka, 1990; Cooper et al., 1993).

Yule (1978) describes the mechanism by which the shear layers are growing and the

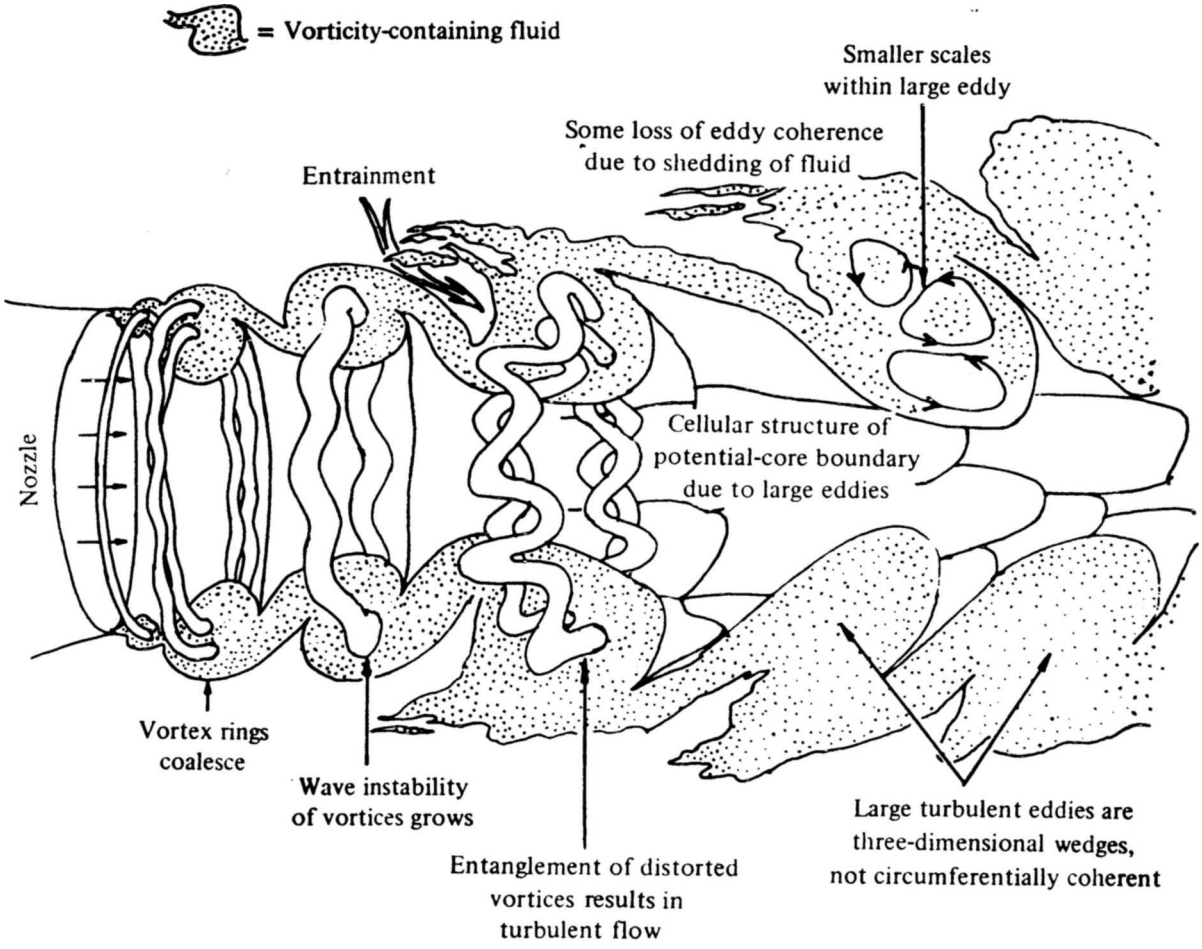

Figure 2.2: Mechanism of eddy formation from ring-vortices in the shear layer of a jet (Yule, 1978).

potential core is breaking down. Though a full description is given by Yule (1978), here only a summary of the most important features is given. The process is sketched in Figure 2.2. Natural instability of the initial shear layer produces a street of vortex rings. As these vortex rings move downstream they generally coalesce with neighboring rings (vortex pairing), so that the scale of the vortex rings and the distance between them increase with distance from the nozzle. There is a considerable random variation in the movements and strengths of the coalescing vortices. Furthermore, the vortex rings lose their phase agreement across the jet as they move downstream. The gradual increase of lateral fluctuations with distance from the nozzle is caused by the gradual, almost linear, growth of orderly wave deformations of the cores of the vortex rings, and this growth also results in a decrease in the level of circumferential cross-correlations. The potential core fluid is alternatively accelerated and decelerated due to the trains of growing vortices (Kataoka, 1990).

In the developing zone the potential core has disappeared. In this zone the axial velocity profile starts decaying and the turbulence level on the jet axis (defined as the ratio between the RMS value of the axial velocity fluctuations and the initial axial velocity) is rising. In the developed zone, starting at about 8 to 10 nozzle diameters downstream of the nozzle, the velocity profile is fully developed (i.e. self-similar) and both the axial velocity and the turbulence level decay (Kataoka, 1990).

Stagnation region

The stagnation region is characterized by the strong curvature of stream lines caused by the flow-obstructing impingement plate. On the basis of the axial mean momentum transport equation, Nishino et al. (1996) show that in this region the axial transport of axial momentum and the turbulent normal stress is converted into static pressure. On the jet center-line the axial momentum transport equation is expressed as follows (in cylindrical coordinates):

$$\langle w\rangle\frac{\partial\langle w\rangle}{\partial z}+\frac{1}{r}\frac{\partial r\langle u'w'\rangle}{\partial r}+\frac{\partial\langle w'^2\rangle}{\partial z}+\frac{1}{\rho}\frac{\partial\langle p\rangle}{\partial z}=0\ , \tag{2.40}$$

where r and z are the radial and axial coordinates, and u and w are the radial and axial velocity components, respectively. Near the impingement plate the term $\partial(r\langle u'w'\rangle)/(r\partial r)$ proved to be negligible on the basis of Particle Tracking Velocimetry (PTV) measurements by Nishino et al. (1996). The contribution of the axial transport of axial momentum is simply due to the deceleration of the axial mean velocity toward the impingement plate. On the other hand, the contribution of the turbulent normal stress implies the occurrence of a substantial momentum transport from the turbulent field to the mean field very near the plate. This contribution of the turbulent normal stress is related to the net negative production of the turbulent kinetic energy near the impingement plate.

In cylindrical coordinates the production of turbulent kinetic energy, P_k, is defined by

$$P_k=-\langle u'^2\rangle\frac{\partial\langle u\rangle}{\partial r}-\langle u'w'\rangle\frac{\partial\langle u\rangle}{\partial z}-\langle u'w'\rangle\frac{\partial\langle w\rangle}{\partial r}-\langle w'^2\rangle\frac{\partial\langle w\rangle}{\partial z}-\langle v'^2\rangle\frac{\langle u\rangle}{r}\ , \tag{2.41}$$

where v is the azimuthal velocity component. On the axis of symmetry the production term can be simplified by using the axisymmetry conditions ($\langle u'^2\rangle=\langle v'^2\rangle$, $\partial\langle u\rangle/\partial r=\langle u\rangle/r$, $\partial\langle w\rangle/\partial r=0$) and the continuity equation ($\partial\langle w\rangle/\partial z=-\partial\langle u\rangle/\partial r-\langle u\rangle/r$):

$$P_k=2\left(\langle w'^2\rangle-\langle u'^2\rangle\right)\frac{\partial\langle u\rangle}{\partial r}\ . \tag{2.42}$$

In other words, the rate of production of the turbulent kinetic energy on the axis of symmetry is proportional to the difference of the turbulent normal stresses. The PTV data by Nishino et al. (1996) show that $(\langle w'^2\rangle-\langle u'^2\rangle)<0$ for distances smaller than 0.1 nozzle diameters from the impingement plate, while $\partial\langle u\rangle/\partial r>0$. Therefore, $P_k<0$ in this region. The pressure diffusion term should compensate for the loss of turbulent kinetic energy caused by the negative production and other terms in this region.

Wall jet region

Poreh et al. (1967) investigated the velocities, turbulence intensities, and wall shear stress in a radial wall jet formed by an impinging circular jet on a flat plate. Due to radial spreading of the wall jet, its velocity will decrease with increasing distance from the stagnation point. Additionally, its height will increase. The authors found for the maximum radial wall jet velocity, U_m:

$$U_m \propto r^{-1.1} \ , \tag{2.43}$$

and for the characteristic wall jet height, δ:

$$\delta \propto r^{0.9} \ . \tag{2.44}$$

Their measurements of turbulence intensities and Reynolds shear stresses indicate that the turbulence level in the wall jet is higher than in boundary layers and pipe flow, suggesting that eddies from the shear layer of the jet penetrated deep into the inner boundary layer increasing the skin friction acting on the wall in this manner. The measurements of the Reynolds' stresses indicate that the turbulent shear stress is not proportional to the local gradient of the mean velocities as assumed by the eddy-viscosity model.

Effect of nozzle shape

The shape of a nozzle has a profound effect on the initial velocity and turbulence profiles of the jets issuing from these nozzles. Slot nozzles (Ichimiya and Hosaka, 1992), rosette nozzles (Huber and Viskanta, 1994b), elliptical nozzles (Arjocu and Liburdy, 1999), and other exotic nozzles are not discussed in this thesis; the focus will be on round nozzles only. Figure 2.3 shows sketches of the mean velocity and turbulent kinetic energy profiles for three different round nozzles. A jet originating from a developed turbulent pipe flow is characterized by a smooth velocity profile. The high turbulent kinetic energy near the edges of the jet originate from wall-friction in the pipe. The bell-shaped nozzle produces a jet with a sharp plug-flow profile and a homogeneous distribution of the turbulent kinetic energy over the jet cross-section. For the jet issuing from a sharp-edged orifice in a flat plate the velocity at the edges is higher than at the center of the jet. Additionally, the cross-section of the jet is smaller and the area-averaged velocity is higher compared to a jet from a bell-shaped nozzle with equal diameter. This is caused by the *vena contracta* effect, which is the contraction of the fluid when it is forced through a sharp-edged orifice. The turbulent kinetic energy profile also shows peaks near the jet edges, because turbulence is generated at the sharp edges of the orifice.

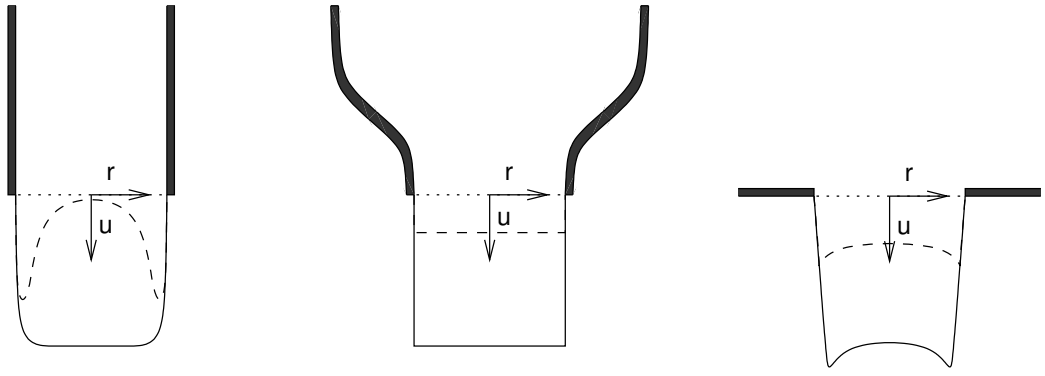

(a) pipe exit (b) bell-shaped nozzle (c) orifice in flat plate

Figure 2.3: Velocity and turbulent kinetic energy profiles in jets issuing from three different nozzles.

2.2.2 Multiple jet flow characteristics

The flow from impinging jets in an array has the same three flow regions as single impinging jets. However, there are some basic differences in the fluid mechanics of single and multiple jets. The individual jets that make up a multi-jet system may be influenced by two types of interactions that do not occur in single jets. First, there is possible interference between adjacent jets prior to their impingement on the surface. The likelihood of such interference effects is enhanced when the jets are closely spaced and when the distance between the nozzle and the impingement plate (nozzle-to-plate distance) is relatively large. Second, there is an interaction due to collision of wall jets associated with the adjacent impinged jets. These collisions are expected to be of increased importance when the jets are closely spaced, the nozzle-to-plate distance is small, and the jet velocity is high (Viskanta, 1993).

The collision of wall jets leads to an interesting flow feature. Barata (1996) presents an investigation of three impinging jets related to the operation of V/STOL aircraft. He identified the existence of an *upwash flow* between two adjacent impinging jets. A schematic of such a flow is given in Figure 2.4. The upwash flow is a result of the above mentioned collision of wall jets. It affects the entrainment of the impinging jets and provides two mechanisms for the discharge of exhaust air (Matsumoto et al., 1999). Part of the exhaust air in the upwash flow is entrained into the adjacent jets, while the other part is discharged along the nozzle plate, avoiding the adjacent jets.

Next to the above mentioned two interaction mechanisms, there is a third one that occurs in arrays of many jets. Exhaust air of the jets in the middle of the array flows outwards, forming a cross-flow for the jets on the edge of the array. For low cross-flow velocities,

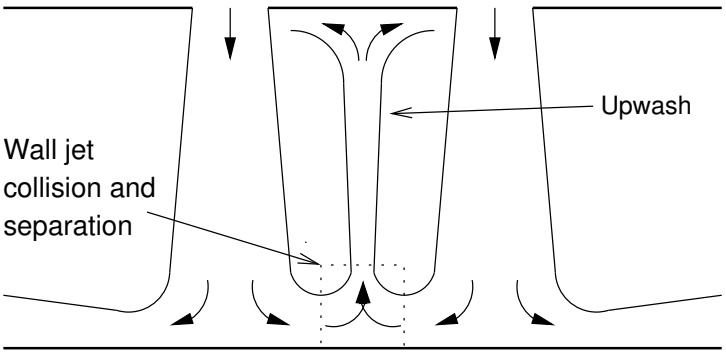

Figure 2.4: The upwash flow created by the collision of two wall jets.

Barata and Durão (2002) found that this gives rise to horse-shoe type vortices wrapped around the jets in the cross-flow. Figure 2.5 presents this horse shoe, which is caused by the interaction between the cross-flow and the wall jet flowing in opposite direction. As a consequence, two counter-rotating vortices trail away from each impingement region. In case of strong cross-flow, impinging jets are deflected and their impingement is delayed or even prevented.

Finally, the spatial arrangement of the nozzles in the array has an influence on the flow characteristics of multiple impinging jets. There are numerous possible spatial arrangements of the nozzles in an array. Figure 2.6 shows the three most common arrangements for round nozzle arrays. The number of nearest neighbors of each nozzle and the impinged area per nozzle differ per arrangement. Therefore, the arrangement of the nozzles determines the way the jets interact with each other.

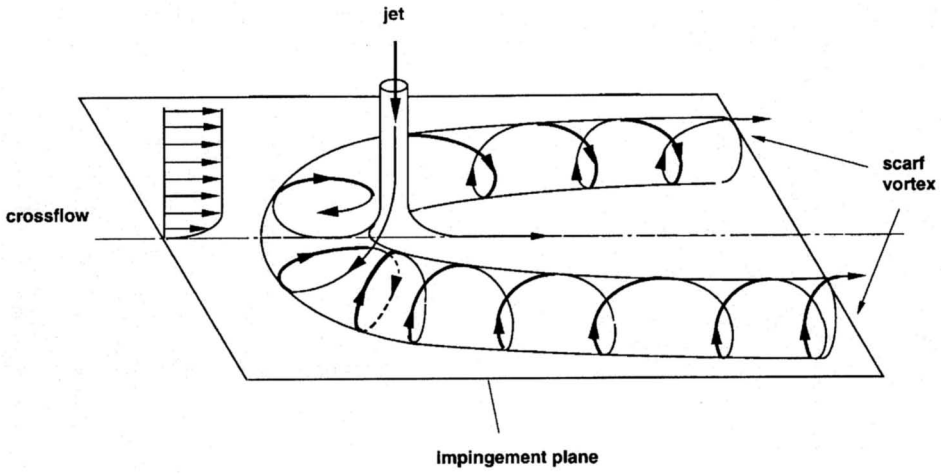

Figure 2.5: Jet impinging on a surface through a low-velocity cross-flow (Barata and Durão, 2002).

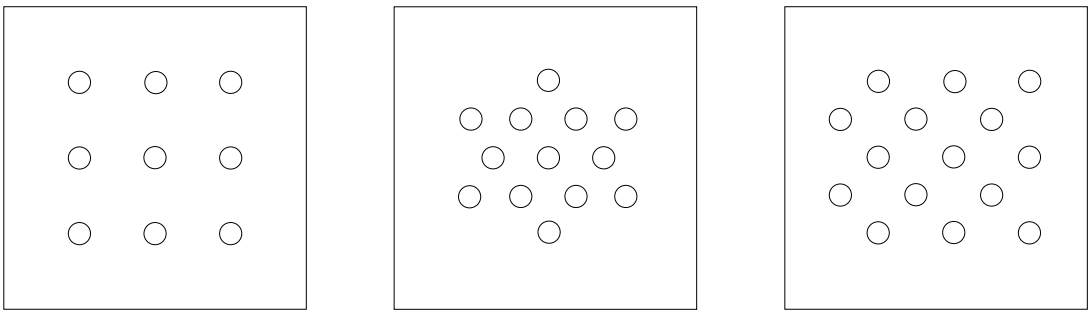

(a) in-line (b) hexagonal (c) staggered

Figure 2.6: Three commonly used nozzle arrangements for impinging jet arrays.

2.2.3 Heat Transfer to a single impinging jet

Many researchers have investigated the heat transfer characteristics of a single impinging jet as a function of the nozzle shape, the nozzle-to-plate distance, the jet Reynolds number, and the presence of external disturbances, such as cross-flow. Below a short description is given of the most important conclusions.

Effect of the nozzle-to-plate distance

Baughn and Shimizu (1989) have investigated the heat transfer characteristics of a single circular turbulent air jet issuing from a long pipe and impinging on a flat stationary surface. They studied the effect of the nozzle-to-plate distance on the radial profiles of the Nusselt number. Figure 2.7 presents their results for a jet with a Reynolds number of 23 750. The Nusselt number (Nu) on the impingement plate is plotted as a function of the radial distance from the stagnation point of the jet (r/D) at four nozzle-to-plate distances (H/D). In general, the Nusselt number is highest in the stagnation point of the jet, for all values of H/D, and gradually decreases with increasing radial distance. This is caused by the growth of the thermal boundary layer in the wall jet and the decrease of wall jet velocity with increasing radial distance.

It is clear that the highest Nusselt number occurs in the stagnation point at H/D=6. This corresponds to the location where the potential core of the jet has just disappeared and turbulence intensities are relatively high. This is confirmed by Kataoka (1990); he suggests that the large scale eddies from the jet shear layer impinge on the surface and destroy the thermal boundary layer. This so-called *surface renewal* effect is dominant in the mechanism for enhancement of the stagnation-point heat transfer. At $H/D > 6$ the strength of the eddies decreases and, correspondingly, the heat transfer decreases.

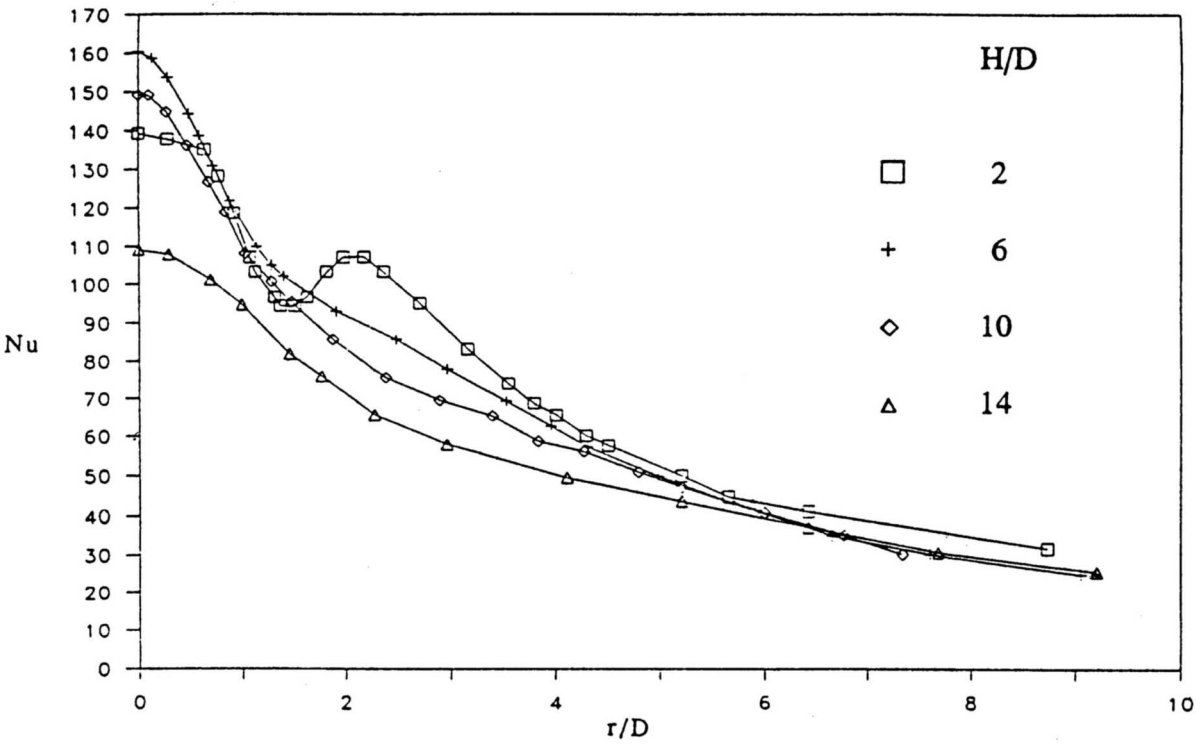

Figure 2.7: Radial distribution of the impingement heat transfer rate from a single impinging jet at different nozzle-to-plate distances (Baughn and Shimizu, 1989).

The secondary maximum appearing at $H/D \approx 2$ is frequently attributed to the laminar-to-turbulent transition of the radial wall jet. Lytle and Webb (1991) show that the location of the secondary maximum coincides with a significant rise in the turbulence intensity of the radial velocity component (see also Gardon and Cobonpue, 1962). Colucci and Viskanta (1996) have found that the location of the secondary maxima is dependent on the Reynolds number, the nozzle-to-plate distance, and the nozzle geometry at low values of H/D (see also Lee and Lee, 2000). The jet is fully turbulent beyond its potential core, so for $H/D \geq 6$ such a transition region does not occur in the wall jet.

Effect of the nozzle shape

Popiel and Boguslawski (1986) measured the heat transfer characteristics of jets issuing from a sharp-edged orifice and from a bell-shaped nozzle at equal Reynolds numbers. The vena contracta causes the sharp-edged orifice to produce a higher center-line velocity than the bell-shaped nozzle. As a consequence, the heat transfer in case of the orifice jet is higher than that in case of the bell-shaped nozzle jet, at all values of r/D. The differences between the local heat transfer profiles will disappear for $H/D > 6$ (Colucci and Viskanta, 1996).

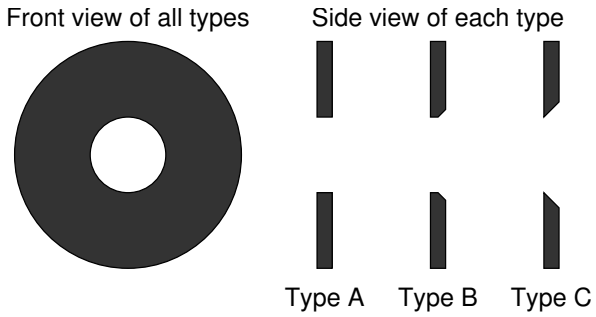

Figure 2.8: Three types of orifices tested in the study of Lee and Lee (2000).

The shape of the *edges* of orifices in flat plates also influences the heat transfer. Lee and Lee (2000) present correlations between the Nusselt number in the stagnation point, the Reynolds number, and the nozzle-to-plate spacing for single round jets issuing from the three types of orifices presented in Figure 2.8. The ratio of the plate thickness and the nozzle diameter is 0.2. The correlations for the three types are:

$$\mathrm{Nu}_{stag} = 0.641\,\mathrm{Re}^{0.566}\,(H/D)^{-0.078} \tag{2.45}$$

for type A,

$$\mathrm{Nu}_{stag} = 0.661\,\mathrm{Re}^{0.571}\,(H/D)^{-0.092} \tag{2.46}$$

for type B, and

$$\mathrm{Nu}_{stag} = 0.698\,\mathrm{Re}^{0.573}\,(H/D)^{-0.116} \tag{2.47}$$

for type C.

It appears that the Reynolds number dependency is comparable for the three types, but the dependency of H/D shows significant differences. The orifice with the sharpest edge (type C) produces a jet with the highest heat transfer, but also the strongest decay with increasing nozzle-to-plate distance. The vena contracta effect is the strongest for this type of orifice, but the sharp edge introduces strong instabilities causing a rapid decay of the potential core.

2.2.4 Heat transfer to multiple jet arrays

Because there are basic differences in the fluid mechanics of single and multiple jets as shown above, the use of experimental heat transfer results of single impinging jets for the design of multiple jet systems is complicated. Additionally, there are more parameters that need to be incorporated in the correlations, such as the jet-to-jet spacing or pitch, s/D, and the arrangement of the nozzles in the array.

Effect of nozzle-to-plate distance

It appears that multiple jet arrays with low values of H/D produce high area-averaged heat transfer coefficients. Metzger et al. (1979) found a maximum average Nusselt number at H/D=1.0, for values of the pitch between 1.67 and 6.67. Huber and Viskanta (1994a) explain that the major degradation of the heat transfer coefficient for the jets in an array is due to adjacent jet interactions which occur before impingement. These interactions increase the decay of the jet velocity and the entrainment of surrounding air (see also Kataoka, 1990). At smaller separation distances, adjacent jet interactions are strongly reduced due to the smaller distance for the interactions to occur.

Gardon and Cobonpue (1962) have found a correlation of the form

$$\mathrm{Nu}_{ave} = 0.993\,\mathrm{Re}^{0.625}\,(H/D)^{-0.625}\,(s/D)^{-0.375} \quad , \tag{2.48}$$

where Nu_{ave} is the area averaged Nusselt number. The H/D dependence is strong, due to the interaction between adjacent jets.

Effect of pitch

Can et al. (2002) investigated the heat transfer from a hexagonal array of round nozzles. They found a maximum area-averaged heat transfer at s/D=5.5, regardless of the value of H/D. At pitches larger than 5.5 the impinged area per jet is large, which causes low area-averaged Nusselt numbers. At pitches smaller than 5.5, there is significant interaction between the jets, causing a decrease of the jet velocity. Although Huber and Viskanta (1994a) used a square array of nozzles, their results agree with this: they found a maximum at s/D=6.

Gardon and Cobonpue (1962) investigated the heat transfer between a flat plate and three adjacent air jets, and compared it to the heat transfer of a single jet. Their conclusion was that, other things being equal, the local heat transfer rates produced by a single jet are everywhere higher than the rates produced by one jet in an array of many (see also Huber and Viskanta, 1994a).

Effect of cross-flow

Obot and Trabold (1987) have investigated the influence of cross-flow on multiple impinging jet heat transfer. Three cross-flow schemes, named minimum, intermediate, and maximum cross-flow, were investigated. The definition of these schemes is shown in Figure 2.9. Obot and Trabold found that cross-flow lowers heat transfer coefficients, because spent fluid from upstream jets in an array can sweep away the downstream jets

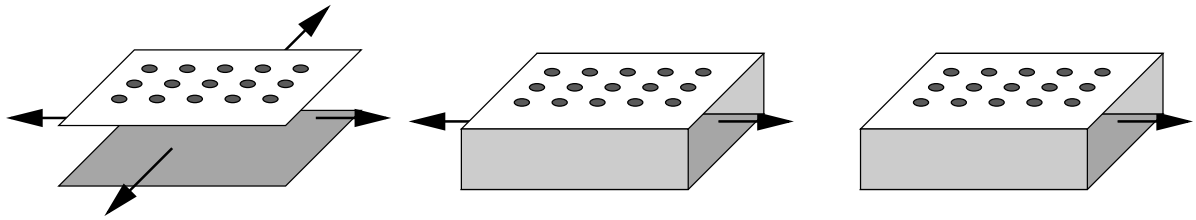

(a) Minimum cross-flow (b) Intermediate cross-flow (c) Maximum cross-flow

Figure 2.9: Definitions of the cross-flow schemes investigated by Obot and Trabold (1987).

and delay impingement. Additionally, they found that the magnitude of this effect increases with increasing nozzle-to-plate distance. The parameters α_1, α_2, and α_3 in the non-dimensional correlation

$$\mathrm{Nu}_{ave} = \alpha_1 \mathrm{Re}^{0.8} \left(H/D\right)^{\alpha_2} \left(s/D\right)^{\alpha_3} \tag{2.49}$$

are dependent on the cross-flow scheme used. The values of α_3 could be stated as 0.815, 0.676, and 0.595 for minimum, intermediate, and maximum cross-flow, respectively. The value of α_2 depends on the pitch and the cross-flow scheme used. The exponent is more negative for strong cross-flow and small values of the pitch. Matsumoto et al. (1999) investigated heat transfer from an impinging jet array with the same cross-flow schemes. Their results agree well with the theory of Obot and Trabold.

Chapter 3

Measurement techniques

In this chapter the techniques will be discussed that were used for velocity and temperature measurements. First, Laser Doppler Anemometry (LDA) and Particle Image Velocimetry (PIV) are presented. Both are non-intrusive velocity measurement techniques, so velocities can be measured without the usage of probes that interfere with the flow. In this way, the measured values of the velocity are not disturbed by any measurement device. Next, Liquid Crystal Thermography (LCT) is discussed. This is a technique to measure the temperature of a surface using the temperature dependence of the color of liquid crystals.

3.1 Laser Doppler Anemometry

In Laser Doppler Anemometry (LDA) the Doppler-shift is determined of light scattered by a small particle that moves with the flow. This Doppler-shift provides a measure of the velocity of the particle, and therefore for the flow velocity. This section focuses on a dual beam LDA system. For a more complete description of the LDA measurement technique the reader is referred to Absil (1995).

3.1.1 Principle of the technique

Figure 3.1 presents a typical dual beam LDA system. A continuous laser produces a light beam with frequency f_0 that is fed to a beam splitter to transform it into two equal intensity beams. A lens focuses the beams in one point, constituting the measurement volume. A seeding particle that crosses the measurement volume will scatter the light of both beams. Due to the Doppler effect the scattered light will consist of two light waves with slightly different frequencies f_{w_1} and f_{w_2}. When these waves are mixed on the

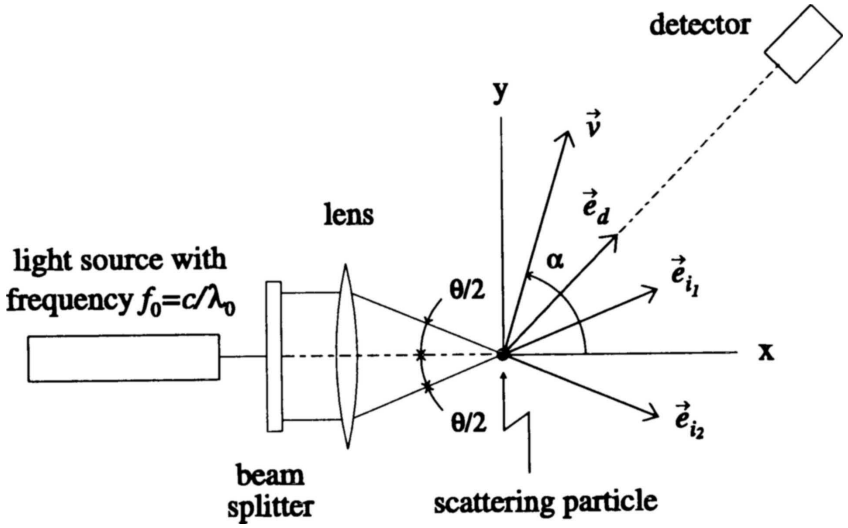

Figure 3.1: Optical arrangement for the dual beam LDA system.

surface of a square-law detector, the output signal oscillates with the difference frequency f_D, which is the Doppler frequency:

$$\left.\begin{aligned} f_{w_1} &= f_0 + \boldsymbol{v}(\boldsymbol{e}_d - \boldsymbol{e}_{i_1})/\lambda_0 \\ f_{w_2} &= f_0 + \boldsymbol{v}(\boldsymbol{e}_d - \boldsymbol{e}_{i_2})/\lambda_0 \end{aligned}\right\} \implies f_D \equiv f_{w_2} - f_{w_1} = \frac{\boldsymbol{v}(\boldsymbol{e}_{i_1} - \boldsymbol{e}_{i_2})}{\lambda_0} , \tag{3.1}$$

where $\boldsymbol{v}$ is the velocity vector of the seeding particle, $\boldsymbol{e}_d$ is the unit vector indicating the direction of the scattered light falling on the detector, $\boldsymbol{e}_{i_1}$ and $\boldsymbol{e}_{i_2}$ are the unit vectors indicating the direction of the incident beams, and λ_0 is the wavelength of the laser light. Figure 3.2 shows the detector output of a typical Doppler burst resulting from a particle passing the measurement volume. After low-pass filtering to remove the noise and high-pass filtering to remove the pedestal a clean Doppler signal remains for the calculation of the passing particle's velocity.

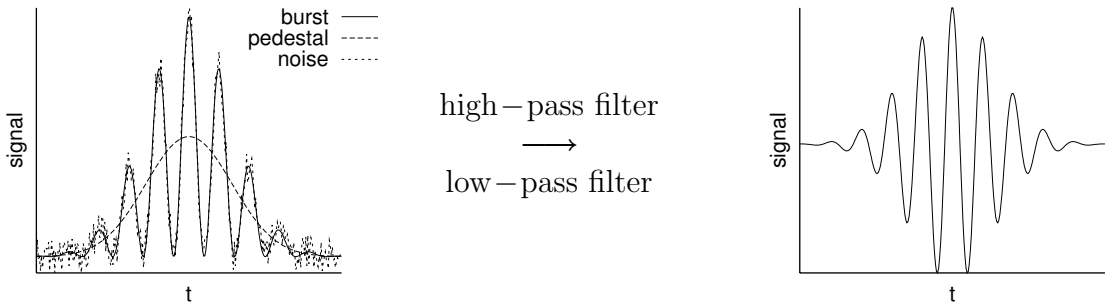

Figure 3.2: Example of the typical detector output for a Doppler burst (left) from which the pedestal and the noise are removed to isolate the Doppler signal (right).

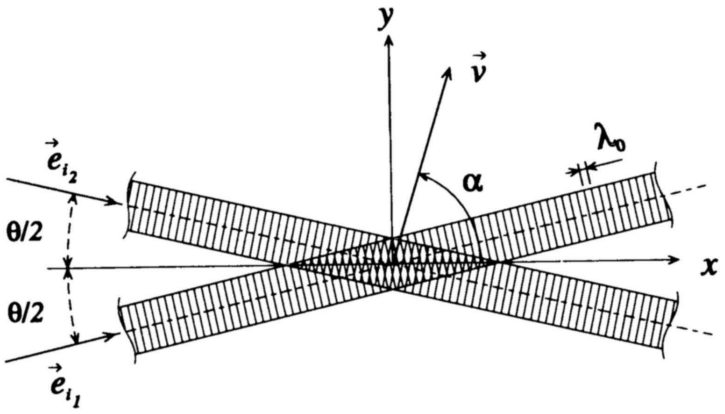

Figure 3.3: The interference pattern of two light waves.

3.1.2 Fringe model

The *fringe model* is an alternative way to derive the relationship between the Doppler frequency and the velocity for a dual-beam LDA system. It is based on the interference pattern formed in the overlap region of the two laser beams as shown in Figure 3.3. Although the fringe model is physically not fully correct (interference takes place on the detector), it provides a convenient way to explain several characteristics of dual-beam systems.

The spacing between the maxima of the light intensity in the interference pattern (the fringes) is defined by

$$d_f = \frac{\lambda_0}{2\sin(\theta/2)} \ , \tag{3.2}$$

where d_f is the fringe spacing and θ is the angle between the light beams. The velocity of a particle can be computed by multiplying the fringe spacing with the measured Doppler frequency.

Velocity measurements with LDA are directionally ambiguous, because the detector cannot discern between two particles that move with velocities $\boldsymbol{v}$ and $-\boldsymbol{v}$ through the measurement volume. To resolve this problem a technique called *frequency pre-shifting* can be applied. The frequency of one of the incident beams is shifted by a constant value f_s. This can be achieved using an acousto-optic Bragg cell. Due to the frequency shift the relationship between Doppler frequency and particle velocity becomes:

$$f_D = f_s + \frac{\boldsymbol{v}(\boldsymbol{e}_{i_1} - \boldsymbol{e}_{i_2})}{\lambda_0} \qquad (f_s \ll f_0) \ . \tag{3.3}$$

If f_s is chosen larger than the Doppler frequency corresponding to the smallest velocity in the flow, each value of $|f_D|$ is uniquely related to one velocity value and the directional

ambiguity is removed. In the fringe model pre-shifting results in a fringe pattern moving with a velocity equal to $f_s d_f$.

To measure two components of the velocity, two LDA systems can be combined. The light from the continuous laser source is first split into its constituent colours. Many practical LDA systems are based on an Argon-ion laser that produces three useful lines at 514.5 nm, 488 nm, and 476.5 nm. Two lines are then used as light sources for the individual channels of the two-component LDA system. The two laser beam pairs are aligned such that their measurement volumes overlap, while the fringe patterns are perpendicular. The measurement volumes of both beam pairs should coincide in order to have valid measurements of the velocity. If the measurement volumes do not overlap in space, there is a possibility that the two measured velocity components do not originate from the same particle. A further measure to prevent this is the use of a *coincidence window*. This is a short period of time in which both channels should produce a Doppler burst. If only one of the channels produces a burst the sample is discarded.

3.1.3 Tracer particles

The tracer or seeding particles need to be small enough to follow the flow faithfully. Too large or too heavy particles exhibit a delayed response to rapid changes of the fluid velocity. The characteristic time scale associated with this lagging behavior is defined by Equation 3.4:

$$\tau_l = \frac{(\rho_p - \rho) d_p^2}{18\eta} \ , \tag{3.4}$$

where τ_l is the particle lag time, ρ_p is the density of the particle, ρ is the density of the fluid, d_p is its diameter, and η is the dynamic viscosity of the fluid. For liquid flows the diameter of the particles is typically of the order of 10–100 μm and for gas flows it is typically 0.1–10 μm.

Gas flows can be seeded by dispersing prefabricated solid particles into the flow or by generating tiny liquid droplets in an atomizer. One way of generating aerosol seeding is to use the Laskin nozzle depicted in Figure 3.4. Various liquids such as olive oil or mixtures of glycerol and water can be used to generate seeding with this apparatus. The liquid is placed inside the air-tight container and pressurized air is supplied to the nozzles. This air will atomize the liquid and produce bubbles containing an aerosol of particles. These bubbles will rise to the surface, after which the smallest particles are transported out of the container while the larger particles collide with the impactor plate and fall back into the liquid bulk. A pressure difference of typically 0.5–1.5 bar between the inlet and outlet of the container is needed to produce seeding with a mean diameter of 1 μm.

In general it can be said that the light scattered by small particles is a function of the ratio of the refractive index of the particles and that of the surrounding medium, the

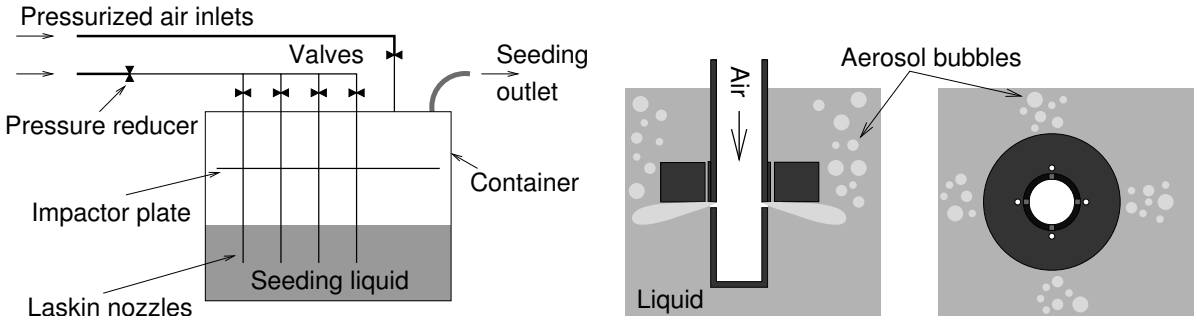

(a) seeding generator.

(b) Laskin nozzles (front and top view).

Figure 3.4: A seeding generator using Laskin nozzles (adapted from Raffel et al. 1998).

particle size, and their shape and orientation. Furthermore, the intensity of the scattered light depends also on polarization and observation angle (Raffel et al., 1998). Figure 3.5 presents the polar distribution of the scattered light intensity for oil particles of 1μm according to Mie's scattering theory. Notice that the intensity scale is logarithmic.

There is an optimum particle size for a given incident laser light intensity. Because both the particle lag time and the scattering intensity are proportional to the square of the particle size, a larger particle will yield a higher scattered light intensity, but it will follow the flow less faithfully. Additionally, the size of the seeding particles in LDA is also limited by the fringe spacing (Absil, 1995). For particles with a size equal to or greater than the fringe spacing the height of the Doppler signal is diminished which affects the signal-to-noise ratio (SNR).

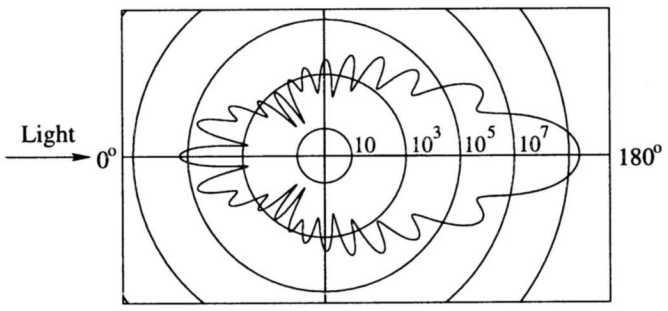

Figure 3.5: Light scattering pattern around a 1μm oil particle in air (Raffel et al., 1998).

3.1.4 Velocity bias

To explain the velocity bias, consider a measuring volume that is placed in a time varying flow. The projection of the measuring volume on the plane normal to the instantaneous velocity vector $\boldsymbol{v}$ is A_p. The expected number of particles that pass through the measuring volume per unit time is then given by

$$\nu_p = \|\boldsymbol{v}\| A_p C_p \ . \tag{3.5}$$

Here, C_p is the particle concentration (the number of particles per unit volume), which is supposed to be constant in flows with constant density. Note that ν_p is a time varying quantity. It is seen from Equation 3.5 that ν_p is proportional to the volume flux through the measuring volume. Hence, the probability of measuring a particle with a high velocity is higher than the probability of measuring a low-velocity particle. As a result, the histogram of measured velocity samples will be biased towards high velocities and statistical quantities that are computed as arithmetic averages will be erroneous (Tummers, 1999).

There are two categories of techniques to correct for velocity bias. It can be done either by altering the sampling technique for acquiring the velocity data, or by using weight functions for calculating statistics in a post-processing process. The former category of techniques replaces the discrete, randomly-sampled time series by a continuous signal that is subsequently re-sampled at regular time intervals. However, it is widely known that these *reconstruction methods* require very high sampling rates, rendering them of limited importance for LDA in gas flows. The latter category uses the randomly-sampled data to calculate statistics using weight factors. The ensemble mean velocity and the variance of the velocity fluctuations are defined as follows:

$$\langle u \rangle = \frac{\sum_{i=1}^{N} w_i u_i}{\sum_{i=1}^{N} w_i} \ , \tag{3.6}$$

$$\langle u'^2 \rangle = \frac{\sum_{i=1}^{N} w_i u_i'^2}{\sum_{i=1}^{N} w_i} \ , \tag{3.7}$$

where w_i is the weight factor for the i^{th} sample, u_i is the velocity of the i^{th} sample, and $u_i' = u_i - \langle u \rangle$.

Three frequently used weight factors are inverse velocity, transit time, and interarrival time. For inverse-velocity weighting the weight factor is defined as the reciprocal value of the expected data rate presented in Equation 3.5 (McLaughlin and Tiederman, 1973). For a two-component system it is simplified to the reciprocal of the velocity vector length in two dimensions. However, due to the missing third velocity component, this weight factor will be systematically high, resulting in an over-correction of the velocity bias (Tummers, 1999). The second possibility is transit time weighting (Hoesel and Rodi, 1977). The transit time is the time for a particle to pass the measurement volume.

Petrie et al. (1988) argued that the transit times of the particles are dependent on the trajectory of the particle through the measurement volume. As a result, the individual transit times exhibit a large scatter around their mean value, thereby increasing the statistical scatter of the mean velocity and the variance of the velocity fluctuations. For 2D velocity weighting the inverse velocity and the transit time will produce almost identical results under the condition that the number samples was sufficient (Tummers, 1999). The final possibility is interarrival-time weighting (Barnett and Bentley, 1974). The interarrival time is defined as the time between two consecutive particles passing the measurement volume. An important advantage of the interarrival-time weighting over the inverse velocity weighting is that it can be used when the particle concentration is correlated with the instantaneous velocity. An important disadvantage is that it can be used only at very high data rates, similar to the reconstruction methods. In the present project transit-time weighting will be used.

3.2 Particle Image Velocimetry

Particle Image Velocimetry, or PIV, is a whole field velocity measurement technique. In other words, instantaneous velocities are measured in one plane in a flow at an instant in time. Small tracer particles added to the flow are illuminated in a plane at least twice within a short time interval. The light scattered by the tracer particles is recorded by a camera either on a single frame or on a sequence of frames. By determining the displacement of particle patterns during the time interval velocities can be evaluated.

In this section the basics will be discussed of single exposure double frame PIV in turbulent air flows. A more complete review of the technique can be found in Westerweel (1993) and Raffel et al. (1998).

3.2.1 Principles of the technique

Tracer particles

The requirements for the seeding particles for PIV are generally equal to those for LDA. Firstly, they need to follow the flow faithfully, which means they should have a lag time (Equation 3.4) smaller than the typical flow time scales. Secondly, they must scatter light with sufficient intensity. Particles crossing the light sheet in the flow scatter the light that is subsequently recorded by a CCD sensor. Since the obtained particle image intensity and therefore the contrast of the PIV recordings is directly proportional to the scattered light power, it is often more effective and economical to increase the images intensity by properly choosing the scattering particles than by increasing the laser power.

Light source

The particles are illuminated by a pulsed light sheet. The duration of the pulse should be short with respect to the typical timescales associated with the flow to avoid motion blurring of the particle images. During this short pulse the light scattered from the small tracer particles will expose the CCD sensor, implying a high power light source. In most PIV systems Nd:YAG lasers (frequency doubled, so λ= 532 nm) are used for this task, because they can provide pulses with a duration in the order of several nanoseconds with constant pulse energy. An additional advantage of the use of lasers is their monochromaticity allowing easy collimation of the light beam.

Because Nd:YAG lasers have a typical repetition rate of 10 to 15 Hz while in PIV the time interval between pulses is typically a few microseconds, two lasers are required. To this end the dual cavity Nd:YAG lasers were developed. These lasers have two laser cavities of which the beams are combined with precision optics. Figure 3.6 shows a schematic representation of the dual cavity laser.

The light from the laser is passed through a combination of lenses that transform the beam into a sheet. One example of a possible lens combination is sketched in Figure 3.7. A concave cylindrical lens is used to create the sheet from the laser beam. A subsequent convex spherical lens can be used to control the sheet thickness and at the same time it limits the spreading of the sheet.

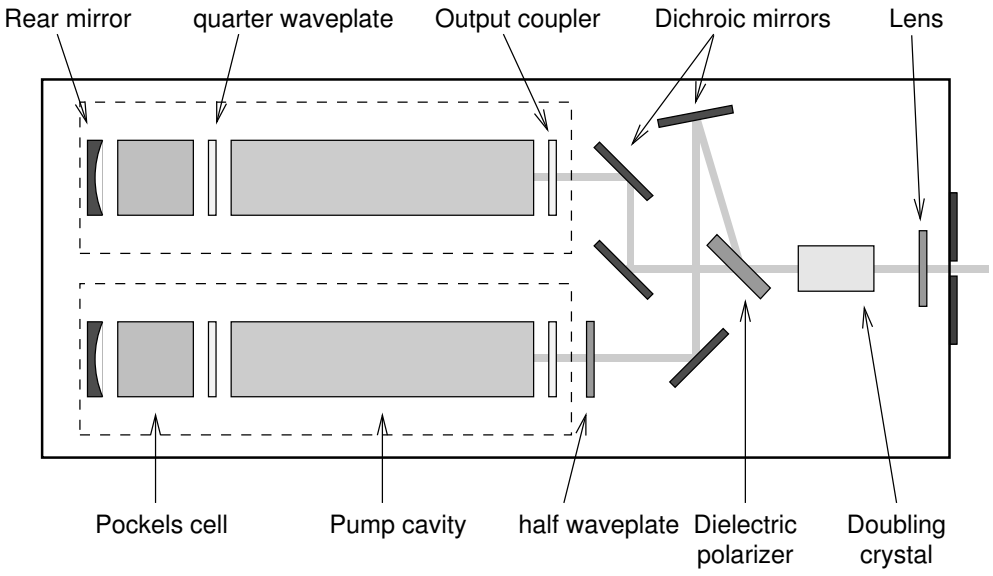

Figure 3.6: Sketch of a typical dual cavity Nd:YAG laser.

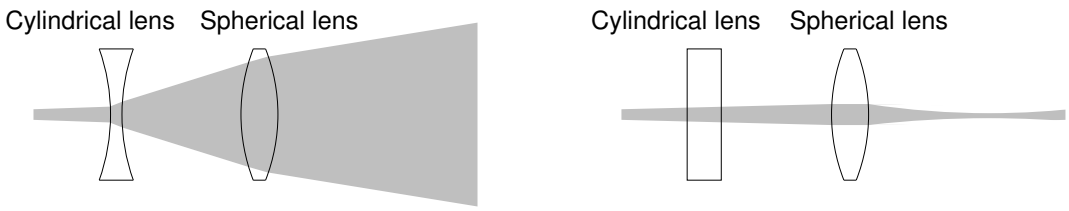

(a) side view. (b) top view.

Figure 3.7: Sketch of a possible configuration for the sheet optics.

Diffraction limited imaging

The particles can be considered point sources of light because of their small size. The projection of a point source onto a screen or image sensor via a lens yields a Fraunhofer diffraction pattern known as the Airy disk. This is the impulse response function of an aberration-free lens. The diameter of the Airy disk d_s represents the smallest particle image (i.e. pulse response) that can be obtained for a given imaging configuration (Raffel et al., 1998):

$$d_s = 2.44 f^{\#}(M+1)\lambda \ , \tag{3.8}$$

where $f^{\#}$ is the numerical aperture of the imaging lens (i.e. the ratio of the focal length f and the aperture diameter D_a), M is the image magnification factor, and λ is the wavelength of the light. The diameter of the particle image on the recording sensor d_τ can be estimated using:

$$d_\tau = \sqrt{(M d_p)^2 + d_s^2} \ . \tag{3.9}$$

For a typical PIV system using a Nd:YAG laser (λ= 532 nm), a numerical aperture of 2.8, and a magnification factor of 0.1 the diameter of the Airy disc is 4.0 μm. This means that the image diameter of 1 μm particles is also 4μm. The image diameter of the particles is therefore controlled by the optics, explaining the term *diffraction limited imaging*. Because the magnification factor is determined by the sizes of the desired field of view and the imaging sensor, and the wavelength of light is fixed by the choice of laser, the particle image size can be controlled by the numerical aperture. By reducing the aperture diameter the numerical aperture will increase and the particle images will be larger, but the intensity of the light collected by the imaging sensor will decrease yielding images with lower contrast.

Image acquisition

Most modern PIV systems use Charge Coupled Device (CCD) cameras for the acquisition of particle images. A CCD chip consists of small semi-conductor cells (typically 7-10 μm)

called pixels that can convert light into electric charge. A modern CCD chip contains typically one to four million pixels.

CCD chips need to be cooled to keep the noise generated by thermal effects in the semiconductor below a certain level. Read-out noise forms another source of error. This limits the number of images that can be acquired per unit of time, because this type of noise increases with the read-out frequency of the chip. The typical CCD sensor has a maximum image acquisition rate of about 10 to 15 images per second.

In single exposure double frame PIV a camera is needed that can acquire two images within a time interval of several microseconds. A special kind of CCD camera was developed for this application. In these cameras an image buffer integrated on the CCD chip temporarily stores the first image while the second image is acquired. After the acquisition both images are stored in a computer for the calculation of velocities.

Data reduction

For the calculation of velocity distributions from PIV images, the images are subdivided into small regions called interrogation areas. In these areas it is assumed the velocity of the flow is uniform, so the particle pattern in the interrogation area will not be distorted during the time interval between the two exposures. Each interrogation area in the first image is correlated with the corresponding area in the second image, as illustrated in Figure 3.8. The calculation of the cross-correlation is done in a fast and computationally efficient way according to the correlation theorem (Priestley, 1981) using Fast Fourier Transformation (FFT). First, both interrogation areas are Fourier transformed (denoted by FT in the figure). Next, the transformed area of image 1 is multiplied by the complex conjugate of the transformed area of image 2, i.e. $\hat{I} \cdot \hat{I}^*$ is computed. The quantity $\hat{I} \cdot \hat{I}^*$ is then inverse transformed (FT^{-1}). The resulting correlation function is shown in Figure 3.9. R_D is the displacement correlation peak. This peak represents the cross-correlation between images of the same particles in the first and the second image. R_C is the convolution of the mean image intensities and R_F is the fluctuating noise component. The location of the displacement correlation peak with respect to the origin

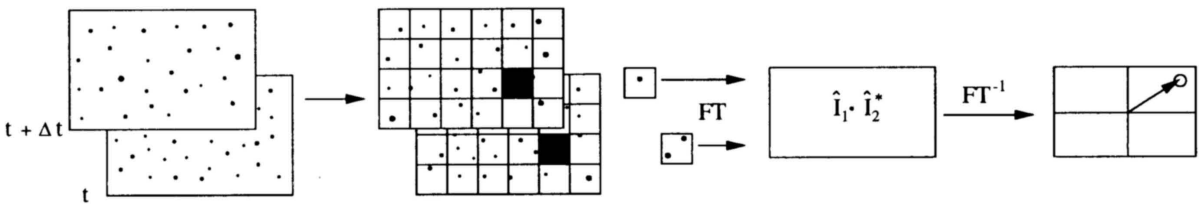

Figure 3.8: Schematic representation of the cross-correlation of interrogation areas (Raffel et al., 1998).

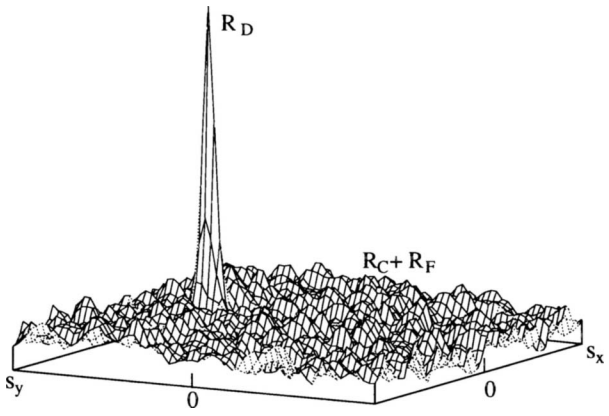

Figure 3.9: An example of a cross-correlation function (Raffel et al., 1998).

of the correlation function represents the mean in-plane particle displacement vector $\boldsymbol{s}$ from which the local mean velocity vector $\boldsymbol{v}$ can be determined using:

$$\boldsymbol{v} = \frac{\boldsymbol{s}}{\Delta t} \ , \tag{3.10}$$

where Δt is the time separation between the two images.

Criteria for accurate velocity measurements

The height and the width of correlation peaks depend on the particle image diameter, the number of particle images present in the interrogation area in both images, and the velocity gradient over the interrogation area. To be able to determine the velocity in an interrogation area sufficiently accurate a number of criteria were defined with regard to the particle image pair density and the velocity gradient over an interrogation area:

- The particle image pair density is the number of particle image pairs per interrogation area, i.e. the number of particles of which images can be found in corresponding interrogation areas in both images. It can be calculated from the concentration of particle images s in one interrogation area, N_I, the fraction of particle images lost due to in-plane displacement, $(1-F_I)$, and the fraction lost due to out-of-plane displacement, $(1-F_O)$. F_I and F_O are equal to one if no pairs were lost and zero if all the pairs are lost. The particle image pair density $N_I F_I F_O$ should exceed 5 to assure a probability of 95% for the detection of at least two particle image pairs (Keane and Adrian, 1992).

  To achieve minimum in-plane loss of pairs (i.e. $F_I \rightarrow 1$) the dimensionless maximum displacement of the particle image pattern should not exceed 0.25:

$$\frac{M|v_{max}|\Delta t}{d_I} < 0.25 \ , \tag{3.11}$$

where v_{max} is the maximum in-plane velocity and d_I is the width of an interrogation area on the image plane. For the out-of-plane displacement a similar criterion was defined ($F_O \rightarrow 1$):

$$\frac{|w_{max}|\Delta t}{\Delta z_0} < 0.25 \ , \tag{3.12}$$

where w_{max} is the maximum out-of-plane velocity and Δz_0 is the thickness of the laser sheet.

- According to Keane and Adrian (1990) the width and the height of the displacement correlation peak strongly depend on the velocity gradient over the interrogation area. In case of strong velocity gradients the peak broadens and its amplitude is diminished, decreasing the likelihood of detecting the displacement peak. This effect is called *detection bias*. Acceptable detection probability exists if

$$\frac{M\Delta u\Delta t}{d_\tau} \leq 1 \ , \tag{3.13}$$

where Δu is the velocity difference over the interrogation area as a consequence of the velocity gradient.

A second effect of velocity gradients is the *gradient bias*. It occurs because the correlation is biased towards the faster moving particle within the measurement volume. This means that the correlation peak is statistically biased towards velocities lower that the average velocity in the interrogation area. The criterion that needs to be satisfied to minimize this effect is

$$\frac{M\Delta u\Delta t}{d_I} < 0.05 \, . \tag{3.14}$$

Displacement estimation

After cross-correlating interrogation areas in the two images the displacement correlation peak is detected by searching for the maximum of the correlation function. Due to the discretization of the function the location of the correlation peak can only be determined in integer numbers of pixels with an uncertainty of ± 0.5 pixels. This can be remedied by using a subpixel displacement estimator. This estimator uses pixels in the direct neighborhood of the correlation peak to make a more accurate estimate of its position. Because correlation peaks can be narrow, only three pixels are taken into account, hence the name three-point estimators.

Most three-point estimators fit a Gaussian function through the three pixels. The particle images have an Airy shaped intensity distribution that can be approximated very well by a Gaussian. The correlation between two Gaussian functions is also Gaussian, so the best fit for the correlation function is a Gaussian. The Gaussian peak estimator is

defined by:

$$x_0 = i + \frac{\ln R_{i-1,j} - \ln R_{i+1,j}}{2\ln R_{i-1,j} - 4\ln R_{i,j} + 2\ln R_{i+1,j}} \ , \tag{3.15}$$

$$y_0 = j + \frac{\ln R_{i,j-1} - \ln R_{i,j+1}}{2\ln R_{i,j-1} - 4\ln R_{i,j} + 2\ln R_{i,j+1}} \ , \tag{3.16}$$

where x_0 and y_0 are the precise coordinates of the peak, i and j are the integer coordinates of the peak, and $R_{i,j}$ is the value of the correlation function at (i, j).

If the size of the particle images is smaller than or equal to the size of one pixel, the correlation peak will be very narrow. As a consequence, a bias error is introduced in the three-point estimator. The resulting velocity data will be biased towards integer displacements yielding a multi-modal velocity histogram. This effect is known as *peak locking* and it can be avoided by adjusting the particle image size (e.g. by choosing another camera lens or increasing the numerical aperture). The optimum particle size is around 2 pixels (Willert, 1996).

Data validation

After the analysis of the PIV images some of the velocity vectors are obviously incorrect, because their magnitude and direction strongly deviates from those of their direct neighbors. These *spurious* vectors result from the incorrect detection of displacement correlation peaks, because they are of the same order of magnitude as the noise in the correlation function. Spurious vectors are often found in regions where one or more of the above mentioned criteria is not satisfied or near walls, where wall reflection of the incident laser light dominates the image. Figure 3.10 shows an example of a vector plot of raw velocity data in a turbulent jet.

There are several statistical methods to detect the spurious vectors and remove them from the data set (for details see Westerweel, 1994). Of these methods the local median filter is the most popular technique. For each vector a 3×3 neighborhood is selected and the median is calculated of the eight vectors surrounding the center vector. The median value of a set of vectors is defined here as either with respect to vector length or with respect to its individual components. The difference between the median vector and the center vector should remain within a certain limit:

$$\|\boldsymbol{v}_{i,j} - \tilde{\boldsymbol{v}}_{\mathrm{surr}(i,j)}\| < \alpha\sigma_{\mathrm{surr}(i,j)} \ . \tag{3.17}$$

where $\boldsymbol{v}_{i,j}$ is the velocity vector on position (i, j) in the grid, $\tilde{\boldsymbol{v}}_{\mathrm{surr}(i,j)}$ is the median of the vectors surrounding the one at (i, j), $\sigma_{\mathrm{surr}(i,j)}$ is the standard deviation of their magnitudes, and α is a parameter determined on the basis of a confidence interval. Because $\sigma_{\mathrm{surr}(i,j)}$ is not known, the sample standard deviation $s_{\mathrm{surr}(i,j)}$ can be used. This method is similar to the median filtering technique from image processing described in Section 3.3.4 and will be discussed in more detail there.

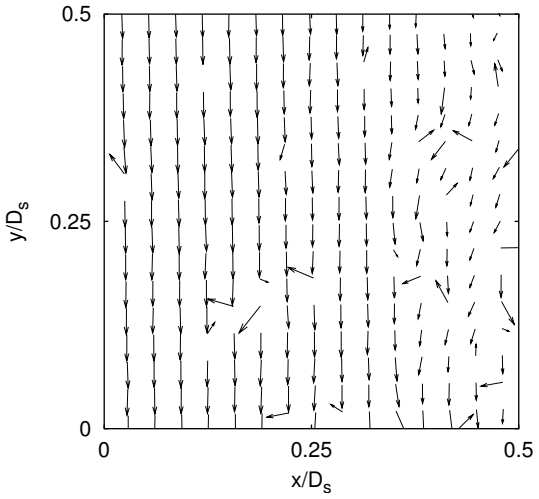

Figure 3.10: Example of raw velocity data resulting from PIV measurements in a turbulent jet.

The probability of finding a spurious vector in the direct neighborhood of another spurious vector is given by a binomial distribution. Usually the aim in a PIV experiment is to have a valid data yield of 95% or more (i.e. less than 5% spurious vectors). In that case the probability of finding two or more neighboring spurious vectors is less than 14.9% (Westerweel, 1994).

After detection the spurious vectors are discarded and the empty spaces filled with vectors resulting from a bilinear interpolation procedure of the neighboring vectors. An additional advantage of bilinear interpolation is that it fulfills continuity (Raffel et al., 1998).

3.2.2 Advanced techniques

Adaptive cross-correlation

The velocities resulting from PIV measurements are affected by measurement noise that is due to the finite number of particle images within the interrogation area and the number of pixels by which the interrogation area is discretized. Westerweel et al. (1997) have shown that the measurement error due to this kind of noise is practically independent of the displacement, except for small displacements (i.e. $\frac{1}{2}$ px) where the measurement error is directly proportional to the displacement. This can be used to improve the precision of PIV measurements.

First the integer displacements are estimated using the cross-correlation procedure de-

scribed above. After filtering out the spurious vectors and interpolating the empty spaces, the procedure is repeated, but now the interrogation areas in the second image are offset with respect to the first image by the local integer displacement. Effectively more particle image pairs are found, so $F_I \rightarrow 1$. Typically, the adaptive correlation has to be done twice to obtain convergence of the offset vectors. The residual displacement is now between $-\frac{1}{2}$ px and $\frac{1}{2}$ px, ensuring low measurement error.

Westerweel et al. (1997) show that the signal-to-noise ratio becomes independent from the fluctuating displacement for low turbulence flows, while there is a threefold improvement of the signal-to-noise ration for high turbulence flows. Additionally, the maximum measurable velocity of the PIV measurement no longer depends on the size of the interrogation area, increasing the dynamic range.

Grid refinement

In order to study flows on a range of length scales that is as wide as possible, the grid on which the the velocity vectors are determined should be as fine as possible. However, standard evaluation schemes cannot use small interrogation areas without losing the correlation signal due to the larger displacements. This can be solved by integrating grid refinement and adaptive cross-correlation.

First a cross-correlation procedure is conducted using large interrogation areas (128×128 or 64×64) that do not overlap each other. Because Fourier transforming large interrogation areas is time consuming, it is also possible to de-sample the images and take smaller interrogation areas. Next the spurious vectors are detected and substituted by interpolated vectors. The resulting vector field is interpolated to a finer grid and the vectors are used as interrogation area offsets for an adaptive cross-correlation on the finer grid. After substituting the spurious vectors again the procedure can be repeated until the desired resolution is obtained. In the last step it is also possible to use overlapping interrogation areas to increase the resolution even further. This procedure is called the *Window Displacement Iterative Multigrid* (WIDIM) method and it is discussed in detail by Scarano and Riethmuller (1999).

Differential quantities

Many terms in the Navier-Stokes equation and the k-equation, and some structure identification methods, are based on spatial derivatives of the velocity field structure identification methods. The calculation of these derivatives implies a certain continuity and smoothness of the velocity field. Because the velocity field is discrete, it needs to be interpolated by fitting an analytical function through the data or by using one of the many discrete differential operators available to estimate the derivatives. Table 3.1 shows a

Operator	Implementation	Accuracy	Uncertainty
Forward difference	$\left(\frac{du}{dx}\right)_{i+1/2} \approx \frac{u_{i+1}-u_i}{\Delta x}$	$\mathcal{O}(\Delta x)$	$\approx 1.41\frac{\delta u}{\Delta x}$
Backward difference	$\left(\frac{du}{dx}\right)_{i-1/2} \approx \frac{u_i-u_{i-1}}{\Delta x}$	$\mathcal{O}(\Delta x)$	$\approx 1.41\frac{\delta u}{\Delta x}$
Centered difference	$\left(\frac{du}{dx}\right)_{i} \approx \frac{u_{i+1}-u_{i-1}}{2\Delta x}$	$\mathcal{O}(\Delta x^2)$	$\approx 0.71\frac{\delta u}{\Delta x}$
4^{th} order Richardson	$\left(\frac{du}{dx}\right)_{i} \approx \frac{u_{i-2}-8u_{i-1}+8u_{i+1}-u_{i+2}}{12\Delta x}$	$\mathcal{O}(\Delta x^4)$	$\approx 0.95\frac{\delta u}{\Delta x}$
Least squares	$\left(\frac{du}{dx}\right)_{i} \approx \frac{2u_{i+2}+u_{i+1}-u_{i-1}-2u_{i-2}}{10\Delta x}$	$\mathcal{O}(\Delta x^2)$	$\approx 0.32\frac{\delta u}{\Delta x}$

Table 3.1: Five examples of difference schemes for the estimation of velocity gradients (after Raffel et al., 1998).

few possible schemes with their accuracy and the measurement uncertainty. Δx is the grid spacing, and δu is the measurement noise in the u-component of the velocity

In discrete derivative computation a compromise needs to be made between the order of the filter, the number of points used for the derivation, the frequency response and the noise amplification. Generally, for classical finite difference schemes, the order increases with the number of points used for the computation. The frequency response increases when the truncation error decreases, which is directly linked to the order of the filter (Foucaut and Stanislas, 2002). However, noise amplification also increases with the order of the filter, so there is an optimum for the order of the filter. By means of spectral analysis Foucaut and Stanislas (2002) show that a second-order central difference scheme is enough to obtain a good accuracy of the derivative.

The grid in PIV data is not necessarily equidistant in space, because of perspective projection for instance. Another possibility is that the grid is rotated with respect to physical coordinates. Figure 3.11 shows both situations. If the derivatives are calculated with respect to the grid of the image, the grid coordinates need to be transformed in order to have accurate estimates of the derivatives with respect to physical coordinates. For velocity component u at position (i, j) in the grid the transformation is as follows:

$$\begin{pmatrix} \frac{\partial u}{\partial x} \\ \frac{\partial u}{\partial y} \end{pmatrix}_{i,j} = \begin{pmatrix} \frac{\partial x}{\partial i} & \frac{\partial y}{\partial i} \\ \frac{\partial x}{\partial j} & \frac{\partial y}{\partial j} \end{pmatrix}^{-1}_{i,j} \begin{pmatrix} \frac{\partial u}{\partial i} \\ \frac{\partial u}{\partial j} \end{pmatrix}_{i,j} = \boldsymbol{J}_{i,j} \begin{pmatrix} \frac{\partial u}{\partial i} \\ \frac{\partial u}{\partial j} \end{pmatrix}_{i,j}, \tag{3.18}$$

where x and y are physical coordinates, i and j are grid coordinates, and $\boldsymbol{J}_{i,j}$ is the Jacobian on position (i, j). The elements of the Jacobian can be calculated from the coordinate mapping that was made during the measurements by acquiring an image of a grid with known spacing. The derivatives with respect to the grid coordinates are estimated using a finite difference scheme.

As was mentioned above, the resolution of PIV can be increased by using overlapping

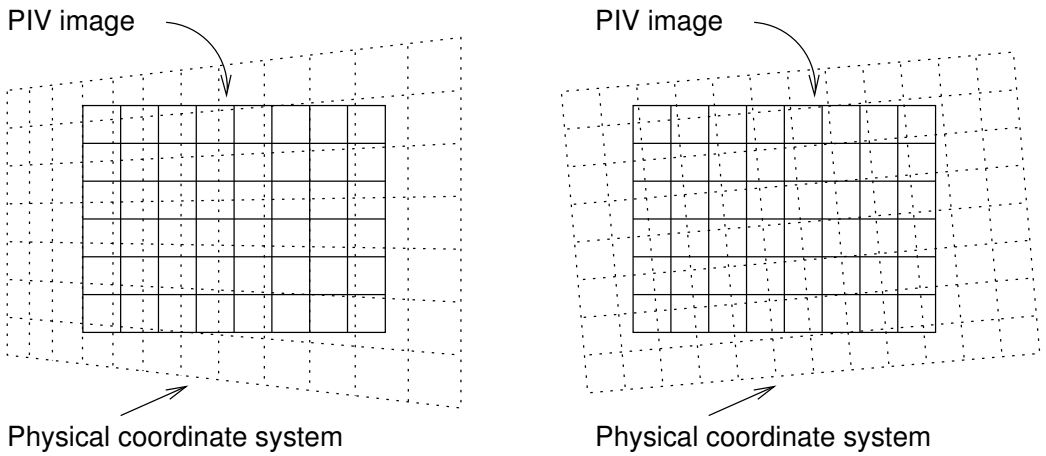

(a) perspective projection (b) rotation

Figure 3.11: Alignment mismatch for PIV measurements

interrogation areas. Because this causes neighboring velocity vectors to be correlated, the estimates of the derivatives will also be affected in some cases. Raffel et al. (1998) show that if the interrogation areas are 50% overlapping, the central difference scheme will not be affected, because data are used from non-overlapping areas.

3.3 Liquid Crystal Thermography

Thermochromic liquid crystals are organic substances that change color as a function of temperature. This property can be used to measure the surface temperature of objects or the internal temperature of liquid flows. This section presents a brief discussion of the properties of these crystals, followed by a detailed explanation of the calibration and measurement procedures.

3.3.1 Liquid Crystals

The liquid crystal phase is an intermediate phase between the isotropic liquid and the crystalline solid state. This is a liquid phase with a degree of structure that is less than for the solid crystalline state, but more than for the isotropic liquid state. On the basis of their molecular structure and their optical properties, liquid crystal structures can be subdivided into three main groups sketched in Figure 3.12.

Liquid crystal compounds consist of large elongated molecules depicted by the ellipsoidal

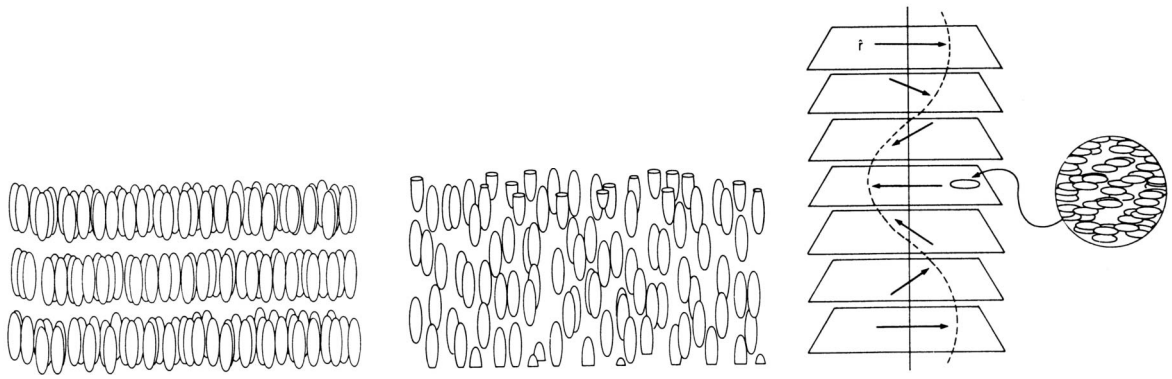

(a) smectic (b) nematic (c) cholesteric

Figure 3.12: The three structural groups of liquid crystal phases (Parsley, 1991)

shapes in Figure 3.12. The *smectic phase* is the most solid-like of the three phases. The molecules are grouped into layers that are stacked on top of each other. The long axes of the molecules are parallel to each other and they are mobile in two directions. In the *nematic phase* the long axes of the molecules are also parallel to each other, but there is no layer structure like in the smectic phase. The molecules are mobile in three directions, which gives rise to a high degree of liquidity. The *cholesteric phase* (also known as chiral nematic or twisted nematic phase) is similar to the nematic phase, except for the fact that it does have a layered structure. The long axes of the molecules in one layer are parallel to each other, but – unlike in the smectic phase – they are also parallel to the layer. For each layer an orientation can be defined according to the direction of the long axes of the molecules in that layer. Passing through the layer structure, the molecular orientation rotates progressively along a helical path. If the crystals are illuminated with white light, the crystals will reflect light with a wavelength that is comparable to the pitch of the helical path. Because the pitch is temperature dependent, the color of the reflected light is determined by the temperature of the crystals.

In contrast to smectic and nematic compounds, cholesteric compounds are known to have special optical properties, owing to their particular structure. The most important properties are described below (Stasiek, 1997):

- **Circular dichroism:** At a given wavelength, incident light is separated into its two circularly polarized components, one right handed and the other left handed. One of the components is reflected, while the other is transmitted totally. The wavelength at which this is taking place depends on the helical pitch of the material. As the pitch is temperature dependent, the wavelength of the reflected component can be used to measure temperature.

- **Bragg scattering:** The layered structure of the liquid crystalline material allows it to behave like a diffraction grating for visible light. This gives rise to iridescent colors of the reflected light and causes the observed wavelength to be dependent on the angles of illumination and observation with respect to the helical structure of the liquid crystal. According to Ferguson (1968) at higher angles of incidence or observation the reflected light shifts to the blue end of the spectrum.

The optical properties cause the cholesteric liquid crystals to reflect visible light of a narrow frequency band depending on temperature when illuminated with white light. The frequency of the selected light depends strongly on the angle of illumination and observation, which makes measurements very sensitive to the configuration of lighting and observation components in the experimental apparatus.

Liquid crystals are difficult to handle because they are very sensitive to aging, chemical reactants (especially fats and solvents), ultra violet light, and mechanical wear and tear. There are two methods for protection of the crystals and for making them easier to handle. One way is to apply them on a thin sheet of acetate or polyester film and covering them with a self-adhesive backing layer. The resultant sheets can be applied easily onto surfaces of which the temperature needs to be monitored. The main advantage is that the layer thickness of the crystals is constant and the surface finish is perfectly smooth, producing a low noise color picture and minimizing the scattering of light on the surface. A clear disadvantage is the thermal inertia of the sheet: due to its thickness (usually 100 μm) there is a phase lag and an amplitude damping for the color changes as a result of temperature changes. The second method of application is spray painting a slurry of microcapsules with liquid crystals inside. This method does not produce homogeneous sheets and the surface can be quite rough, producing a signal that is noisier than that resulting from a sheet, but the response time of a spray painted coating is much higher than that for a sheet. This is mainly due to the missing acetate film. Additionally, sheets show a greater angle dependence of the reflected wavelength (Kasagi et al., 2001).

Figure 3.13 shows a schematic representation of the reflected wavelength as a function of temperature. At a certain temperature, the *red start*, the crystals enter their cholesteric state and reflect the red light from the incident white light. The red start temperature is the lower limit of the measurable temperature range or *color play band*. The upper limit is located near the *blue start*, the temperature at which the crystals turn blue. Increasing the temperature even further will eventually change the crystals to the isotropic liquid phase. The temperature at which this happens is called the *clearing point*.

An important and sometimes annoying effect is the hysteresis that occurs when liquid crystals are heated to temperatures above their clearing point and subsequently cooled. The colors of the crystals will be shifted towards blue on the cooling curve. Cooling the crystals to below the red start will shift the curve back to its original position. Details can be found in (Baughn et al., 1999).

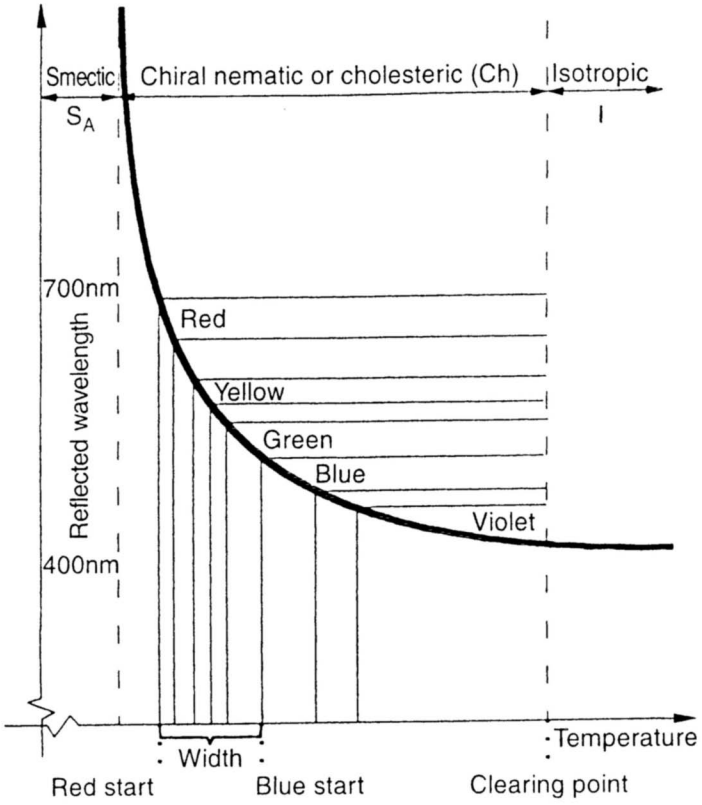

Figure 3.13: Reflected wavelength as a function of temperature for a temperature-sensitive liquid crystal mixture (Stasiek, 1997).

3.3.2 Colorimetry

To determine a complete temperature distribution on a surface simultaneously, a method is necessary by which different colors can be identified. In the early days researchers used narrow-band liquid crystals and black-and-white cameras to determine isotherms. Nowadays, wide-band crystals are applied more frequent. Some researchers use black-and-white cameras equipped with optical filters that exhibit a narrow band-pass transmittance to isolate monochromatic regions. These regions identify isolines of temperature on the surface (see Ichimiya, 1994). Akino et al. (1989) used 18 filters for constructing a temperature distribution. The use of optical filters or narrow-band liquid crystals is a very crude method, because the resulting temperature distribution is discrete with very low resolution.

A way to get a more continuous distribution is to use a full-color image processing system consisting of a white light source and a color CCD camera or a video camera to record the complete color distribution. This implies a method for quantifying colors in a unique way. A color camera or a video camera equipped with a frame grabber will decompose

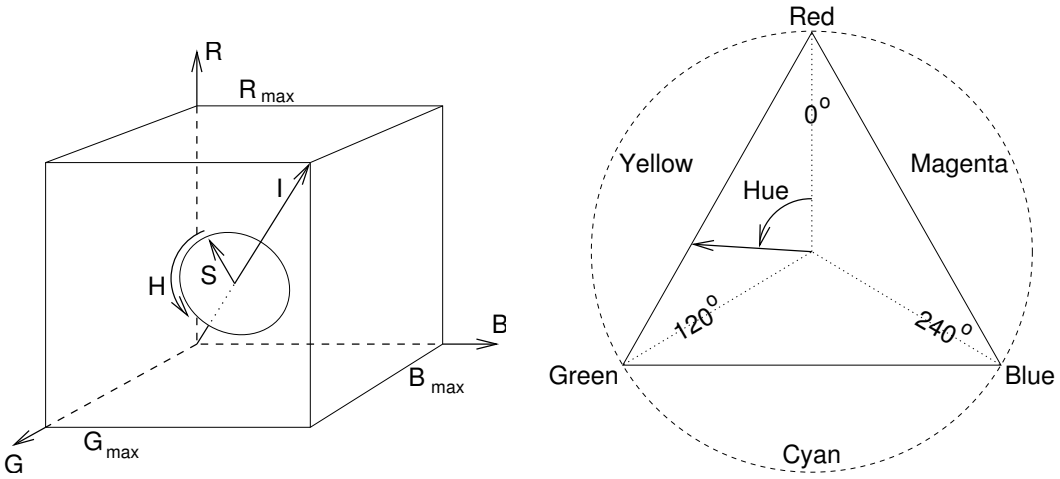

(a) transformation from RGB to HSI

(b) a definition of hue

Figure 3.14: The relationship between the RGB and the HSV color spaces

colors and represent them by three signals N_1, N_2, and N_3. This decomposition is called a *trichromic decomposition* and N_1, N_2, and N_3 are called the *tristimulus* or *trivariance* (Hay and Hollingsworth, 1996). There are several standards for the choice of primaries, but most framegrabbers and CCD cameras will use red, green, and blue (R, G, and B). This RGB color space is defined by the National Television Systems Committee (NTSC).

There are several ways to associate temperature with the values of a tristimulus. Akino et al. (1987) used a simple linear combination of the primaries:

$$T = \alpha N_1 + \beta N_2 + \gamma N_3 + \lambda \ , \tag{3.19}$$

where α, β, γ, and λ are constants determined by linear regression. Hay and Hollingsworth (1996) show that the uncertainties of this technique are unacceptably high compared to other techniques. Park et al. (2001) use a back-propagation neural network to calculate temperatures from RGB-values. This method proved to produce high uncertainty levels, especially at the extreme edges of the temperature range.

The most common way to relate tristimuli to temperature is to transform the RGB color space into the HSI (or HSV) color space. The color signal is separated into the three components *hue* (H), *saturation* (S), and *intensity* (I, also called *value*). The hue identifies the dominant wavelength of the light and the saturation represents the brightness of the color. Figure 3.14a presents a sketch of the transformation from the RGB to the HSI color space (Behle et al., 1996). The axes are given by R, G, and B. Hue is defined as an angle in the polar RGB colorspace as depicted by Figure 3.14b. For each color a unique hue can be calculated, varying from 0° to 359°.

Several different definitions of hue can be found in literature. Hay and Hollingsworth (1996) evaluated three common transformations for the use with liquid crystal colors and found that the one defined by Equation 3.20 yields the lowest average uncertainty while retaining computational simplicity.

$$H = \arctan\left(\frac{\sqrt{3}(G-B)}{2R-G-B}\right) \tag{3.20}$$

$$S = \sqrt{\frac{2}{3}}\sqrt{R^2+G^2+B^2-RG-RB-GB} \tag{3.21}$$

$$I = \frac{1}{3}(R+G+B) \tag{3.22}$$

Roesgen and Totaro (2002) describe a very elegant method for calibrating the crystals using a linear transform of the RGB data. Instead of transforming the RGB data into HSI data and taking the hue to make a calibration, a proper orthogonal decomposition is done on the covariance matrix of normalized RGB data. Calculating the inner product of the normalized RGB vector and the eigenvector associated with the principal eigenvalue of the matrix yields a scalar that can be used instead of the hue. The main advantage of this method over the RGB-to-HSI transformation is the fact that the resulting data are uncorrelated, whereas H and S are correlated, in other words, they are not independent from each other. A disadvantage is the huge computational cost due to the calculation of the covariance matrix. Additionally, Roesgen and Totaro (2002) show their method produces a scalar which is very similar to the hue-angle. In the present project the RGB-to-HSI method is used because of its simplicity and convenience.

3.3.3 Lighting and camera

Liquid crystals are very sensitive to the lighting system used. The light preferably has a white spectrum and a constant intensity throughout the measurement and calibration procedures. Infra-red radiation from the light source can heat the crystals causing erroneous temperature measurements and should therefore be avoided.

Other effects that influence the perceived color of liquid crystals include the presence of light reflection, the optical properties of the viewing optics, the spectral response of the sensing device, and the angles from which the crystals are illuminated (lighting angle) and observed (viewing angle). For a complete and thorough analysis of the effects of the illumination source, the sensing device, and reflections see Anderson and Baughn (2002). Calibrating the liquid crystals and performing measurements in the same rig avoids problems caused by varying lighting and viewing angles, variations in background illumination, and reflections. Effects of spectral characteristics of the light source, the

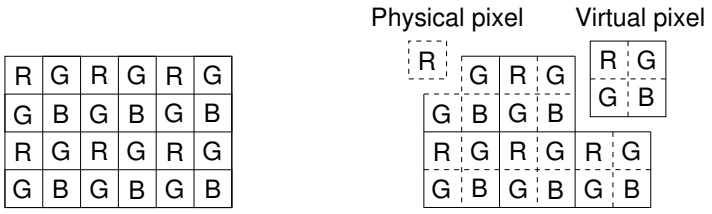

(a) Bayer filter layout (b) definition of virtual pixels

Figure 3.15: Filter layout and color signal reconstruction in single chip cameras

viewing optics, and the sensing device can be minimized by adjustment of the *white balance* of the sensing device. This is done by offering the sensing device samples of known colors and tuning the signals the device produces to correctly represent these colors. However, this is only possible if the light of the illumination source contains all colors.

Modern image acquisition systems include color CCD cameras that provide fast data transfer to a computer for data analysis. Decomposition of colors into their red, green, and blue components is done using chip mounted color filters. Color CCD cameras either have one or three CCD chips. The latter type of camera contains three identical chips. The incoming light is split into its red, green, and blue components and offered to all three chips simultaneously. The single chip type provides a cheaper alternative. In this type of camera each light sensitive element (or *pixel*) of the chip has its own color filter. The filters are red (R), green (G), and blue (B) Bayer filters that are distributed over the chip in an alternating fashion presented in Figure 3.15a. Notice that the number of green pixels equals twice the number of red or blue pixels. In this way, the sensitivity of the CCD chip is comparable to the human eye that is more sensitive to green than to red and blue light.

In a 3CCD camera there is a red, a green, and a blue signal providing full color information for each pixel. The single chip camera has only one signal per pixel. To solve this problem pixels are clustered four by four to form virtual pixels consisting of one red, one blue, and two green physical pixels. This is shown in Figure 3.15b. The green signal of a virtual pixel is constructed by taking the average signal of the two green physical pixels. For one virtual pixel the red signal is acquired at another location than the blue signal or the green signal. Theoretically, the smallest structure that can be recorded in full color has the size of one virtual pixel. Therefore, the resolution of the camera is effectively divided by four.

An important disadvantage of a Bayer filtered camera is the color aliasing effect illustrated in Figure 3.16. As an example, a white streak is recorded by a Bayer filtered CCD chip. On the left side the position of the streak's image on the chip is shown for two

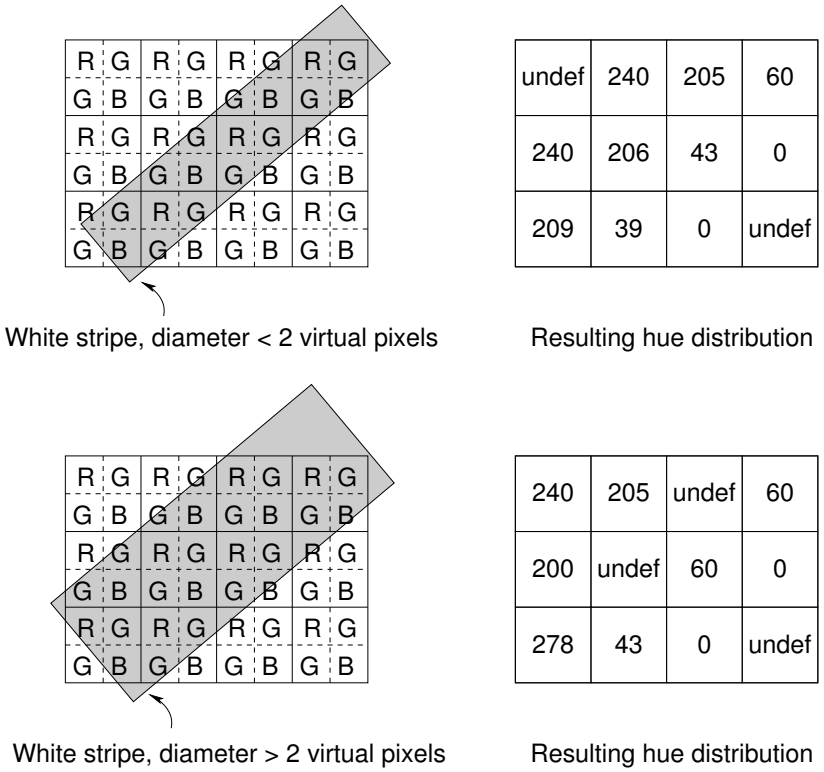

Figure 3.16: Illustration of the color aliasing effect

cases, one where the streak diameter is smaller than two virtual pixels and one where it is wider. On the right side the resulting hue-angles are shown for each virtual pixel. If the white streak has a diameter smaller than two times the width of one virtual pixel, the resulting color image will contain a streak with different colors, but not white. The hue-angle of white and black is undefined (undef in the figure), so the hue distribution should only contain undefined values.

If the streak's diameter is larger than two virtual pixels, the image will contain a streak of which the edges still have different colors, but at least the middle is white. This means that the minimum length scale for images of objects is equal to two virtual pixels to correctly reproduce the object's colors. Nevertheless, color aliasing will always appear when an image contains strong color gradients. The magnitude of the effect is dependent on both color gradient strength and direction with respect to the Bayer filter pattern.

The use of digital equipment to record images introduces another source of error. Due to digitization, signals will be quantized causing quantization errors as illustrated in Figure 3.17. The maximum error is $\frac{1}{2}$ graylevel, and the RMS value is $\frac{1}{6}\sqrt{3}$ graylevel.

Assuming the uncertainty of the red, the green, and the blue components of the color signal is equal to the RMS quantization error, the uncertainty of the hue δH due to

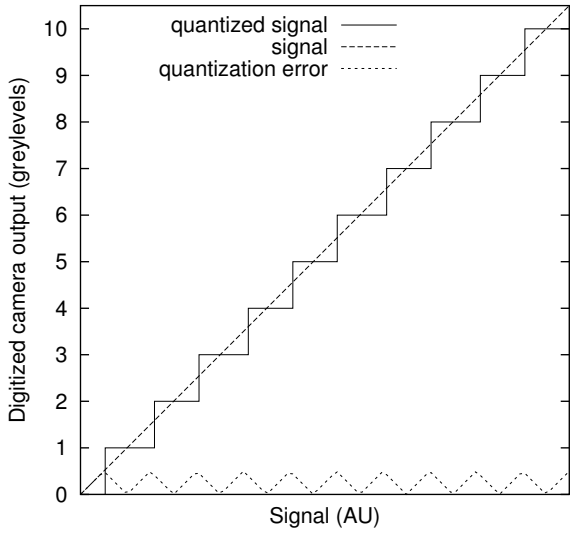

Figure 3.17: Illustration of the quantization error resulting from the digitization of the color signal.

quantization can be calculated using Equation 3.23.

$$\delta H^2 = \left(\frac{\partial H}{\partial R}\right)^2 \delta R^2 + \left(\frac{\partial H}{\partial G}\right)^2 \delta G^2 + \left(\frac{\partial H}{\partial B}\right)^2 \delta B^2 \tag{3.23}$$

The partial derivatives can be evaluated from Equation 3.20 so that:

$$\delta H^2 = \frac{1}{3} \frac{(B-G)^2 \delta R^2 + (R-B)^2 \delta G^2 + (G-R)^2 \delta B^2}{S^4} \ . \tag{3.24}$$

Figure 3.18 presents the uncertainty of the hue calculated from Equation 3.24. It is clear that the accuracy is almost constant over the complete hue range. In this figure it is assumed S and I are maximized, so R, G, and B are determined by H. Because $\delta H \propto S^{-2}$ decreasing saturation has a dramatic effect on the uncertainty of the hue. Therefore it is important to maximize the saturation in experiments.

3.3.4 Image processing

Application of the liquid crystals by spray painting them onto the impingement surface will cause the image of the crystals to be speckled. Speckles typically smaller than 2 virtual pixels can cause color aliasing, as was discussed in Section 3.3.3 (page 49). One way of reducing the effect of aliased pixels on the image is smoothing. Smoothing the data by using a moving average filter will remove some of the high frequency noise and it will diminish the color deviation of aliased pixels, but it will not remove them. In fact,

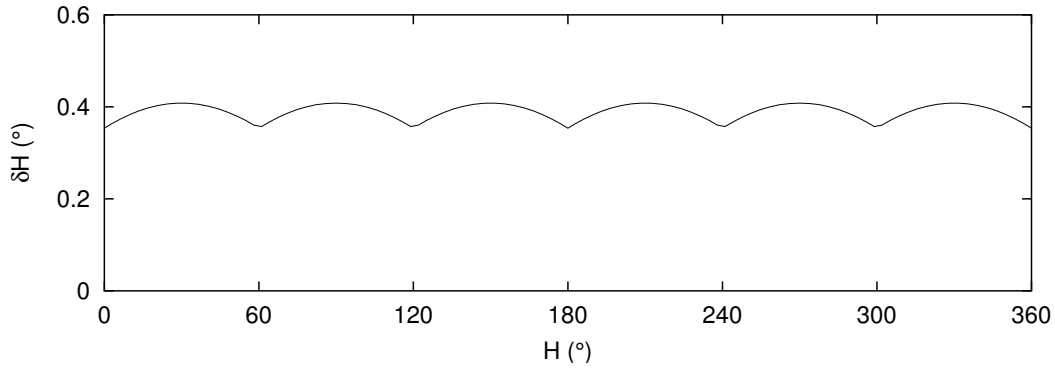

Figure 3.18: Hue error due to quantization of R, G, and B.

smoothing will spread the erroneous data over the data set, biasing pixels that had a 'correct' color. Hence, aliased pixels need to be removed from images to fully eliminate their effect.

Methods for removal of outliers include the local mean and local median tests, both well known techniques in digital image processing (e.g. Jähne, 1991 and Pitas, 1993). These methods consider all pixels in an image individually by comparing them to the pixels in their direct neighborhood. For example, consider a color image of liquid crystals that was transformed into a two-dimensional array of hue-angle. Consider one pixel in an image of the liquid crystals at position (i, j). The expected value of the hue-angle $H_{i,j}$ can be estimated on the basis of the measured value $h_{i,j}$.

The local mean test determines whether $h_{i,j}$ significantly differs from the mean hue-angle of the eight direct neighbors of pixel (i, j). The following criterion should then be satisfied:

$$|h_{i,j} - \overline{h}_{\mathrm{surr}(i,j)}| < \alpha \, s_{H_{\mathrm{surr}(i,j)}} \ , \tag{3.25}$$

where α is a parameter determined on the basis of a confidence interval. Assuming the probability density function of hue-angle is Gaussian, α is equal to 1.96 for a 95% confidence interval. If the criterion is not satisfied $\overline{h}_{\mathrm{surr}(i,j)}$ is substituted for $h_{i,j}$. $\overline{h}_{\mathrm{surr}(i,j)}$ is the mean hue-angle of the eight direct neighbors of point (i, j):

$$\overline{h}_{\mathrm{surr}(i,j)} = \frac{1}{8}\left[\left(\sum_{k=-1}^{1}\sum_{l=-1}^{1} h_{i+k,j+l}\right) - h_{i,j}\right] \tag{3.26}$$

and $s_{H_{\mathrm{surr}(i,j)}}$ is the sample standard deviation of the hue-angles of the eight neighbors with respect to the mean:

$$s^2_{H_{\mathrm{surr}(i,j)}} = \frac{1}{7}\left[\left(\sum_{k=-1}^{1}\sum_{l=-1}^{1} (h_{i+k,j+l} - \overline{h}_{\mathrm{surr}(i,j)})^2\right) - (h_{i,j} - \overline{h}_{\mathrm{surr}(i,j)})^2\right] \ . \tag{3.27}$$

The local median test is very similar to the mean test, except it uses the median $\tilde{h}_{\mathrm{surr}(i,j)}$ of the eight direct neighbors instead of the mean value $\overline{h}_{\mathrm{surr}(i,j)}$. In this case the median $\tilde{h}_{\mathrm{surr}(i,j)}$ is substituted for $h_{i,j}$ if the criterion is not satisfied. The median value is the middle value in a size ordered sequence of elements.

Median filtering appears especially effective in the removal of so called *salt-and-pepper* noise. Grayscale images affected by this kind of noise display randomly distributed black and white pixels, hence the name (see Gonzalez and Woods, 2002). This definition can easily be expanded to color images.

The main advantages of the local mean test over the local median test are its easy implementation and its greater speed. However, this doesn't counter-balance the advantage of the local median test of being more robust than the local mean test. Therefore, the median test is preferred over the mean test for processing color images of liquid crystals.

Once the erroneous hue-angle are eliminated from the data, a smoothing filter is used to eliminate high frequency noise.

$$\Phi(h_{i,j}) = \frac{\sum_{k=-N}^{N} \sum_{l=-N}^{N} \gamma_{i+k,j+l} h_{i+k,j+l}}{\sum_{k=-N}^{N} \sum_{l=-N}^{N} \gamma_{i+k,j+l}} \tag{3.28}$$

Here Φ is the smoothing filter operator, N is the half-width of the filter kernel (integer value), and $\gamma_{i,j}$ is a weight factor depending on the type of filter kernel. For the present experiments a tophat filter ($\gamma_{i,j}$ is equal to 1 for all values of i and j) is used with N=1.

3.3.5 Calibration

To derive quantitative information from full color images of liquid crystals a hue-to-temperature relationship needs to be established. The most common method consists of acquiring images of the crystals at a number of constant, known temperatures. The liquid crystal surface does, however, not display a uniform distribution of color at constant temperatures due to the lighting and viewing angle dependency of the perceived colors. For this reason the calibration curve of the crystals depends strongly on the position in the viewing area. Sabatino et al. (2000) propose a point-wise calibration technique that establishes the relationship between the hue and temperature for each position on the viewing area. The additional benefits of this technique according to the authors are:

1. No assumptions are required concerning the isolation and removal of reflective components of the lighting;

2. Defects in the black paint substrate and liquid crystal layers are inherently compensated for;

3. The technique allows calibration of test surfaces with significant lighting/viewing angle variations;

4. It is fully applicable to digitally-based liquid crystal temperature measurement systems.

The point-wise calibration yields a three-dimensional table of hue-angles for each pixel at each of the constant temperature values. This table can be used as a lookup table in conjunction with either a linear or cubic spline interpolation routine, to convert each pixel of the subsequent data images from hue to temperature. This method was employed by Sabatino et al. (2000) and is also be used in the present project.

Fitting polynomials of arbitrary order to the curves at each position provides another method of calibration. The main advantage of this method is the strong reduction in size of the calibration table, because only the polynomial coefficients have to be stored. However, there is no physical reason as to what order the polynomial should be. This is only determined by the shape of the calibration curves. For instance, Behle et al. (1996) suggest polynomials up to order 10 and Hay and Hollingsworth (1998) use polynomes of 5^{th} order.

Chapter 4

Experimental Apparatus

Experiments were performed in two different configurations: a single impinging jet and multiple impinging jet arrays. In Section 4.1 the experimental rig is discussed that was used for the flow measurements in the single jet configuration with both PIV and LDA. The flow and heat transfer measurements conducted in the multiple impinging jet arrays is presented in Section 4.2. First the wind tunnel that provided the air flow for the jets is discussed. After that, the heat transfer measurements with liquid crystals are discussed, together with the calibration of the crystals. In the last part of Section 4.2 the flow experiments using PIV are presented.

4.1 Single impinging jet

Experimental rig

Figures 4.1a and 4.1b show sketches of the single impinging jet rig equipped with the PIV and the LDA systems, respectively. A straight pipe with an inner diameter D_s of 36 mm and length of 2.73 m ($76D_s$) was placed perpendicularly to a smooth, flat impingement plate with dimensions 1.0 x 1.2 m^2. The high length-to-diameter ratio of the pipe assures a fully developed turbulent pipe flow at the outlet, as was confirmed by measurements. The pipe was connected to a fan via a flexible hose. To suppress any secondary motion, a honeycomb (100 mm length and 5 mm cells) was inserted in the inlet of the pipe. The distance between the pipe outlet and the plate H was $2D_s$.

Figure 4.2 depicts the flow configuration of the single impinging jet with the measurement regions for both the LDA and the PIV measurements. An orthogonal x,y-coordinate system was defined having its origin at the intersection of the pipe center line and the impingement plate. The y-axis is measured along the pipe axis and is taken positive in

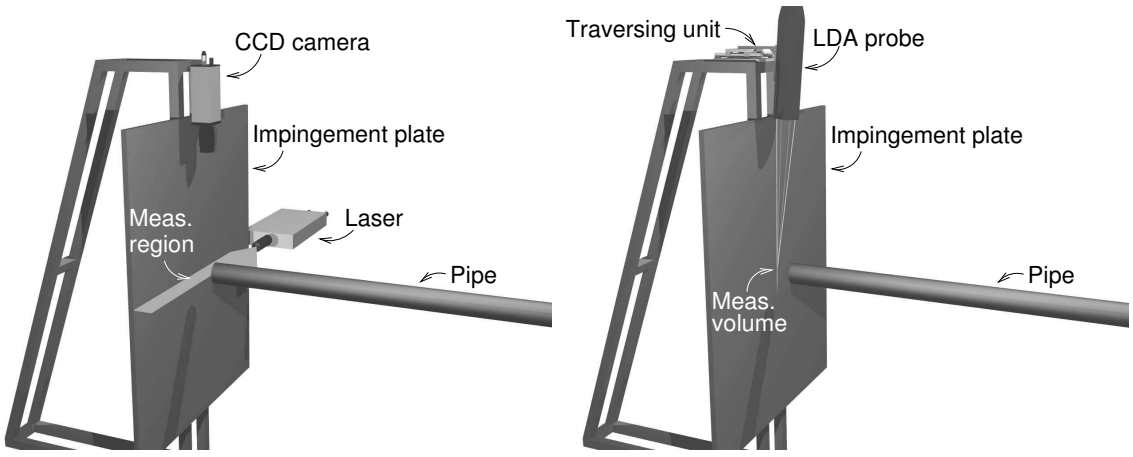

(a) PIV set-up.

(b) LDA set-up.

Figure 4.1: Sketches of the experimental rigs for the single impinging jet.

the upstream direction. The x-coordinate is measured along surface of the impingement plate. The LDA measurements were performed at three stations x/D_s =0.0, 0.5, and 1.0 for $0 < y/D_s < 1.36$ in about 60 positions per station. PIV measurements were obtained from an area given by -0.4 $< x/D_s <$ 1.6 and $0.0 < y/D_s < 1.6$. All measurements were performed at a constant Reynolds number of $2.3{\times}10^4$ (based on the pipe diameter), corresponding to a bulk velocity of approximately 9.6 m/s.

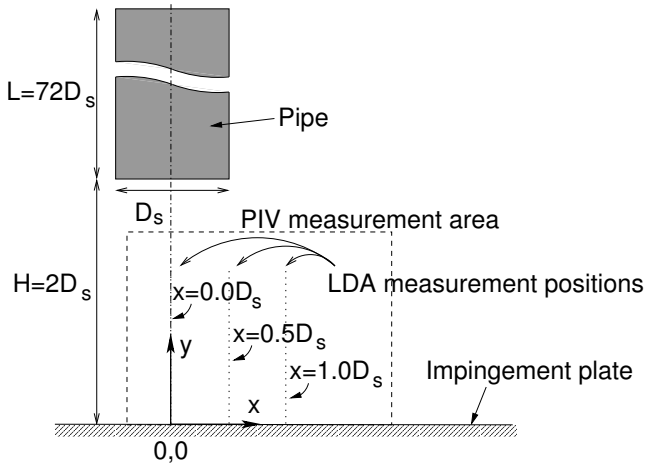

Figure 4.2: Flow configuration for the single impinging jet measurements.

PIV measurements

The PIV system (manufactured by Optical Flow Systems, OFS) included a double pulsed Nd:YAG laser (Continuum Minilite) with a pulse energy of 25 mJ. This laser was used to produce a 1 mm thick sheet that illuminated the flow. A PCO Sensicam camera with a resolution of 1280 $\times$ 1024 pixels recorded images of the seeding particles in the laser sheet. The commercial software VidPIV Rowan v4.0 developed by OFS/ILA was used to analyze the images.

The camera was equipped with a 55 mm focal length lens and a numerical aperture of 5.4. The time separation between the two laser pulses was 30.21 μs. There was a time lag of 0.5 s between two PIV image pairs, resulting in statistically independent samples of the velocity field. Approximately 1500 image pairs were acquired to accurately determine flow statistics up to the second moments.

The images were analyzed in two consecutive steps. In the first step, 50% overlapping interrogation areas of 32 $\times$ 32 pixels were cross-correlated. After filtering out the spurious vectors, the resulting particle displacements were used as window displacements for an adaptive cross-correlation with non-overlapping interrogation areas of 16 $\times$ 16 pixels (0.9×0.9 mm^2). Velocities between 0.2 and 15 m/s can be resolved in this configuration. A local median filter was used to remove spurious vectors (about 3% of the total amount of vectors) and the resulting empty spaces were filled with interpolated values from the surrounding interrogation areas.

The seeding particles were generated by Laskin nozzles submerged in an aqueous dialcohol-glycerol mixture. The seeding droplets had a mean diameter of about 1 μm. To assure a homogeneously seeded measurement area, a large enclosure was built around the set-up. By connecting the inlet of the fan to the enclosure a closed loop was created in which the seeded air was recycled.

LDA measurements

The LDA measurements were performed using a two-component, fiber optic TSI system. The green (514.5 nm) and blue (488.0 nm) colors of a 5 W Argon-ion laser were used to measure two components of the velocity simultaneously. One beam of each color was frequency pre-shifted 40 MHz by a Bragg cell to detect instantaneous flow reversals. The length and the diameter of the two overlapping measuring volumes were 1.7 mm and 0.12 mm, respectively. Scattered light was collected in backscatter mode. The photo-multiplier output signals were electronically down-mixed to an effective pre-shift of 5 MHz, and subsequently fed to two (TSI) IFA-750 signal processors. The commercial FIND software was used to extract the mean velocity components and the Reynolds stresses from the raw data files.

At each position 1.8×10^4 samples were taken to calculate the mean velocity components and the Reynolds stresses. All statistics were computed as transit-time weighted results to eliminate the effects of the velocity bias. The measurement time varied between approximately 100 seconds for positions far away from the wall to 600 seconds for positions in the near wall region.

For the LDA measurements the same seeding system was used as for the PIV measurements.

4.2 Multiple impinging jet array

4.2.1 Wind tunnel

Well defined boundary conditions are crucial to the investigation of the flow of an impinging jet array. All jets in the array should exhibit the same initial velocity profile and turbulence levels. Additionally, the jets must be swirl-free, implying a swirl-free flow upstream of the nozzle plate. A wind tunnel was constructed that met these demands. The wind tunnel depicted in Figure 4.3 was designed on the basis of rules of thumb devised by Mehta and Bradshaw (1979).

A centrifugal fan fed air to a square channel via a flexible hose and a rotary flow meter (Instromet, Q-75 K). The flow was controlled by a variable power supply (Eurotherm drives). In order to have an accurate flow measurement, a round pipe with a diameter of 95 mm and a length of 950 mm was placed upstream of the flow meter and a pipe with the same diameter and a length of 475 mm was placed downstream of the flow meter, according to the flow meter specification.

The square supply channel transports the air to the end section of the wind tunnel. The two bends in the square supply channel are equipped with circular guiding vanes to prevent the formation of streamwise swirl in the flow.

The end section of the wind tunnel can be subdivided in three main elements. The first element in the end section is a square wide angle diffuser with an area ratio of 6.25 and an angle of 30°. To prevent flow separation gauze screens were installed at the inlet and the outlet of the diffuser.

The second element of the end section is a settling chamber. It is divided into four equal square sections with a length of 125 mm and a cross-section of 500×500 mm^2. Screens were placed between consecutive sections. In the upper section of the settling chamber a honeycomb is installed to remove swirl and lateral mean velocity variations. The cell width of the available honeycomb was 3.4 mm and the length 80 mm, equivalent to 23.5 cell diameters. The total number of cells is about 21.6×10^3. Because the cells are rela-

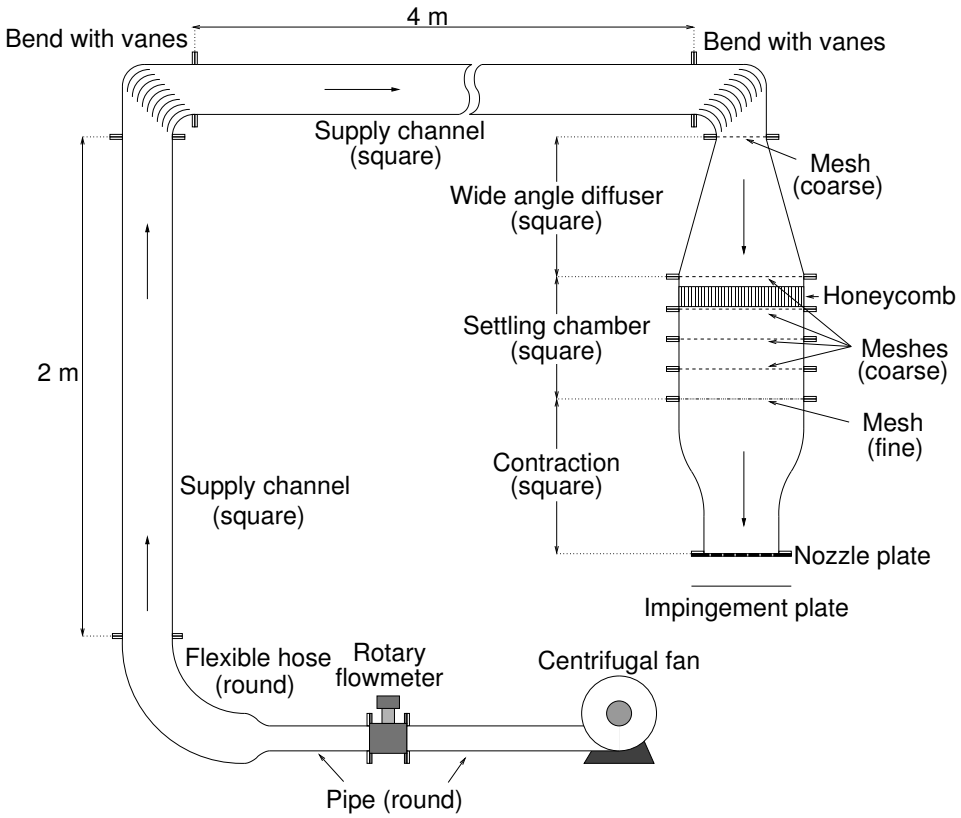

Figure 4.3: Schematic drawing of the wind tunnel

tively long, the turbulence level of the flow is expected to increase due to the honeycomb. For this reason the screens in the settling chamber were chosen conservatively.

Just downstream of the settling chamber a thin flange was placed containing probes to measure the air temperature and pressure. The temperature was measured using a Pt-100 probe (S1320 series, Systemteknik AB) and the pressure was measured by a micromanometer (FC012, Furness Controls Ltd).

The diffuser allows the screens and the honeycomb to be in the low speed region (reducing pressure losses) and to reduce the mean and fluctuating velocity variations with respect to the average velocity. A contraction downstream of the settling chamber reduces the cross section of the channel again. The contraction was shaped according to a fifth order polynomial yielding straight in- and outlets. The width of of the outlet was 300 mm, and the contraction ratio (inlet area over outlet area) was 2.78. At the outlet several different nozzle plates can be attached. For the precise measures of the end section and the corner bends, see Appendix A.

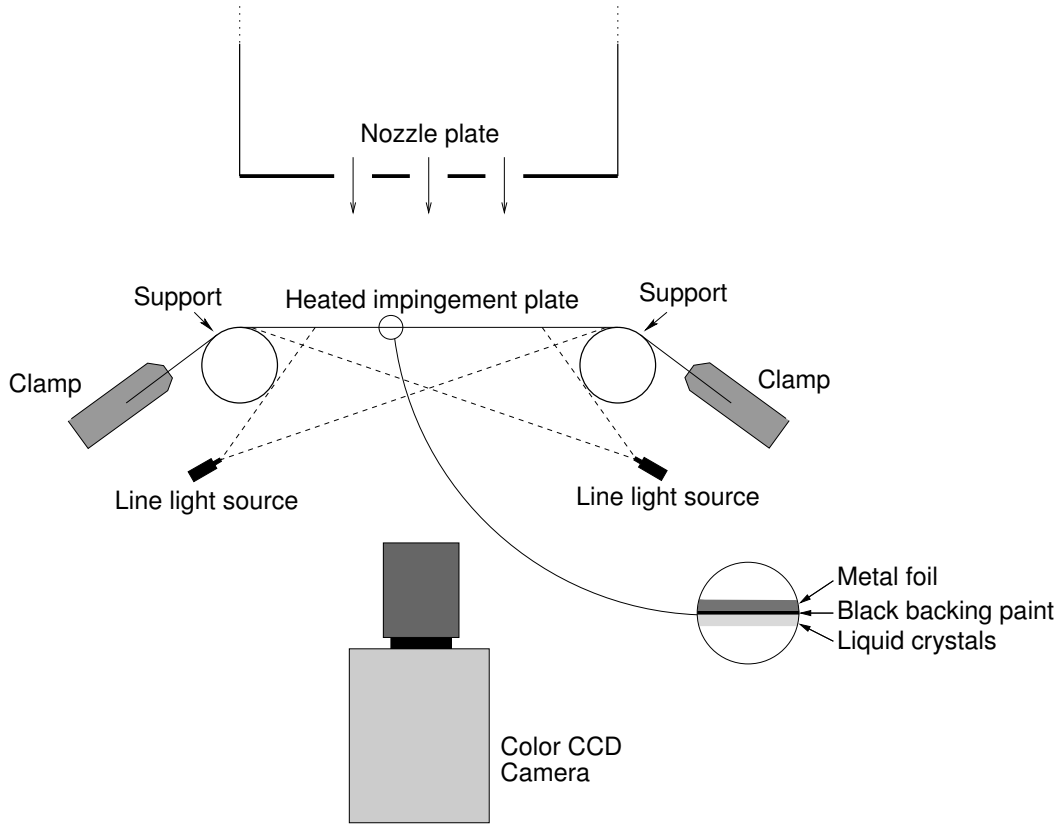

Figure 4.4: Experimental rig for temperature measurements

4.2.2 Heat transfer experiments

Experimental rig

Figure 4.4 shows the experimental rig used for impinging jet heat transfer measurements. The air issued from a nozzle plate impinges upon a stainless steel (type 304) sheet with a thickness of 25 μm. This sheet is stretched between two clamps. Two cylindrical supports bend the sheet downwards on both ends to prevent the clamps from disturbing the flow.

The impingement sheet is heated electrically by means of a current source (Delta Elektronika) that can supply up to 100 A at 4 V. Figure 4.5 shows a schematic drawing of the electrical components to heat the impingement plate and measure the electrical dissipation. A voltmeter (3465B, Hewlett Packard) measures the voltage drop over the impingement plate, while a combination of a 1 mOhm series resistance and another voltmeter (8000A, Fluke) measure the current through the plate.

The bottom side of the sheet is covered with a layer of black backing paint of about

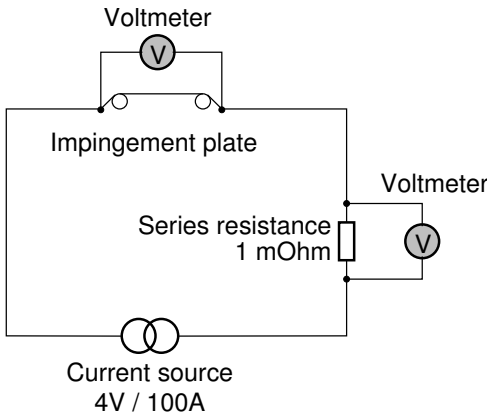

Figure 4.5: Electrical scheme for measuring the dissipation in the impingement plate

5 μm and a layer of liquid crystals (BM/R30C20W/C17-10, Hallcrest) of about 15 μm to monitor the temperature of the sheet. The thickness of the liquid crystal layer proved to be sufficient for producing colors with sufficient saturation.

Four 150 W light sources (DCR III, Schott-Fostec LLC) were used to illuminate the liquid crystals. The light from these sources is guided through four glass fiber bundles and transferred to two 13" Light Lines (Schott-Fostec, LLC). In these devices the fibers from the bundles are ordered to produce light lines of homogeneous intensity. The infrared radiation that the crystals receive from the light source is reduced to a minimum by an IR-filter before the light is coupled into the fibers. The color temperature associated with the spectrum of the light is about 3200 K.

A PCO SensiCam SVGA color camera was used to acquire snapshots of the liquid crystals. The camera contains a 2/3" CCD chip with 1280×1024 pixels that record the intensity of the incident light. The CCD chip is equipped with Bayer filters to distinguish colors (see page 49).

Measurements

The liquid crystal thermography measurements focused on the heat transfer resulting from nozzle plates with two different nozzle arrangements: in-line and hexagonal. The in-line arrangement consists of 3×3 nozzles as shown in Figure 4.6a and the hexagonal arrangement consists of 13 nozzles as shown in Figure 4.6b.

There were two shapes of the nozzles in the hexagonal arrangement. Figure 4.7 shows these shapes. The sharp orifice plates consist of aluminum plates with bored holes, and the contoured nozzle plates consist of a stainless steel plates with holes that are punched, creating a contoured shape. The diameter of the nozzles D_m was 13 mm for all nozzle

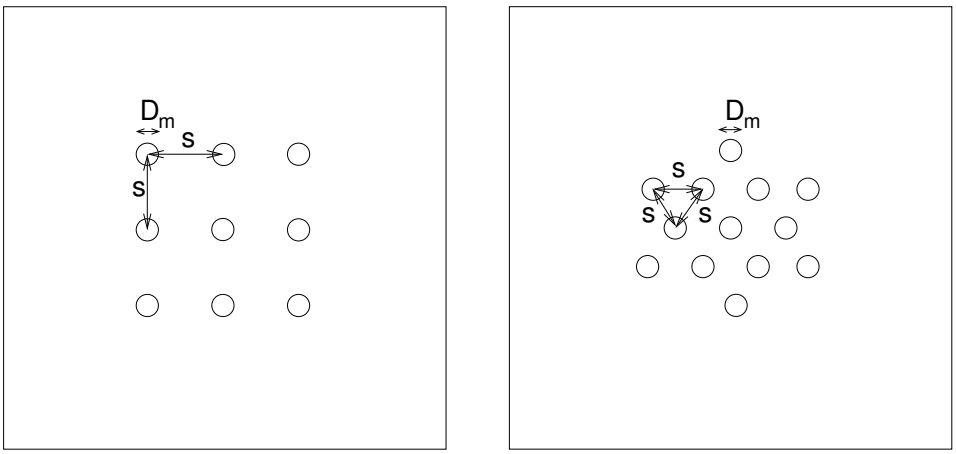

(a) in-line arrangement. (b) hexagonal arrangement.

Figure 4.6: Two different nozzle arrangements for velocity measurements.

(a) sharp orifices (b) contoured nozzles

Figure 4.7: Cross-sections of the two nozzle shapes

plates.

The three parameters that were varied in the experiments are the distance between the nozzles (or pitch, s/D_m), the distance between the nozzle plate and the impingement plate H/D_m, and the Reynolds number. Table 4.1 presents all possible combinations of the parameters (in total 140) that were studied.

Table 4.1: Experimental parameters for all nozzle configurations.

Configuration	Nozzle shape	s/D_m	H/D_m	Re$\times 10^3$
Hexagonal	sharp	2, 4, 6	3, 4, 6, 8, 10	5, 10, 15, 20
	contoured	2, 4, 6	3, 4, 6, 8, 10	5, 10, 15, 20
In-line	sharp	4	3, 4, 6, 8, 10	5, 10, 15, 20

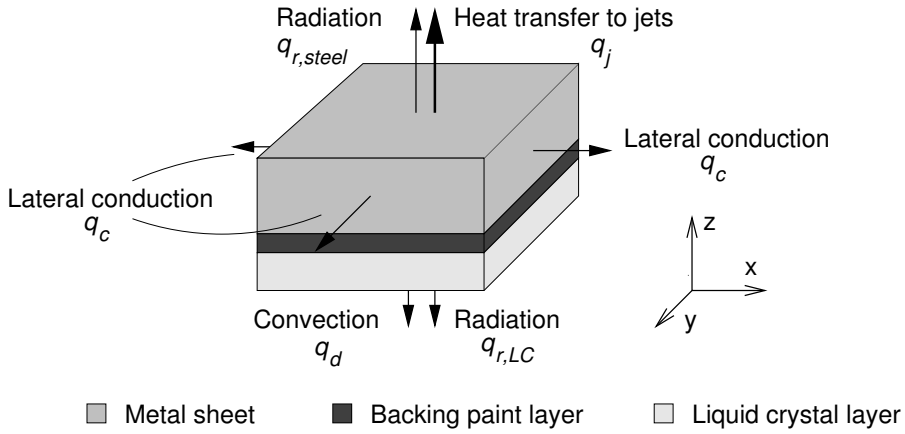

Figure 4.8: Overall energy balance over a small element of the impingement plate

Data reduction

After filtering the images acquired by the camera with a median filter and a smoothing filter, temperatures are determined from hue values by using a lookup table as described in Section 3.3.4. The values of the impinging jets heat transfer coefficient h_j can be calculated from an energy balance over a small element of the impingement plate as shown in Figure 4.8. On the top side of the sheet heat is transferred to the environment by by forced convection due to the impinging jets (q_j) and radiation ($q_{r,steel}$). Within the metal sheet lateral conduction is taking place (q_c) and on the bottom side of the sheet heat is transferred to the environment by radiation ($q_{r,LC}$) and by convection (q_d). The convection on the bottom of the sheet is caused by disturbances due to draught. The sum of all the heat transfer terms is balanced by the heat production through electrical dissipation (q_e) in the metal sheet.

$$q_e = q_j + q_d + q_{r,steel} + q_{r,LC} + q_c \tag{4.1}$$

q_e is given by $\frac{VI}{LB}$, where V is the voltage over the steel sheet (V), I is the current through the sheet (A), B is the width of the sheet (0.32 m), and L is the length of the sheet (0.38 m).

$$\begin{aligned} \frac{VI}{LB} &= h_j(T - T_s) + h_d(T - T_s) + (\varepsilon_{steel} + \varepsilon_{LC})\sigma(T^4 - T_s^4) \\ &\quad -\lambda_{steel}\, d_{steel} \left(\frac{\partial^2 T}{\partial x^2} + \frac{\partial^2 T}{\partial y^2} \right) \end{aligned} \tag{4.2}$$

T is the sheet temperature (K), T_s is the temperature of the surroundings (K), h_d is the heat transfer coefficient due to draught (estimated at 1.1 W m^{-2}K^{-1})[1], ε_{steel} is the

[1]on the basis of Nu= 0.332·Re$^{0.5}$·Pr$^{0.33}$ (flow along a flat plate, Janssen and Warmoeskerken 1991) and a draught velocity of 10 cm/s

emission coefficient of the sheet (≈0.15), ε_{LC} is the emission coefficient of the paint and crystals (estimated at 0.9), σ is the Stefan-Boltzmann constant (5.67×10^{-8} W m^{-2}K^{-4}), λ_{steel} is the conduction coefficient of the sheet (16 W m^{-1}K^{-1}), d_{steel} is its thickness, and x and y are the coordinates parallel to the sheet (m).

Because the conduction term q_c amounts to only 1% of the total heat transferred in the element, it was not taken into account in the calculation of q_j. Additionally, incorporation of this term unnecessarily complicates the procedure, because second derivatives of temperature are involved. Small errors in the measured temperatures will be amplified by the calculation of derivatives and would imply additional filtering.

The mean heat transfer was calculated from 200 images for each of the 140 different combinations of the experimental parameters. The uncertainty of h_j calculated using the method of Kline and McClintock (1953) was about 2% on average, with a maximum of 9%.

In some cases the calibrated temperature range of the liquid crystals was exceeded, causing the measured temperature to be undefined. On average this occurred at 6.4% of all points. The highest percentage of undefined temperatures is 28.8%. The probability of undefined temperatures is highest in the region outside the impingement zone for low H/D_m values, low s/D_m, and low Reynolds numbers. These undefined points were excluded from the calculation of mean values of the Nusselt number by substituting zero for the Nusselt number at these points:

$$\langle \mathrm{Nu}(x,y) \rangle = \frac{\sum_{i=1}^{N} \mathrm{Nu}(x,y)_i}{N - n_{undef}(x,y)} \ , \tag{4.3}$$

where $\langle \mathrm{Nu}(x,y) \rangle$ is the ensemble averaged Nusselt number on the position (x,y), N is the total number of images in the ensemble, $\mathrm{Nu}(x,y)_i$ is the Nusselt number at (x,y) from image i, and $n_{undef}(x,y)$ is the number of undefined temperatures at (x,y) in the ensemble.

Temperature bias

The heat flux from the liquid crystal layer will cause the temperature of the liquid crystals to be lower than the temperature of the metal sheet. This heat flux only consists of a (draught) convection and a radiation term that are defined by:

$$q"_{r,LC} = \ \varepsilon_{LC}\sigma(T_{LC}^4 - T_s^4) = \ 179 \ \frac{\mathrm{W}}{\mathrm{m}^2} \ , \tag{4.4}$$

$$q"_{d} = \ \ h_d(T_{LC} - T_s) = \ \ 34.3 \ \frac{\mathrm{W}}{\mathrm{m}^2} \ , \tag{4.5}$$

where T_{LC} is the temperature on the surface of the liquid crystal layer (50 °C in the worst case) and T_s is the temperature of the surrounding air (20 °C).

On the basis of these fluxes an estimate can be made of the temperature difference between the metal sheet and the surface of the liquid crystals in the steady state:

$$\Delta T = (q"_{r,LC} + q"_{d}) \left(\frac{d_{paint}}{\lambda_{paint}} + \frac{d_{LC}}{\lambda_{LC}} \right) = 0.016 \text{ K} , \tag{4.6}$$

where ΔT is the temperature difference between metal sheet and liquid crystal layer, d_{paint} is the thickness of the backing paint layer (5 μm), d_{LC} is the thickness of the liquid crystal layer (15 μm), λ_{paint} is the heat conductivity of the backing paint (1.0 W m^{-1}K^{-1}), and λ_{LC} is the heat conductivity of the liquid crystals (0.21 W m^{-1}K^{-1}). These values were taken from Praisner et al. (2001), who used the same types of backing paint and liquid crystals.

Dynamic behavior

To assess the dynamic behavior of the sheet, characteristic time scales of all processes involved in the color change of the liquid crystals should be compared. Equations 4.7, 4.8, and 4.9 provide estimates for the characteristic time scale of heat conduction in the steel foil, the black paint, and the liquid crystals, respectively.

$$\tau_{steel} = \frac{d^2_{steel}}{a_{steel}} = \frac{(25\times10^{-6})^2}{4\times10^{-6}} = 156\mu s , \tag{4.7}$$

$$\tau_{paint} = \frac{d^2_{paint}}{a_{paint}} = \frac{(5\times10^{-6})^2}{2.5\times10^{-6}} = 10\mu s , \tag{4.8}$$

$$\tau_{LC} = \frac{d^2_{LC}}{a_{LC}} = \frac{(15\times10^{-6})^2}{0.34\times10^{-6}} = 662\mu s , \tag{4.9}$$

where τ is the characteristic heat conduction time scale of a certain layer, d is the layer thickness, and a is heat diffusivity of the layer material.

Rearranging the molecular structure of liquid crystals typically takes a time period of the order of tens of milliseconds (Moffat, 1990), two orders of magnitude longer than the conductive processes. It can therefore be concluded that temperature gradients over the metal sheet, the paint, and the crystal layers will be negligible. Additionally, the typical time scales of the air flow in a multiple impinging jet array with D_m=13 mm and Reynolds numbers between 5×10^3 and 20×10^3 (see Table 4.1 on page 62), range from 560 μs to 2.3 ms. Therefore, LCT cannot be used to produce instantaneous snapshots of the temperature field in this case; only ensemble mean temperature distributions will be used for the analysis of impinging jet heat transfer.

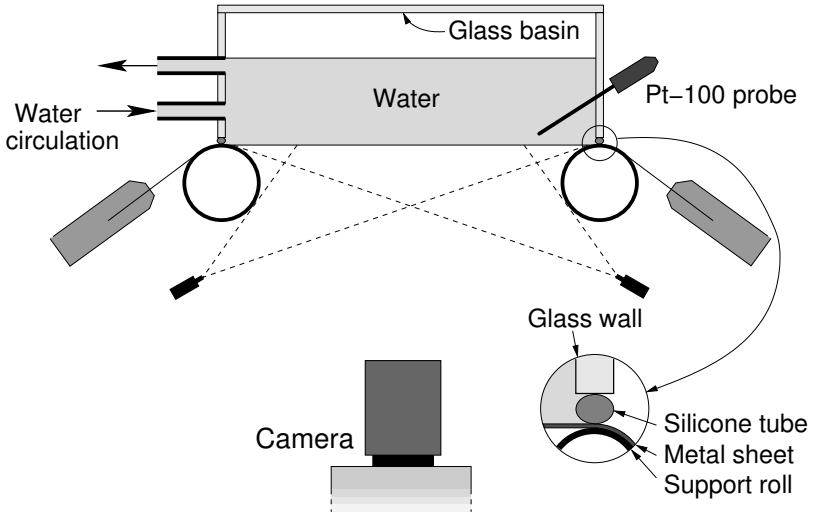

Figure 4.9: Experimental rig for calibration of liquid crystals

4.2.3 Liquid crystal calibration

Calibration rig

The calibration of the liquid crystals is done in the same experimental rig as the measurements to keep all external factors constant. It is especially important to keep lighting and viewing angles constant, because they strongly affect the perceived color of the crystals (see Section 3.3.1 on page 45). Water of a known temperature is recirculated on the impingement plate to provide the crystals with a constant and known temperature at which their color is recorded. A detailed sketch of the calibration rig is given in Figure 4.9.

The water must be in direct contact with the impingement plate; there should be no thermal resistance. To this end, a glass basin with an open bottom rests on silicone tubes on the steel impingement sheet. A constant temperature bath (Colora) circulates water through the basin, while the temperature is monitored using a Pt-100 probe (S1320 series, Systemteknik AB). In this way, the temperature of the water can be maintained constant within about 0.02 °C. The precision of the Pt-100 probe is 0.01 °C.

The correspondence between pixel coordinates and world coordinates can be determined with special purpose alignment pins for the nozzles shown in Figure 4.10. Three pins are inserted in the nozzles and the impingement foil is traversed upwards until it just touches the tips of the pins. Next the foil is heated and the camera records the thermal imprint of the pins on the foil. In this way the pixel coordinates of the centers of the nozzles can be found and linked to their world coordinates using linear mapping.

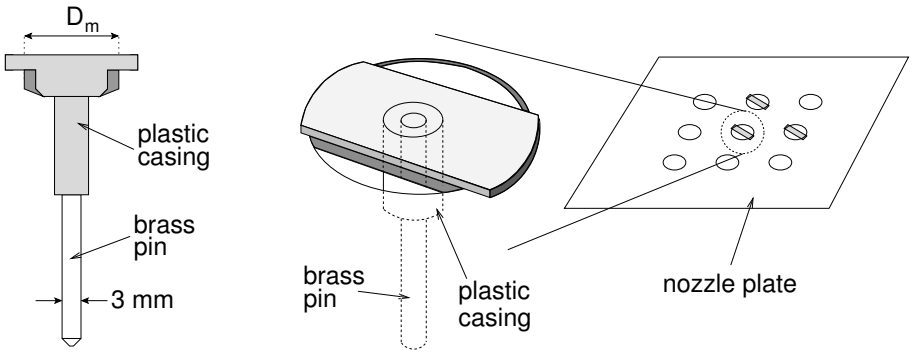

(a) alignment pin (b) use of alignment pins

Figure 4.10: Sketch of the alignment pins used for position calibration for heat transfer measurements.

Procedure

The liquid crystals were calibrated at about 90 to 100 points spread over the full temperature range. Typically ten snapshots are taken from the liquid crystals at each (constant) temperature level of the water bath. After that, all snapshots are processed by the local median test and the smoothing filter. All snapshots at one temperature level are used to calculate average hue values and standard deviations of hue on each pixel position in the viewing area. Finally, arrays of these two quantities are stored in a lookup table.

In Figure 4.11a three calibration curves are plotted that map hue values to temperatures. These curves were taken at three different positions in the view field of the camera depicted in Figure 4.11b. Although the curves show a similar trend, hue values are mapped onto different temperatures by the three curves. Differences are of the order of 0.9 °C at maximum. Given a total range of about 10 °C this is a 9% difference. If only one calibration curve would be used for a whole image, errors of this magnitude would be introduced. This is the reason for using a per-pixel approach, as was illustrated above.

Uncertainties

The uncertainty of the temperature measurement can be determined from the uncertainty of the hue value, given by the matrix of hue standard deviations stored in the calibration file. The uncertainty of the temperature will then be:

$$\delta T = \left| \frac{dT}{dH} \right| \delta H \ , \tag{4.10}$$

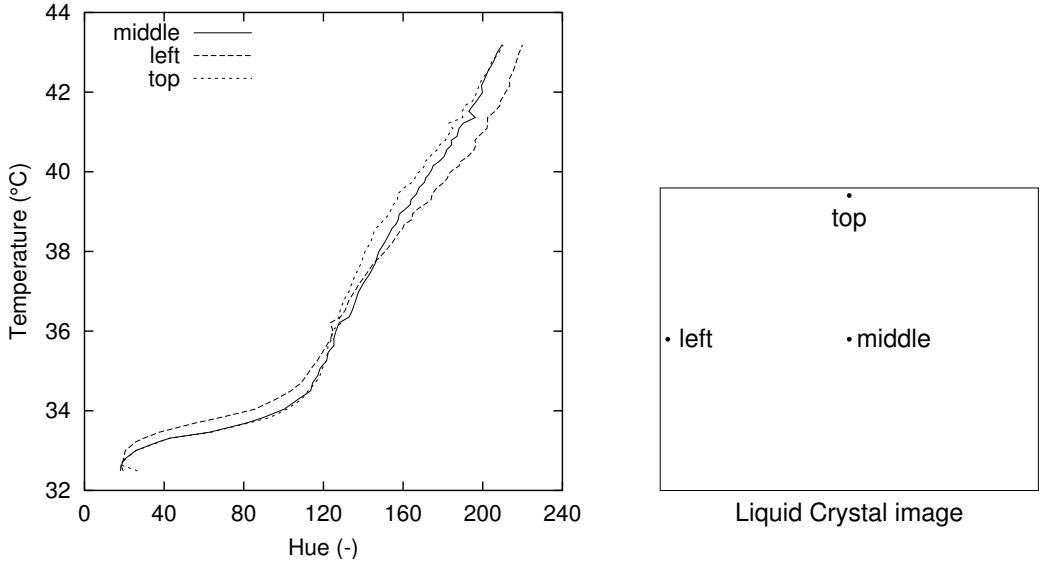

(a) Three calibration profiles

(b) Positions of the profiles

Figure 4.11: Three hue-to-temperature calibration lines at different positions

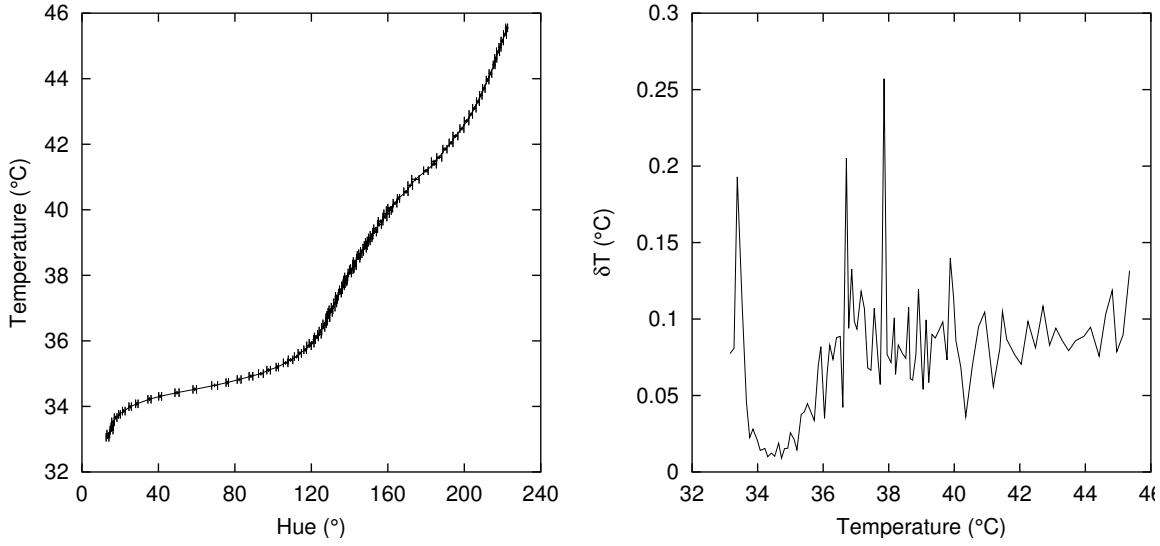

(a) Calibration with error in hue

(b) Resulting error in temperature

Figure 4.12: Calibration line with measurement error and the error in temperature

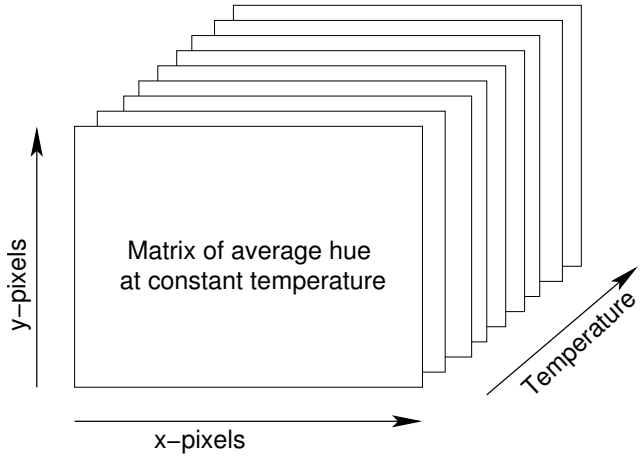

Figure 4.13: A schematic representation of the calibration matrix

where $\frac{dT}{dH}$ is the slope of the calibration curve and δH is the uncertainty of the hue value. A sample of a calibration curve is shown in Figure 4.12a with horizontal error-bars representing the uncertainty of the hue. This was derived from the standard deviation of the hue resulting from the calibration procedure. Figure 4.12b shows a plot of the uncertainty of the temperature for the whole temperature range. The uncertainty is around 0.1 °C, i.e. 1% with respect to the temperature range, which is a typical value for liquid crystals according to Kasagi et al. (2001). The uncertainties are very low between 34 and 36 °C, because of the high sensitivity in that region: the slope of the calibration curve is very flat.

Calibration matrix structure

Figure 4.13 shows a sketch of the structure of the calibration data set. For each temperature there is a matrix of hue values and these matrices are stacked. Each pixel in a snapshot of the liquid crystals has its own calibration curve, that can be obtained by traversing through the data set at constant x and y. Matrices of the standard deviations of hue are stored in a similar way.

The calibration data are stored in the NetCDF format designed by the University Corporation of Atmospheric Research (UCAR) in Boulder (CO,USA). This data file format was originally created for storing large data sets from atmospheric experiments, but can be used for a wide variety of experimental data. Next to the matrices of average hue and hue standard deviation, also information describing the experiment can be stored. In order to keep track of the validity of hue values at all positions, a matrix is stored containing the number of erroneous hue values encountered. This matrix is also stored in the NetCDF file. In this way it can be determined how frequently errors occur at certain positions.

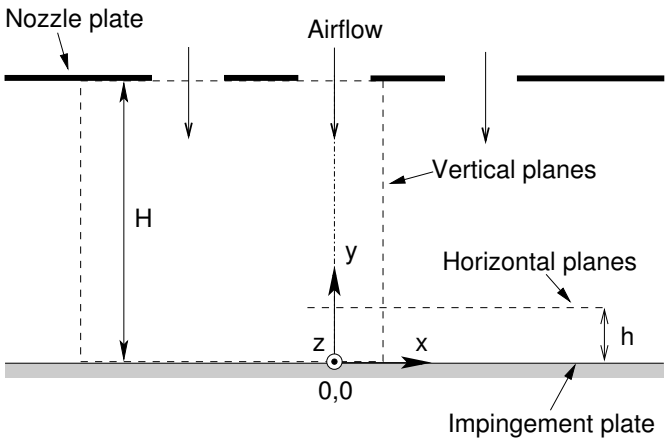

Figure 4.14: Flow configuration for both the hexagonal and the in-line jet array

4.2.4 Flow experiments

Figure 4.14 shows the flow configuration for the jet array flow measurements. Air from the wind tunnel was issued through a nozzle plate, after which it impinged on an impingement plate parallel to the nozzle plate. For this purpose a glass plate was used to enable PIV velocity measurements in planes parallel to the impingement plate. Measurements were conducted using a distance between the nozzle plate and the impingement plate H of $4D_m$, for both nozzle configurations.

In the hexagonal nozzle configuration measurements were done in three planes parallel to the jets (the vertical planes 1 to 3), as shown in Figure 4.15a. Vertical plane 1 intersects the central jet and one of its direct neighbors, vertical plane 3 intersects the central jet and one of the outer jets, and vertical plane 2 is placed along the bisector of planes 1 and 3. The origin of a x,y,z-coordinate system is at the intersection of the center line of the central jet and the surface of the impingement plate. The y-axis is measured along this centerline and assumed to be positive in the upward direction. The x- and z-axes are measured along the surface of the impingement plate. The measurement area was defined by -4.4$< x/D_m <$1.0 and 0.0$< y/D_m <$4.0 for all vertical planes in the hexagonal configuration.

Next to that, velocity measurements were done in the same configuration in two planes parallel to the impingement plate (the horizontal planes), characterized by their height above the impingement plate h (see Figure 4.14). One plane is at h=0.25D_m and the other one at h=1.5D_m. These planes all focus on the same four jets: the central jet, two of its direct neighbors and one of the outer jets. The position of the measurement area was -0.6 $< x/D_m <$ 3.5 and -0.7 $< z/D_m <$ 2.6 for all horizontal planes in the hexagonal configuration.

In the in-line nozzle configuration measurements were done in three vertical planes

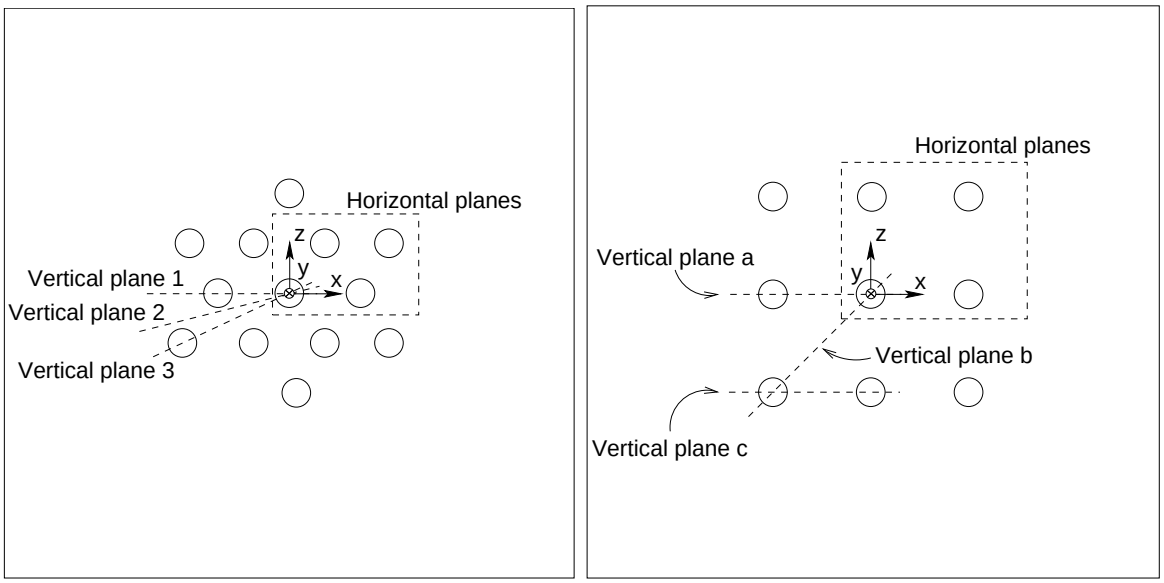

(a) hexagonal configuration (b) in-line configuration

Figure 4.15: The orientation of the measurement planes with respect to the nozzle plates

(planes *a*, *b*, and *c*) depicted in Figure 4.15b. Plane *a* intersects the central jet and one of its direct neighbors, plane *b* intersects the central jet and one of the outer jets, and plane *c* intersects one of the central jet's direct neighbors and one of the outer jets. The measurement area was defined by -1.2 $< x/D_m <$ 5.0 and 0.0 $< y/D_m <$ 4.0 for vertical planes *a* and *c*, and -0.7 $< x/D_m <$ 6.6 and 0.0 $< y/D_m <$ 4.0 for vertical plane *b*.

Finally, measurements were done in three horizontal planes in the in-line configuration. One plane is at h= $0.23D_m$, one is at h= $0.54D_m$, and the last one is at h= $0.92D_m$. These planes all focus on the same four jets: the central jet, two of its direct neighbors and one of the outer jets. The position of the measurement area was $-1.9 < x/D_m < 5.3$ and $-0.8 < z/D_m < 5.0$ for the horizontal planes at h= $0.23D_m$ and h= $0.54D_m$, and $-1.4 < x/D_m < 6.0$ and $-0.8 < z/D_m < 5.0$ for the horizontal plane at h= $0.92D_m$ in the in-line configuration.

The impingement flow was investigated using the PIV system described in Section 4.1 (page 57). The seeding was produced by the apparatus described in Section 4.1 (page 57). The configurations of the PIV system for the vertical and the horizontal plane measurements are presented in Figures 4.16a and b, respectively. For the measurements in the vertical planes the laser produced a light sheet perpendicular to the impingement plate and the nozzle plate and the camera recorded images of particles in the light sheet from the side. For the horizontal planes the light sheet was parallel to both

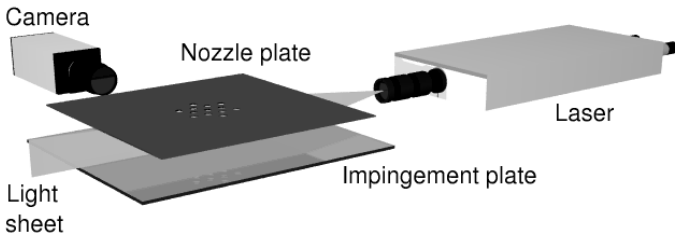

(a) vertical planes

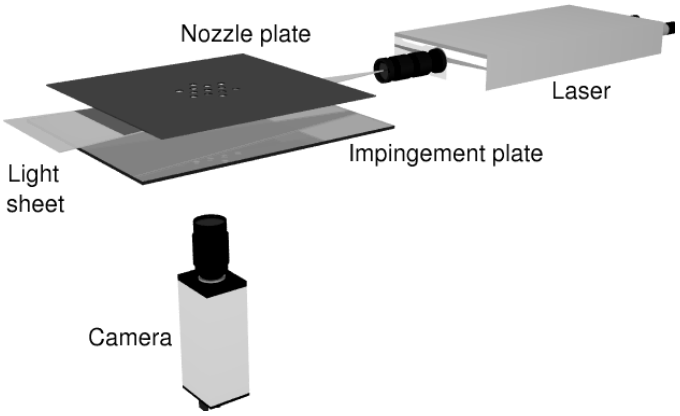

(b) horizontal planes

Figure 4.16: PIV configuration for the impinging jet arrays

the impingement plate and the nozzle plate, and the camera recorded images from the bottom, through the glass impingement plate.

Table 4.2 presents the recording parameters of the PIV system for the four different configurations. The values are averages of the values for the different planes in each of the four configurations. As can be seen in Table 4.2, the interrogation areas in the horizontal planes in both arrays were twice the size of the interrogation areas in the vertical planes. Because the noise level in the PIV images in the horizontal planes was higher than that in the vertical planes, more particle images were needed for a good signal-to-noise ratio. The reason for the higher noise level is the fact that the images were

Table 4.2: PIV recording parameters for all experiments

	Hexagonal jet array		In-line jet array	
	Horizontal	Vertical	Horizontal	Vertical
Focal length lens (mm)	55	105	55	55
Numerical aperture (-)	8	11	8	8
Field of view (mm^2)	53.3×42.9	71.2×52.0	85.2×66.2	75.5×52.0
Interrogation area size (px)	64×64	32×32	64×64	32×32
(mm^2)	2.7×2.7	1.8×1.8	4.7×4.7	2.0×2.0[a]
				2.4×2.4[b]
Interrogation area overlap	50%	50%	50%	50%
Pulse delay (μs)	11.7	20.0	10.0[c]	21.8[a]
			6.0[d]	25.8[b]
Dynamic velocity range (m/s)	0.36 : 57	0.28 : 22	0.73 : 116	0.29 : 23
			1.2 : 198	
Reynolds number	18×10^3	18×10^3	20×10^3	20×10^3
Number of snapshots	1000	3000	3000	3000

[a] planes a and c
[b] plane b
[c] plane at h=$0.23D_m$
[d] planes at h=$0.54D_m$ and $0.92D_m$

taken through the impingement plate which was gradually fouled by seeding deposition. Between every 200 images the impingement plate had to be cleaned.

Additionally, it can be seen that the number of snapshots in the ensemble is only 1000 for the horizontal planes of the hexagonal jet array, whereas it is 3000 for the other configurations. Cleaning of the impingement plate took a large amount of time. After these measurements the cleaning system was automated and sped up, so more measurements could be done in the same time.

The images resulting from all configurations were analyzed in three consecutive steps. First, the interrogation areas were cross-correlated and a local median filter was used to discard the spurious vectors. The resulting empty spaces were filled with interpolated values from the surrounding interrogation areas. The resulting displacement fields were used as window displacements for an adaptive cross-correlation of the same interrogation areas in the second step. After filtering out and replacing the spurious vectors the second step is repeated. The percentage of spurious vectors was 4% on average for all vertical planes and about 3% for all horizontal planes. Compared to the analysis of the single jet data, the analysis of the jet array data has one step extra. The motivation for the extra step is a significant reduction of the number of spurious vectors, while this step gave no such improvement for the single jet data.

Chapter 5

Results

5.1 Single impinging jet

In this section LDA and PIV velocity measurements are compared. These measurements were aimed at verifying the PIV experiments, which were subsequently used for detailed exploration of multiple jets. In addition, these measurements have provided some new information on single impinging jet flow dynamics and structure. The mean and RMS values of the radial and axial components of the velocity are presented at three stations in the flow. Deductions from the results regarding the mechanisms of turbulence energy production in the impingement zone are also discussed. The reader is referred to Figure 4.2 (on page 56) for the notations and the positions of the three stations at which the results are presented.

Figure 5.1a and 5.1b show mean and RMS values of the radial and axial velocity components u and v as a function of the wall-normal distance y, at the station x/D_s= 0.0 which is located along the center line. All velocity values are non-dimensionalized by the velocity averaged over the cross-section of the orifice, U_{bulk}, and the wall-normal distance is normalized by the pipe diameter D_s. The continuous lines represent the data resulting from PIV measurements and the symbols represent the data obtained from LDA. From these figures it is clear that the results of both measurement techniques are in good agreement. However, there appears to be a small, but noticeable, systematic difference in the RMS values of u in regions where the mean value of u is close to zero. The cause of the difference is still not fully clear. It could not be explained by velocity bias or the possible effects of random noise contributions in the instantaneous velocity samples. Close to the wall only LDA data is available, because LDA is superior to PIV in this region. The turbulence intensity, defined as $\sqrt{\langle v'^2 \rangle}/\langle v \rangle$, at the center of the pipe exit equals 5.1% which is close to earlier measurements of e.g. Baughn and Shimizu (1989). Also, the measured radial mean velocity is nearly zero everywhere along the centerline, suggesting good axial flow symmetry.

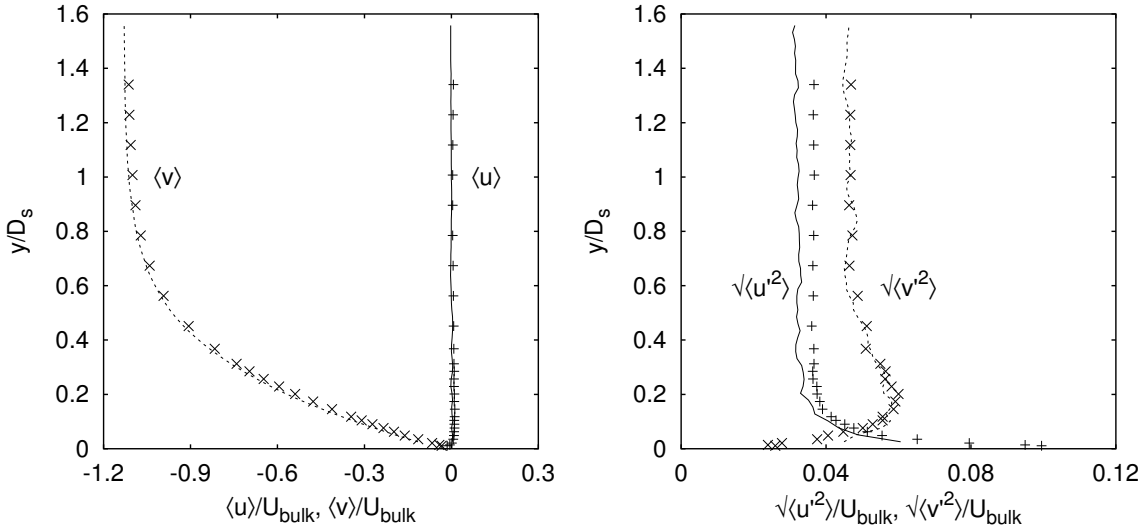

(a) mean velocities.

(b) RMS velocities.

Figure 5.1: LDA (symbols) and PIV (lines) profiles in single jet at x/D_s=0.0.

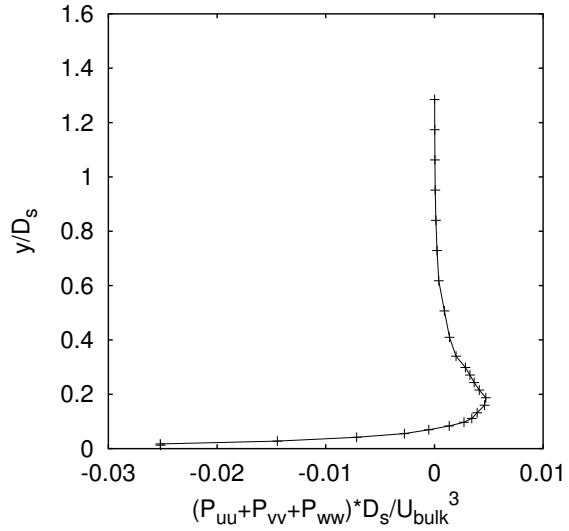

Figure 5.2: Profile of the normal production in the center line of the single jet, estimated from the LDA data.

For $y/D_s > 1.0$ the mean axial velocity $\langle v \rangle$ is nearly constant, because the growing shear layers on the edge of the jet have not yet reached the center line and the flow is not affected by the presence of the impingement wall. For lower values of y/D_s the flow is decelerated, but the shear layers still have not reached the jet core. The latter is illustrated by the fact that the values of $\sqrt{\langle u'^2 \rangle}$ and $\sqrt{\langle v'^2 \rangle}$ remain at a constant level down to $y/D_s = 0.3$. It can therefore be concluded that the length of the jet core is higher than the distance between the nozzle and the impingement plate. This is consistent with the findings of Cooper et al. (1993) and Kataoka (1990), who have shown the jet core of turbulent round jets to be about 4 to 6 nozzle diameters in length.

In the near wall region ($y/D_s < 0.1$) the values of $\sqrt{\langle v'^2 \rangle}$ appear to extrapolate to zero, while the values for $\sqrt{\langle u'^2 \rangle}$ increase monotonically towards the wall. The increase of $\sqrt{\langle u'^2 \rangle}$ in this region is caused by mild oscillations of the impingement position that were observed from instantaneous PIV velocity fields. The anisotropy of the Reynolds normal stresses plays an important role in the production of turbulence kinetic energy as can be seen from the expression for the production on the centerline: $P_k = (\langle u'^2 \rangle - \langle v'^2 \rangle) \partial \langle v \rangle / \partial y$. Since $\partial \langle v \rangle / \partial y$ is negative everywhere on the centerline, it follows from Figure 5.1b that negative production takes place for $y/D_s < 0.1$, as is illustrated by Figure 5.2. Note that the normal production in this figure is non-dimensionalized by U_{bulk}^3/D_s. Nishino et al. (1996) also reported the change in sign of $(\langle u'^2 \rangle - \langle v'^2 \rangle)$ at $y/D_s = 0.1$, despite differences in Reynolds number and nozzle-to-impingement-plate distance.

A decrease of $\sqrt{\langle u'^2 \rangle}$ to zero on the wall cannot be observed from the measurements because of limitations of the experimental techniques. For the single-jet experimental set-up, the minimum wall distances for PIV and LDA are approximately 0.9 mm and 0.1 mm, respectively. For smaller wall distances both measurement techniques are adversely affected by laser light scattered by the impingement wall, giving rise to erroneous instantaneous velocities and too high values for the RMS of velocity fluctuations.

Figures 5.3a and b show mean velocities and RMS values of the radial and axial velocity components u and v as a function of y/D_s at the station $x/D_s = 0.5$. Results from PIV and LDA are again in reasonable agreement, except for the discrepancy in $\sqrt{\langle u'^2 \rangle}$ at low values of $\langle u \rangle$ that also appeared at $x/D_s = 0.0$. Since this station roughly coincides with the shear layer between the jet and the ambient air, high RMS velocity fluctuations are also observed for large distances from the impingement wall. The turbulence intensity $\sqrt{\langle v'^2 \rangle}/\langle v \rangle$ in this region is approximately 30%. Furthermore, this station is characterized by a strong deflection of the mean flow streamlines from axial to radial direction.

In the shear layer of the jet ($y/D_s > 0.6$) the average direction of the fluid is perpendicular to the impingement wall, as $\langle u \rangle$ equals zero and $\langle v \rangle$ equals approximately half of the bulk velocity. Shear causes instabilities resulting in strong velocity fluctuations. The difference in RMS values of the radial and axial velocity fluctuations indicate strong anisotropy. Due to the spreading of the jet by entrainment $\langle v \rangle$ is rising slightly towards

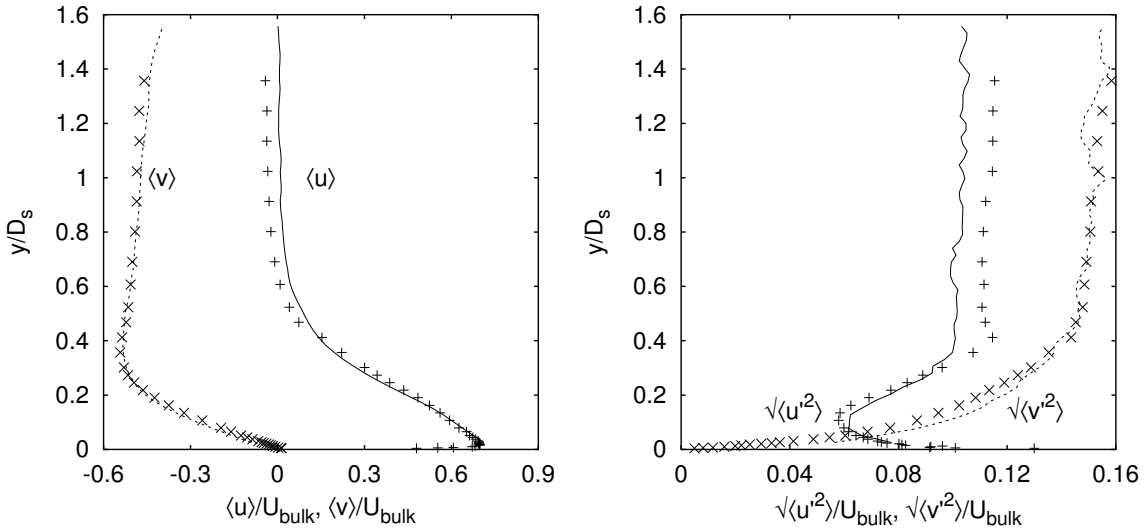

(a) mean velocities.

(b) RMS velocities.

Figure 5.3: LDA (symbols) and PIV (lines) profiles in single jet at x/D_s=0.5.

the impingement plate. For $y/D_s < 0.5$ the presence of the wall causes a deflection of the mean flow and a damping of the fluctuations. The increase of $\langle u'^2 \rangle$ closer to the wall is due to high turbulence production caused by wall friction. The subsequent decrease of $\langle u'^2 \rangle$ to zero at the wall could not be measured due to the previously mentioned scattering of laser light on the impingement plate.

At x/D_s= 0.5 the same anisotropy of turbulence is found as reported at x/D_s= 0.0. Because $\partial\langle u \rangle/\partial x$ is positive for $y/D_s < 0.4$, the production of k due to normal Reynolds stresses $\langle v'^2 \rangle$ and $\langle u'^2 \rangle$ is also similar. However, the magnitude of the normal production is greater at x/D_s= 0.5 due to the higher Reynolds stresses and the stronger velocity gradients. For $y/D_s > 0.4$ the similarity is lost because the normal production of k extrapolates to zero and production due to shear stresses gains importance when traversing towards the pipe exit. For very low values of y/D_s the wall parallel Reynolds stress component $\langle u'^2 \rangle$ does not extrapolate to zero due to measurement errors induced by laser light scattering on the impingement plate.

The mean and RMS velocities in the wall jet emerging from the impingement zone are presented in Figures 5.4a and 5.4b. The results of both measurement techniques are again in reasonable agreement. However, the PIV data of $\langle u'^2 \rangle$ for $y/D_s < 0.25$ do not coincide with the LDA data. This can be explained by the strong gradient of $\langle u \rangle$ in this zone. Due to the relatively large size of the interrogation areas it is not possible to fully resolve strong gradients with PIV. The probability for particles with a high velocity to form image pairs within the limits of one interrogation area is lower than for particles

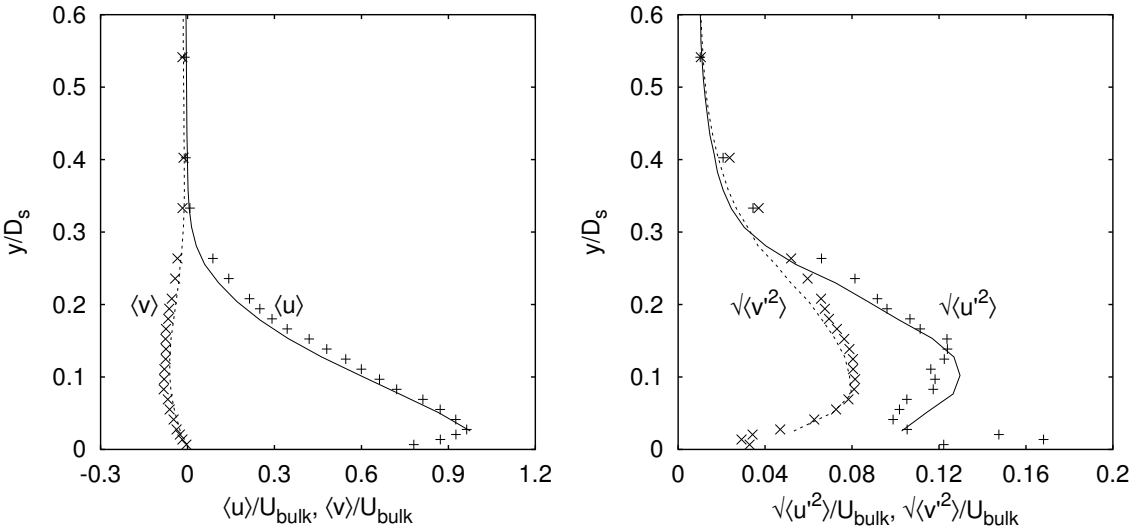

(a) mean velocities.

(b) RMS velocities.

Figure 5.4: LDA (symbols) and PIV (lines) profiles in single jet at x/D_s=1.0.

with a low velocity. Hence, PIV shows a tendency towards the lower velocity in these regions.

The wall jet is concentrated in the region for $y/D_s < 0.3$, because for higher values of y the mean velocity components equal zero and the fluctuating components approach zero. In the wall jet the fluctuations are still quite strong. However, at this station $\sqrt{\langle u'^2 \rangle}$ is greater than $\sqrt{\langle v'^2 \rangle}$ at all y-positions, whereas this was not the case at the other two stations. Because the fluid is flowing parallel to the wall, now the dominant contributions to the turbulent kinetic energy are wall friction and fluid entrainment into the wall jet. This is the reason why the production of the turbulent kinetic energy is not negative. The shear component greatly exceeds the normal one.

5.2 Multiple impinging jet array

PIV was used to provide mean velocity fields and turbulence quantities in the flow of two different multiple impinging jet arrays. This proved to be essential for detecting some salient features of the multiple-jet dynamic. Next to that, LCT was used to measure mean heat transfer distributions on the impingement plate. On the basis of these data, an empirical correlation is determined between the Nusselt number and the Reynolds number, the inter-nozzle spacing, and the nozzle-to-plate spacing for all three nozzle configurations presented in Table 4.1 on page 62. Heat transfer is subsequently correlated

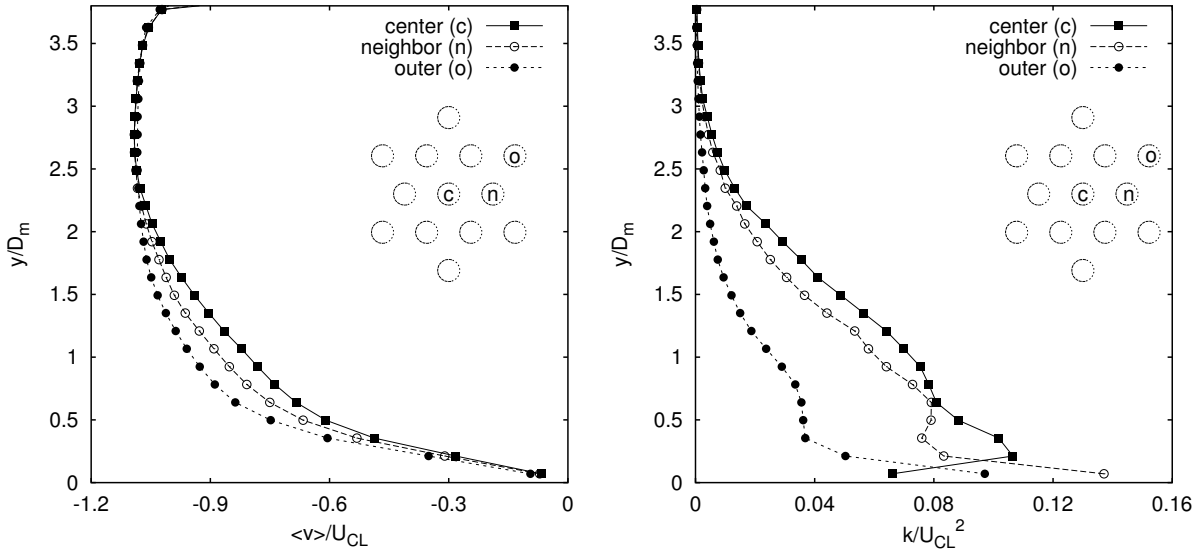

(a) mean velocities.

(b) turbulent kinetic energy.

Figure 5.5: Profiles in the center lines of the central jet, a neighboring jet, and an outer jet.

with velocity and turbulence quantities just above the impingement plate to investigate the effect of mean flow features on the heat transfer. Finally, the structure identification methods described in Section 2.1.3 are applied to PIV velocity data. The dynamics of the jets are investigated on the basis of POD filtered snapshots. Additionally, the POD filtered snapshots are used to locate vortices and calculate their sizes to see how they are distributed in the flow.

5.2.1 Fluid mechanics

Hexagonal configuration

Figures 5.5a and 5.5b show the mean axial velocity component $\langle v \rangle$ and the turbulent kinetic energy k as a function of the wall-normal distance y on the center lines of the center jet at $(x/D_m,\, z/D_m)= (0.0,\, 0.0)$, the neighbor jet at $(x/D_m,\, z/D_m)= (2.0,\, 0.0)$, and the outer jet at $(x/D_m,\, z/D_m)= (3.0,\, \sqrt{3.0})$. All velocity values are non-dimensionalized by the center line exit velocity of the center jet, U_{CL}, and the wall-normal distance is non-dimensionalized by the nozzle diameter D_m. The turbulent kinetic energy k was estimated from the two-component PIV data in the vertical planes as $\frac{1}{2}(2\langle u'^2 \rangle + \langle v'^2 \rangle)$, assuming that the magnitude of the unmeasured (out-of-plane) third velocity component $\langle w'^2 \rangle$ was comparable to that of $\langle u'^2 \rangle$. Figure 5.5a indicates an overshoot of the axial

velocity just after the nozzle exit for all three jets. This is caused by the *vena contracta* that is characteristic for jets emerging from sharp-edged constant-area nozzles. Experiments reported by Geers et al. (2001) showed that the mean velocities on the axis of the jets on either side of the central jet were nearly equal indicating good flow symmetry.

Three regions can be discerned for the axial velocity component of all three jets. In the initial (free) jet region, for approximately $y/D_m > 2.3$, the axial velocity is fairly constant and the turbulence intensity is low. Compared to the center jet, the initial jet region appears to be longer for the neighbor jet and much longer for the outer jet. This can be explained as effects of interaction with the surrounding jets. The center jet is surrounded by six jets and it is therefore strongly affected by the interaction with its neighbors. The upwash flow between the center jet and its six neighbors augments the axial velocity gradient in the shear layers of the jets. This amplifies the instabilities in the shear layer and causes momentum of the mean flow to be converted to turbulent stresses. The neighbor jet is surrounded by five jets while the outer jet has only two neighbors and is therefore least disturbed.

Further downstream in the development region ($0.7 < y/D_m < 1.5$) the center jet appears to decelerate more than the neighbor jet and much more than the outer jet. The decay of the axial velocity of the jets coincides with a monotonic rise of k towards the impingement wall, illustrating the gradual transformation of the energy of the mean flow into turbulent energy. The decay of the central jet is the strongest, corresponding to the highest values of k.

In the impingement region ($0 < y/D_m < 0.5$) the differences between the axial velocity profiles of the three jets vanish. Apparently the effect of the impingement wall on the jets is stronger than the effect of jet-to-jet interactions in this region. The strong adverse pressure gradient in the impingement region causes the gradient of k to decrease and even k to decrease in the center jet and in the neighbor jet. Notice that k does not extrapolate to zero due to the above mentioned laser light reflection from the impingement wall.

Figures 5.6a to 5.6e show the mean velocity vectors and contours of the turbulent kinetic energy k in the three vertical planes and the two horizontal planes (indicated in Figure 5.6f) obtained from PIV measurements. In the vertical planes only a quarter of the total amount of vectors is shown for reasons of clarity. Recall that the turbulent kinetic energy k in the vertical planes was estimated from the two-component PIV data as $\frac{1}{2}(2\langle u'^2\rangle + \langle v'^2\rangle)$. The values of k in the horizontal plane were simply computed from the PIV data as $\langle u'^2\rangle + \langle w'^2\rangle$, since no realistic approximation for the unmeasured third velocity component could be made. The circles shown in Figures 5.6d and 5.6e are vertical projections of the nozzles on the horizontal measurement planes.

In Figure 5.6a the data are presented for vertical plane 1 with the center jet and its neighbor. Note that the out-of-plane mean velocity is zero here due to flow symmetry. The air injected through the nozzles impinges on the plate and short wall jets are formed. The wall jets emerging from the impingement regions collide and separate from the

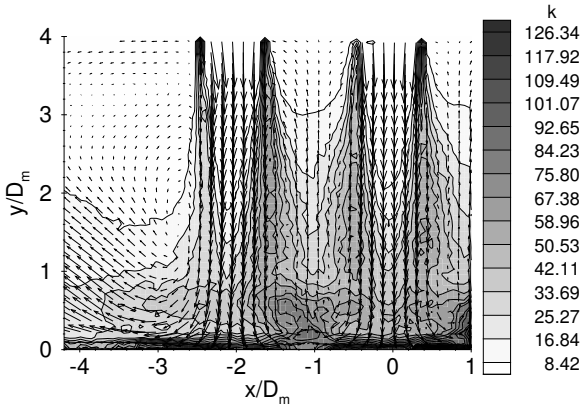

(a) Vertical plane 1.

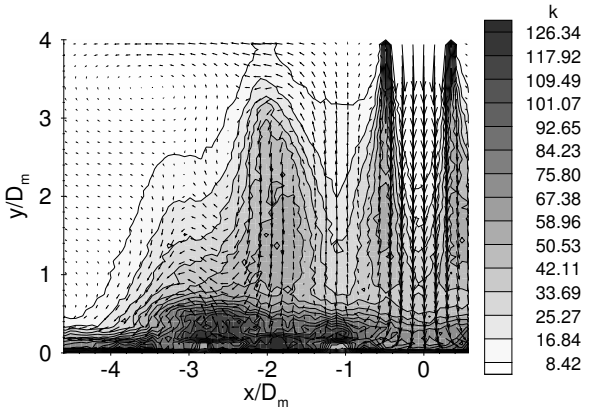

(b) Vertical plane 2.

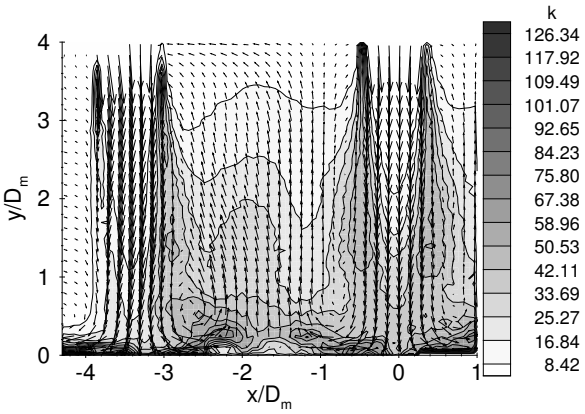

(c) Vertical plane 3.

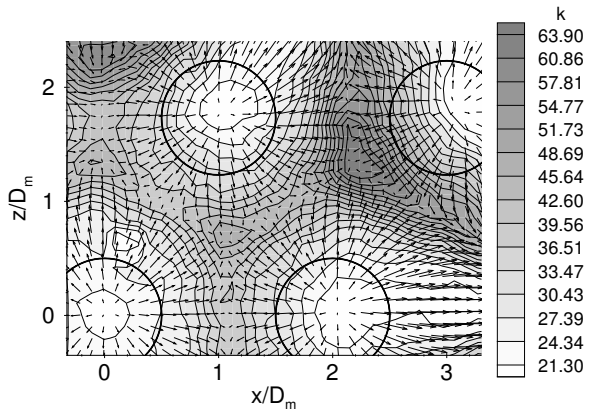

(d) Horizontal plane at h=0.25D_m.

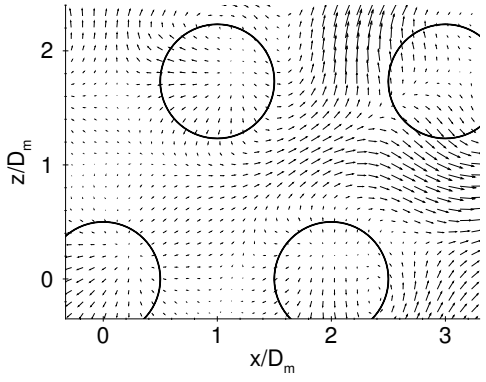

(e) Horizontal plane at h=1.5D_m.

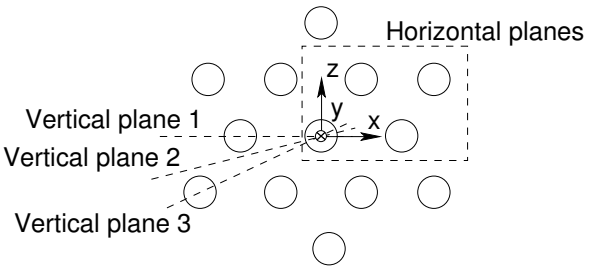

(f) Definitions of planes.

Figure 5.6: Mean velocity and k distributions in the hexagonal jet array resulting from PIV measurements.

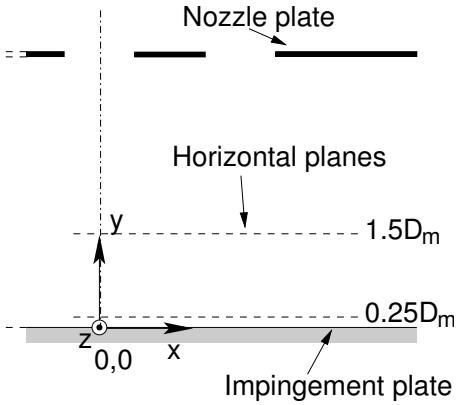

Figure 5.7: Definition of the horizontal planes in the hexagonal configuration.

impingement plate. Two counter-rotating recirculation zones are generated between the two jets inducing a strong upwash flow. Part of the upwash flow is entrained into the neighboring jet and discharged after re-impinging on the surface. Another part of the upwash discharges by flowing around the neighbor jet and the outer jet. This second discharge mechanism is illustrated in Figure 5.6e, which depicts the mean velocity vectors in the horizontal plane at $h = 1.5D_m$ (Figure 5.7). Both discharge mechanisms were also detected by Matsumoto et al. (1999).

Interaction between the wall jets and the cross flow forms a horse-shoe type vortex that circumscribes the outer jet. The center of this vortex can be discerned in Figure 5.6b at position (x/D_m, y/D_m) $\approx$ (-3.1, 0.3). The vortex forces air, entrained by a neighbor jet to be deflected towards the impingement surface before it flows out. Note that the vortex is also visible in Figure 5.6c at position (x/D_m, y/D_m) $\approx$ (-2.7, 0.5), and that this position coincides with the region of intense velocity fluctuations in Figure 5.6d.

In the present experiment the cross flow is *self induced* as exhaust air can flow away through all four sides of the experimental rig. Consequently, the cross flow is absent at the central jet but its strength increases with increasing distance from this center. The cross flow is apparently too weak to produce a horse-shoe vortex in the region between the center jet and the neighbor jets, even though it can be seen in Figure 5.6d that the impingement positions of the neighbor jets do not exactly coincide with the geometrical centers of the nozzles. The outward displacement of these neighbor jets may not be large, but the outer jet is displaced significantly by the cross flow.

Figures 5.6a and 5.6c show a symmetrical distribution of k around the axis of the center jet, whereas it is highly asymmetrical around the axes of the neighboring jet and the outer jet. In both figures k is relatively high on the inner side of the jets and relatively low on the outer side. The stronger velocity fluctuations are produced by the interaction of the jets and the upwash flow in the region between jets. On the outer side of the jets this upwash is absent, causing the velocity gradient in the shear layer, and therefore k,

to be lower.

In Figures 5.8, 5.9, and 5.10 profiles are plotted of the wall normal mean velocity, the Reynolds normal stresses and shear stress, respectively, at different heights above the impingement plate. The profiles are taken from vertical plane 1. Each point corresponds to a single interrogation area and the lines show simple connection of the measuring points. The resolution in the area $y/D_m > 2.5$ seems insufficient for resolving thin shear layers at the jets edges (hence peaks in the curves), but this does not affect the general quality of the results, especially since we are interested more in the impingement area. In Figure 5.8 two distinct jets with sharp velocity gradients at the edges can be discerned at $y/D_m = 3.5$. Note the decay of the individual jets and the upwash in between the jets. Figure 5.9 shows that the distribution of $\langle v'^2 \rangle$ around the neighbor jet is highly asymmetric, illustrating the effect of jet-jet interaction on the normal stresses. Figure 5.10 shows that the Reynolds shear stresses around the center jet and on the right hand side of the neighbor jet are of similar magnitude, whereas the shear stress on the left hand side of the neighbor jet is lower by a factor 1.5. Presumably this is caused by the upwash flow.

Figures 5.11, 5.12, and 5.13 present profiles of the wall parallel mean velocity, the Reynolds normal stresses and the Reynolds shear stress, respectively, at different distances from the center line of the center jet. These profiles are also taken at vertical plane 1. The previously mentioned discharge mechanisms can be recognized in the profile at $x/D_m = -3.0$ in Figure 5.11. The outflow above $y/D_m = 3.4$ is very weak because of blockage by the neighbor jet. The combined effect of cross-flow and the wall jets originating from the neighbor jet cause the strong outflow below $y/D_m = 2.0$.

Figure 5.12 illustrates that the anisotropy in the Reynolds normal stresses found for the single impinging jet is qualitatively similar to that of the jet array at $x/D_m = 0.0$ and $x/D_m = -2.0$. However, the single jet already had an anisotropy originating from the pipe flow, which is not the case for the multiple jets issuing from orifices in a flat plate. In the array the jets initially have a very low, nearly isotropic, turbulence level. Gradually moving towards the impingement plate the difference between the two normal stresses grows and changes sign just above the impingement plate. As in the case of the single jet this causes negative production of the turbulent kinetic energy P_k for both jets, because the shear stresses are almost zero on the center lines just above the impingement plate, as is shown in Figure 5.13.

The normal and shear production of turbulent kinetic energy in vertical plane 1 are presented in Figure 5.14a and 5.14b, respectively. In Figure 5.14a the dark gray and black areas depict regions of positive normal production and the light gray and white areas depict regions of negative normal production. The white diamond shaped spots on the line $y/D_m = 3.9$ are regions where no valid data were available.

The normal stress contribution to the production of k is seen to rise towards the impingement plate on the center lines of both jets, reaching a maximum at $0.35D_m$ above the

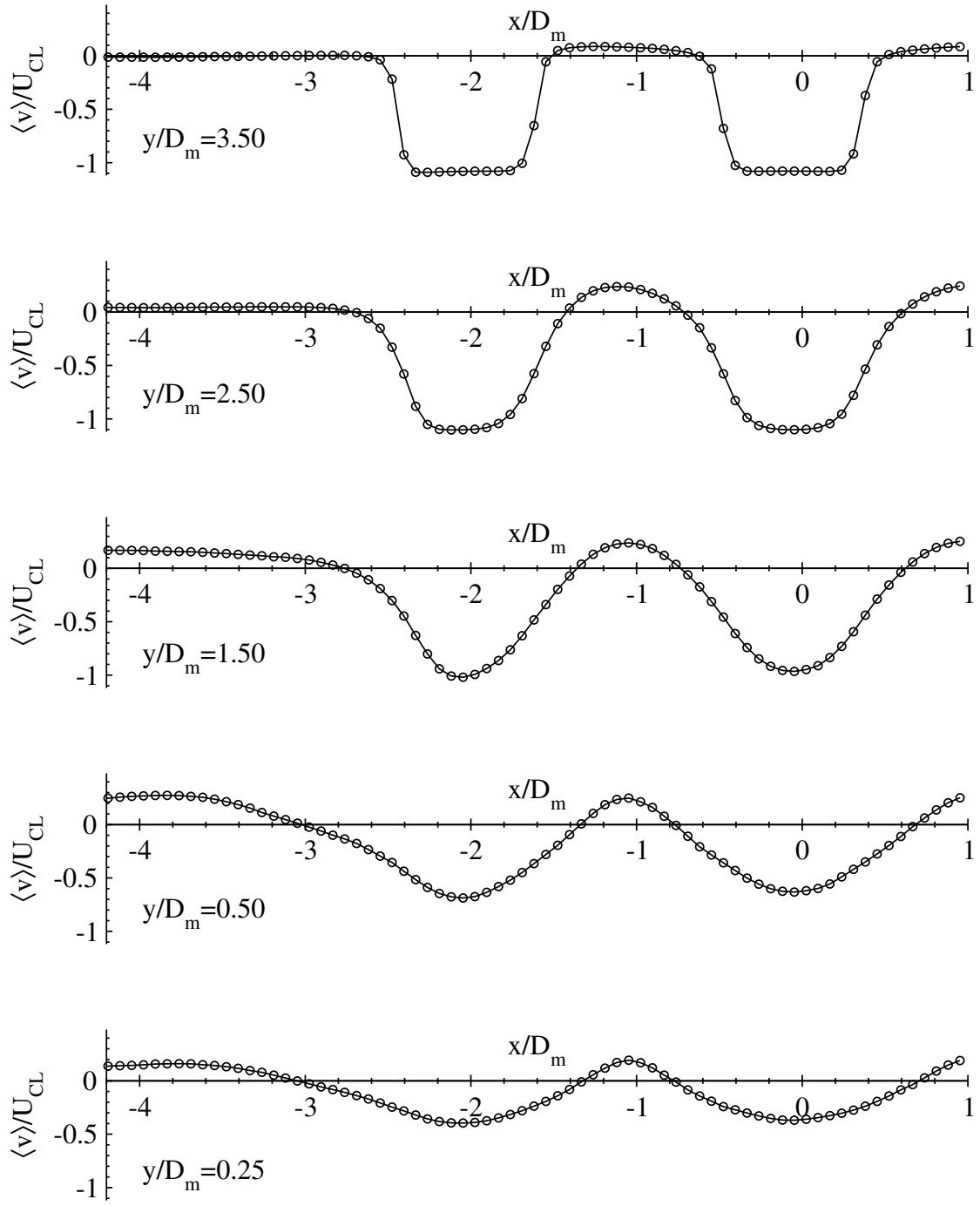

Figure 5.8: Profiles of $\langle v \rangle$ at different heights above the impingement plate for the hexagonal array.

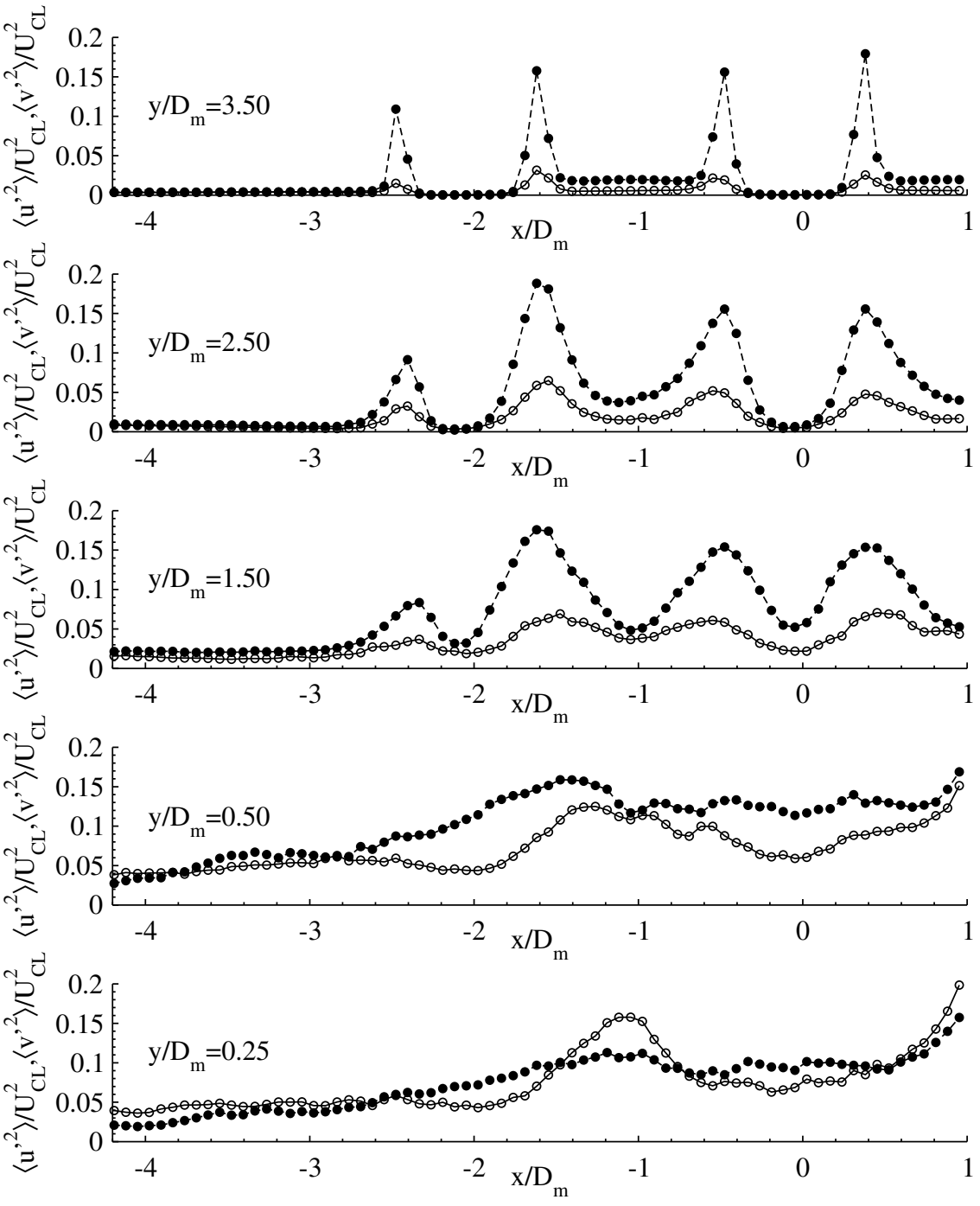

Figure 5.9: Profiles of $\langle u'^2 \rangle$ (—○—) and $\langle v'^2 \rangle$ (– ● –) at different heights above the impingement plate for the hexagonal array.

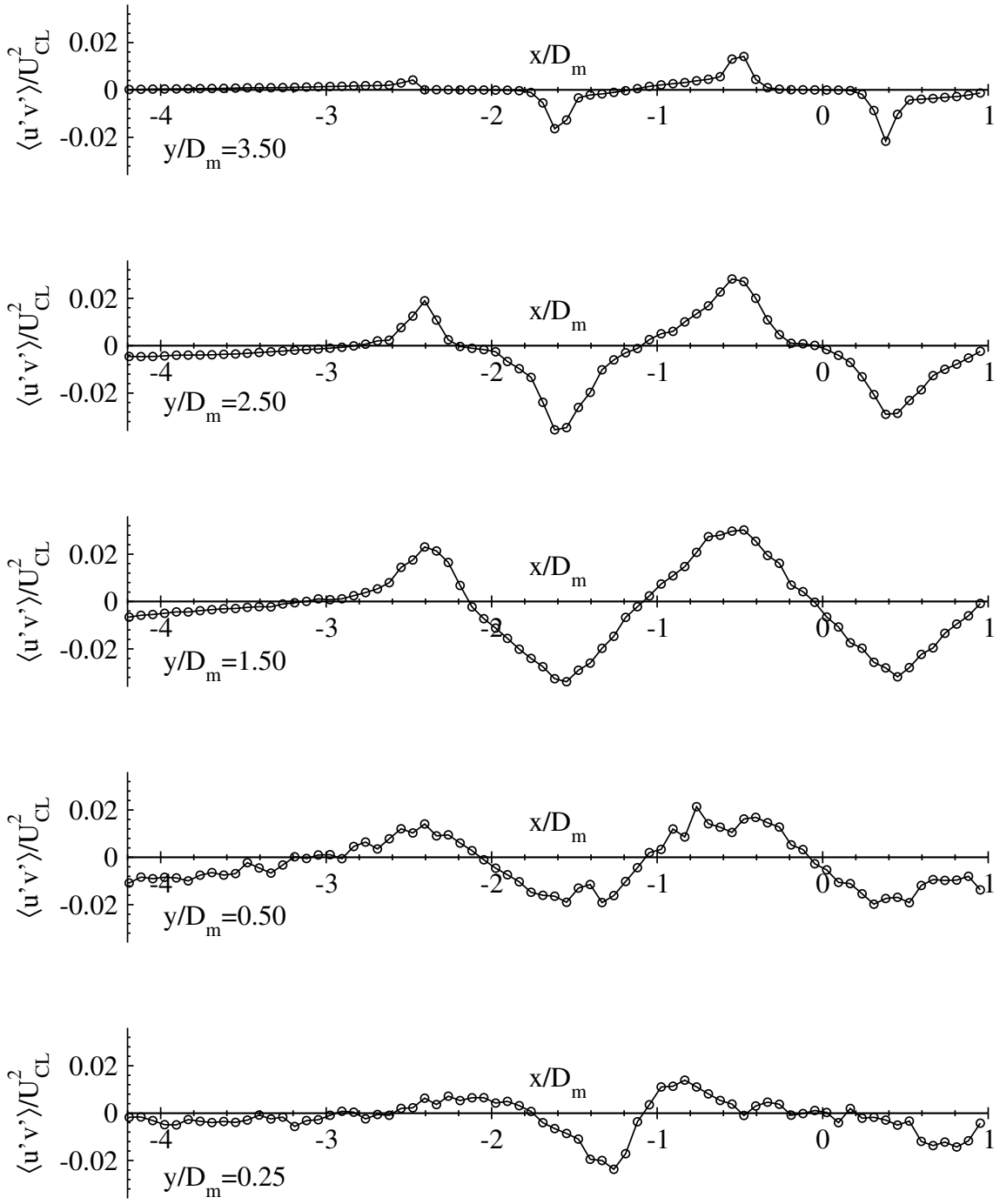

Figure 5.10: Profiles of $\langle u'v' \rangle$ at different heights above the impingement plate for the hexagonal array.

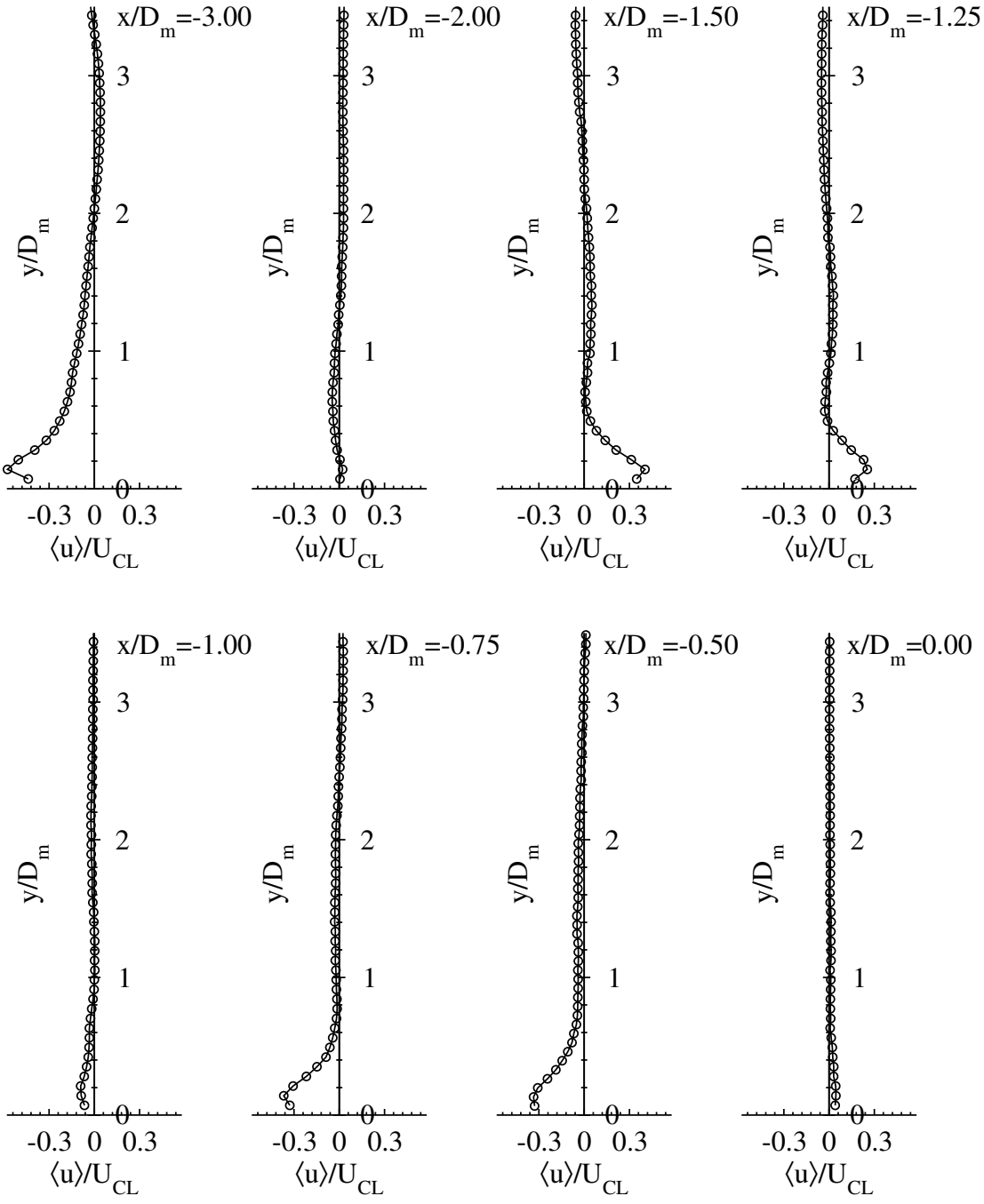

Figure 5.11: Profiles of $\langle u \rangle$ at different distances from the center jet for the hexagonal array.

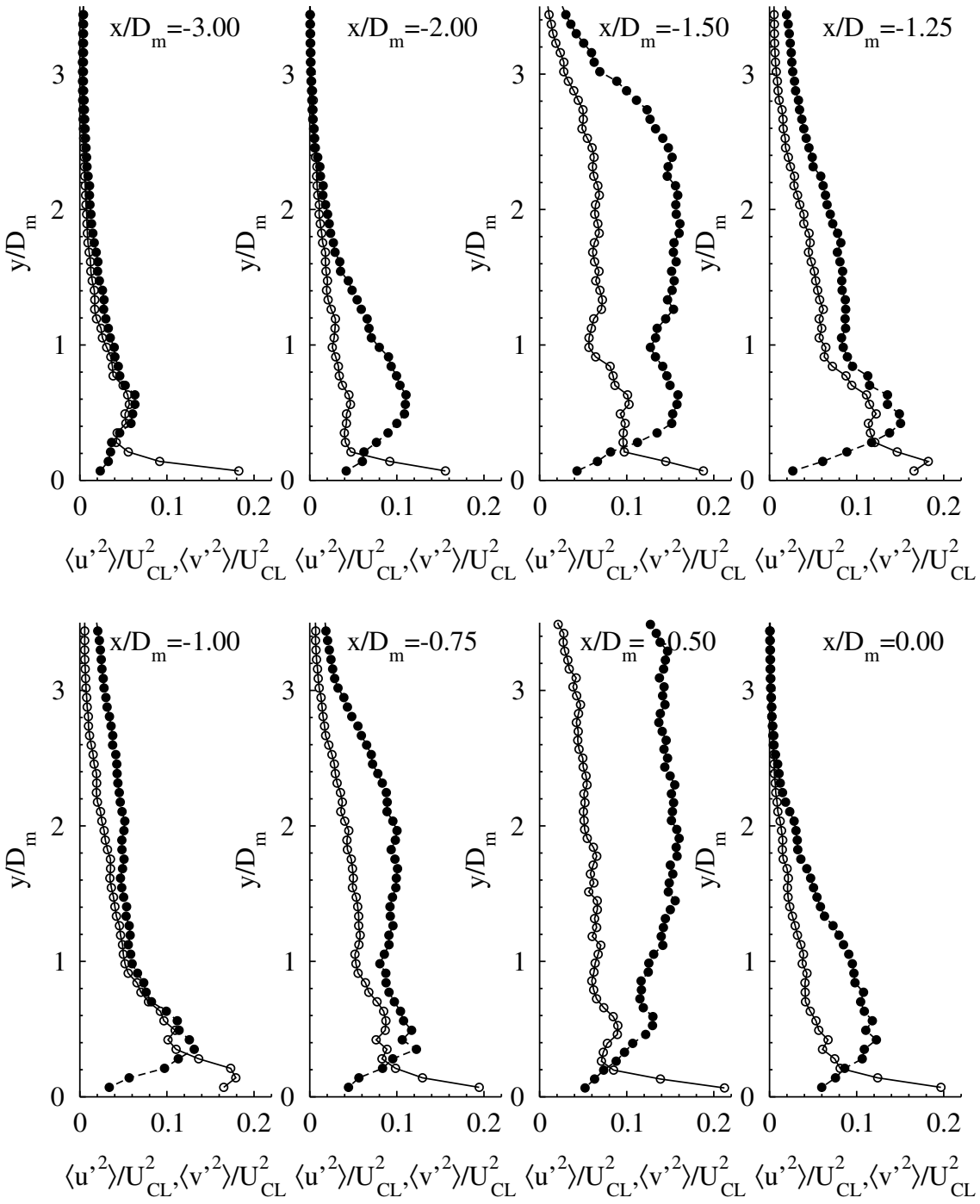

Figure 5.12: Profiles of $\langle u'^2 \rangle$ (—○—) and $\langle v'^2 \rangle$ (– • –) at different distances from the center jet for the hexagonal array.

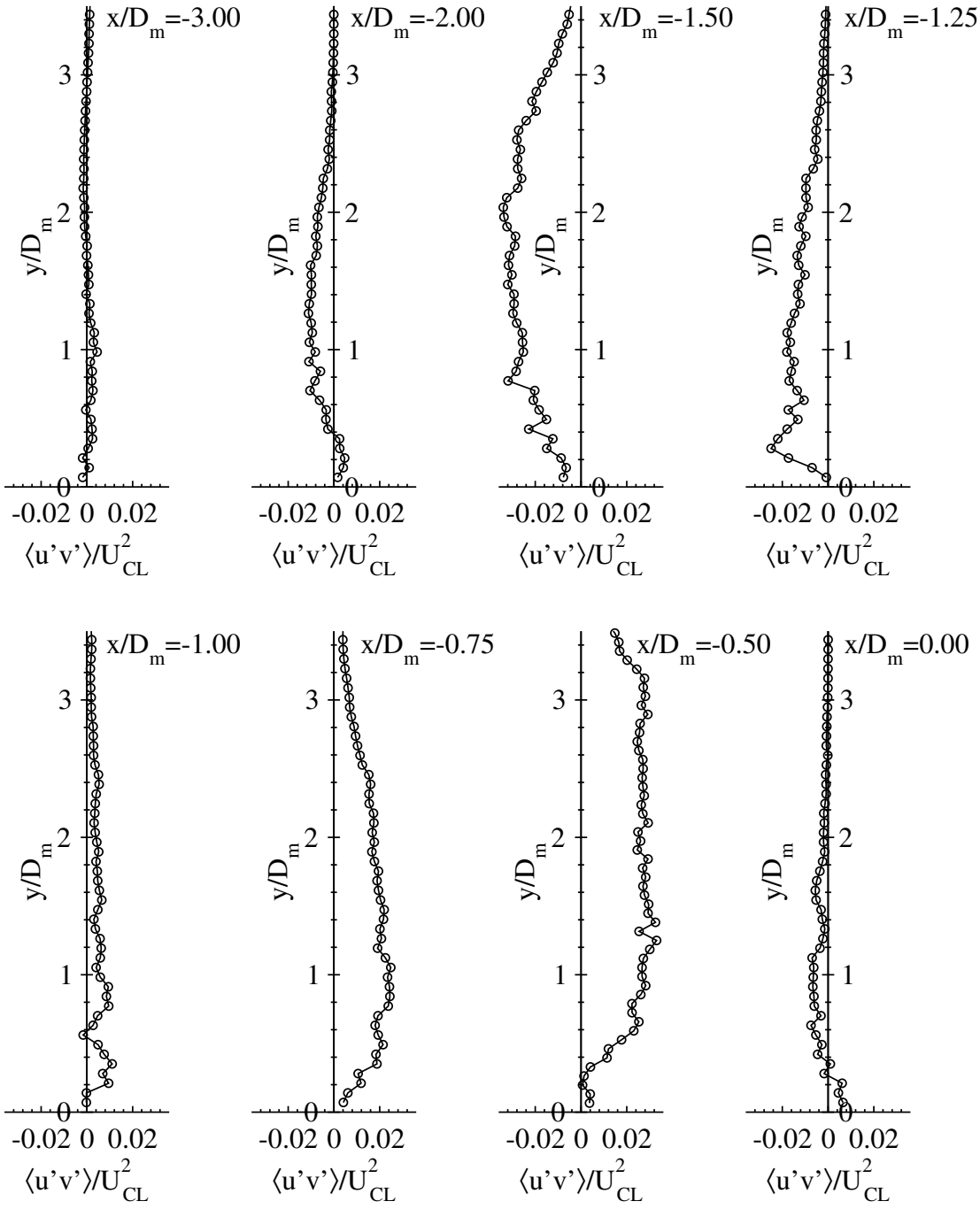

Figure 5.13: Profiles of $\langle u'v' \rangle$ at different distances from the center jet for the hexagonal array.

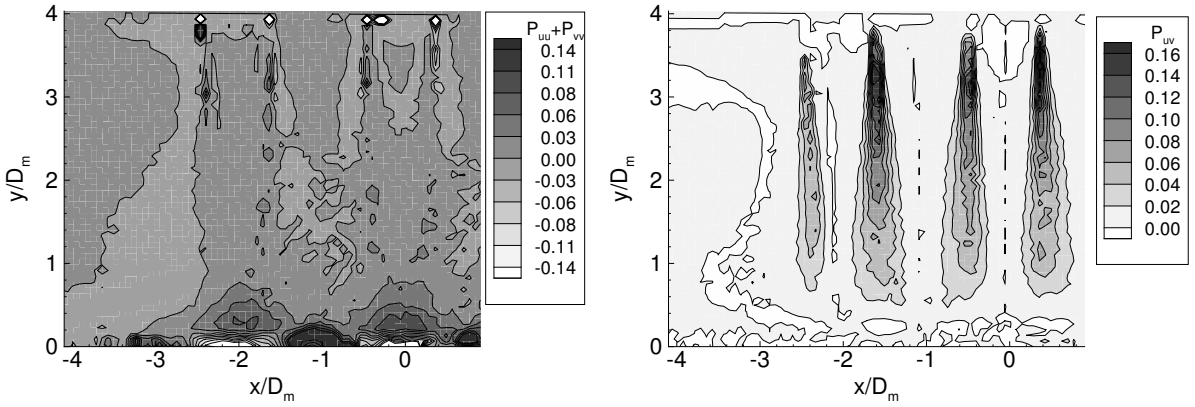

(a) k-production by normal stresses $P_{uu} + P_{vv}$.

(b) k-production by shear stresses P_{uv}.

Figure 5.14: Distribution of normal and shear production of k in vertical plane 1 of the hexagonal array non-dimensionalized by U_{CL}^3/D_m.

plate. Closer to the plate the normal production becomes negative, due to the reversal of the normal stress difference $\langle u'^2 \rangle - \langle v'^2 \rangle$. Near the impingement position the mean flow changes direction from axial to radial under the formation of a thin wall jet. Near $x/D_m = -1.0$ the wall jets separate from the impingement surface thus forming the upwash flow. The deceleration of the wall jets towards the stagnation point at $x/D_m = -1.0$ results in large positive values of the normal production of k mainly through the term $-\langle u'^2 \rangle \partial \langle u \rangle / \partial x$. The production due to shear is evidently strongest in the shear layers of the jets. The profiles of both contributions to the turbulence energy production along several vertical cross-sections are shown in Figure 5.15 providing another quantitative look at the mechanism described above.

Figure 5.16a to 5.16d present instantaneous *snapshots* of the velocity field in vertical plane 1. These snapshots were randomly selected from the total ensemble of 3000 snapshots acquired in this plane. Contrary to what one would expect, the jets do not reach the impingement wall at all time instances. The jets are either broken up or severely displaced in the out-of-plane direction before impingement takes place. It is not known whether this large-scale phenomenon has a random or quasi-periodic behavior.

The severe distortions of the jets seem to occur below $y/D_m = 2.0$, coinciding with the rapid decay of the mean axial velocity component and the increase of k towards the wall. The distortions may be caused by the destabilization of the jets due to the upwash flow, as was mentioned above. Another cause may be the collision of the wall jets originating from jet impingement. These collisions cause instabilities in the direction of the upwash. The interaction of the jets with the cross-flow cannot explain the distortion. Although the outer jets experience a stronger cross-flow than the center jet, they are less disturbed, as was illustrated by Figure 5.5.

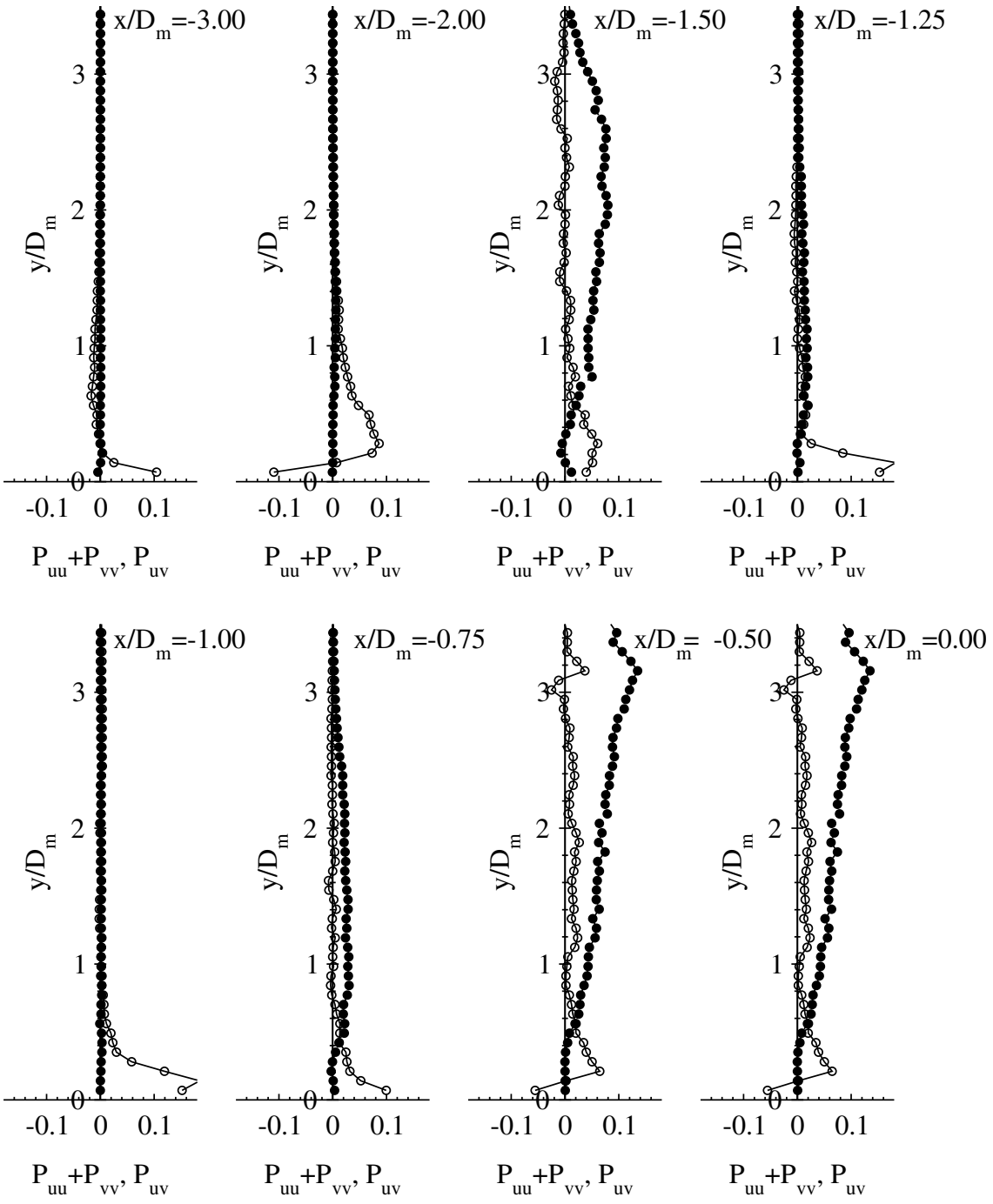

Figure 5.15: Profiles of normal and shear production of k at different distances from the center jet non-dimensionalized by U_{CL}^3/D_m.

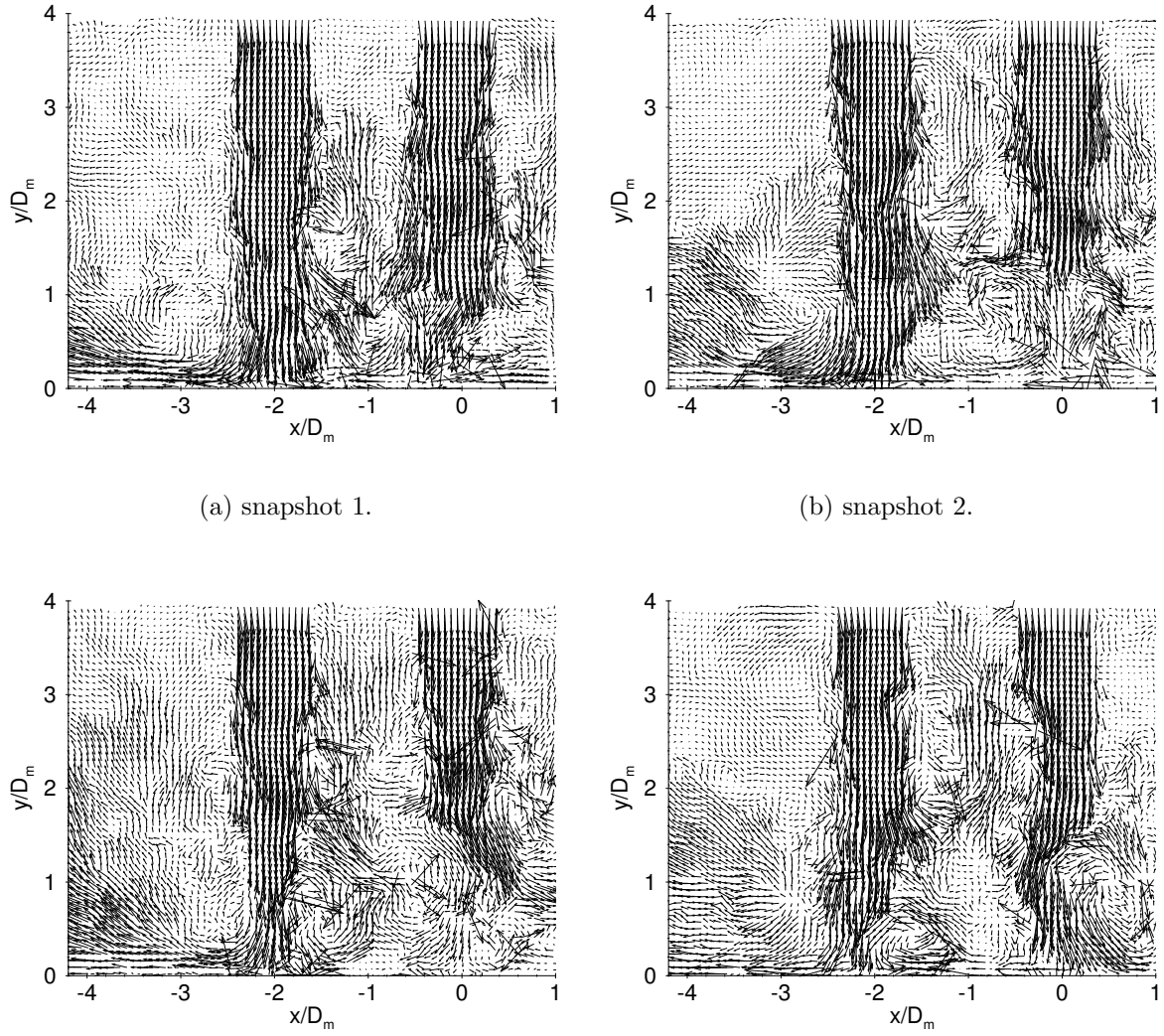

(a) snapshot 1.

(b) snapshot 2.

(c) snapshot 3.

(d) snapshot 4.

Figure 5.16: Instantaneous velocities in plane 1 of the hexagonal array.

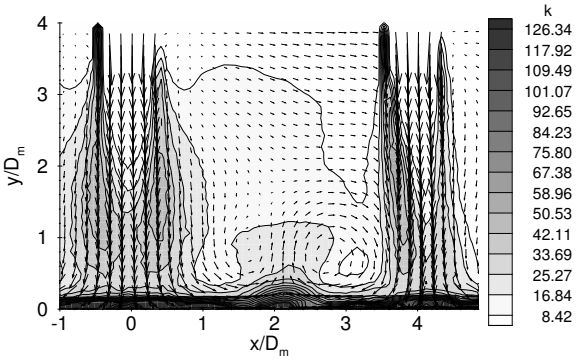

(a) Vertical plane a.

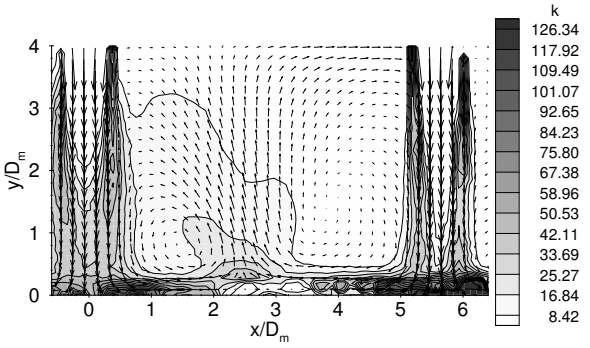

(b) Vertical plane b.

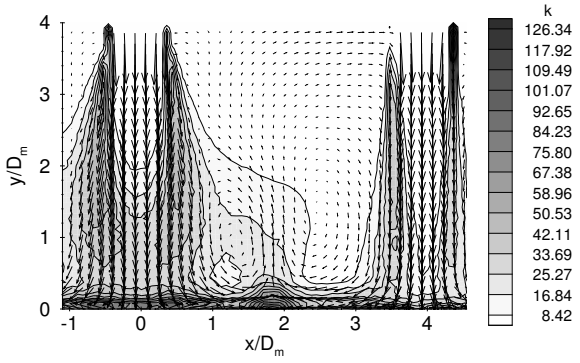

(c) Vertical plane c.

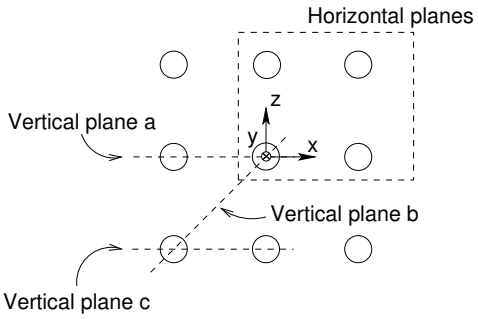

(d) Definitions of planes.

Figure 5.17: Mean velocity and k distributions in the three vertical planes for the in-line array.

In-line configuration

The mean velocity vectors and the turbulent kinetic energy k are presented in Figures 5.17a to 5.17c in the three vertical planes for the in-line jet array shown in Figure 5.17d. Similar to the vertical planes in the hexagonal array k is estimated from the two-component PIV data as $\frac{1}{2}(2\langle u'^2\rangle + \langle v'^2\rangle)$. Only a quarter of the total amount of vectors is shown for reasons of clarity.

A clear distortion of the jet at $x/D_m = 4.0$ can be seen in Figure 5.17a. The edge of the jet at $x/D_m = 3.5$ is deflected outwards, while the edge at $x/D_m = 4.5$ is perpendicular to the impingement wall. The cross-section of the jet seems to get smaller. This phenomenon appears clearly in Figure 5.19, in which profiles are presented of the

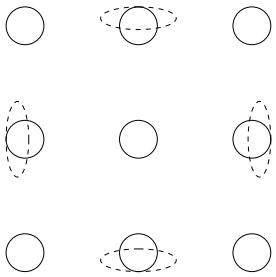

Figure 5.18: Sketch of the neighbor jet distortion

wall-normal velocity component at different heights above the impingement plate. The wall-parallel distance to the center jet x was non-dimensionalized by the jet diameter, D_m, and the velocity was non-dimensionalized by the center line exit velocity of the center jet, U_{CL}. As can be seen in Figure 5.19 the center jet (at x/D_m= 0.0) is increasing in width, while the width of the neighbor jet (at x/D_m= 4.0) is decreasing. Note that the profiles of the two jets are similar and have comparable maxima. Hence, the neighbor jet must get wider in the out-of-plane direction and assume an ellipsoidal shape as it approaches the impingement plate. A clarifying sketch is presented in Figure 5.18.

The profiles of the Reynolds normal stresses at different values of y/D_m presented in Figure 5.20 also reveal the distortion of the neighbor jet. The stresses are non-dimensionalized by U_{CL}^2. Due to the finite resolution of the PIV measurement the sharp shear layer at the jet edge could not be resolved for $y/D_m > 3.50$, hence the asymmetric peaks at the positions of the shear layers of the jets. For smaller values of y/D_m the profile of the center jet is symmetric around its geometric center line at x/D_m =0.0, but the profile of the neighbor jet is not symmetric around x/D_m =4.0. This is due to the outflow of spent air from the center jet, which produces a cross-flow that interferes with the neighbor jet.

The upwash due to the collision of wall jets at x/D_m= 2.0 extends over a much shorter distance than the upwash in the hexagonal array. This is obviously caused by the much greater jet spacing, but also by the geometry of the array. In the hexagonal array six nearest neighbors are interacting with the center jet, but for the in-line array there are only four nearest neighbors. Unlike the hexagonal array, there is no horse-shoe vortex detected around the outer jets or the neighbor jets of the in-line array. Most likely this is caused by difference in pitch (s/D_m).

Figures 5.21a to 5.21c present the mean velocity vectors in the three horizontal planes and k in the plane at $0.23D_m$ above the impingement plate. For this plane k was computed as $\langle u'^2 \rangle + \langle v'^2 \rangle$, since no realistic approximation could be made for the unmeasured third velocity component. The circles in these figures represent the projection of the nozzles on the impingement plate. The positioning of all horizontal planes in the measurement section is shown in Figure 5.21d. Due to fouling of the impingement plate by impacting

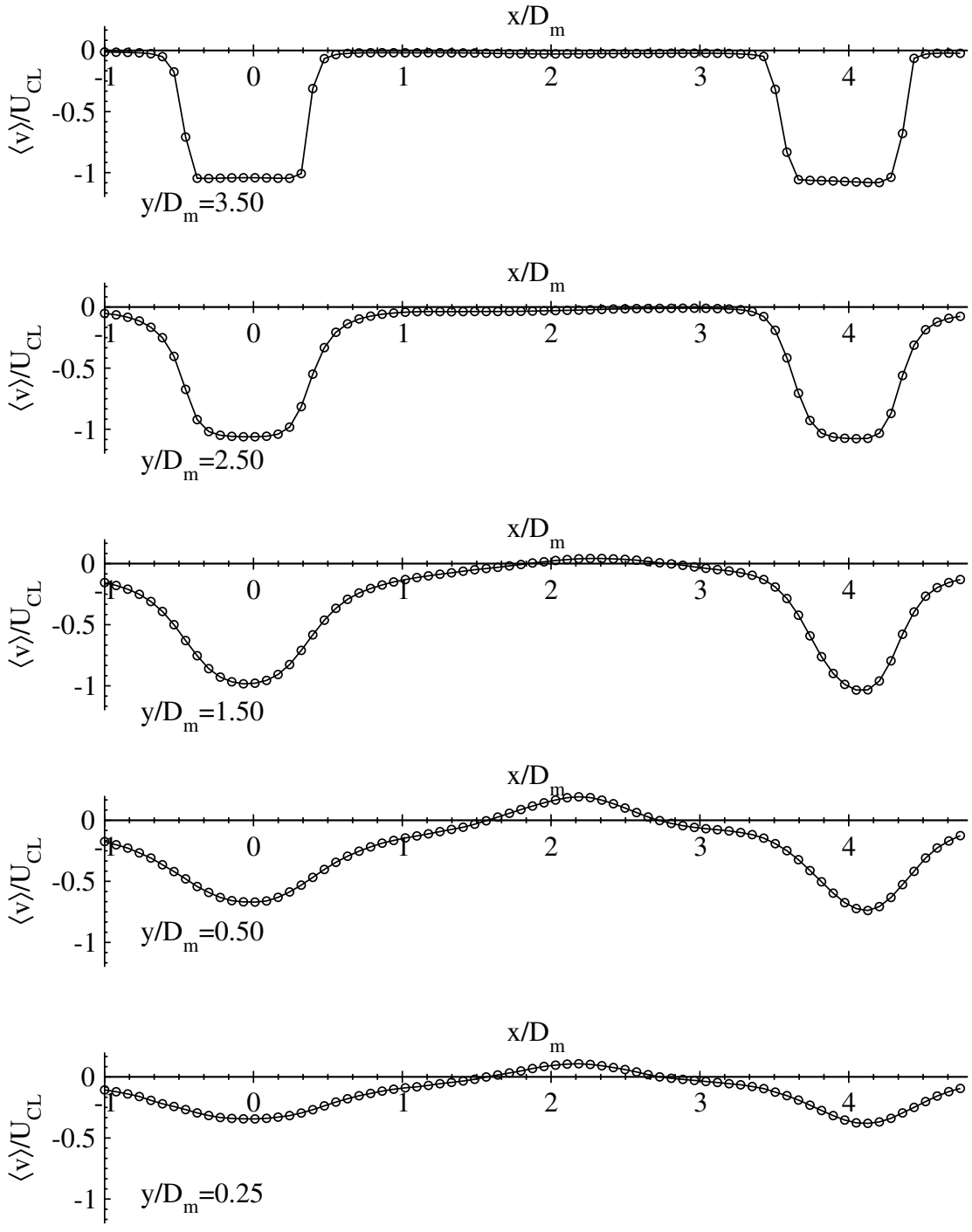

Figure 5.19: Profiles of $\langle v \rangle$ at different heights above the impingement plate for the in-line array.

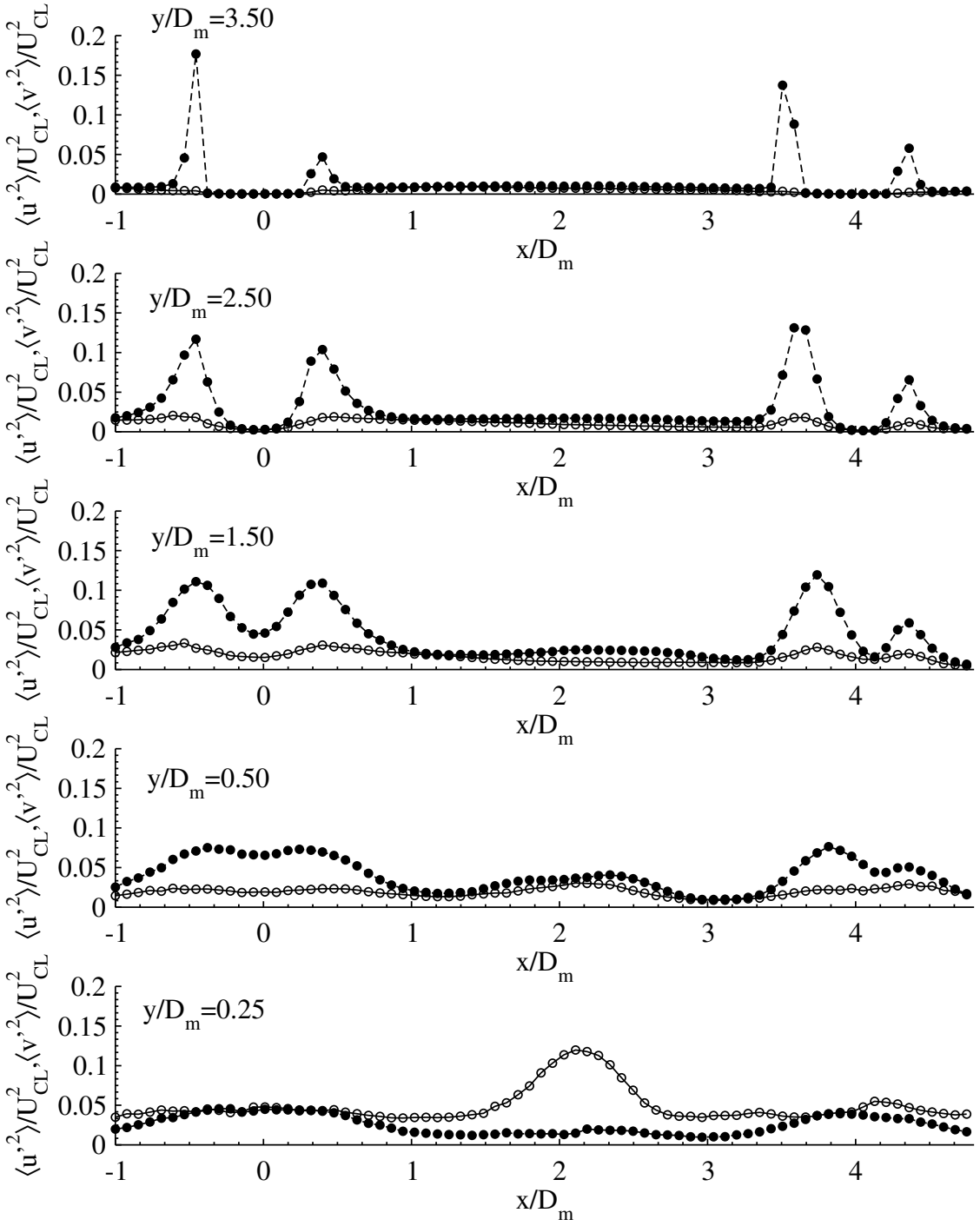

Figure 5.20: Profiles of $\langle u'^2 \rangle$ (—○—) and $\langle v'^2 \rangle$ (– • –) at different heights above the impingement plate for the in-line array.

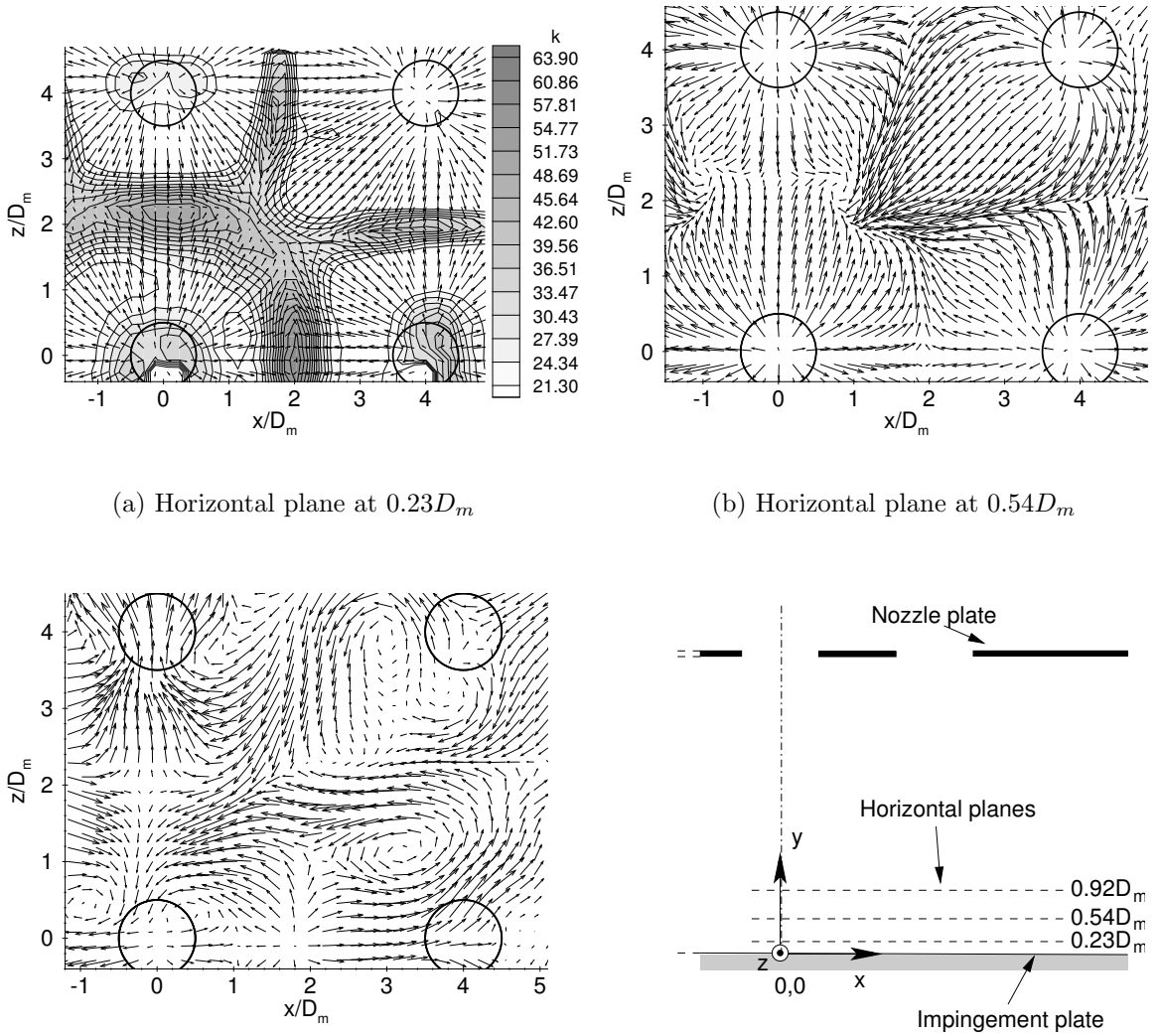

(a) Horizontal plane at $0.23D_m$

(b) Horizontal plane at $0.54D_m$

(c) Horizontal plane at $0.92D_m$

(d) Definitions of planes.

Figure 5.21: Mean velocity and k distributions in all horizontal planes resulting from PIV measurements for the in-line array.

seed particles the percentage of spurious vectors in the impingement points of the jets was higher than in the areas around the impingement points. This explains the white 'holes' in the distribution of k at the impingement points of the center and the neighbor jets. For this reason quantitative conclusions can not be drawn from the horizontal planes. The vectors in Figures 5.21a to 5.21c are scaled up in order to see the velocity field.

The impingement pattern at $0.23D_m$ above the plate in Figure 5.21a also shows the distorted neighbor jets. They are somewhat deflected outwards, but the outer jet at

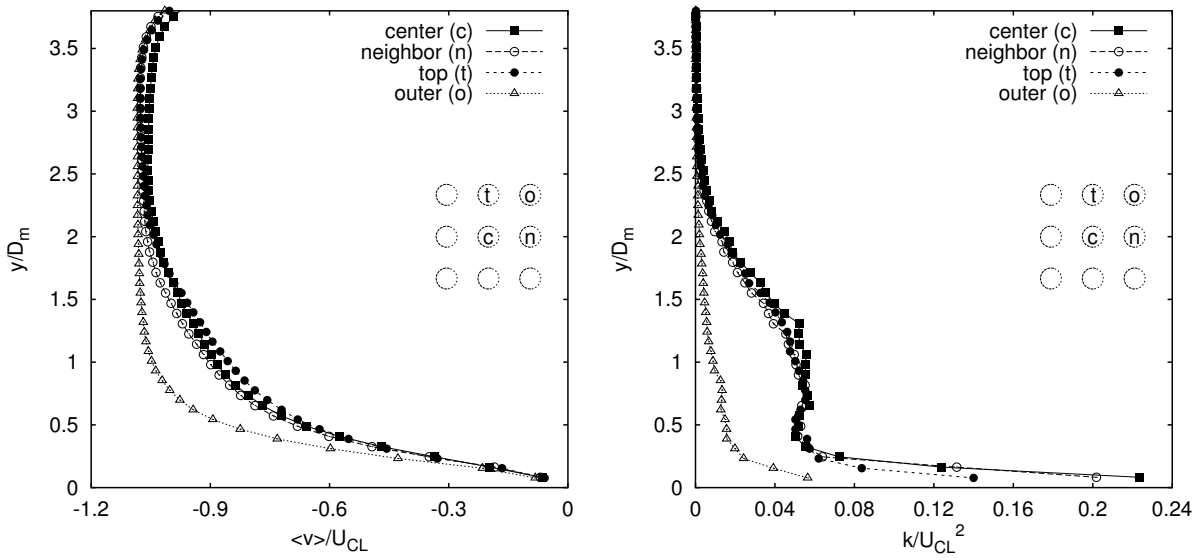

(a) mean velocities.

(b) turbulent kinetic energy.

Figure 5.22: Profiles of the mean velocity $\langle v \rangle$ and the kinetic energy k along the center lines of the central jet, two neighboring jets, and an outer jet.

$(x/D_m,\, z/D_m)= (4.0,\, 4.0)$ appears unaffected. This is also clear from the profiles of the center line velocity and k in Figures 5.22a and 5.22b. While the center, the neighbor at $(x/D_m,\, z/D_m)= (4.0,\, 0.0)$, and the neighbor at $(x/D_m,\, z/D_m)= (0.0,\, 4.0)$ (top jet) have comparable profiles for both $\langle v \rangle$ and k, the outer jet profiles differ significantly. Interaction between jets and their nearest neighbors can explain this phenomenon, as the outer jet only has two nearest neighbors while the center has four and the neighbor and top jets both have three.

The three zones of the jet mentioned in Section 5.2.1 (on page 81) also appear in Figure 5.22 for the center, top, and neighbor jets. For the in-line configuration there is also a small overshoot due to the vena contracta in the initial jet ($y/D_m > 2.3$) region, which is characterized by a constant center-line velocity and low values of k. In the development region ($0.7 < y/D_m < 2.0$) deceleration occurs, combined with increased levels of k. Finally, in the impingement region ($y/D_m < 0.5$) the differences between the center, top, and neighbor jets disappear. The outer jet appears to have a longer undisturbed jet core and lower levels of k. Both the center-line velocity profile and the k profile of the outer jet resemble those of a single impinging jet.

At $0.54D_m$ above the impingement plate (Fig. 5.21b) an interesting flow structure can be observed. Contrary to expectations there is no symmetry around the line $x = z$. In the upper left corner the flow exhibits a swirling motion at $(x/D_m,\, z/D_m) \approx (0.9, 2.3)$. On the basis of geometrical symmetry of the nozzle plate in the diagonal $x = z$, it is

highly likely that the vortex also occurs on the other side of the diagonal. In fact, from studying 150 individual snapshots randomly picked from the ensemble a clear vortex was found above the diagonal in 20% of the snapshots and below the diagonal in 10% of the snapshots, while no clear evidence of a vortex was found in the remaining 70%. In other words, the vortex can occur at both positions, but there is a preference for the vortex to be *above* the diagonal. It is unlikely that the vortex is caused by some imperfection of the experimental setup (e.g. scratches or burrs on the edges of the nozzle) that would break the symmetry. The fact that the vortex is also occurring at (-0.9, 2.3) is an indication for this. The intensity of the vortex is low compared to the impinging jets, and hence it can be sensitive to external disturbances. Possibly the preferential position of the vortex is determined by obstacles in the far field of the flow (i.e. beyond the measurement zone). Comparison to numerical simulations proved the existence of such a vortex (see Section 5.2.3). Because in numerical simulations ideally symmetric boundary and inflow conditions are imposed, the appearance of the asymmetry suggests that this is a genuine phenomenon and that it is not caused by experimental imperfection. Its cause is probably the natural asymmetry specific to this particular jet configuration and relatively large pitch: a low momentum circulation region is created and trapped on either upper or lower corner. Examining the vector field at y/D_m= 0.92 in Figure 5.21c shows that the above mentioned vortex only extends over a small distance, because it has disappeared at this height.

Figures 5.23a and 5.23b present the non-dimensional normal and shear production distributions of k in vertical plane a of the in-line array. The same features are seen as for the hexagonal array. Negative normal production in the impingement points, positive production in the region where wall jets collide and high shear production in the shear layers of the jets. The disturbance of the neighbor jet can clearly be distinguished in

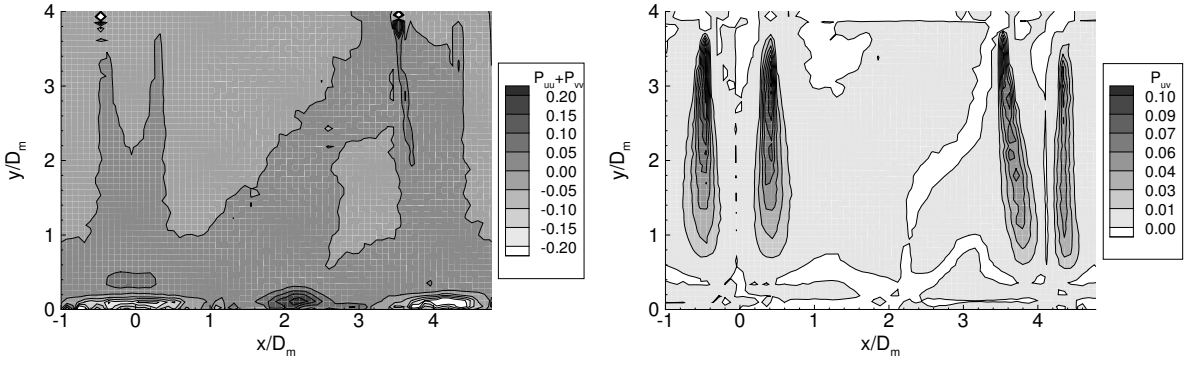

(a) normal production $P_{uu} + P_{vv}$.

(b) shear production P_{uv}.

Figure 5.23: Distribution of normal and shear production of k in vertical plane a of the in-line array non-dimensionalized by U_{CL}^3/D_m.

Figure 5.23b.

Summary

It was shown for both the in-line and the hexagonal configuration with sharp nozzles that closely spaced impinging jets in an array consist of three flow regions. In the initial region, which is the potential core region, the center-line velocity of the jets is approximately constant and the turbulent kinetic energy is low. A small overshoot in the center-line velocity signifies the vena contracta caused by the sudden contraction of the flow through the sharp-edged orifices. In the jet shear layers the Kelvin-Helmholtz instability causes axisymmetric ring vortices to appear. These instabilities are amplified by the presence of an upwash flow that originates from the collision of wall jets. In this way, interaction between neighboring jets shortens the potential cores. In fact, the potential core length of a jet decreases with increasing number of nearest neighbor jets. For this reason k is distributed asymmetrically around the geometric center for neighbors of the central jet. For the in-line configuration this even leads to a deformation of the neighbor jets causing the impingement pattern to have an elliptical shape instead of a circular one.

The development zone is characterized by decreasing center-line velocity and increased levels of turbulent kinetic energy. In this zone the potential cores of the jets have vanished and large scale eddies emerge, that originate from the coalescence of the ring vortices around the jets. On the basis of randomly selected snapshots of the flow it was shown that these large eddies in the development zone cause the impinging jets to break up or be severely displaced in the out-of-plane direction.

Finally, in the impingement zone the effect of the impingement wall on the impinging jets is stronger than the effects of interaction between jets and between jets and upwash flows. All velocity profiles collapse onto one and k levels are comparable. In this zone the production of k is shown to be negative below the impinging jets, due to a change of sign of $\langle u' \rangle^2 - \langle v' \rangle^2$, which is also the case for single impinging jets.

The outer jet in the in-line configuration forms an exception, because it does not have these three zones. It resembles a single impinging jet in that its k-values are much lower compared to one of the other jets in the array, its potential core is longer and there is no sign of a distinct development zone. This jet only has two neighbors, rendering it the least disturbed of all jets, hence the deviation of its center line profiles.

An interesting feature in the flow of the hexagonal configuration is the appearance of a horse-shoe vortex around the outer jets. This vortex is sustained by the spent air outflow from the center and neighbor jets, and the wall jet of the outer impinging jet. The flow of the in-line configuration does not show this phenomenon. Most likely this is caused by the higher pitch in the in-line configuration.

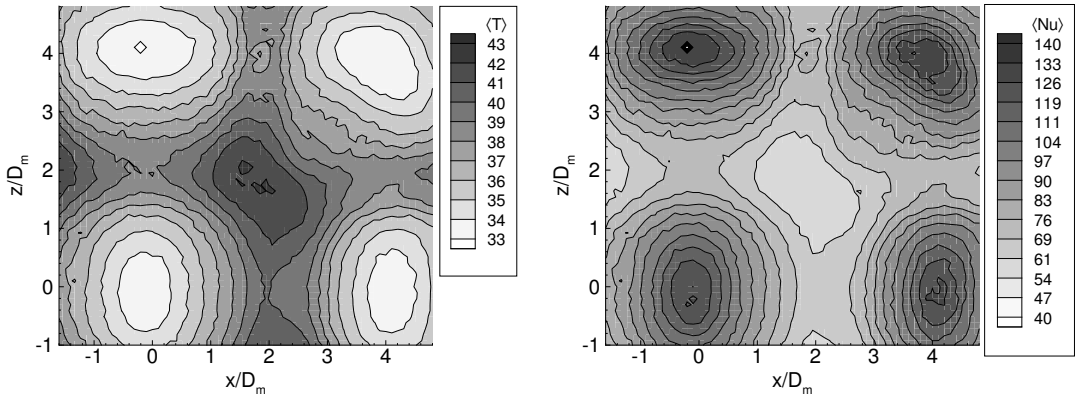

(a) Mean surface temperature

(b) Mean heat transfer

Figure 5.24: Example of the mean temperature distribution of the in-line configuration with s/D_m=4, Re=2.0×10^4, and H/D_m=4.

The in-line configuration produces another interesting structure: the flow field in a plane parallel to the impingement plate appears to be asymmetrical in the diagonal $x = z$, because a vortex was identified on one side of the diagonal. In the next section the effects of the flow features on the heat transfer will be presented.

5.2.2 Heat transfer and the effect of turbulence

In this section results are presented of heat transfer on the impingement plate obtained from Liquid Crystal Thermography measurements.

Local heat transfer

In Figure 5.24 a typical surface temperature distribution is presented together with the corresponding Nusselt number distribution for the in-line configuration with s/D_m= 4.0 and H/D_m= 4.0, at Re= 2.0×10^4. In the impingement points of the four jets the temperature is lowest due to the efficient cooling effect of jet impingement. In between the impingement points the temperature can increase up to a maximum of 43°C, which is approximately 10°C higher than in the impingement points. This is mainly due to the decrease of the radial wall jet velocity with increasing distance from the jet impingement point and the heating of the air in the wall jet. Because the Nusselt number is inversely proportional to the temperature difference between the impingement plate and the jets, the mean heat transfer distribution is very similar to the mean temperature distribution.

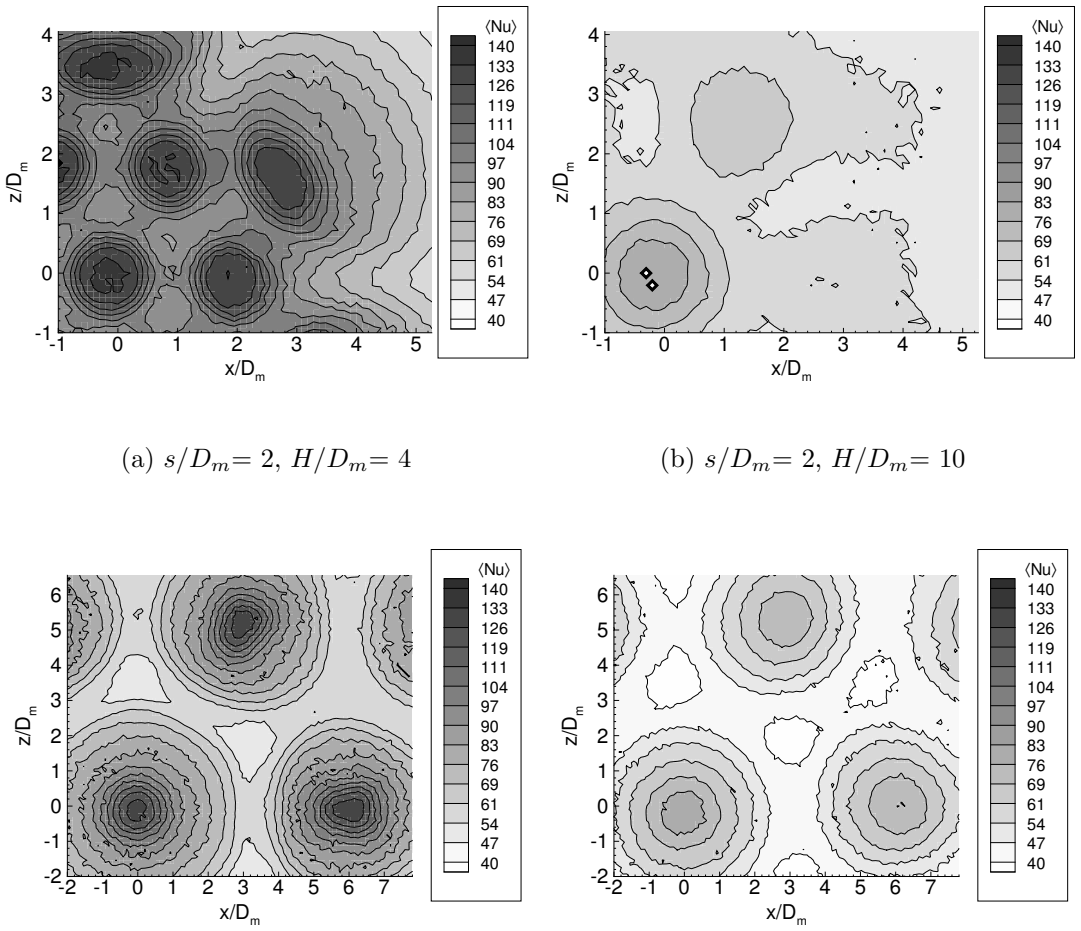

(a) s/D_m= 2, H/D_m= 4

(b) s/D_m= 2, H/D_m= 10

(c) s/D_m= 6, H/D_m= 4

(d) s/D_m= 6, H/D_m= 10

Figure 5.25: Ensemble averaged Nusselt numbers for four configurations of the hexagonal array with sharp-edged orifices at Re=2.0×10^4.

The impingement zones of the neighbor jets at $(x/D_m, z/D_m)$= (4.0, 0.0) and (0.0, 4.0) appear to be oval shaped due to the distortion of these jets, as explained in Section 5.2.1 on page 95. Contrary to what was expected, the center jet also produces an oval shaped heat transfer pattern. It is likely that this effect is caused by the asymmetrical flow field at $0.54D_m$ above the impingement plate discussed in the previous section (see page 100).

Contour plots of mean heat transfer results for the hexagonal array with sharp-edged orifices are presented in Figure 5.25 for two values of the pitch (s/D_m= 2 and 6) and two nozzle-to-plate spacings (H/D_m= 4 and 10) at a Reynolds number of 2.0×10^4. In Figure 5.25a the impingement pattern of the jets can be seen clearly, whereas at higher nozzle-to-plate distance this pattern appears to deteriorate (The two white spots near

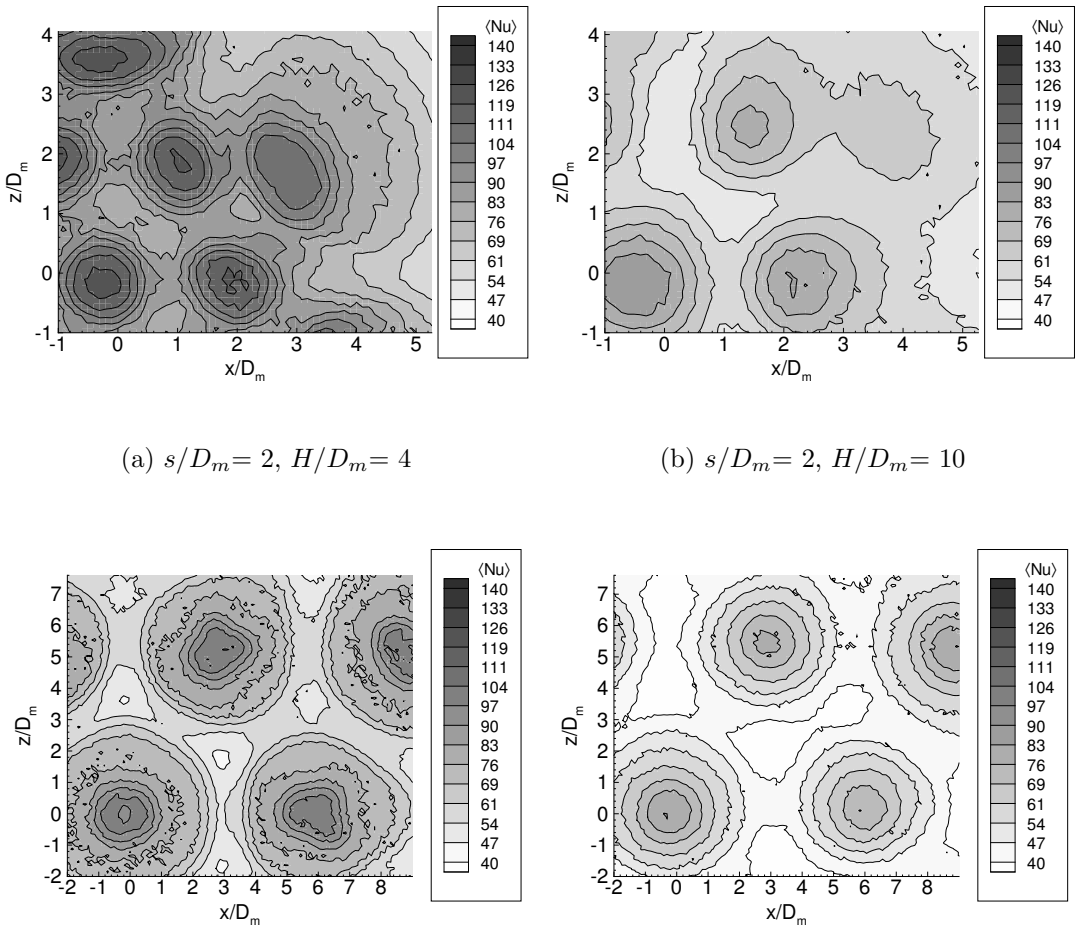

(a) s/D_m= 2, H/D_m= 4

(b) s/D_m= 2, H/D_m= 10

(c) s/D_m= 6, H/D_m= 4

(d) s/D_m= 6, H/D_m= 10

Figure 5.26: Ensemble averaged Nusselt numbers for four configurations of the hexagonal array with contoured nozzles.

(0,0) in Figure 5.25b are caused by erroneous values) due to the strong jet-jet interaction. At $H/D_m = 10$ the individual jets have lost their identity due to mixing by the large scale structures in the flow. In case of a larger pitch ($s/D_m = 6$, Figure 5.25c and d) the distortion of the jets is less, and the impingement pattern can still be discerned at $H/D_m = 10$.

The investigation of the heat transfer in the hexagonal array with contoured nozzles yields similar results. Figure 5.26 presents these results for the same values of s/D_m, H/D_m, and Re as for the hexagonal array with sharp orifices shown above. At $H/D_m = 4$ the heat transfer in the impingement points is higher for the sharp-edged orifices than for the contoured nozzles. The reason for this is that the jets emerging from the sharp-edged

orifices have a higher initial velocity due to the vena contracta. In case of the contoured nozzles the vena contracta effect is much smaller or maybe even absent. At $H/D_m = 10$ the differences in heat transfer are much smaller.

Figure 5.27 shows profiles of the Nusselt number along a line through the center jet and one of its direct neighbors as a function of H/D_m at Re=2.0×10^4 for both hexagonal configurations. The results are given for the sharp-edged nozzles (left) and the contoured nozzles (right) for three values of the pitch. In all cases, the Nusselt number is decreasing with increasing nozzle-to-plate distance, because the jet center-line velocity decreases due to entrainment and jet-jet interaction.

An interesting feature in Figures 5.27a and b is the apparent outward displacement of the neighbor jet at x/D_m= 2.0. The magnitude and trend of this displacement can be judged better by investigating the distance between the peak Nusselt numbers (that is, assuming the peak Nusselt numbers correspond to the impingement points of the jets). In Figure 5.28 the non-dimensional distance between the Nusselt number peaks $\Delta x_I/D_m$ is plotted versus the nozzle-to-plate spacing for both hexagonal configurations at s/D_m= 2.0. The positions of the peaks were found by fitting Gaussian functions to the Nusselt number profiles shown in Figure 5.27a and b.

A small but noticeable displacement exists already for $H/D_m \leq 6.0$: the peaks are a distance of about 2.1-2.2D_m apart, instead of the geometric pitch of $2D_m$. There is a strong increase in the displacement of the outer jet when the nozzle-to-plate distance is increased beyond the jets' potential core. Possible causes for the displacement are the collision of wall jets emerging from the jet impingement zones, and the outflow of spent air from the center jet forming a cross-flow that interacts with neighboring jets.

In Figure 5.27a the impingement pattern of the neighbor jet at x/D_m= 2.0 has nearly vanished for H/D_m= 10.0. This is most likely caused by a combination of jet-jet interaction prior to impingement and cross-flow induced by the outflow of spent air from the center jet. Both these effects are particularly strong at small values of the pitch. Additionally, spent air is already heated before it mixes with fresh air from neighboring jets, explaining the lower peak Nusselt number for the neighbor jet. Figure 5.27b shows a different profile for the contoured nozzle plate. The impingement pattern of the jet at x/D_m= 2.0 is still clearly visible. Because the potential core of jets issuing from a sharp-edged orifice is shorter than for jets from a contoured nozzle, interaction with neighboring jets affects the flow stronger in case of the sharp-edged orifice.

Finally, note the occurrence of local minima and maxima at $x/D_m \approx 2.0$ and $x/D_m \approx 4.0$ in Figure 5.27f, and to a lesser extent, in Figure 5.27e. These minima and maxima only occur at small nozzle-to-plate spacings, say $H/D_m \leq$4. Gardon and Cobonpue (1962) conjectured a transition from laminar to turbulent flow to be the cause of the humps. Following this conjecture it can be stated that the laminar-turbulent transition is clearer for the contoured nozzle jets, because they have a longer potential core than the sharp orifice jets. For low nozzle-to-plate spacings the impingement plate is placed well into the

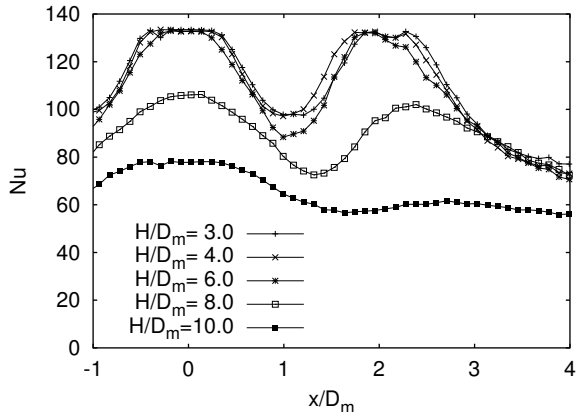

(a) sharp-edged orifices, $s/D_m = 2$

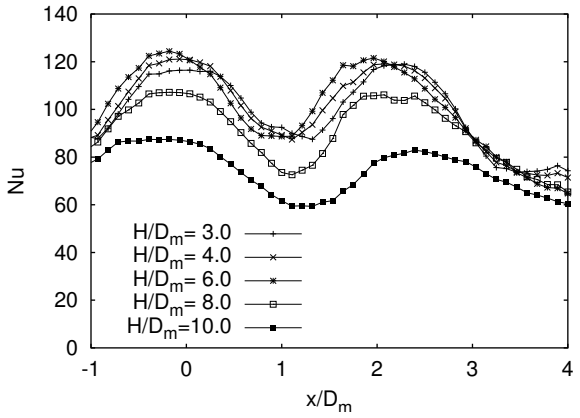

(b) contoured nozzles, $s/D_m = 2$

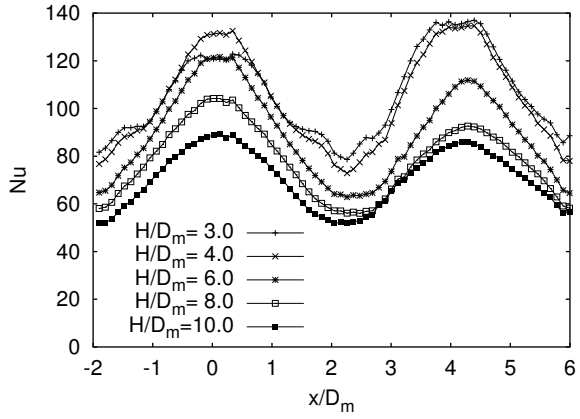

(c) sharp-edged orifices, $s/D_m = 4$

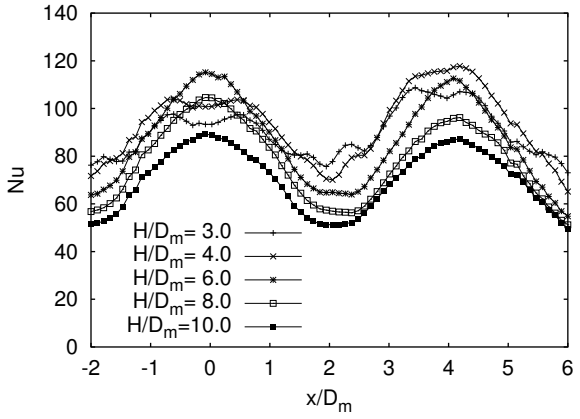

(d) contoured nozzles, $s/D_m = 4$

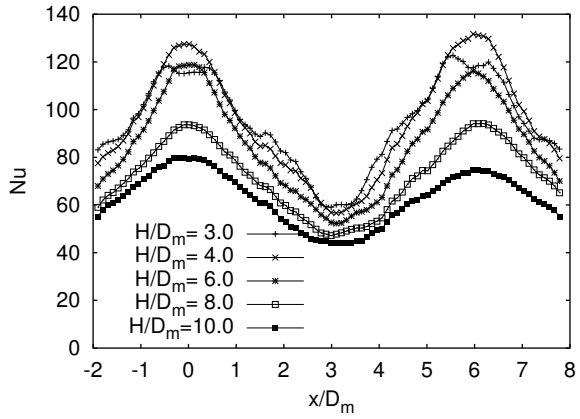

(e) sharp-edged orifices, $s/D_m = 6$

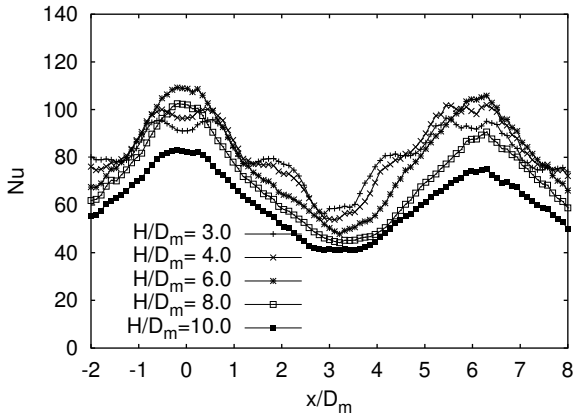

(f) contoured nozzles, $s/D_m = 6$

Figure 5.27: Profiles of the local Nusselt number for all hexagonal configurations at Re= 2.0×10^4.

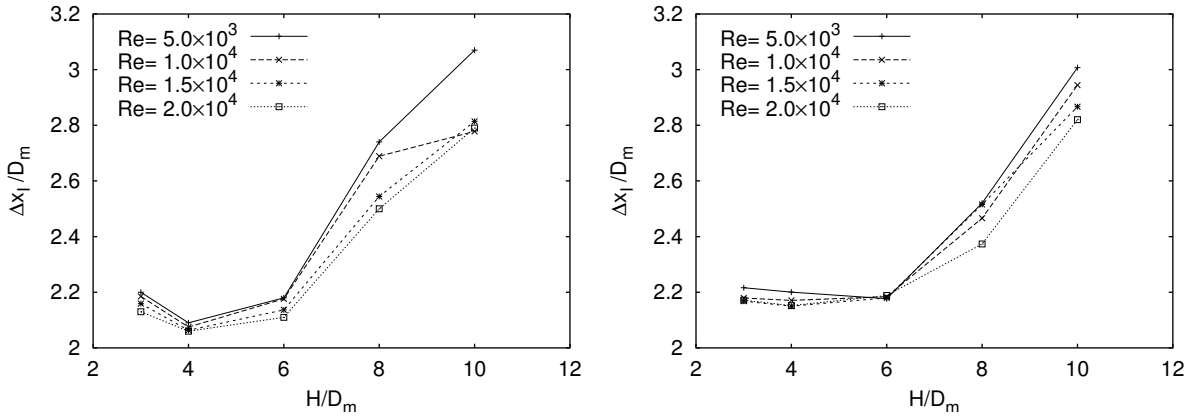

(a) sharp orifices

(b) contoured nozzles

Figure 5.28: Distance between the peaks in the Nusselt number profiles for both hexagonal configuration at s/D_m= 2.0.

potential core of the contoured nozzle jet, but it is already at or beyond the end of the core of sharp-edged orifice jet. Popiel and Boguslawski (1986) confirm these conclusions.

Stagnation point heat transfer

The Nusselt number in the stagnation point of the central jet Nu_{stag} is presented in Figures 5.29 and 5.30 for all configurations and Reynolds numbers. Figures 5.29a, c, and e show the data for the hexagonal plate with sharp-edged orifices for s/D_m=2, 4, and 6, respectively. For the same values of s/D_m, Figures 5.29b, d, and f show the data for the hexagonal plate with contoured nozzles. The data for the in-line configuration is shown in Figure 5.30. For all configurations the stagnation Nusselt number is multiplied by the Reynolds number raised to a power $-\alpha_1$. The reason for this will become clear in the next subsection.

From Figure 5.29 it appears that the maximum value of $\mathrm{Nu}_{stag}\mathrm{Re}^{-\alpha_1}$ is at H/D_m=4 for the sharp-edged orifices, while it is at H/D_m=6 for the contoured nozzles. This is explained by the fact that the potential core of a jet from a sharp-edged orifice is smaller than the core of a jet from a contoured nozzle. Below the nozzle-to-plate spacing at which $\mathrm{Nu}_{stag}\mathrm{Re}^{-\alpha_1}$ is maximum the impingement plate is in the potential core region where the level of turbulence is very low and the jet is stable. At the end of the potential core the turbulence level (defined as $\sqrt{\langle u'^2 \rangle}/U_{CL}$) rises and the center-line velocity decreases. The maximum stagnation point Nusselt number is obtained in the region with high center line velocity and maximum turbulence level (Kataoka, 1990). If the impingement plate is placed even further away from the nozzle plate, both the center-line velocity

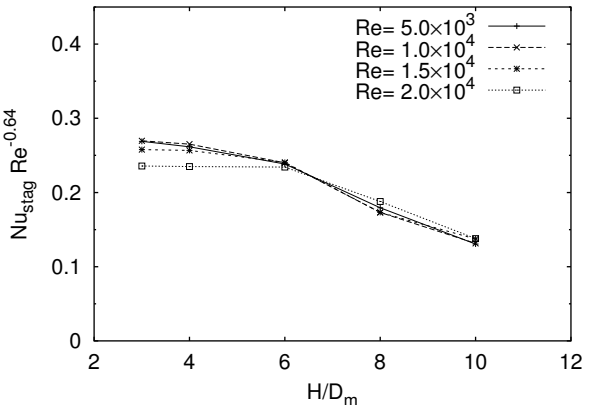

(a) sharp-edged orifices, $s/D_m = 2$

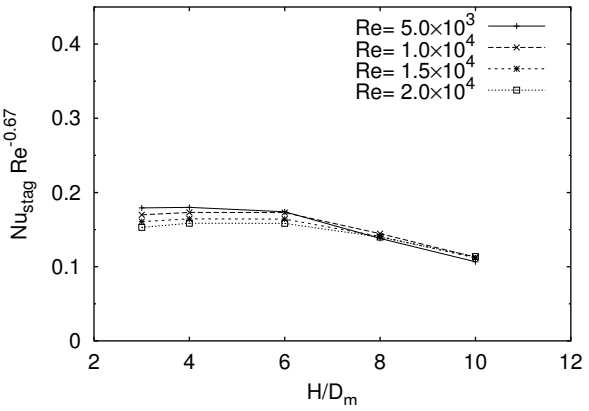

(b) contoured nozzles, $s/D_m = 2$

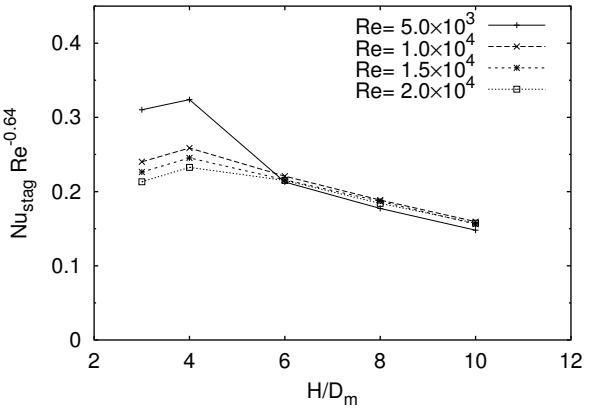

(c) sharp-edged orifices, $s/D_m = 4$

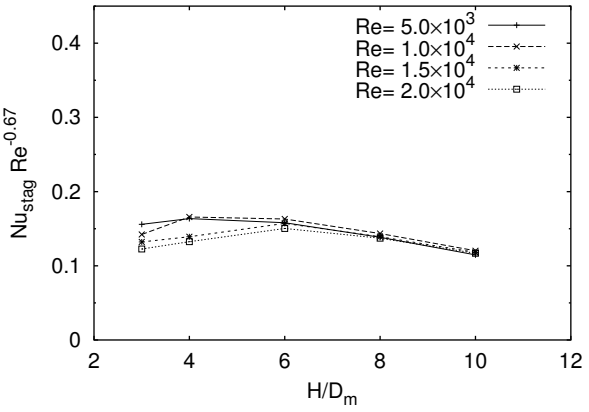

(d) contoured nozzles, $s/D_m = 4$

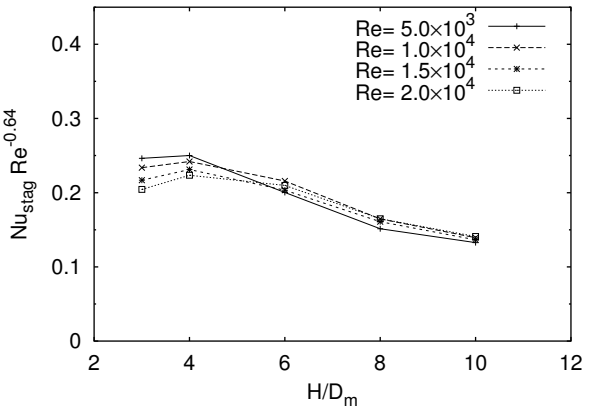

(e) sharp-edged orifices, $s/D_m = 6$

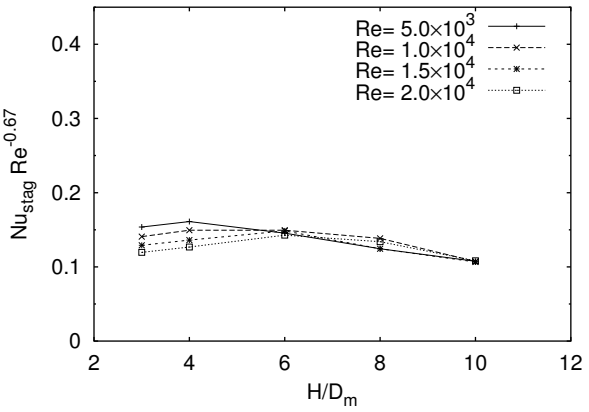

(f) contoured nozzles, $s/D_m = 6$

Figure 5.29: Stagnation point Nusselt numbers for all hexagonal configurations.

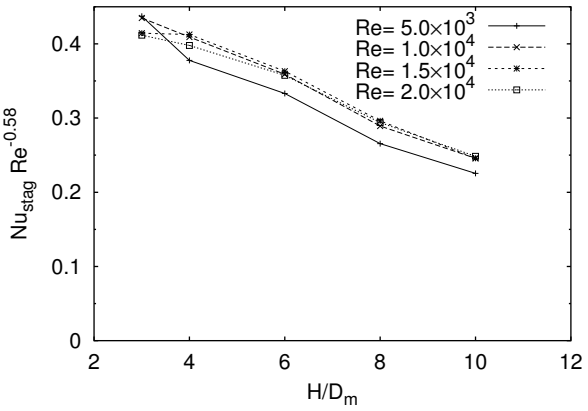

Figure 5.30: Stagnation point Nusselt numbers for the in-line configuration.

and the turbulence level drop significantly, which causes a drop in the heat transfer rate. Additionally, large scale turbulence will mix spent air and fresh air, so the average temperature of the air increases and heat transfer deteriorates.

A comparison of the stagnation Nusselt numbers of the two different nozzle shapes reveals that the values of the sharp-edged orifice plates are higher than those of the contoured nozzle plates for low H/D_m. This is caused by the vena contracta that occurs when the flow is passed through a sharp-edged orifice (Popiel and Boguslawski, 1986). This effect is negligible in case of the contoured nozzle. Due to this effect the apparent nozzle diameter is smaller for the sharp-edged orifices and the center-line velocity is higher at equal Reynolds numbers yielding a higher heat transfer rate in the impingement point. At high H/D_m values the jets expand, the velocity drops, and heat transfer rates are comparable for both nozzle shapes.

Area-averaged heat transfer

The area-averaged Nusselt number was calculated for all 140 cases described in Section 4.2.2 (page 62). Only a part of the total impingement plate surface is taken into account to compare average Nusselt numbers. Figure 5.31 shows the regions on which average Nusselt numbers were calculated.

Goldstein and Seol (1991) suggested an empirical correlation between the area averaged Nusselt number and the Reynolds number, the nozzle pitch s/D_m and the nozzle-to-plate spacing H/D_m for a row of circular jets. The functional form of their correlation was

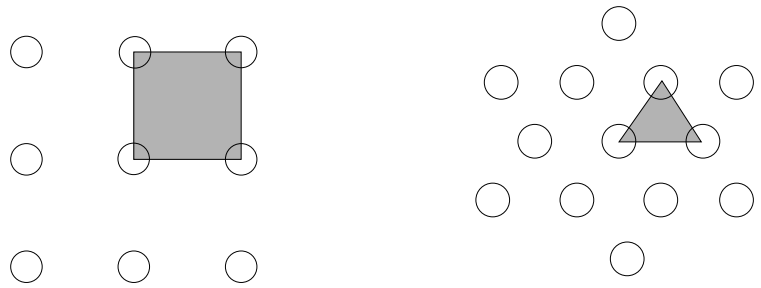

(a) In-line configuration. (b) Hexagonal configuration.

Figure 5.31: Definitions of the region of interest for hexagonal and in-line nozzle plates.

used to construct a new correlation for the present investigation:

$$\mathrm{Nu}_{ave} = \mathrm{Re}^{\alpha_1} \frac{\exp\left\{\alpha_2 \left(\frac{H}{D_m}\right)^{\alpha_3}\right\}}{\left(\frac{s}{D_m}\right)^{\alpha_4} \left(\frac{H}{D_m}\right)^{\alpha_5}} \ , \tag{5.1}$$

where α_1 to α_5 are coefficients calculated from a Marquardt-Levenberg non-linear fit (Press et al., 1992) of the equation to the experimental data in each configuration. Table 5.1 gives an overview of the values for these coefficients for all three nozzle configurations. An estimate of the variance resulting from the fitting procedures is also given. The values of the coefficients α_1 to α_5 vary from one case to another as expected, because the correlation of Equation 5.1 is too simple to account in a general form for all configuration parameters. Surprisingly, however, the differences are not large, indicating that the form of this correlation is a reasonable representation of the multiple jet heat transfer.

The resulting correlations are plotted together with the measured data in Figures 5.32

Table 5.1: Coefficients in equation 5.1 for all configurations and the variances from the fitting procedures.

Configuration Nozzle shape	In-line sharp	Hexagonal sharp	Hexagonal contoured
α_1	0.58	0.64	0.67
α_2	-3.68	-3.23	-3.19
α_3	-3.00	-1.64	-1.14
α_4	n.a.	0.33	0.29
α_5	0.51	0.79	0.90
Variance	5.01	8.74	7.12

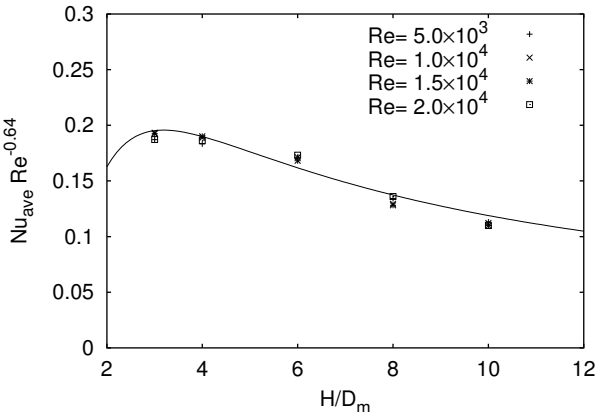

(a) sharp-edged orifices, $s/D_m = 2$

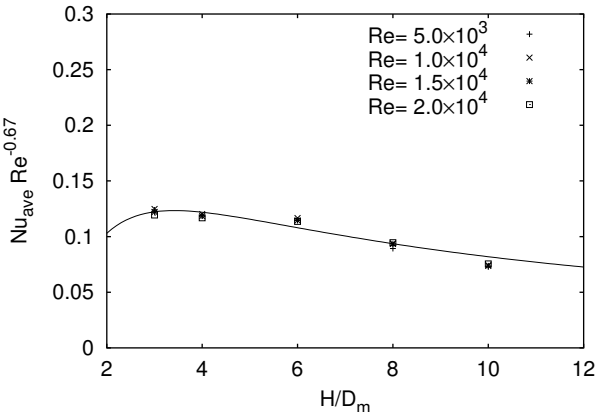

(b) contoured nozzles, $s/D_m = 2$

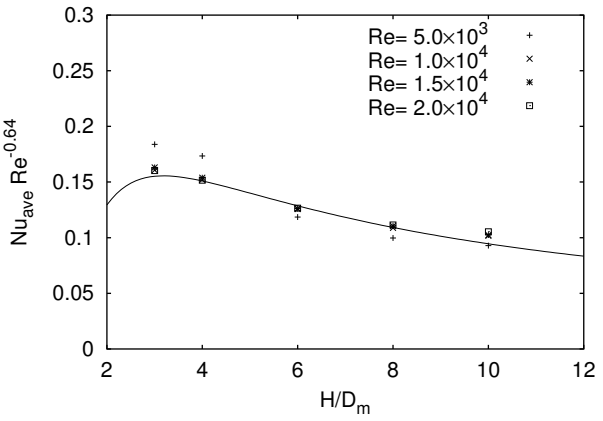

(c) sharp-edged orifices, $s/D_m = 4$

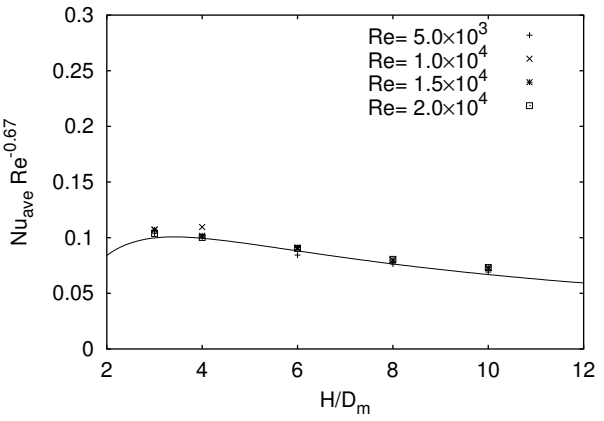

(d) contoured nozzles, $s/D_m = 4$

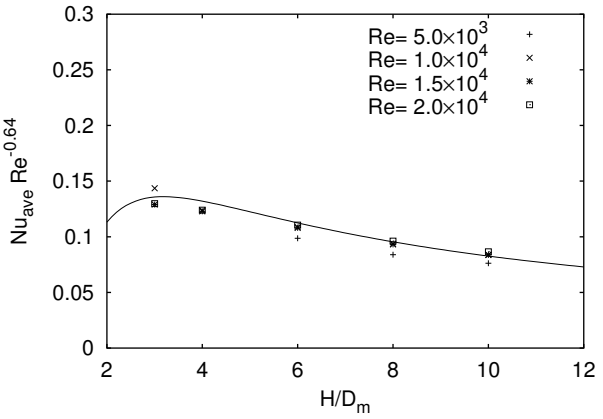

(e) sharp-edged orifices, $s/D_m = 6$

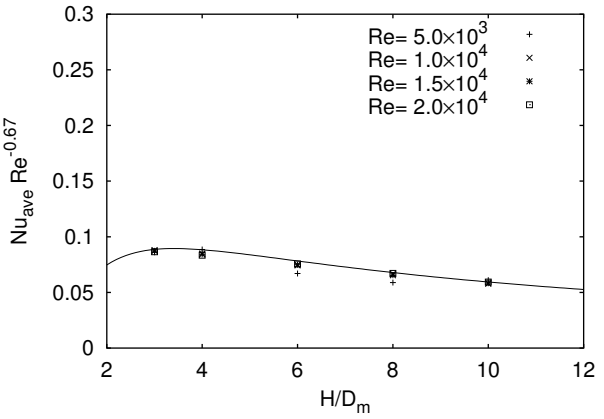

(f) contoured nozzles, $s/D_m = 6$

Figure 5.32: Experimental data and correlations plotted for the hexagonal configurations.

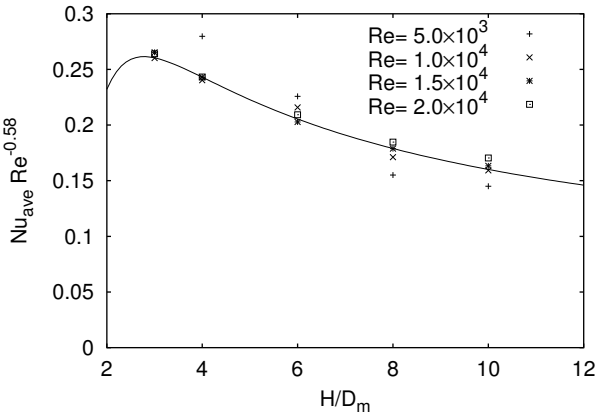

Figure 5.33: Experimental data and correlations plotted for the in-line configuration.

and 5.33. In each figure the area averaged Nusselt number multiplied by the Reynolds number to the power $-\alpha_1$ is plotted against the nozzle-to-plate spacing for a particular configuration and nozzle pitch. The points represent the experimental data and the lines represent the fits for the particular configurations. Each figure contains the data for each of the four Reynolds numbers investigated.

The values of the coefficients for the Reynolds number in Equation 5.1 agree well with the values found in literature. Gardon and Cobonpue (1962) measured the heat transfer from in-line arrays of 5×5 and 7×7 jets issuing from a set of small pipes. They found a value of $\alpha_1 = 0.625$. Martin (1977) has reported a value of $2/3 \approx 0.67$ for both hexagonal and in-line sharp-edged orifice plates. Goldstein and Seol (1991) investigated a row of round jets and found a value of 0.7 for α_1. However, Obot and Trabold (1987), who have investigated the influence of cross-flow on the heat transfer of an in-line array of sharp-edged nozzles, presented a value of 0.8. Other coefficients could not be compared to values found by other researchers, because the functional forms of the correlations found were not comparable, except for the Reynolds number dependency.

The coefficient α_4 for the hexagonal sharp-edged orifice plate is slightly higher than for the contoured nozzle plate. This means that the Nusselt number deteriorates faster with increasing pitch for the sharp-edged orifice plate. As was shown earlier, the sharp-edged orifice jets produce more turbulence that causes spent air of the center jets to mix with fresh air from the neighboring jets. This causes the strongly decreasing Nusselt number values in the impingement zones of the neighboring jets, which in turn affects the area averaged Nusselt numbers.

For the hexagonal configuration with sharp-edged orifices the mean Nusselt numbers do not vary much with H/D_m for $H/D_m < 4$, similar to the Nusselt number profiles shown in Figure 5.27. Above H/D_m= 4 the Nusselt number decreases with increasing H/D_m. The effect is strongest for $s/D_m = 2$. The same trend can be seen in the data of

the hexagonal configuration with contoured nozzles, except, the decrease of the Nusselt number sets in as $H/D_m > 6$. Again this is most clear for $s/D_m = 2$. This effect can be attributed to the potential core length of the jets.

Heat transfer and turbulence

Combining the previously presented results of the flow field and the heat transfer, conclusions can be drawn regarding the thermal imprint of the flow field and the turbulence on the impingement plate. To this end, wall-parallel profiles are extracted from the flow field in the vertical measurement planes just above the impingement surface. These profiles are then compared to the heat transfer on the impingement surface at the position of the planes.

In vertical plane 1 of the hexagonal sharp-orifice configuration profiles are determined of the mean velocity components $\langle u \rangle$ and $\langle v \rangle$, the turbulent kinetic energy k, the turbulent shear stress $\langle u'v' \rangle$, and the normal and shear components of the production of kinetic energy P_k. Figure 5.34 compares these profiles to the Nusselt number as measured at the intersection of plane 1 and the impingement plate. The presented flow quantities were all taken at $0.07D_m$ above the impingement plate, because this is the velocity sample position closest to the wall. All flow quantities are non-dimensionalized with the jet center-line velocity U_{CL} and the nozzle diameter D_m. Figure 5.35 presents the combination of heat transfer data and flow data for vertical plane 3 in the hexagonal sharp-orifice configuration. The flow data were also acquired at $0.07D_m$ from the impingement wall. Figures 5.36 and 5.37 present similar figures for the in-line configuration in vertical planes a and b, respectively. In these cases the flow data were acquired at $0.09D_m$ above the impingement plate.

The top graph in Figure 5.34 displays the Nusselt profile that has two peaks at the positions where the jets impinge on the surface. The second graph shows both components of the mean velocity. The wall-normal component $\langle v \rangle$ is very small. The wall-parallel component $\langle u \rangle$ shows very strong gradients at the impingement points of the jets and a net outflow at $x/D_m > 3$ forming the wall jet. The distribution of k in the third graph is almost uniform and shows no clear correlation to the Nusselt number curve. The Reynolds shear stress component $\langle u'v' \rangle$ in the fourth graph is also uniformly distributed and its magnitude is negligible in comparison to k. From Figure 5.11 on page 88 the wall-parallel velocity appears to be at its maximum value around $0.15D_m$ for all values of x/D_m, so the gradient $\partial\langle u \rangle/\partial y$ is around zero. According to Boussinesq's eddy viscosity theory, $\langle u'v' \rangle$ is proportional to $\partial\langle u \rangle/\partial y + \partial\langle v \rangle/\partial x$ and as $\partial\langle v \rangle/\partial x$ is negligible at the current position, $\langle u'v' \rangle$ will also be negligible.

The bottom graph in Figure 5.34 shows the normal and shear components of the pro-

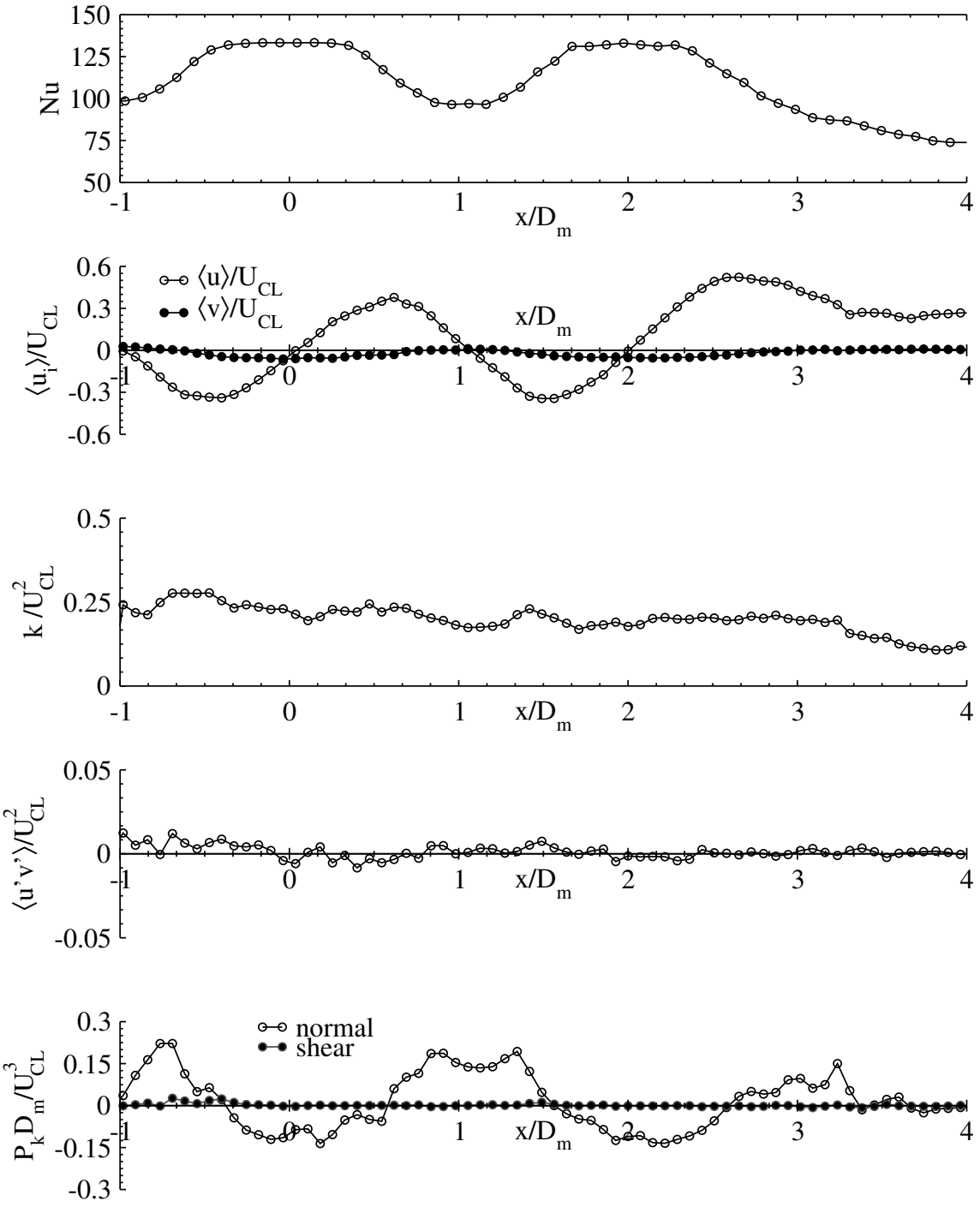

Figure 5.34: Comparison between Nu and several flow and turbulence quantities at $0.07D_m$ from the wall in plane 1 of the hexagonal configuration with sharp-edged orifices.

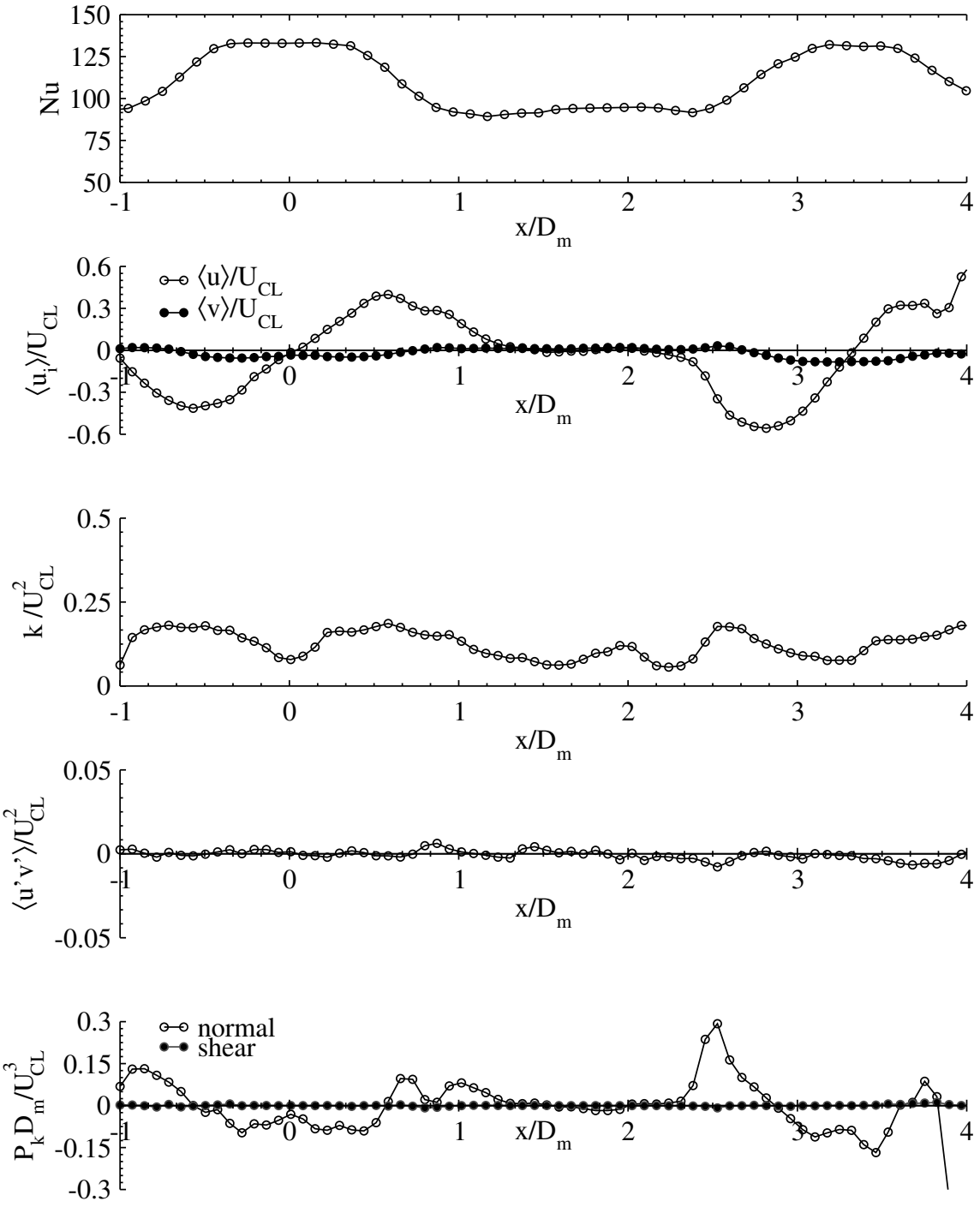

Figure 5.35: Comparison between Nu and several flow and turbulence quantities at $0.07D_m$ from the wall in plane 3 of the hexagonal configuration with sharp-edged orifices.

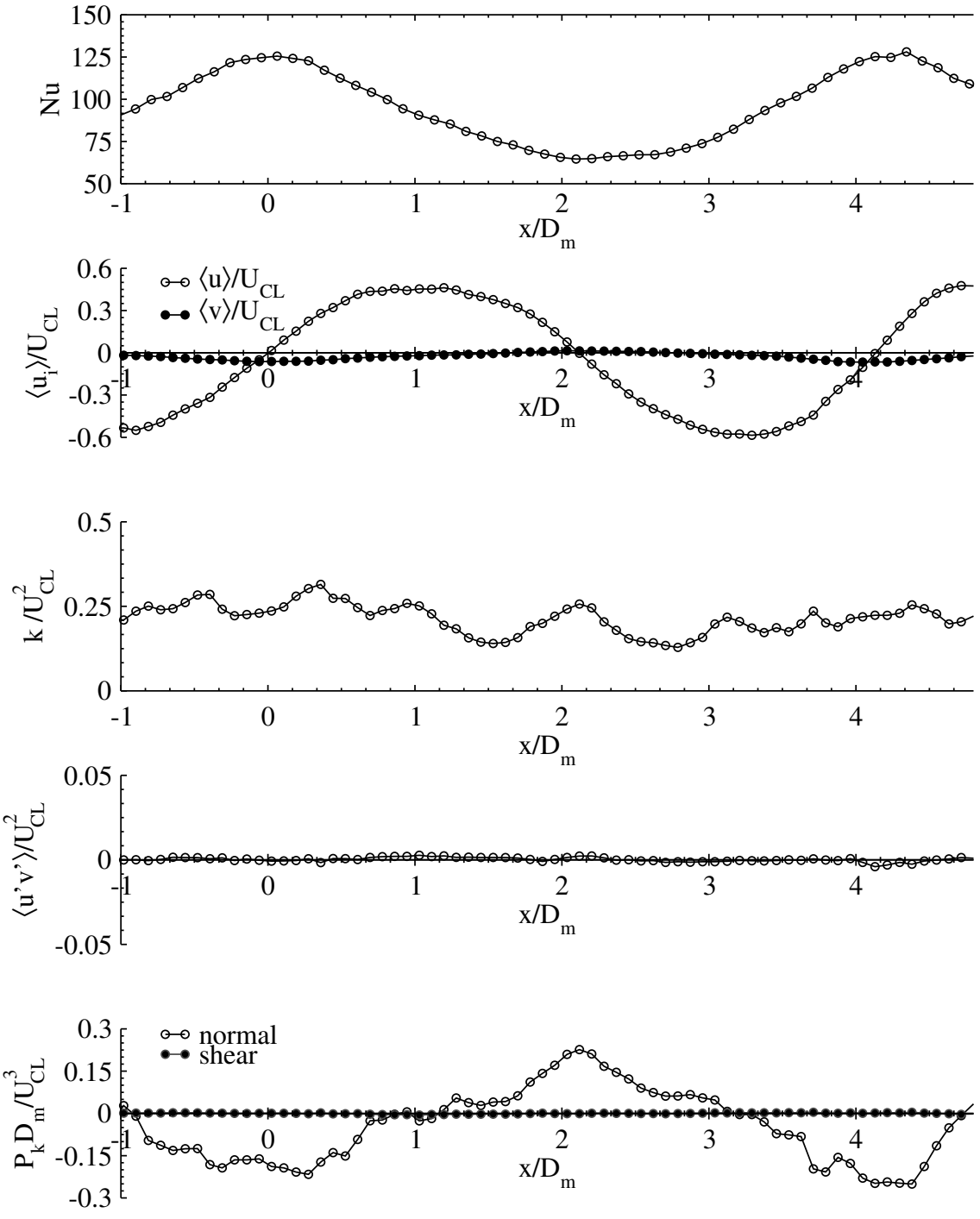

Figure 5.36: Comparison between Nu and several flow and turbulence quantities at $0.08D_m$ from the wall in plane a of the in-line configuration.

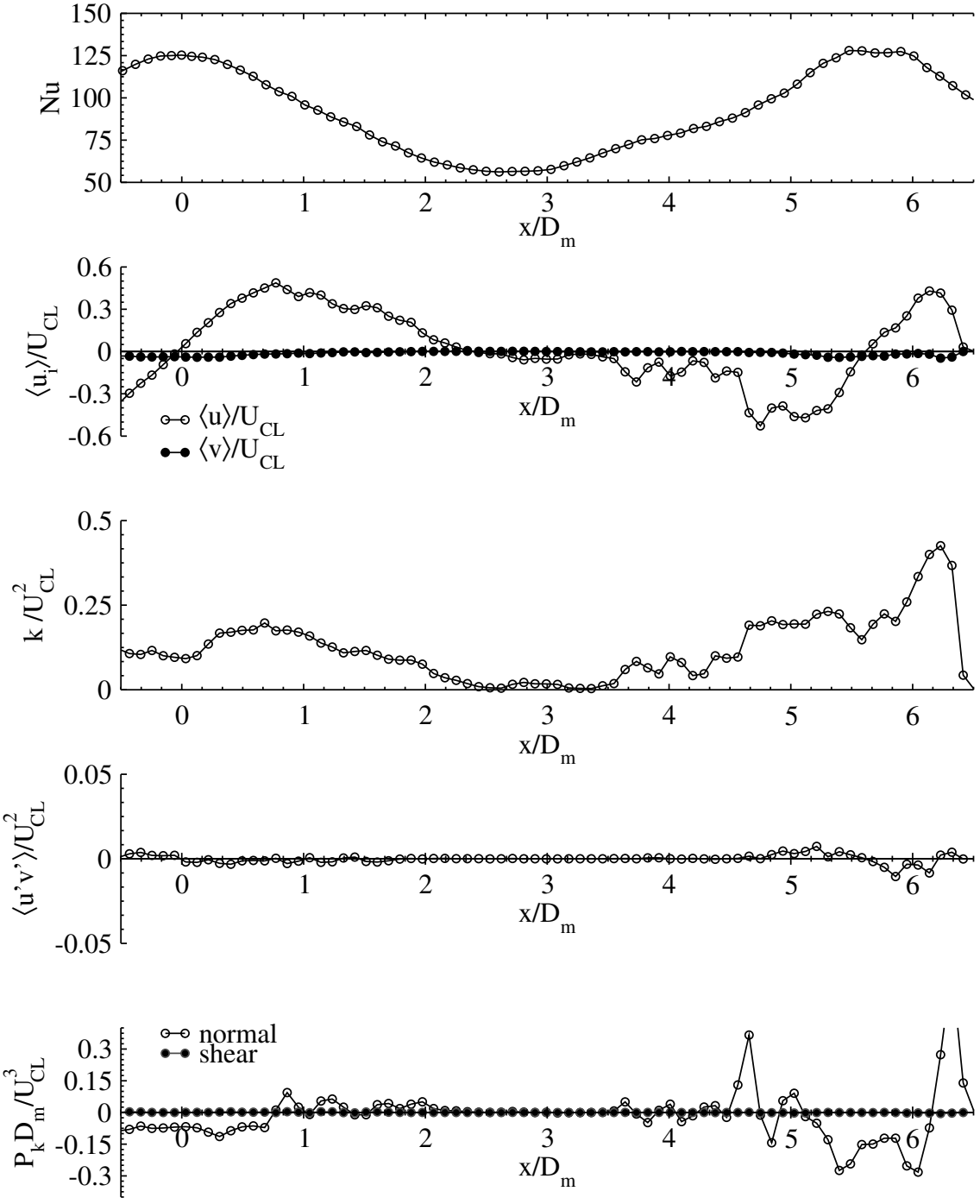

Figure 5.37: Comparison between Nu and several flow and turbulence quantities at $0.09D_m$ from the wall in plane b of the in-line configuration.

duction of kinetic energy. These components are defined by

$$P_{k,normal} = -\langle u'^2 \rangle \frac{\partial \langle u \rangle}{\partial x} - \langle v'^2 \rangle \frac{\partial \langle v \rangle}{\partial y} \ , \tag{5.2}$$

$$P_{k,shear} = -\langle u'v' \rangle \left(\frac{\partial \langle u \rangle}{\partial y} + \frac{\partial \langle v \rangle}{\partial x} \right) \ . \tag{5.3}$$

$P_{k,shear}$ is negligible compared to $P_{k,normal}$ due to the small values of all three (right-hand) terms in Equation 5.3. The normal production, on the other hand, is very large and negative in the regions where the Nusselt number is high. Because $\langle u'^2 \rangle$ is the dominating contribution to k and the gradients in $\langle u \rangle$ are much stronger than those in $\langle v \rangle$, the first term on the right in Equation 5.2 is the main contribution to $P_{k,normal}$. Comparing the production of kinetic energy with the Nusselt number, there seems to be a correlation between the negative normal production and the Nusselt number. However, this is a mere coincidence: the major cause of the increase in Nu is the combination of an oscillating impingement position due to large vortical structures and a very strong acceleration of the fluid from the center of the jet outwards. In the impingement point the boundary layer is very thin and the temperature gradient is very steep, enabling impinging vortices to encapsulate and remove heat in an effective way. Beyond a distance of about $0.5D_m$ from the stagnation point, the fluid is decelerating and the boundary layer thickens (Colucci and Viskanta, 1996), thereby reducing the heat transfer.

If the jet were laminar and the stagnation point of the jet stagnant, there would be a local minimum in the Nusselt number profile at the position of the stagnation point. This is also the case for a turbulent impinging jet where the impingement plate is placed inside the potential core, as was shown earlier by Gardon and Cobonpue (1962), Popiel and Boguslawski (1986), Lytle and Webb (1991) and Colucci and Viskanta (1996). If the plate is placed at or beyond the end of the potential core, fluctuations will have penetrated into the core, causing a moving stagnation point, i.e. non-zero $\langle u'^2 \rangle$. Combined with the strong velocity gradient at the stagnation point, these fluctuations will cause high heat transfer. The dip in the Nusselt number will then disappear. This contradicts the conjecture that the Nusselt number would be linked to regions of high k alone. The above described features also appear in Figures 5.35, 5.36, and 5.37.

Summary

In this section heat transfer results were presented in all three nozzle configurations, for different values of s/D_m and H/D_m. For a few cases the imprint of the flow on the heat transfer on the impingement plate were presented. For the in-line configuration elliptical impingement patterns were recognized in the heat transfer of the neighbor jets as a result of the jet distortion presented in the previous section. The elliptical pattern for the center jet can be explained by the asymmetrical flow pattern above the impingement plate.

For $s/D_m = 2$, in both hexagonal arrangements, the heat transfer profiles reveal an interesting fact: the impingement points of the neighbor jets are displaced outwards as the nozzle-to-plate spacing is increased. This is a result of the jet-jet interaction after impingement. The wall jets emerging from the impingement points collide and push the jets away from each other. Next to that, there is an effect of the cross-flow of spent air pushing the neighbor jet outwards. Due to the strong mixing as a result of these interactions, the Nusselt number shows a more homogeneous profile at high H/D_m, than for the cases where $s/D_m > 4$. In those cases the interactions are less strong, so the jets keep their identity up to high values of H/D_m.

Jets gradually lose their identity in the downstream direction due to turbulence in the development zone. Therefore, the heat transfer deteriorates and its distribution becomes more homogeneous with increasing nozzle-to-plate spacing. Shear layers of individual jets can interact with each other, with upwash flows, and with cross-flow generated by the outflow of spent air, resulting in a lower mean jet velocity. Additionally, spent air mixes with fresh air, which diminishes the temperature difference between the impingement plate and the air. Both these mechanisms result in lower Nusselt numbers. The extent in which the Nusselt number deteriorates depends on the shape of the nozzles. Compared to contoured nozzles, sharp-edged orifices produce a higher center-line velocity, causing higher Nusselt numbers. On the other hand, the velocity decay of a sharp-edged orifice jet is stronger than the one of a contoured nozzle jet, so the Nusselt numbers of a sharp-edged orifice jet decay more strongly with increasing nozzle-to-plate distance. With increasing nozzle-to-plate spacing, the difference in Nusselt numbers (both stagnation point and area-averaged) between both nozzle shapes decreases, because the jets gradually 'forget' their initial conditions. The heat transfer appears to be maximized if the impingement plate is placed at the end of the potential core, because at this position a high jet velocity is combined with a high degree of turbulence. If the distance is increased, both the velocity and the turbulence level drop and therefore the heat transfer drops.

By means of a non-linear fitting procedure an empirical correlation was found between the area averaged Nusselt number, the pitch, the nozzle-to-plate spacing, and the Reynolds number for all three nozzle configurations. The exponent of the Reynolds number appeared to agree well with the values presented by other researchers, although the range of presented values was relatively large. Other coefficients could not be compared to

values found by other researchers, because the functional forms of the correlations found were not comparable, except for the Reynolds number dependency. However, the values of the exponent of s/D_m could be compared for the two hexagonal configurations. It appeared the value was more negative for the sharp-edged orifices because of the strong velocity decay and the high degree of mixing, compared to the contoured nozzles.

Comparing the production of kinetic energy with the Nusselt number, there seems to be a correlation between the negative normal production and the Nusselt number. However, this is a mere coincidence: the major cause of the increase in Nu is the combination of an oscillating impingement position due to large vortical structures and a very strong acceleration of the fluid from the center of the jet outwards. In the impingement point the boundary layer is very thin and the temperature gradient is very steep, enabling impinging vortices to encapsulate and remove heat in an effective way.

5.2.3 Vortical structure

The structure identification methods described in Section 2.1.3 were applied to the experimental velocity data obtained with PIV. In this section the techniques based on the velocity gradient tensor will be discussed first. Next, the results obtained by POD analysis will be presented. POD can be used to define a non-homogeneous low-pass filter for the velocity field for investigating structures on the largest most-energetic scales, while uncorrelated noise is filtered out. Once vortices are identified, they are located and sized in order to investigate the positions of eddies of different sizes. Finally, a qualitative comparison is made between the experiments and numerical computations done in a parallel project. This is only done for the horizontal plane at $0.54D_m$ above the impingement plate of the in-line configuration, because that is where symmetry breaking occurs.

Velocity gradient based techniques

Because the PIV system used in the present project only produced two-dimensional velocity fields for two components of the velocity vector, two-dimensional representations of the vorticity vector magnitude $\|\boldsymbol{\omega}\|$, the second invariant of the velocity gradient tensor Q, and the kinematic vorticity number N_k are used. Instead of the magnitude of the vorticity vector $\boldsymbol{\omega}$, the absolute value of the vorticity vector's out-of-plane component is used. Q and N_k are calculated from the two-dimensional velocity gradient tensor. Critical point analysis and the λ_2 method described in Section 2.1.3 on page 11 will not be considered here, because they are equivalent to the Q-method within a two-dimensional reference frame (Jeong and Hussain, 1995).

When these techniques are applied to instantaneous velocity fields from PIV, the results

need to be interpreted with caution. As explained in Section 3.2.2, in order to have high frequency response and low truncation error, a high order interpolation scheme should be used for the calculation of derivatives. However, the inevitably present experimental noise will then be amplified. Next to that, the values of the velocity gradient will not be independent of each other, which affects the resolution and can introduce unwanted artifacts in the $|\omega_z|$-map, the Q-map, and the N_k-map. In general, lower order schemes affect the resolution less and are less sensitive to noise.

A second reason for caution is the gradient smoothing behavior of PIV. Due to the size of the interrogation windows being the smallest measurable length scale, steep velocity gradients will appear smoothed in the velocity fields obtained from PIV. This means

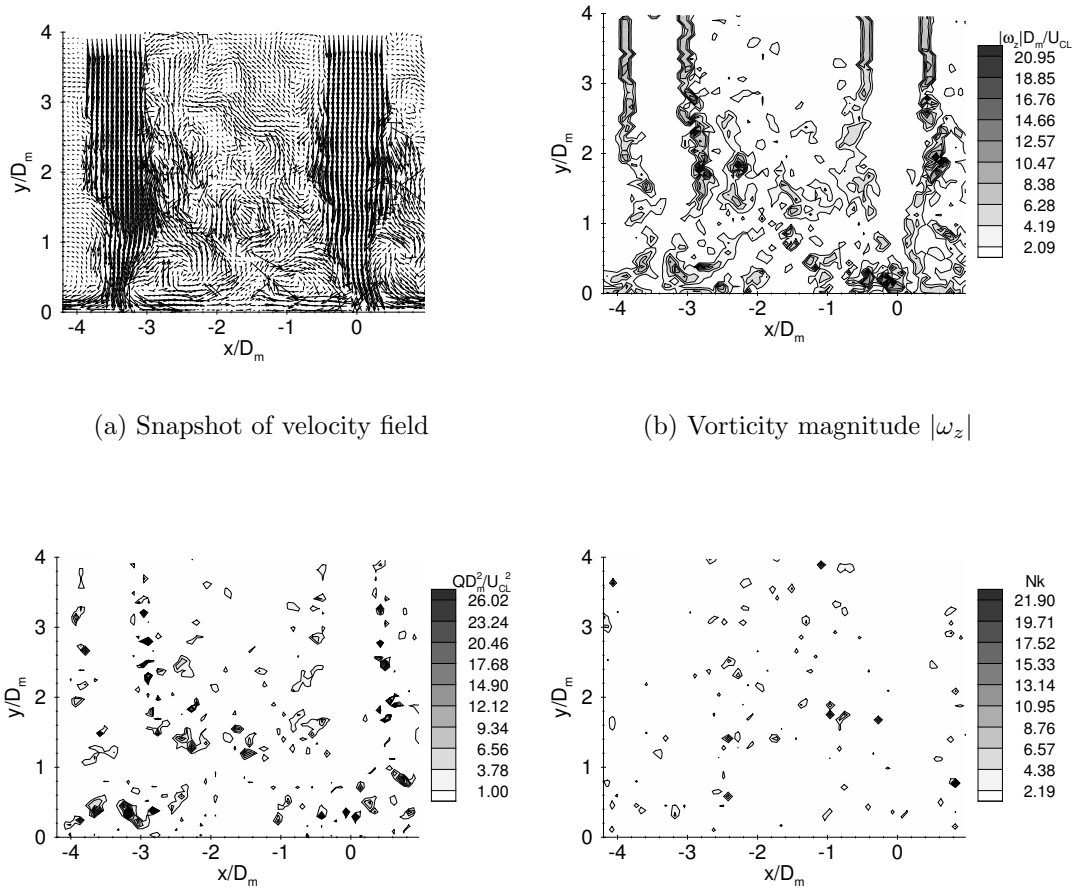

(a) Snapshot of velocity field

(b) Vorticity magnitude $|\omega_z|$

(c) 2^{nd} invariant of velocity gradient Q

(d) Kinematic vorticity number N_k

Figure 5.38: A snapshot of the velocity field in vertical plane 3 for the hexagonal configuration and plots of $|\omega_z|$, Q, and N_k.

that the values of the velocity gradients will be under-estimated. A second order central differencing scheme was chosen for the approximation of the gradients to maintain the resolution.

Figure 5.38a presents the velocity vectors for a single realization of the flow field in plane 3 of the hexagonal configuration. The center jet and one of the outer jets can be identified. Structures of different sizes and shapes strongly affect the jets, mainly in the impingement region. Vortex cores with a (nearly) zero convection velocity with respect to the fixed reference frame of the snapshot can be identified. Moving or distorted vortices are harder to identify by eye.

Figure 5.38b shows the $|\omega_z|$-map associated with the velocity snapshot. The vorticity magnitude is non-dimensionalized by the nozzle diameter and the center-line velocity of the jets. The vorticity magnitude is large in the strong mixing layer directly downstream of the nozzle edges. However, it is not possible to identify the more or less regular arrays of toroidal vortices that are formed in this region, as can be seen in Figure 5.38a. The reason for this is that $|\omega_z|$ is not only sensitive to the local swirling motion typical for a vortex, but also to shear. Further downstream of the nozzles isolated regions with a high vorticity are found, some of them coincide with the locations of the vortices visible in the velocity plot.

Figure 5.38c shows the values of Q computed from the instantaneous velocity field of Figure 5.38a. Q is non-dimensionalized with the nozzle diameter and the center line velocity. In comparison to the vorticity magnitude, a Q-map better identifies the individual toroidal vortices that form in the mixing layers downstream of the nozzles. Distinct islands of high Q are found, even in the shear layers directly downstream of the nozzles.

A plot of the kinematic vorticity number is presented in Figure 5.38d. Since N_k is non-dimensionalized by the magnitude of the strain rate, the peak N_k value is oblivious of the dynamical significance of a vortex (Jeong and Hussain, 1995). In other words, N_k does not discriminate between vortices with small vorticity in a flow with small shear and vortices with large vorticity in a flow with large shear. This can be seen clearly when the N_k-map is compared to the Q-map. Vortices identified with similar N_k values can have very different Q-values. This is even more clear from Figure 5.39. In this figure regions are plotted where Q and N_k exceed a certain threshold level. On the left the Q-maps are presented and on the right the N_k-maps. For the lowest threshold values (Figure 5.39a and b) both methods yield exactly the same results. This follows from the relationship between N_k and Q presented in Equation 2.24 (page 10). In Figures 5.39c and d the results are presented using moderate threshold values. In Figure 5.39c structures are identified with different sizes and shapes. The toroidal vortices in the shear layers of the jets can be discerned clearly and the largest structures appear near the impingement plate and in the region between the jets, where the upwash is located. In between the jets, towards the nozzle plate only some smaller structures appear, because this regions is

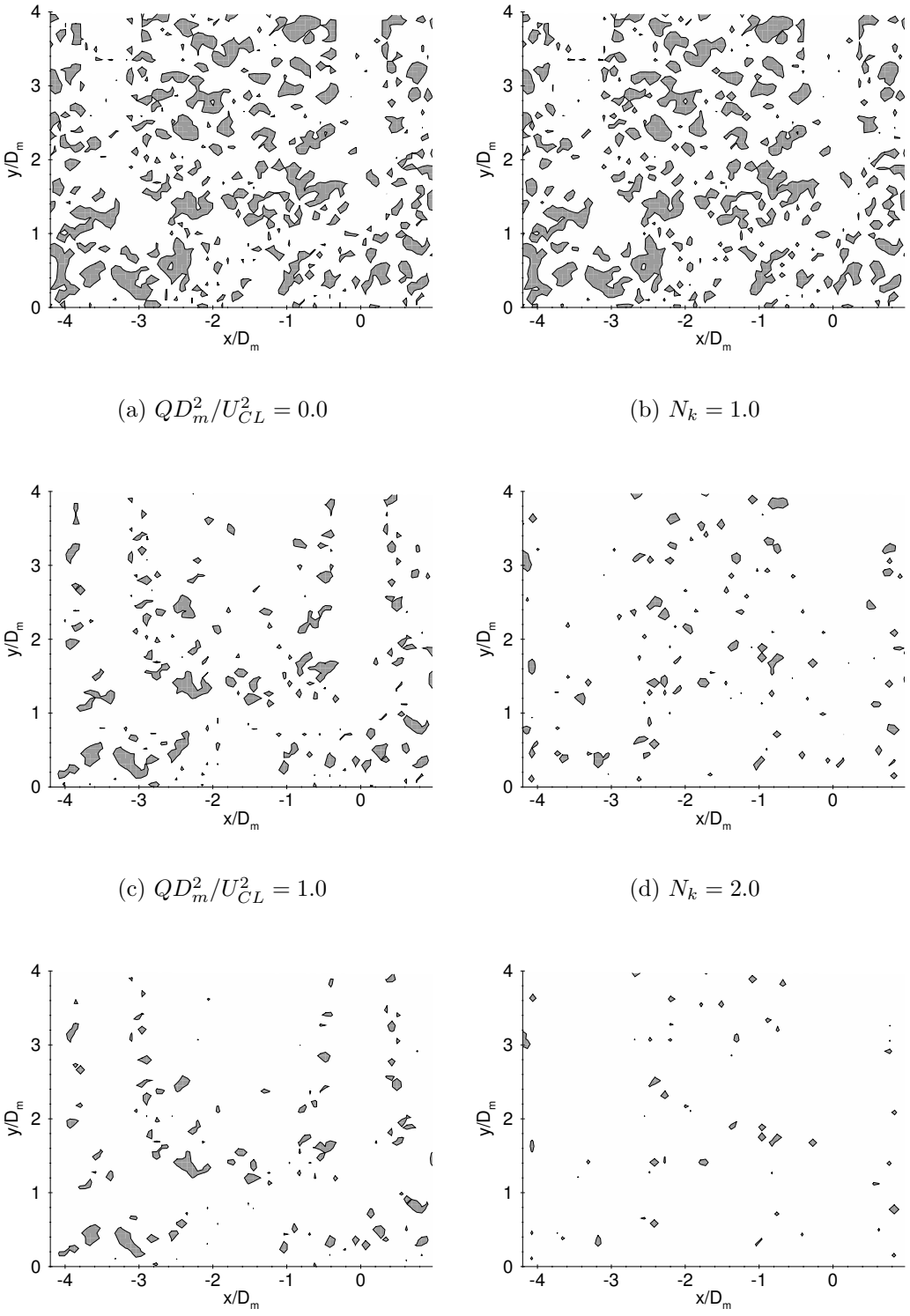

(a) $QD_m^2/U_{CL}^2 = 0.0$

(b) $N_k = 1.0$

(c) $QD_m^2/U_{CL}^2 = 1.0$

(d) $N_k = 2.0$

(e) $QD_m^2/U_{CL}^2 = 2.0$

(f) $N_k = 3.0$

Figure 5.39: Comparison of vortical structures in plane 3 of the hexagonal configuration with sharp nozzles for different values of Q and N_k.

relatively quiescent as can also be seen in the snapshot of the velocity field (Figure 5.38). However, using N_k structures are identified *outside* the shear layers and everywhere in between the jets, but none is identified *inside* the shear layers. In the snapshot of Figure 5.38a the fluid appears to be almost stagnant in this zone and no clear vortices are visible there.

Figure 5.39e and f present the Q- and N_k-maps, respectively, at high threshold values. In both cases less structures are identified. In case of Q, the shear layer vortices can still be seen and also the eddies in the upwash region near the impingement plate. In case of N_k, still the most structures are found in the upwash region near the nozzle plate, and nothing in the shear layers.

Additionally, it appears N_k is very sensitive to noise originating from the estimates of the velocity gradients in low shear regions, whereas Q is sensitive to noise in the high shear regions. This can easily be concluded from a standard error analysis (see Kline and McClintock, 1953) for the example of the vortex in a shear layer mentioned in Equation 2.25 on page 11. In this case the error δN_k in N_k as a function of the errors in the shear s and the vorticity ω is defined by

$$\delta N_k^{\,2} = \frac{1}{s^2}\delta\omega^2 + \frac{\omega^2}{s^4}\delta s^2 \tag{5.4}$$

and the error δQ in Q is defined by

$$\delta Q^{\,2} = \frac{1}{4}\left[(\omega - s)^2\delta\omega^2 + \omega^2\delta s^2\right] \ , \tag{5.5}$$

where δs and $\delta\omega$ are the errors in s and ω respectively.

Proper Orthogonal Decomposition

Dedicated software was written to calculate the POD from an ensemble of PIV data according to the procedure described in Section 2.1.3 (page 12). First the two-point temporal correlation tensor of the velocity data $\boldsymbol{C}$ is determined by numerically integrating the two-point temporal velocity correlation according to a trapezoidal scheme. Next, a Householder reduction of $\boldsymbol{C}$ yields its tri-diagonal form and a QL-algorithm can be applied to calculate the eigenvalues and eigenvectors. Descriptions of these two algorithms are given by Press et al. (1992).

The eigenvalue spectrum of a POD can be constructed by plotting eigenvalues versus modes. To check the effect of sample size on eigenvalue spectra, PODs were calculated for ensembles of different sizes taken from a single data set. It appeared that there was no significant difference between the spectra for the first 50 modes, when the sample size was over 1000. For the hexagonal configuration PODs were calculated for all three vertical planes and for the horizontal plane at $0.25D_m$ from the impingement plate. For

Table 5.2: Percentages of spatial energy per 10 modes for vertical and horizontal planes in the hexagonal and the in-line configurations.

	modes	1 – 10	10 – 20	20 – 30	30 – 40	40 – 50
Hexagonal	Vertical #1	23.6	7.7	5.1	3.7	3.0
	Vertical #2	19.8	6.9	4.4	3.3	2.8
	Vertical #3	25.4	8.6	5.5	4.0	3.2
	Horizontal	30.5	11.4	7.4	1.8	0.1
In-line	Vertical a	34.4	6.9	4.8	3.8	3.2
	Vertical b	25.6	7.3	5.1	4.0	3.4
	Vertical c	29.9	7.7	5.1	3.8	3.2
	Horizontal	29.2	8.0	5.5	4.2	3.5

the in-line configuration PODs were also calculated for all three vertical planes and for the horizontal plane at $0.23D_m$ above the impingement plate. For all planes the ensemble size was 1000.

The spectra depicted in Fig. 5.40 show the eigenvalues of the PODs for the vertical and the horizontal planes of the hexagonal and in-line configurations. The eigenvalues of all modes λ^n are plotted against the mode number n on a double logarithmic scale. All spectra show a very gradual decrease of energy going to higher POD modes and they

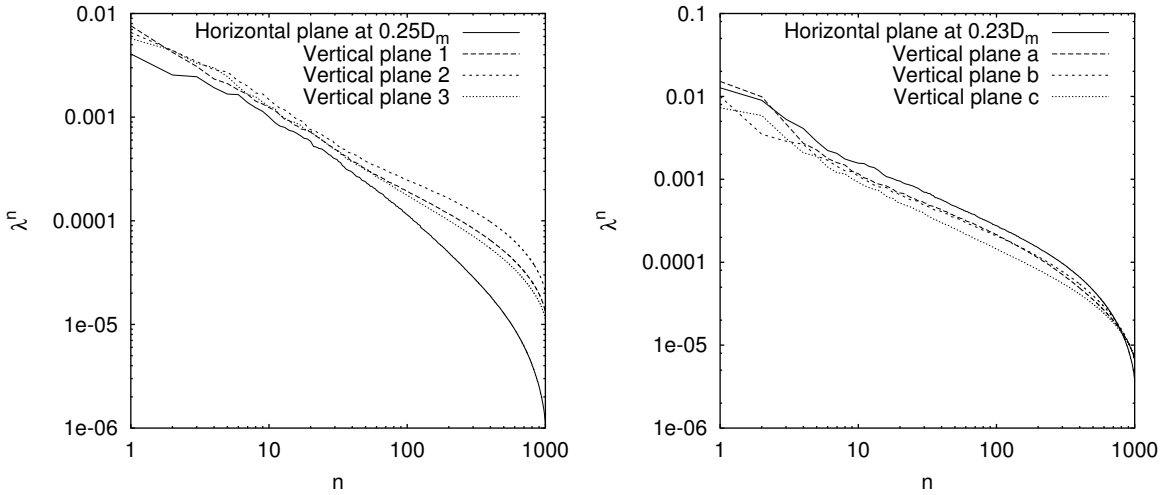

(a) Hexagonal configuration

(b) In-line configuration

Figure 5.40: POD Eigenvalue spectra for vertical and horizontal planes in both the hexagonal and the in-line configuration.

extend over a large range of modes. The high Reynolds number will cause a very wide spectrum of turbulent kinetic energy, which means there is energy in structures of a wide range of scales. Therefore, a considerable number of modes should be taken into account to cover the larger part of the turbulent kinetic energy.

Table 5.2 gives an idea of how the energy is distributed over the first few modes for all measurements. The percentages are summed values for the energy contribution to the ensemble of the structures in groups of ten modes. The energy of mode zero, representing the average velocity field, is not taken into account; the presented percentages refer to the fluctuations only. It is clear that roughly one third of the total energy of the fluctuations is contained in the first twenty modes of the POD for all cases. Figure 5.41 presents the same snapshot as the one in Figure 5.38 and its POD filtered equivalent using the first twenty-one modes including mode zero, to see the effect of the large scale disturbances on the ensemble averaged flow field. The POD filtered snapshot shows the large scale eddies present around the jets and their impingement positions, while these structures appear masked or deformed in the original snapshot. Because the energy content of the modes above mode twenty is very low, the large scale features of the velocity fields are well represented by the first twenty modes.

PODs of the hexagonal configuration

Figure 5.42 presents four randomly picked snapshots of the flow in vertical plane 1 of the hexagonal configuration. These snapshots are reconstructed from the POD using the mean field (mode 0) and the first 20 modes to investigate only the large scale features of the flow. The center jet and its direct neighbor can be discerned clearly. They appear to be largely unaffected down to $y = 2D_m$, but below this position the jets are disturbed by eddies originating from the interaction of the jets with the impingement surface. For

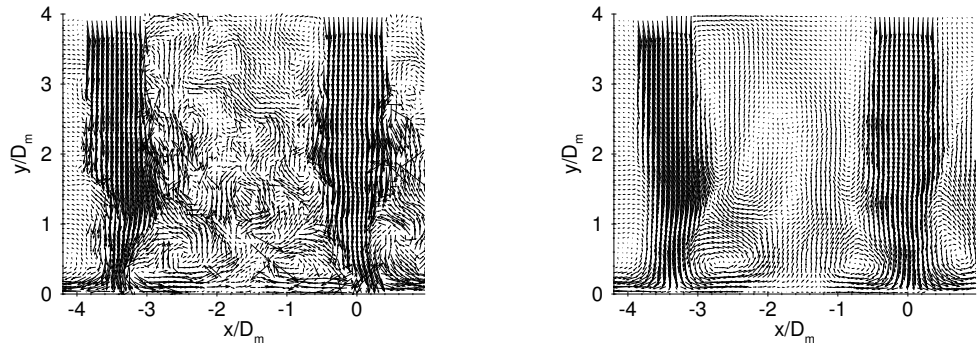

(a) Original snapshot

(b) POD filtered snapshot

Figure 5.41: Example of a snapshot in plane 3 of the hexagonal configuration and its POD filtered equivalent (20 modes + mode 0).

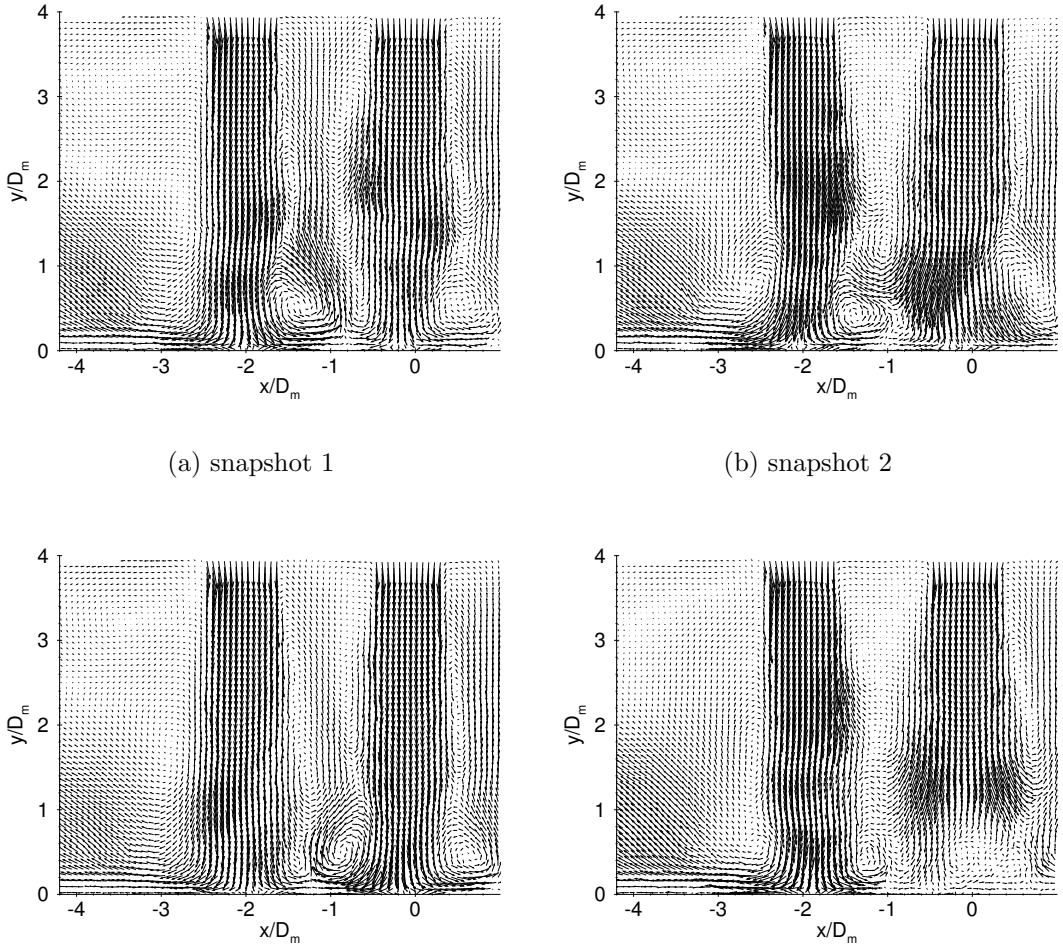

(a) snapshot 1

(b) snapshot 2

(c) snapshot 3

(d) snapshot 4

Figure 5.42: POD filtered snapshots (mean field and the first 20 modes) in vertical plane 1 of the hexagonal arrangement.

instance, in Figure 5.42d the center jet is either broken up or severely displaced out-of-plane. This explains the rising levels of k and the strong deceleration of the jet velocity in the center lines of the jets shown in Figure 5.5 on page 80.

The POD filtered snapshots show more clearly what happens to the upwash than the unfiltered snapshots do in Figure 5.16 (page 93). The upwash flow is strongly affected by eddies near the impingement point of the two jets. In Figure 5.42a the upwash is directed towards the neighbor jet due to an eddy near the neighbor jet, while an eddy near the center jet directs the upwash to the center jet in Figure 5.42c.

Figure 5.43 shows four POD filtered snapshots at vertical plane 2 of the hexagonal

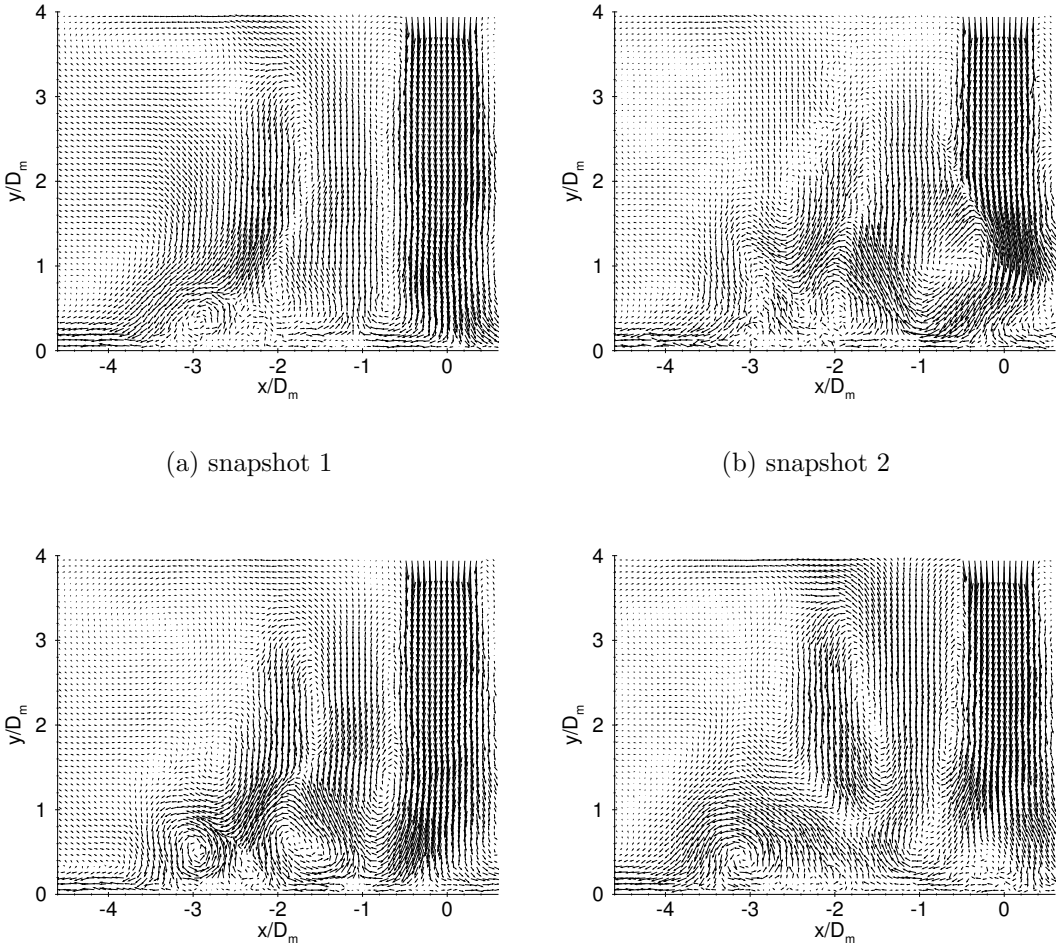

(a) snapshot 1

(b) snapshot 2

(c) snapshot 3

(d) snapshot 4

Figure 5.43: POD filtered snapshots (mean field and the first 20 modes) in vertical plane 2 of the hexagonal arrangement.

configuration. The center jet is clearly visible again. Because this plane is positioned very near a neighbor jet, its influence on the surrounding air can be recognized by the relatively strong down-flow around $x = -2D_m$. Additionally, the upwash caused by colliding wall jets is visible. The two discharge mechanisms mentioned in Section 5.2.1 (page 83) can be recognized in Figures 5.43a, c, and d. Part of the upwash flows outwards along the nozzle plate, while another part is being engulfed in the down-flow of the neighbor jet.

Figures 5.43a, c and d show the horse shoe vortex induced by the wall jet of the nearest outer jet and the spent air flowing outwards. This vortex also appears in Figure 5.44. This figure presents four snapshots in plane 3 of the hexagonal configuration. The

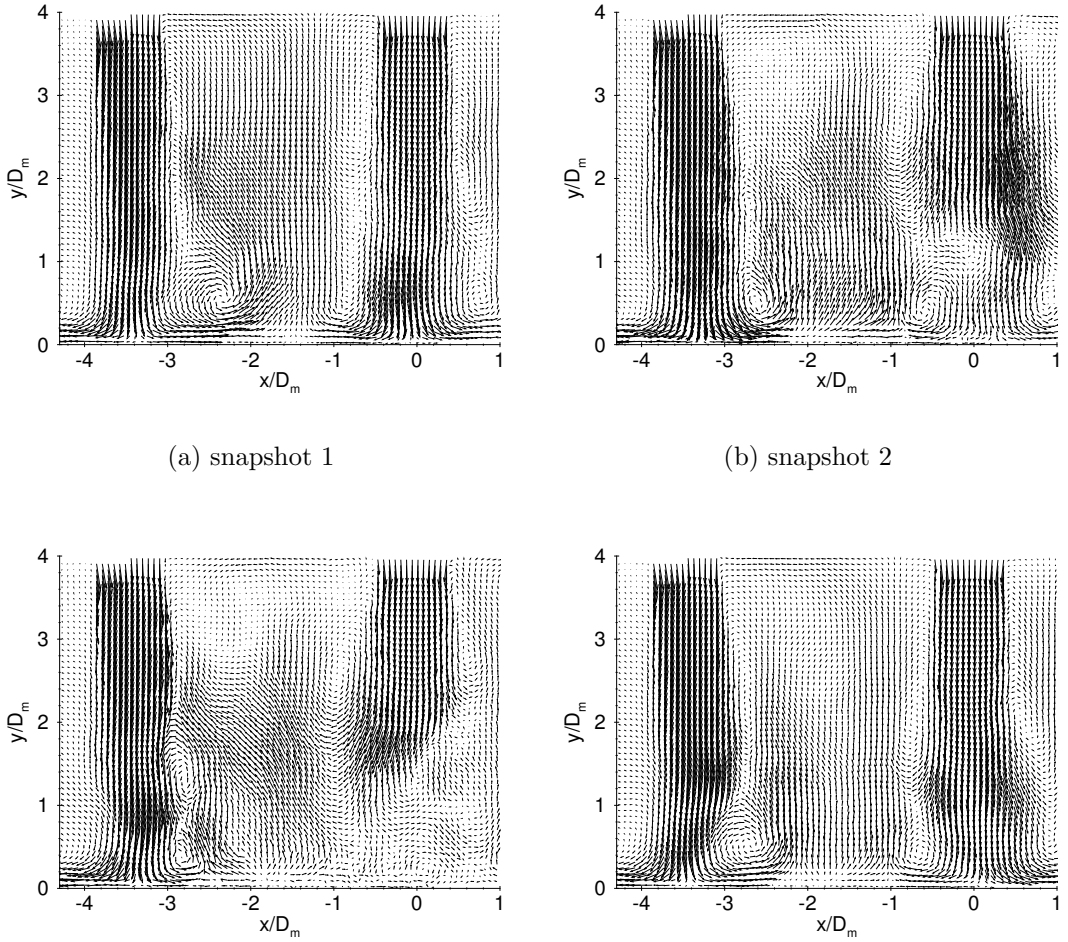

(a) snapshot 1

(b) snapshot 2

(c) snapshot 3

(d) snapshot 4

Figure 5.44: POD filtered snapshots (mean field and the first 20 modes) in vertical plane 3 of the hexagonal arrangement.

vortex does not have a steady position near the outer jet, which explains the fact that the ensemble mean velocity field also shows this vortex, but less clearly.

In Figure 5.44c a large elongated eddy is formed in the shear layer of the outer jet at $(x/D_m, y/D_m) \approx (2.8, 1.4)$. As was mentioned above, the upwash amplifies the instabilities in the shear layer of the jets, resulting in this kind of eddies. On the other side of the outer jet no upwash is present, so the shear layer on that side is not producing such eddies. For this reason k is asymmetrically distributed around the outer jets.

The mean velocity plot in the horizontal plane at $0.25D_m$ above the impingement plate (Figure 5.6, page 82) showed that the collision of wall jets produces turbulent kinetic

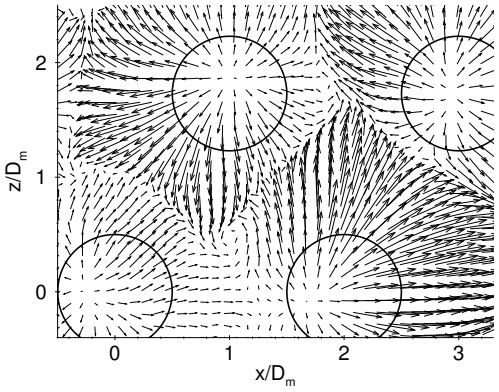

(a) snapshot 1

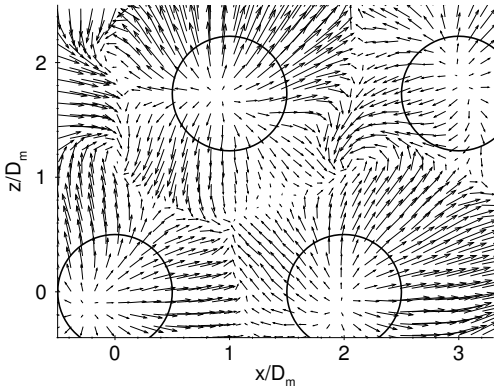

(b) snapshot 2

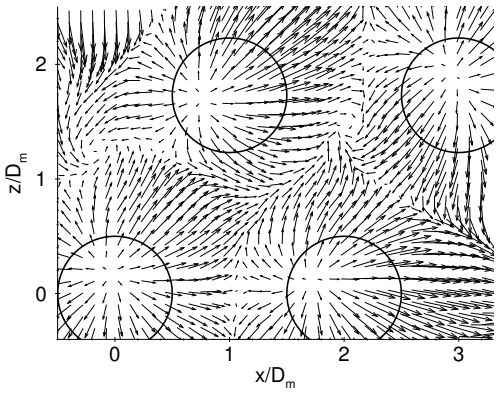

(c) snapshot 3

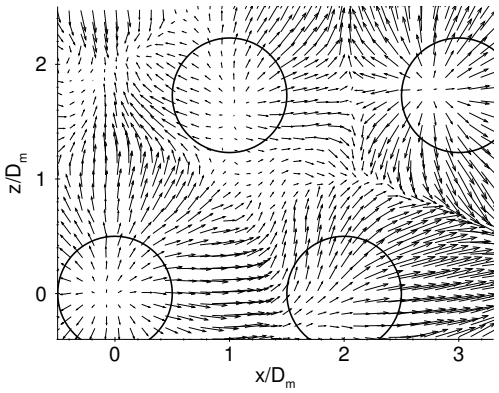

(d) snapshot 4

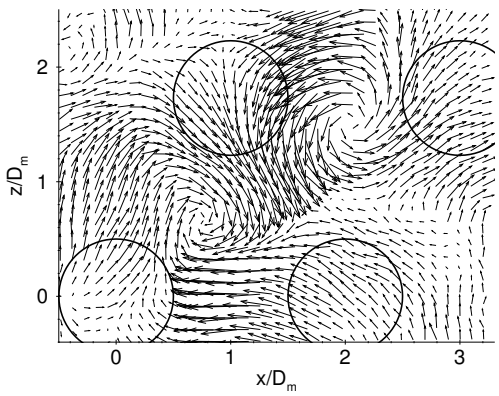

(e) POD mode 9

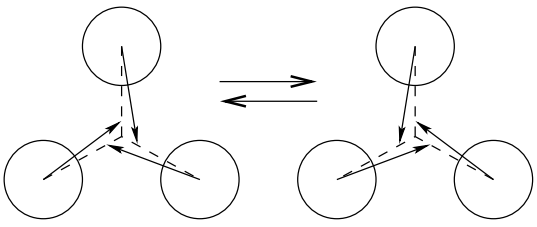

(f) Instable wall jet collision

Figure 5.45: POD filtered snapshots (mean field and the first 20 modes) and the 9^{th} mode in the horizontal plane at $0.25D_m$ above the impingement plate of the hexagonal arrangement.

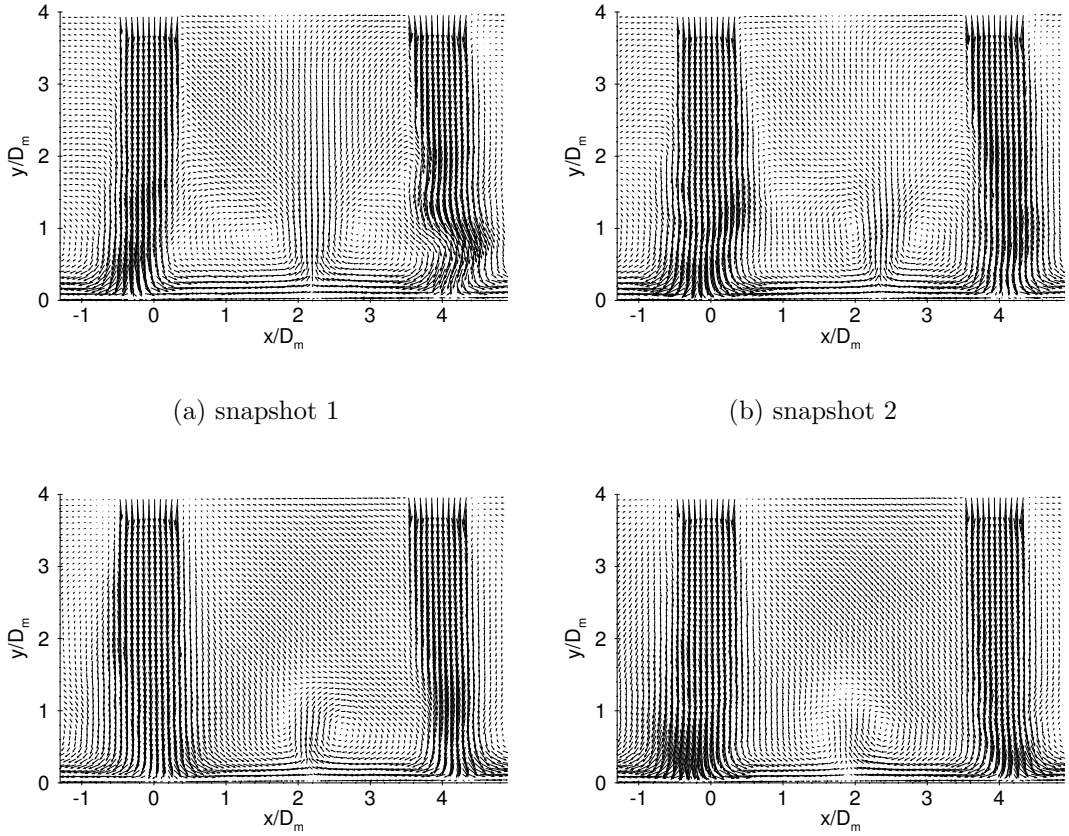

(a) snapshot 1

(b) snapshot 2

(c) snapshot 3

(d) snapshot 4

Figure 5.46: POD filtered snapshots (mean field and the first 20 modes) in vertical plane a of the in-line arrangement.

energy, especially in the points where three wall jets collide. The POD filtered snapshots in this plane presented in Figure 5.45 reveal that these points are very unstable, in the sense that they do not have fixed positions. Figures 5.45a, b, and c show swirling motion appearing at some of these collision points. This motion constitutes a strong structure in terms of spatial energy, because it originates from one of the lower modes (mode 9) of the POD presented in Figure 5.45e. It is conjectured here that the eddies are formed by the unstable collision of three wall jets in one point. Naturally present fluctuations in the direction of the wall jets can cause the eddies in their collision points to rotate in either direction. This is illustrated by Figure 5.45f, which shows the two possible orientations of the eddies in the collision point of three wall jets. As the probability for each orientation is equal, the mean velocity field cannot register the eddies.

All figures of the POD filtered snapshots in the vertical planes show that the flow is inherently unstable and that the energetic low mode number vortical structure oscillates

from one to another neighbor jet.

The snapshot in Fig 5.45a seems more or less conventional in the sense that it shows the impingement locations in a roughly hexagonal pattern. However, slight displacements from the geometrical centers of the nozzles occur due to oscillations in the individual jets. This is in line with the observations made from the POD filtered snapshots in the vertical planes.

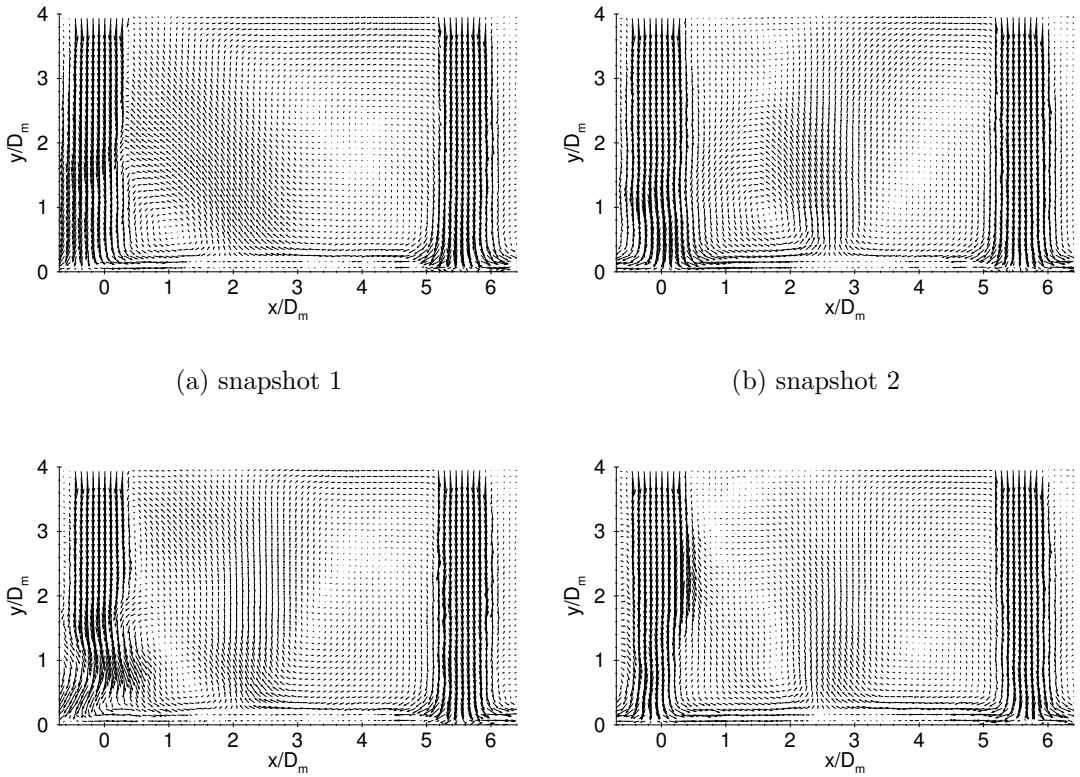

(a) snapshot 1

(b) snapshot 2

(c) snapshot 3

(d) snapshot 4

Figure 5.47: POD filtered snapshots (mean field and the first 20 modes) in vertical plane b of the in-line arrangement.

PODs of the in-line configuration

In the POD filtered snapshots in vertical plane a of the in-line configuration in Figure 5.46 a short upwash can be discerned between the two neighboring jets. Because the nozzle pitch s/D_m of the in-line configuration is twice as big as the pitch of the hexagonal configuration, the wall jets spread out over a greater surface area causing the upwash to be less strong, but more regular and located in or very close to the center between the two jets.

The jets appear much more stable in comparison to the hexagonal configuration, because there is less direct interaction between the jets and because the jets are less disturbed by large eddies. In the in-line configuration no horse-shoe like structures were found. This is most likely caused by the higher pitch in the in-line configuration.

Four POD filtered snapshots in vertical plane b in the in-line configuration are presented

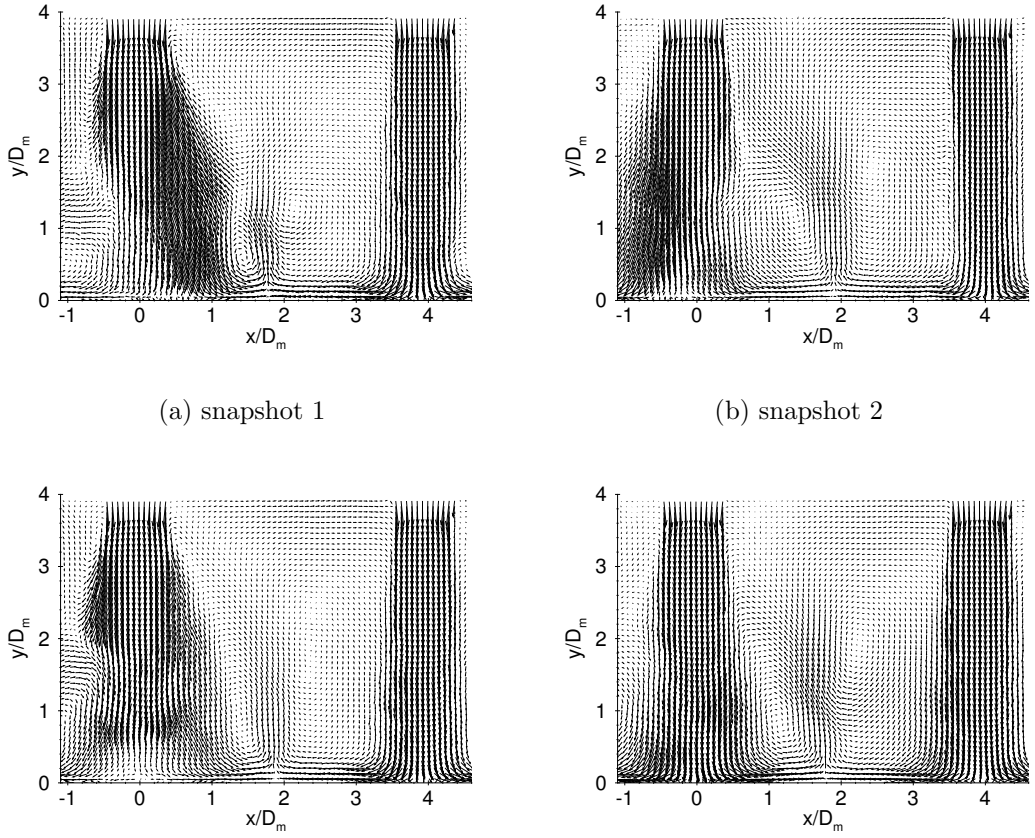

(a) snapshot 1

(b) snapshot 2

(c) snapshot 3

(d) snapshot 4

Figure 5.48: POD filtered snapshots (mean field and the first 20 modes) in vertical plane c of the in-line arrangement.

in Figure 5.47. Apart from some small oscillations of the jets, these snapshots resemble the ensemble averaged flow field.

More intriguing are the snapshots in vertical plane c in the in-line configuration shown in Figure 5.48. The jet at $x/D_m = 0.0$ appears to be dilated, like it was shown in Figure 5.17 on page 94. Next to that, its shear layers show strong fluctuations. In Figure 5.48a there is a strong down-flow on the right side of the jet, while in Figure 5.48b it is on the left and in Figure 5.48d it is absent. This indicates a swinging motion of the jet. In Figure 5.48c the jet at $x/D_m = 0.0$ is roughly symmetric in its center line, but it is distorted below $y/D_m \approx 1.0$.

The jet at $x/D_m = 4.0$ appears undisturbed in all snapshots of Figure 5.48. This confirms the differences between the center line velocity- and k-profiles of the jets in the in-line configuration presented in Figure 5.22 (page 99). The jet at $x/D_m = 4.0$ in plane c is the

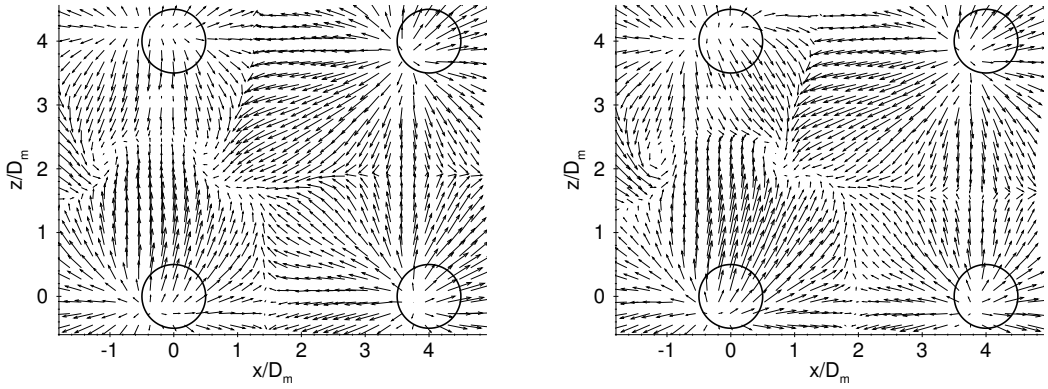

(a) snapshot 1

(b) snapshot 2

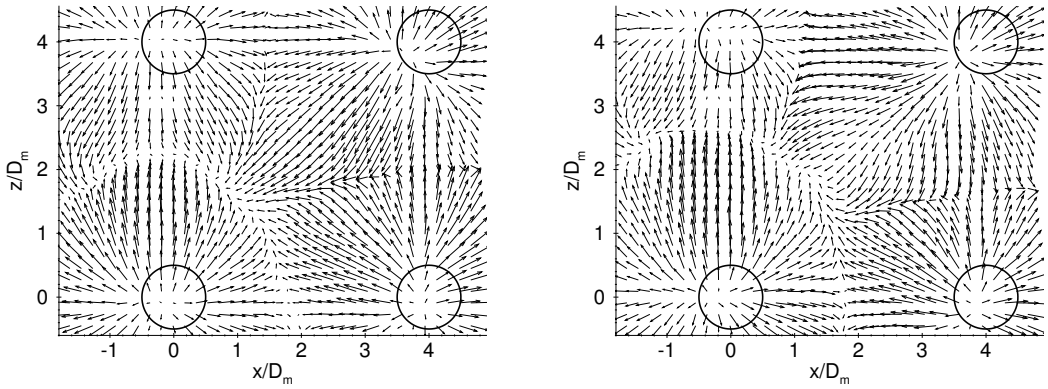

(c) snapshot 3

(d) snapshot 4

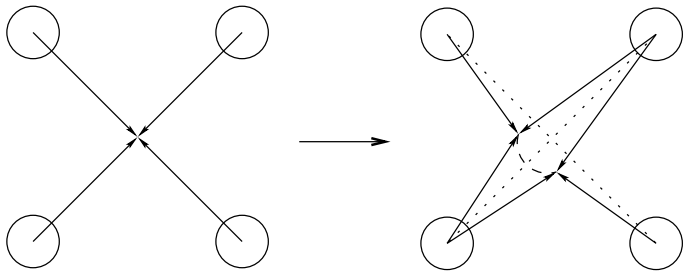

(e) Schematic of colliding wall jets

Figure 5.49: POD filtered snapshots (mean field and the first 20 modes) in the horizontal plane at $0.23D_m$ above the impingement plate of the in-line arrangement.

least disturbed because it has fewer neighbors to interact with, compared to the other jets.

In Figure 5.49 POD filtered snapshots are presented in the horizontal plane at $0.23D_m$ above the impingement plate for the in-line configuration. At $(x/D_m, z/D_m) \approx (-0.1, 3.1)$ there is a cluster of three vectors that are significantly shorter than the surrounding vectors. These are errors introduced by the fouling of the impingement plate by impinging seeding particles, as was mentioned in Section 5.2.1 on page 98. The stagnation points of the jets show some oscillation, though not as strong as for the hexagonal configuration.

There is no point where four wall jets collide. Instead there appear to be two points where three wall jets meet, connected by a line where two wall jets meet. This is illustrated by Figure 5.49e. The drawing on the left shows the four nozzles under investigation and the wall jets they produce. Intuitively, the wall jets are expected to meet in (or at least near) the geometrical center of the four jet impingement points. Instead, near the geometrical centre a region exists where the wall jets of the center and the outer jet meet (the dashed line) and at either end of this region there is a collision point of three wall jets, schematically depicted in the right drawing of Figure 5.49e.

A second interesting feature is the occurrence of vortex-like structures at some of the collision points of three wall jets, similar to the snapshots in the horizontal plane of the hexagonal configuration. They are clearly visible in Figures 5.49a and b around $(x/D_m, z/D_m) \approx (-1, 2.1)$ and $(0.6, 2.2)$. However, these vortices do not appear in the ensemble averaged flow field at $0.23D_m$ above the impingement plate (see Figure 5.21a, page 98). The ensemble averaged flow field at $0.54D_m$ above the impingement plate (Figure 5.21b) does show the vortices and the asymmetry in the line $x = y$ as a consequence of the preferred position of the vortices.

Vortex size distribution

The Q-criterion can be used as a vortex identifier to the POD filtered snapshots. This has the advantage that small scale disturbances do not interfere with the location of large eddies. An example of Q-maps associated with the raw snapshot and their POD filtered equivalent (presented in Figure 5.41 on page 126) can be found in Figure 5.50. Comparing Figure 5.50b with Figure 5.50a, it is clear that the structures in the POD filtered snapshot are larger than the ones in the original snapshot. Next to that, a lot of smaller vortices in the original snapshot do not appear in the POD filtered one. The most energetic structures are trapped by the identification method after POD filtering, whereas smaller and less energetic structures are ignored.

For a more quantitative investigation of the large eddies, Q-maps of POD filtered snapshots are used to locate and determine their size. By choosing an appropriate threshold level for Q, individual eddies can be isolated and their position can be determined using:

$$x_e = \frac{\iint_A x \cdot Q(x,y)dxdy}{\iint_A Q(x,y)dxdy} \tag{5.6}$$

and

$$y_e = \frac{\iint_A y \cdot Q(x,y)dxdy}{\iint_A Q(x,y)dxdy} \ , \tag{5.7}$$

where x_e and y_e denote the position of the centre of an eddy, and A is the area enclosing the eddy (i.e. where $Q(x,y)$ exceeds the threshold level).

Because the shape of an eddy identified with Q can be quite irregular, there is no unique way to measure its diameter. For this reason a *characteristic* diameter D_e is calculated on the basis of the total area enclosed by the eddy:

$$D_e = \sqrt{\iint_A dxdy} \ . \tag{5.8}$$

It should be noted that this diameter strongly depends on the chosen threshold value for Q. Therefore, it is only to be used for deriving qualitative conclusions regarding the size distribution of eddies.

Finally, the positions of the eddies, ordered according to their size, are presented in graphs. As an example, Figure 5.51 presents the distributions of all eddies identified in an ensemble of 1000 POD filtered snapshots in vertical plane 3 of the hexagonal configuration with sharp-edged orifices. Each dot represents an eddy. The distributions have been plotted for four size classes, ranging from $0.1D_m$ to $0.5D_m$.

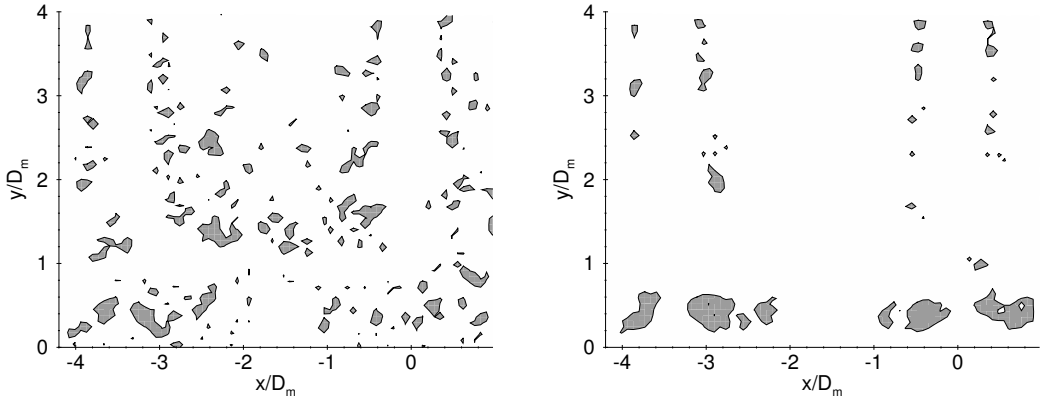

(a) Original snapshot

(b) POD filtered snapshot

Figure 5.50: Comparison of the eddies found in a snapshot in plane 3 of the hexagonal configuration and its POD filtered equivalent with threshold $QD_m^2/U_{CL}^2 = 1.0$.

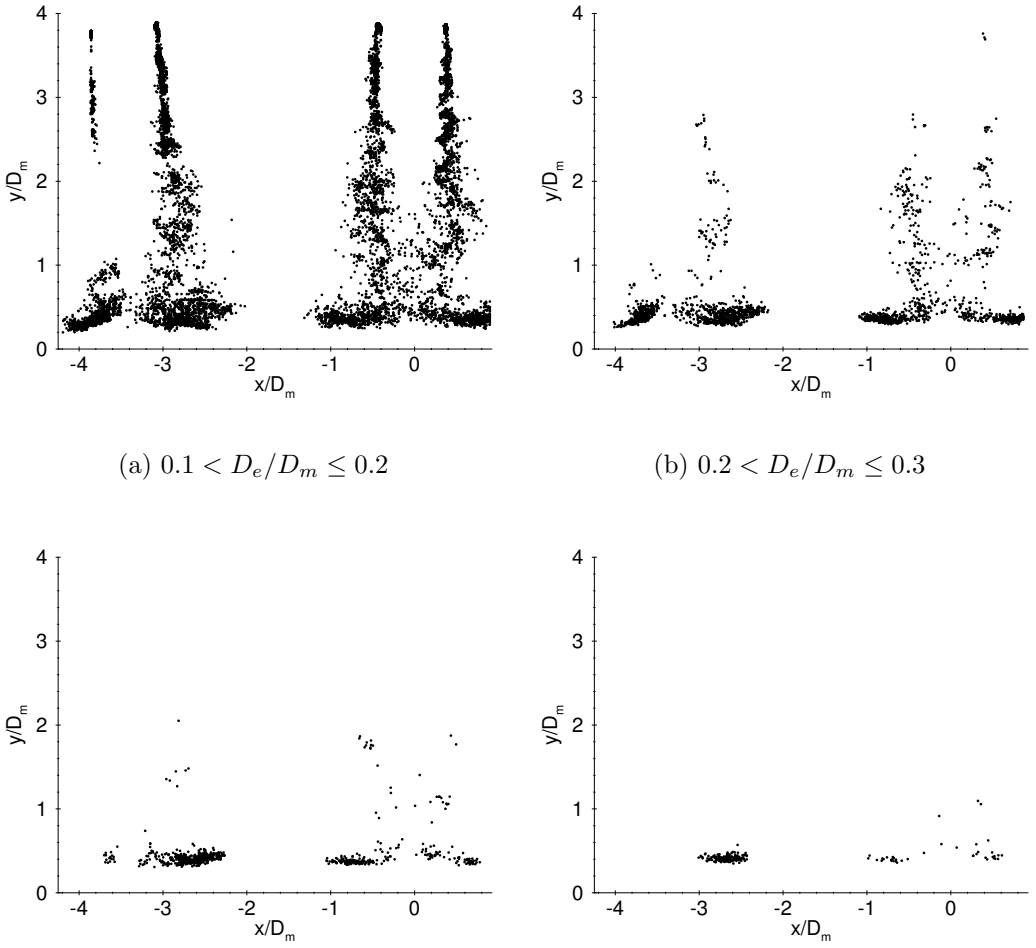

(a) $0.1 < D_e/D_m \leq 0.2$

(b) $0.2 < D_e/D_m \leq 0.3$

(c) $0.3 < D_e/D_m \leq 0.4$

(d) $0.4 < D_e/D_m \leq 0.5$

Figure 5.51: Size distribution of eddies located in vertical plane 3 of the hexagonal configuration with sharp-edged orifices.

In Figure 5.51a the impinging jets are clearly visible by the eddies in the shear layers and near the impingement points. In the downstream direction of the jets, the spreading of the shear layers is clear from the broadening of the regions of eddies. The highest eddy density is found in the direct neighborhood of the impingement points. This is the area where vortices originating from the shear layers impinge on the wall and are possibly destroyed.

As was already shown in Figure 5.6c on page 82, the turbulent kinetic energy is distributed asymmetrically around the axis of the outer jet. The value of k is relatively high on the inner side of the jet and low on the outer side. Figures 5.51a and b shows that more eddies appear on the inner side of the jet, where k is high. These eddies are

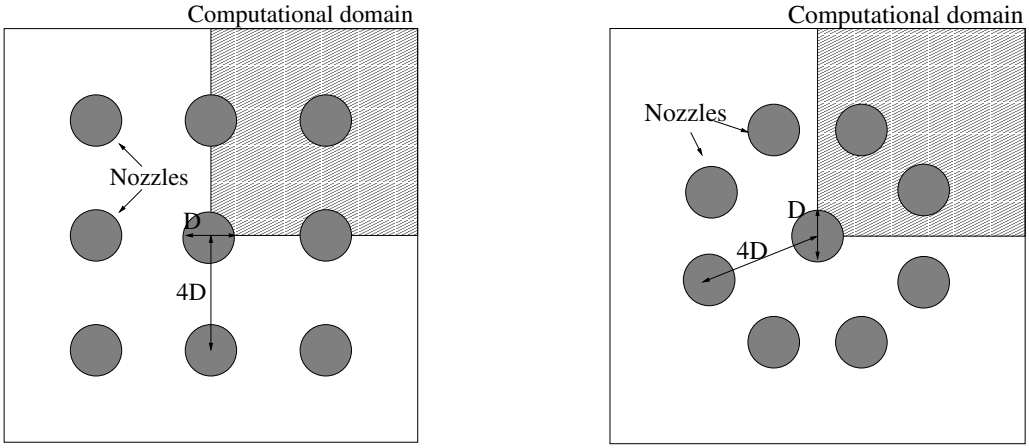

(a) in-line nozzle configuration

(b) circular nozzle configuration

Figure 5.52: Two configurations used for numerical simulations (Thielen et al., 2003).

a consequence of the instabilities induced by the interaction of the outer jet and the upwash flow between the jets.

It appears from Figures 5.51c and d that the largest eddies are found just above the wall, next to the impingement points of the jets. The highest concentration of large eddies is found at the position of the horse-shoe vortex that circumscribes the outer jet. Eddy size distributions in other vertical planes in the hexagonal and the in-line configurations were very similar to the presented distributions and will not be presented here.

Comparison with numerical results

Numerical simulations were conducted by Thielen et al. (2003) in the two different nozzle configurations presented in Figure 5.52a and b. The nozzle pitch of the in-line configuration is $4D_m$ and for the circular configuration the distance between the center nozzle and the eight surrounding nozzles is also $4D_m$. The distance between the impingement plate and the nozzle plate was $4D_m$ and the Reynolds number was $20{\times}10^3$. The turbulence models used were the standard $k-\varepsilon$ model with wall functions and the $\overline{v^2}-f$ model (Durbin, 1991) with integration to the wall. For further details regarding the computations the reader is referred to Thielen et al. (2003) and Thielen (2003).

Figure 5.53 presents path lines in a horizontal plane $0.01D_m$ above the impingement plate for the in-line and the circular configurations. From Figure 5.53a it appears that the asymmetric flow field discussed above also occurs in the numerical results. At first this was thought to be a numerical artifact, because no experimental data were available

for the in-line configuration at the time of discovery. For this reason, special care was taken to ensure that the asymmetry did not have a numerical origin. The computations were checked on their dependence of the grid, the differencing scheme used, the initial conditions, the fact that the calculations were steady or unsteady, and the computer code used to calculate the flow field. Based on the results of this analysis and the experimental evidence given above it is concluded that the asymmetry is physical in nature.

For the circular configuration both turbulence models predict a flow field that reflects all the symmetries of the physical situation. This is clear from Figure 5.53b, which presents the path line plot in a horizontal plane at $0.01D_m$ above the impingement plate for the circular configuration. Because the circular configuration can be obtained by moving the nozzles in the corners of the in-line setup slightly towards the center, it is expected that there is a transition point between the asymmetric in-line case and the symmetric circular case. However, simulations of an in-line configuration with only a marginal displacement of the outermost nozzles towards the center results in a symmetric flow field. This remains the case for all intermediate configurations, up to the circular one (Thielen et al., 2003). Unfortunately no experimental data is available for these intermediate configurations and for the circular configuration.

Summary

Results were presented for the vorticity magnitude $|\omega_z|$, the second invariant of the velocity gradient tensor Q, and the kinematic vorticity number N_k. These three techniques were compared for their applicability to the identification of eddies. It appeared that Q

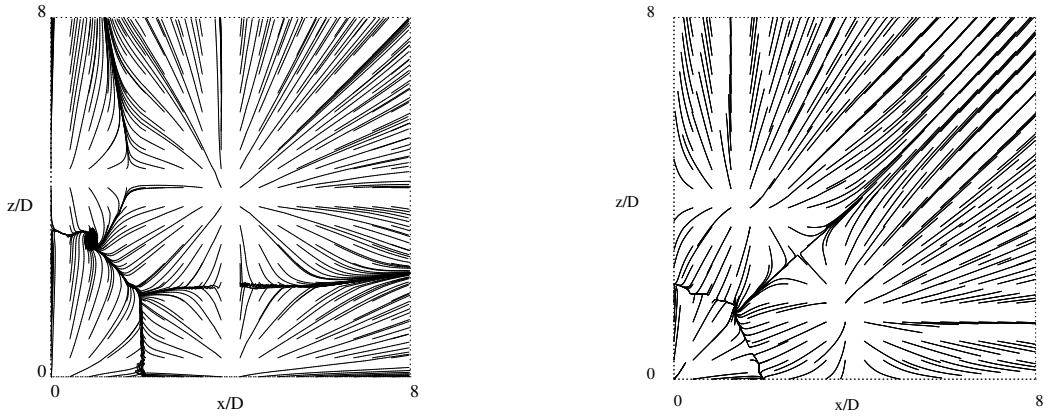

(a) in-line nozzle configuration

(b) circular nozzle configuration

Figure 5.53: Path lines in horizontal planes at $0.01D_m$ above the impingement plate for both configurations (Thielen et al., 2003).

is the most adequate technique of the three, because $|\omega_z|$ does not distinguish vortices from background shear and N_k appeared to be, at least for the flow considered, oblivious to the dynamical significance of a vortex.

POD is subsequently presented as a technique to apply inhomogeneous low-pass filtering of snapshots to reveal the large scale dynamics of the flow snapshots resulting from PIV measurements. The POD eigenvalue spectra for all measurement planes appeared to extend over a large range of modes due to the high Reynolds number of the flow. A considerable number of modes should be taken into account to cover the larger part of the turbulent kinetic energy. However, for the investigation of the large scale dynamics it sufficed to reconstruct snapshots using only 21 modes.

For the hexagonal configuration the jets appear to be largely unaffected down to $y = 2D_m$, but below this position the jets were disturbed by eddies originating from the interaction of the jets with the impingement surface. These eddies also cause the upwash flows between jets to oscillate, which in turn affects their interaction with the impinging jets. In the POD filtered snapshots in vertical plane 3 clear evidence was presented of the horse shoe vortex around the outer jet. This vortex did not have a steady position near the outer jet.

The POD filtered snapshots in the horizontal plane at $0.25D_m$ above the impingement plate were presented. It was conjectured that vortical motion between the impingement points of three adjacent jets is caused by the unstable collision of the three wall jets in that point. As both orientations of the eddies can appear equally likely, the mean velocity field did not show the eddies.

Due to the larger pitch in the in-line configuration, the upwash between the jets was shorter than the one in the hexagonal configuration. As a result, the interaction between the jets was less and they appeared much more stable in comparison to the hexagonal configuration. The lack of a horse shoe vortex around the outer jets in the in-line configuration was most likely caused by the higher pitch. In the POD filtered snapshots the distortion of the neighbor jets was clearly visible. The jet appeared to be swinging, causing strong fluctuations in its shear layer. Finally, the outer jet appeared undisturbed, confirming the differences between the center line velocity- and k-profiles presented earlier.

In the horizontal snapshots in the in-line configuration there appeared to be no points of collision for four wall jets. Contrary to intuition, there were two collision points of three wall jets connected by a collision line of two wall jets. In the two collision points vortices can exist, but there is a clear preference for one of the two points. The existence of a vortex in one of the collision points inhibits the appearance of a second vortex in the other one.

On the basis of Q-maps of the POD filtered snapshots in vertical plane 3 of the hexagonal configuration, eddies were identified. Subsequently, the eddies were arranged in four size

classes that were presented in graphs. The asymmetric k-distribution around the outer jet presented earlier coincided with a region where many eddies are present. The largest eddies were found just above the impingement wall in the vicinity of the jet impingement points, and at the position of the horse-shoe vortex circumscribing the outer jet.

The experimental results in a horizontal plane in the in-line configuration were compared with numerical simulations conducted in a parallel project. The symmetry breaking vortex also appears in the numerical simulations. After a thorough analysis of both the experiments and the computations it was concluded that the asymmetry is physical in nature. However, on the basis of simulations the existence of asymmetry appears to be very sensitive to geometrical changes of the nozzle configuration, because the flow-field became symmetric after a marginal displacement of the outermost nozzles towards the center.

Chapter 6

Conclusions

The goal of the project was to investigate the interaction between the flow features of impinging jets and the heat transfer on the impingement surface on the basis of flow and heat transfer measurements in a number of impinging jet configurations. Major conclusions regarding the flow in a single impinging jet and the flow and heat transfer in multiple jet arrays are presented. This is followed by conclusions regarding the use of structure identification methods with PIV velocity data. Finally, the application of Liquid Crystal Thermography to impingement heat transfer is discussed.

Single impinging jet flow

Measurements of the mean and fluctuating velocity components were presented in a single impinging jet flow using the PIV technique. For comparison, and a more detailed insight in the near-wall region, also LDA measurements have been performed. In the jet impingement region the turbulence stress field is characterized by a strong anisotropy. Very close to the wall in the impingement zone the lateral fluctuations exceed the wall-normal fluctuations causing a reversal of the sign of the turbulent kinetic energy production by the normal stresses. Around the jet axis, where the shear production is small, this leads to local zones of negative total production of the turbulent kinetic energy.

In the wall jet the lateral fluctuations always dominate the wall-normal fluctuations, but the production of the turbulent kinetic energy remains positive. The shear component of the production greatly exceeds the normal component at this station.

Multiple impinging jet array flow and heat transfer

PIV was used to provide mean velocity fields and turbulence quantities in the flow of two different multiple impinging jet arrays: an in-line configuration and a hexagonal configuration of sharp-edged orifices. This proved to be essential for detecting some salient features of the multiple-jet dynamics. Subsequently, LCT measurements provided mean distributions of the heat transfer from the impingement plate to the impinging jets in both above mentioned configurations and in a hexagonal configuration of contoured nozzles. These measurements were done at different values for the nozzle-to-plate spacing, H/D_m, the nozzle pitch, s/D_m, and the Reynolds number, Re. Finally, a non-dimensional empirical correlation was derived for the area-averaged Nusselt number, Nu_{ave}:

$$\mathrm{Nu}_{ave} = \mathrm{Re}^{\alpha_1} \frac{\exp\left\{\alpha_2 \left(\frac{H}{D_m}\right)^{\alpha_3}\right\}}{\left(\frac{s}{D_m}\right)^{\alpha_4} \left(\frac{H}{D_m}\right)^{\alpha_5}} \ , \tag{6.1}$$

where α_1 to α_5 are coefficients calculated from a Marquardt-Levenberg non-linear fit of the equation to the experimental data in each configuration. Table 5.1 gives an overview of the values for these coefficients for all three nozzle configurations. An estimate of the variance resulting from the fitting procedures is also given.

A comparison was made between the center-line profiles of the axial velocity and the turbulent kinetic energy for different jets in the in-line and the hexagonal arrays. Except for the outer jets in the in-line array, it appeared that all jets display similar profiles, consisting of three regions. In the initial region the axial velocity is fairly constant and the turbulent kinetic energy is low. This is the potential core region of the jet: the disturbances in the shear layer are growing in a downstream direction, but have not yet reached the center of the jet. The length of this region for a particular jet is shorter as the jet has more neighboring jets, because jet-jet interaction causes amplification of the instabilities in the shear layer. One of the main mechanisms for this is the upwash, which is formed when two wall jets emerging from jet stagnation zones collide and separate from the impingement plate. The number of vortices in a shear layer adjacent to an upwash is significantly larger than in a shear layer without upwash. Correspondingly, the turbulent kinetic energy is higher in case of an adjacent upwash.

The region below the initial region is characterized by a strong axial velocity decay and a monotonic rise of the turbulent kinetic energy. Kinetic energy of the mean flow is transformed into turbulent kinetic energy, because the turbulent kinetic energy production is positive and rising towards the wall. The levels of turbulent kinetic energy become higher and the velocity decay stronger with increasing numbers of neighboring jets.

The final region is the impingement region, where the profiles of both the velocity and the turbulent kinetic energy for different jets collide. The effect of the impingement wall on the jets is stronger than the effect of jet-to-jet interactions in this region. The strong adverse pressure gradient causes a decrease of the turbulent kinetic energy. Additionally,

close to the wall the production of turbulent kinetic energy becomes negative. Analogously to the single impinging jet, this is possible because the shear component of the production of turbulent kinetic energy appears to be negligible on the jet center-line, just above the impingement plate, and the normal component is dominated by the wall-parallel contribution. This contribution is the product of the wall-parallel gradient of the mean wall-parallel velocity component on the one hand, and the wall-parallel component of the Reynolds normal stress on the other hand. In the absence of fluctuations, the impingement point of the jet would be stationary, causing a minimum Nusselt number in the impingement point because there is no flow. However, in the presence of fluctuations the flow does not have a stationary impingement point, but, instead the impingement point is moving. The combination of a moving impingement point with the strong wall-parallel velocity gradient causes a maximum Nusselt number in the stagnation region.

The effect of the nozzle shape on the flow is clear from the center-line velocity profile of one jet emerging from a sharp-edged orifice: there is a clear overshoot of the velocity due to the vena contracta. For jets emerging from contoured nozzles, this effect is smaller. As a result, the heat transfer in case of sharp-edged nozzle jets is everywhere higher than for contoured nozzle jets for equal Reynolds numbers. The difference in Nusselt numbers between these two cases is diminishing with increasing nozzle-to-plate spacing, because the jets tend to 'forget' their initial conditions with increasing distance from the nozzle exit. From the empirical correlation of Equation 6.1 it appeared that the deterioration of the Nusselt number with increasing nozzle-to-plate distance was stronger for the sharp-edged orifice jets than for the contoured nozzle jets. This is caused by the higher level of instabilities in case of a sharp-edged orifice.

At small nozzle pitches, the jets interact strongly, causing a strong decay of the jet velocity and strong mixing due to turbulence. Additionally, mixing of fresh air with spent air diminishes the beneficial temperature difference between the air and the impingement plate. As a result the heat transfer distribution on the impingement plate will be more homogeneous than for a configuration with a large pitch. Evidence of the strong jet-to-jet interaction is displayed in several ways. The impingement points of closely spaced jets appear to push each other away due to their wall jets colliding.

The neighbor jets in the in-line nozzle configuration are distorted due to the interaction between jets. These jets are deflected outwards, causing compression of their diameter in one direction and an expansion in the direction perpendicular to it. From POD filtered snapshots it appeared that the shear layers of the neighbor jets are very unstable: they show a swinging motion. On average, this results in the above mentioned expansion of the jet diameter in one direction. The heat transfer distribution on the impingement surface shows the thermal imprint of the elliptical jets.

A striking fact is that the heat transfer pattern corresponding to the center jet in the in-line configuration is also elliptical, while this jet is approximately circular. It is conjectured that this effect is caused by the asymmetry of the flow discovered in a plane parallel

to the impingement surface. Contrary to expectations, there is no symmetry around the diagonal intersecting the center jet and the outer jet: a vortex appears only on one side of the diagonal in the ensemble mean velocity field. On the basis of a random check of individual snapshots of the flow, it was found that the vortex can occur on both sides of the diagonal, but there is a clear preference for one of the sides. The ensemble mean flow velocity distribution in a corresponding plane in the hexagonal nozzle configuration does not show such an asymmetry.

The collision of wall jets produces high levels of turbulent kinetic energy, especially in the points where three wall jets collide. POD filtered snapshots reveal that these points are very unstable, in the sense that they do not have fixed positions. The swirling motion appearing occasionally on these collision points constitutes a strong structure in terms of spatial energy, because it originates from one of the lower POD modes. It is conjectured that the eddies are formed by the unstable collision of three wall jets in one point. Because the eddies have two possible orientations that appear equally likely, the mean velocity field does not show the eddies at all.

There is no point where four wall jets collide. This is clear from the ensemble mean velocity distribution in a plane parallel to the impingement plate, at a small distance from it. Intuitively, the wall jets are expected to meet in (or at least near) the geometrical center of the four jet impingement points. Instead, there appear to be two points where three wall jets meet, connected by a line where two wall jets meet. The collision points of three wall jets behave as described in the previous paragraph.

Finally, there is another interesting flow feature in the hexagonal nozzle configuration. There is a horse-shoe vortex surrounding the outer jets. The vortex is induced by the wall jet of an outer jet flowing towards the center jet and the outflow of spent air originating from the center jet and its direct neighbors. POD filtered snapshots reveal that the vortex does not have a steady position, explaining the fact that its appearance in the ensemble mean flow field is less clear. It remains unclear what influence this horse shoe vortex has on the heat transfer.

Structure identification from PIV images

Three methods for the identification of vortices in snapshots of the velocity field in turbulent impinging jets were compared. The methods were based on the absolute value of the vorticity, the second invariant of the velocity gradient tensor, and the kinematic vorticity number. It appeared that the second invariant of the velocity gradient tensor is the most adequate identifier of the three, because the vorticity does not distinguish vortices from background shear and the kinematic vorticity number is oblivious to the dynamical significance of a vortex. There are other methods, based on a critical-point analysis or on a negative second eigenvalue of the sum of the squared symmetric and the antisymmetric parts of the velocity gradient tensor. However, in planar flows these

methods are similar to the method of the second invariant of the velocity gradient tensor.

A Proper Orthogonal Decomposition (POD) was applied to ensembles of velocity field snapshots in multiple impinging jet arrays resulting from PIV measurements. It is used as an inhomogeneous low-pass filter to reveal the large scale dynamics of the flow. The POD eigenvalue spectra for all measurement planes extended over a large range of modes due to the high Reynolds number of the flow. A considerable number of modes should be taken into account to cover the larger part of the turbulent kinetic energy. However, for the current investigation it sufficed to reconstruct snapshots using only 21 modes.

Application of LCT to impingement heat transfer

A Liquid Crystal Thermography (LCT) system was developed to measure the temperature of a heated metal foil serving as impingement plate for jets. The foil was coated with a layer of black backing paint and a layer of thermochromic liquid crystals. The color changes of the crystals as a function of temperature were recorded with a color CCD camera. The mosaic filters mounted on the CCD chip introduced salt-and-pepper like noise into the images that was reduced by a median filtering procedure.

Because of the viewing and lighting angle dependence of the observed color of the crystals, an in-situ calibration procedure was used to convert the hue angles of the crystal colors into temperatures. The viewing and lighting angle dependence also demands a position dependent calibration: for all pixels in the CCD array a separate calibration curve was determined. Differences up to 0.9°C were observed for pixels with the same hue angle at different positions in the CCD array. The calibration curves were stored in the form of a lookup table. In this way, no specific functional dependency between temperature and hue angle was assumed, and hence, no additional noise due to function fitting procedures was introduced. The accuracy of temperature measurements in the current LCT system was about 0.1°C.

LCT was only used to provide ensemble mean distributions of the impingement surface temperature. Rearranging the molecular structure of liquid crystals as a result of temperature changes typically takes a time period of the order of tens of milliseconds, which was longer than the typical time scales of the flow, that ranged from 560 μs to 2.3 ms. For this reason, the technique was not suited for providing instantaneous snapshots of the temperature of the impingement surface.

Appendix A

Specification of the wind tunnel

In this appendix the precise measures of the wind tunnel are presented, together with the specifications of the gauzes, the honeycomb and the contraction. The wind tunnel was designed on the basis of rules of thumb given by Mehta and Bradshaw (1979).

Corner bends

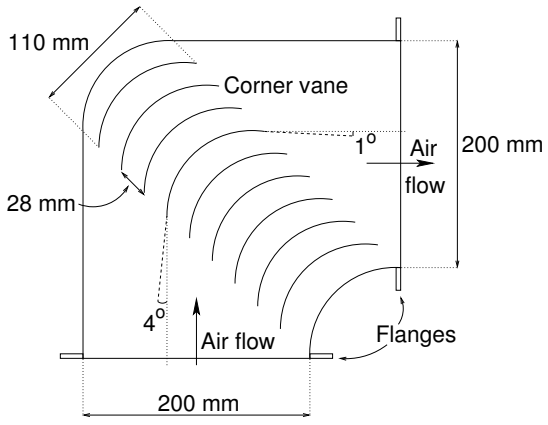

Figure A.1: Measures of the bends in the supply channel of the wind tunnel

Figure A.1 presents a sketch of one of the two 90° corner bends used in the wind tunnel. It is equipped with guiding vanes to prevent the formation of Dean vortices. Due to their inertial nature, these vortices may have a life time exceeding their residence time in the supply channel of the wind tunnel. The leading edge is set to a positive angle of incidence of 4° to the axis of the upstream leg of the channel and the trailing edge over-turns 1°, resulting in an included angle of 93°. The ratio of the gap between the

vanes (measured from leading edge to leading edge) to the chord should not exceed about 0.25.

End section of the wind tunnel

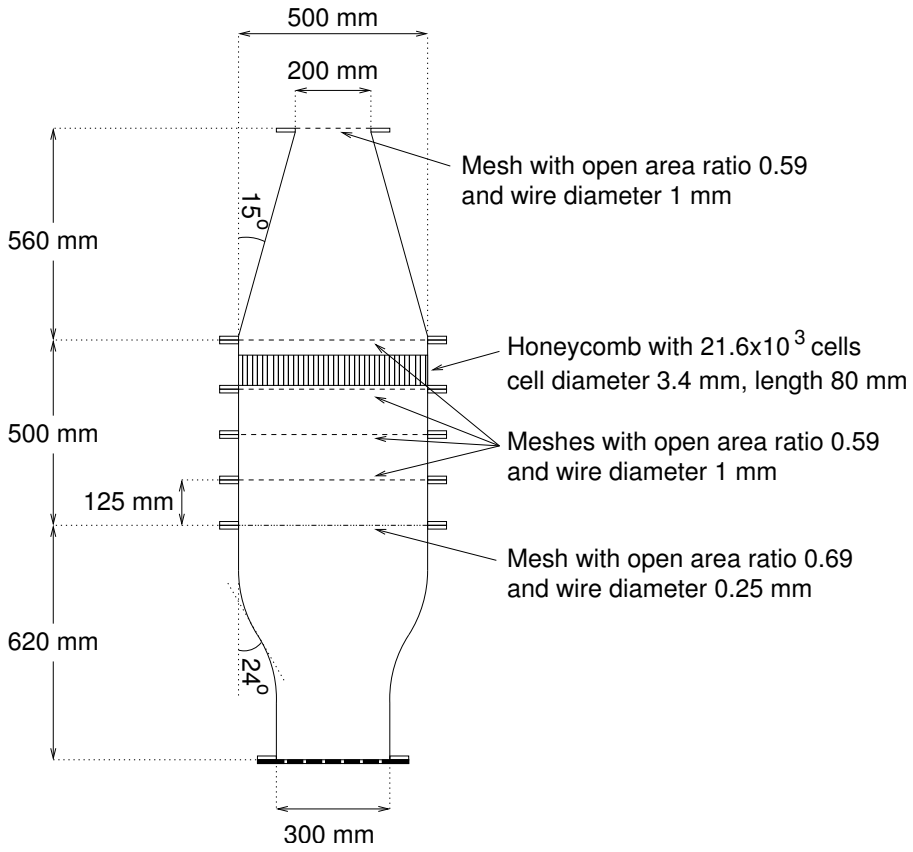

Figure A.2: Measures of the wind tunnel and specification of its parts.

Figure A.2 presents a sketch of the end section of the wind tunnel with the specifications of all constituent parts. All the different sections will be discussed shortly below.

The diffuser has an area ratio of 6.25 and an angle of 30°. For these conditions, one wire mesh screen is needed in the inlet of the diffuser and one on the outlet to prevent flow separation. For succesful operation the sum of the pressure drop coefficients of these screens should exceed 4.6. The screens both have an open-area ratio β of 0.59 and a wire diameter of 1 mm, resulting in pressure drop coefficients K of about 1.66 for the screen at the inlet and 3.06 for the screen at the outlet. All K values were calculated on the basis of a jet Reynolds number of 2.0×10^4 using 13 nozzles.

The settling chamber is divided into four equal square sections separated by wire mesh screens. According to Mehta and Bradshaw the optimum spacing between the screens has

been found to be 0.2 times the width of the channel, restricting the length of each section to 125 mm for a cross-section of 500×500 mm^2. The screens between the sections had β=0.59 and d=1 mm. As a result K=3.06 of each of these screens. To avoid unwanted production of flow instabilities, the screen at the end of the settling chamber has a higher β (0.69) and d= 0.25 mm, resulting in K=2.69.

In the upper section of the settling chamber a honeycomb is installed to remove swirl and lateral mean velocity variations. The optimal length of the honeycomb cells is 5-10 cell diameters. A total number of about 25×10^3 cells in the cross section of the settling chamber is adequate. In the present project, the cell width of the available honeycomb was 3.4 mm and the length 80 mm, equivalent to 23.5 cell diameters. The total number of cells is about 21.6×10^3. Because the cells are relatively long, the turbulence level of the flow is expected to increase due to the honeycomb. For this reason the screens in the settling chamber were chosen conservatively.

Just below the settling chamber a thin flange was placed containing probes to measure the air temperature and pressure. The last element of the end section is a contraction to allow the screens and the honeycomb to be in the low speed region (reducing pressure losses) and to reduce the mean and fluctuating velocity variations with respect to the average velocity. The contraction was shaped according to a fifth order polynomial yielding a straight inlet and a straight outlet. The width of of the outlet was 300 mm, and the contraction ratio (inlet area over outlet area) was 2.78. At the outlet several different nozzle plates can be attached.

Bibliography

Absil, L. H. J. (1995). *Analysis of the laser Doppler measurement technique for application in turbulent flows*. PhD thesis, Delft University of Technology, Delft.

Akino, N., Kunugi, T., Ichimiya, K., Mitsushiro, K., and Ueda, M. (1989). Improved liquid crystal thermometry excluding human color sensation. *Trans. ASME - J. Fluids Eng.*, 111.

Akino, N., Kunugi, T., Ichimiya, K., Ueda, M., and Kurosawa, A. (1987). Liquid crystal thermometry based on automatic color evaluation and applications to measure turbulent heat transfer. In *Second Int. Symp. Transport Phenomena in Turbulent Flows*, pages 627–640, Tokyo.

Anderson, M. R. and Baughn, J. W. (2002). Model of a thermochromic liquid crystal imaging system and effect of illumination spectral characteristics. *received through personal communication.*

Arjocu, S. C. and Liburdy, J. A. (1999). Near surface characterization of an impinging elliptic jet array. *Trans. ASME - J. Fluids Eng.*, 121:384–390.

Barata, J. M. M. (1996). Fountain flows produced by multiple impinging jets in a crossflow. *AIAA Journal*, 34(12):2523–2530.

Barata, J. M. M. and Durão, D. F. G. (2002). Laser-Doppler Measurements of Impinging Jet Flows Through a Crossflow. In *Proceedings of the 11^{th} International Symposium on Applications of Laser Techniques to Fluid Mechanics*, Lisbon.

Barnett, D. O. and Bentley, H. T. (1974). Statistical bias of individual realization laser velocimeters. In *Proceedings of the Second International Workshop on Laser Velocimetry*, volume 1, pages 428–444.

Baughn, J. W., Anderson, M. R., Mayhew, J. E., and Wolf, J. D. (1999). Hysteresis of thermochromic liquid crystal temperature measurement based on hue. *Trans. ASME - J. Heat Transfer*, 121(4):1067–1072.

Baughn, J. W. and Shimizu, S. (1989). Heat transfer measurements from a surface with uniform heat flux and an impinging jet. *Trans. ASME - J. Heat Transfer*, 111:1096–1098.

Beek, W. J. and Mutzall, K. M. K. (1975). *Transport Phenomena*. John Wiley and Sons Ltd., London.

Behle, M., Schulz, K., Leiner, W., and Fiebeg, M. (1996). Color-based image processing to measure local temperature distributions by wide-band liquid crystal thermography. *Applied Scientific Research*, 56:113–143.

Can, M., Etemoğlu, A. B., and Avci, A. (2002). Experimental study of convective heat transfer under arrays of impinging air jets from slots and circular holes. *Heat Mass Transfer*, 38:251–259.

Chong, M. S., Perry, A. E., and Cantwell, B. J. (1990). A general classification of three-dimensional flow fields. *Phys. Fluids A*, 2(5):765–777.

Colucci, D. W. and Viskanta, R. (1996). Effect of nozzle geometry on local convective heat transfer to a confined impinging air jet. *Exp. Thermal Fluid Sci.*, 13:71–80.

Cooper, D., Jackson, D. C., Launder, B. E., and Liao, G. X. (1993). Impinging jet studies for turbulence model assessment — I. Flow-field experiments. *Int. J. Heat Mass Transfer*, 36(10):2675–2684.

Durbin, P. A. (1991). Near-wall turbulence closure modeling without damping functions. *Theoret. Comput. Fluid Dynamics*, 3:1–13.

Ferguson, J. L. (1968). Liquid Crystals in nondestructive testing. *Applied Optics*, 7(9):1729–1737.

Findlay, M. J., Salcudean, M., and Gartshore, I. S. (1999). Jets in a crossflow: Effects of geometry and blowing ratio. *Trans. ASME - J. Fluids Eng.*, 121:373–378.

Foucaut, J. M. and Stanislas, M. (2002). Some considerations on the accuracy and frequency response of some derivative filters applied to particle image velocimetry vector fields. *Meas. Sci. Technol.*, 13:1058–1071.

Gamard, S., George, W. K., Jung, D., and Woodward, S. (2002). Application of a "slice" proper orthogonal decomposition to the far field of an axisymmetric turbulent jet. *Phys. Fluids*, 14(7):2515–2522.

Gardon, R. and Cobonpue, J. (1962). Heat transfer between a flat plate and jets of air impinging on it. In *International Developments in Heat Transfer*, pages 454–460, New York. ASME.

Geers, L. F. G., Tummers, M. J., Bart, G. C. J., and Hanjalić, K. (2001). LDA and PIV measurements applied to single and multiple impinging jets. In Celata, G. P., Marco, P. D., Goulas, A., and Mariani, A., editors, *Experimental Heat Transfer, Fluid Mechanics and Thermodynamics 2001*, volume 2, pages 1201–1206.

Goldstein, R. J. and Seol, W. S. (1991). Heat transfer to a row of impinging circular air jets including the effect of entrainment. *Int. J. Heat Mass Transfer*, 34(8):2133–2147.

Gonzalez, R. C. and Woods, R. E. (2002). *Digital Image Processing*. Prentice Hall, New Jersey, 2^{nd} edition.

Hay, J. L. and Hollingsworth, D. K. (1996). A comparison of trichromic systems for use in the calibration of polymer-dispersed thermochromic liquid crystals. *Exp. Thermal Fluid Sci.*, 12:1–12.

Hay, J. L. and Hollingsworth, D. K. (1998). Calibration of micro-encapsulated liquid crystals using hue angle and a dimensionless temperature. *Exp. Thermal Fluid Sci.*, 18:251–257.

Hoesel, W. and Rodi, W. (1977). New biasing elimination method for laser doppler velocimeter counter processing. *Rev. Sci. Instrum.*, 48(7):910–919.

Holmes, P., Lumley, J. L., and Berkooz, G. (1996). *Turbulence, coherent structures, dynamical systems and symmetry*. Cambridge University Press.

Huber, A. M. and Viskanta, R. (1994a). Effect of jet-jet spacing on convective heat transfer to confined, impinging arrays of axisymmetric air jets. *Int. J. Heat Mass Transfer*, 37(18):2859–2869.

Huber, A. M. and Viskanta, R. (1994b). Impingement heat transfer with a single rosette nozzle. *Exp. Thermal Fluid Sci.*, 9:320–329.

Hunt, J. C., Wray, A. A., and Moin, P. (1988). Eddies, stream and convergence zones in turbulent flows. Report CTR-588, Centre for Turbulence.

Hwang, J.-J. and Cheng, C.-S. (1999). Augmented heat transfer in a triangular duct by using multiple swirling jets. *Trans. ASME - J. Heat Transfer*, 121:683–690.

Ichimiya, K. (1994). Heat transfer and flow characteristics of a single circular impinging jet considered on heat conduction in a heated section. In *Int. Symp. Turb., Heat Mass Transfer*, volume 1, pages 2.2.1–2.2.6, Lisbon.

Ichimiya, K. and Hosaka, N. (1992). Experimental study of heat transfer characteristics due to confined impinging two-dimensional jets. *Exp. Thermal Fluid Sci.*, 5:803–807.

Jähne, B. (1991). *Digital Image Processing - Concepts, Algorithms and Scientific Applications*. Springer Verlag, Berlin, 2^{nd} edition.

Janssen, L. P. B. M. and Warmoeskerken, M. M. C. G. (1991). *Transport Phenomena - Data Companion*. DUM, Delft, 2^{nd} edition.

Jeong, J. and Hussain, F. (1995). On the identification of a vortex. *J. Fluid Mech.*, 285:69–94.

Kasagi, N., Moffat, R. J., and Hirata, M. (2001). *Handbook of flow visualisation*, chapter 8. Taylor & Francis, New York, 2^{nd} edition.

Kataoka, K. (1990). Impingement heat transfer augmentation due to large scale eddies. In *Heat Transfer 1990*, volume 1 of *Proc. 9^{th} Int. Heat Transfer Conf.*, pages 255–273.

Keane, R. D. and Adrian, R. J. (1990). Optimization of particle image velocimeters — part I: Double pulsed systems. *Meas. Sci. Technol.*, 1:1202–1215.

Keane, R. D. and Adrian, R. J. (1992). Theory of cross-correlation analysis of piv images. *Appl. Sci. Res.*, 49:191–215.

Kline, S. J. and McClintock, F. A. (1953). Describing Uncertainties in Single-sample Experiments. *Mech. Eng.*, 75:3–8.

Lee, J. and Lee, S.-J. (2000). The effect of nozzle configuration on stagnation region heat transfer enhancement of axisymmetric jet impingement. *Int. J. Heat Mass Transfer*, 43:3497–3509.

Livingood, J. N. B. and Hrycak, P. (1973). Impingement heat transfer from turbulent air stream jets to flat plates – a literature survey. NASA TM X-2778, NASA.

Loève, M. M. (1955). *Probability Theory*. Van Nostrand, New York.

Lumley, J. L. (1967). The structure of inhomogeneous turbulent flows. In *Atmospheric Turbulence and Radio Wave Propagation*, pages 166–178, Nauka, Moscow.

Lytle, D. and Webb, B. W. (1991). Secondary heat transfer maxima for air jet impingement at low nozle-to-plate spacings. In Keffer, J. F., Shah, R. K., and Ganić, E. N., editors, *Experimental Heat Transfer, Fluid Mechanics, and Thermodynamics*, pages 776–783, New York.

Manhart, M. and Wengle, H. (1993). A spatiotemporal decomposition of a fully inhomogeneous turbulent flow field. *Theoret. Comput. Fluid Dynamics*, 5:223–242.

Martin, H. (1977). *Advances in Heat Transfer*, volume 13, pages 1–60. Academic Press.

Matsumoto, R., Ishihara, I., Yabe, T., Ikeda, K., Kikkawa, S., and Senda, M. (1999). Impingement heat transfer within arrays of circular jets including the effect of crossflow (AJTE99-6386). In *Proc. 5^{th} ASME/JSME Joint Thermal Eng. Conf.*, pages 1–8.

McLaughlin, D. K. and Tiederman, W. G. (1973). Biasing correction for individual realization of laser anemometer measurements in turbulent flows. *Phys. Fluids*, 16:7.

Mehta, R. D. and Bradshaw, P. (1979). Design rules for small low speed wind tunnels. *Aeronautical J.* Technical note.

Metzger, D. E., Florschuetz, L. W., Takeuchi, D. I., Behee, R. D., and Berry, R. A. (1979). Heat transfer characteristics for inline and staggered arrays of circular jets with crossflow of spent air. *Trans. ASME - J. Heat Transfer*, 101:526–531.

Moffat, R. J. (1990). Experimental heat transfer. In *Proc. 9^{th} Int. Heat Transfer Conf.*, volume 1, pages 187–205, Jerusalem, Israel.

Nishino, K., Samada, M., Kasuya, K., and Torii, K. (1996). Turbulence statistics in the stagnation region of an axisymmetric impinging jet flow. *Int. J. Heat and Fluid Flow*, 17:193–201.

Obot, N. T. and Trabold, T. A. (1987). Impingement heat transfer within arrays of circular jets: Part 1 – effects of minimum, intermediate, and complete crossflow for small and large spacings. *Trans. ASME - J. Heat Transfer*, 109:872–879.

Park, H. G., Dabiri, D., and Gharib, M. (2001). Digital particle image velocimetry/thermometry and application to the wake of a heated circular cylinder. *Exp. Fluids*, 30:327–338.

Parsley, M. (1991). *Handbook of Thermochromic Liquid Crystal Technology*. Glenview, (IL,USA).

Peper, F., Leiner, W., and Fiebig, M. (1995). Drying performance and surface forces of a pair of impinging radial jets. *Heat Mass Transfer*, 30:313–320.

Petrie, H. L., Samimy, M., and Addy, A. L. (1988). Laser Doppler Velocity Bias in Separated Turbulent FLows. *Exp. Fluids*, 6:80–88.

Pitas, I. (1993). *Digital Image Processing Algorithms*. Prentice Hall, New York, 1^{st} edition.

Popiel, C. O. and Boguslawski, L. (1986). Mass or heat transfer in impinging single, round jets emitted by a bell-shaped nozzle and sharp-ended orifice. In *Heat Transfer 1986*, volume 3 of *Proc. 8^{th} Int. Heat Transfer Conf.*, pages 1187–1192.

Poreh, M., Tsuei, Y. G., and Cermak, J. E. (1967). Investigation of a turbulent radial wall jet. *J. Appl. Mech.*, 34:457–463.

Praisner, T. J., Sabatino, D. R., and Smith, C. R. (2001). Simultaeneously combined liquid crystal surface heat transfer and PIV flow-field measurements. *Exp. Fluids*, 30:1–10.

Press, W. H., Teukolsky, S. A., Vetterling, W. T., and Flannery, B. P. (1992). *Numerical Recipes in C – The art of scientific computing*. Cambridge University Press, Cambridge, 2^{nd} edition.

Priestley, M. B. (1981). *Spectral Analysis and Time Series*, volume 1. Academic Press Inc., New York.

Raffel, M., Willert, C., and Kompenhans, J. (1998). *Particle Image Velocimetry — A Practical Guide*. Springer-Verlag, Berlin, 1^{st} edition.

Reynolds, O. (1895). On the dynamical theory of incompressible viscous fluids and the determination of the criterion. *Philosophical Transactions of the Royal Society of London – Series A*, 186:123–164.

Roesgen, T. and Totaro, R. (2002). A statistical calibration technique for thermochromic liquid crystals. *Exp. Fluids*, 33:732–734.

Sabatino, D. R., Praisner, T. J., and Smith, C. R. (2000). A high-accuracy calibration technique for thermochromic liquid crystal temperature measurements. *Exp. Fluids*, 28:497–505.

Scarano, F. and Riethmuller, M. L. (1999). Iterative multigrid approach in PIV image processing with discrete window offset. *Exp. Fluids*, 26:513–523.

Sirovich, L. (1987). Turbulence and the dynamics of coherent structures: I, II, III. *Quart. Appl. Math.*, 45(3):561–590.

Stasiek, J. (1997). Thermochromic liquid crystals and true colour image processing in heat transfer and fluid-flow research. *Heat Mass Transfer*, 33:27–39.

Tennekes, H. and Lumley, J. L. (1972). *A First Course in Turbulence*. The MIT press, Cambridge.

Thielen, L. (2003). *Modelling and Calculation of flow and heat transfer in multiple impinging jets*. PhD thesis, Delft University of Technology.

Thielen, L., Jonker, H. J. J., and Hanjalić, K. (2003). Symmetry breaking of flow and heat transfer in multiple impinging jets. *Int. J. Heat and Fluid Flow*, 24(4):444–453.

Tummers, M. J. (1999). *Investigation of a turbulent wake in an adverse pressure gradient using laser Doppler anemometry*. PhD thesis, Delft University of Technology, Delft.

Viskanta, R. (1993). Heat transfer to impinging isothermal gas and flame jets. *Exp. Thermal Fluid Sci.*, 6:111–134.

Westerweel, J. (1993). *Digital Particle Image Velocimetry - Theory and Application*. PhD thesis, Delft University of Technology, Delft.

Westerweel, J. (1994). Efficient detection of spurious vectors in particle image velocimetry data. *Exp. Fluids*, 16:236–247.

Westerweel, J., Dabiri, D., and Gharib, M. (1997). The effect of a discrete window offset on the accuracy of cross-correlation analysis of digital PIV recordings. *Exp. Fluids*, 23:20–28.

Willert, C. (1996). The fully digital evaluation of photographic PIV recordings. *Appl. Sci. Res.*, 56:79–102.

Yule, A. J. (1978). Large-scale structure in the mixing layer of a round jet. *J. Fluid Mech.*, 89(3):413–432.

Nomenclature

Roman symbols

Symbol	Description	Units
$\boldsymbol{A}$	Matrix of uncorrelated coefficients $a^n(t)$	$\mathrm{m}^{3/2}\ \mathrm{s}^{-1}$
A	Area enclosing an eddy	m^2
A_p	Cross-section of the measurement volume	m^2
a	Heat diffusivity ($\lambda/(\rho c_p)$)	$\mathrm{m}^2\ \mathrm{s}^{-1}$
a, b	Wall-normal velocity gradients	s^{-1}
$a^n(t)$	Coefficient of mode n on time instant t	$\mathrm{m}^{3/2}\ \mathrm{s}^{-1}$
B	Width of the impingement sheet	m
B	Blue part of a color signal (only in Section 3.3)	
B_{max}	Maximum value for blue signal	
$\boldsymbol{C}$	Two-point temporal correlation tensor of a velocity field	$\mathrm{m}^3\ \mathrm{s}^{-3}$
$C(t, t')$	Two-point temporal correlation function of a velocity field	$\mathrm{m}^3\ \mathrm{s}^{-3}$
C_p	Particle concentration in the flow	m^{-3}
c_p	Heat capacity of a substance at constant pressure	$\mathrm{J\ kg}^{-1}\ \mathrm{K}^{-1}$
$\mathcal{D}$	Characteristic length scale	m
D	Nozzle diameter	m
D_a	Aperture diameter of an imaging lens	m
D_e	Characteristic eddy diameter	m
D_k	Turbulent kinetic energy transport due to viscosity	$\mathrm{m}^2\ \mathrm{s}^{-3}$
D_m	Nozzle diameter in the multiple jet array	m
D_s	Nozzle diameter of the single jet pipe	m
d	Layer thickness	m
d	Wire diameter (only in Appendix A)	m
d_f	Fringe spacing	m
d_I	Width of an interrogation area on the image plane	m
d_p	Seeding particle diameter	m
d_s	Diameter of an Airy disk	m
d_τ	Diameter of a particle image on the recording sensor	m
E_{fluct}	Total energy of the fluctuations in a flow field	$\mathrm{m}^3\ \mathrm{s}^{-2}$

E_{tot}	Total energy of a flow field	$m^3\ s^{-2}$
$E_V(t)$	Time dependent spatial energy of a flow field	$m^3\ s^{-2}$
$\boldsymbol{e}_d$	Unit direction vector of scattered light falling on a detector	
$\boldsymbol{e}_{i_1}, \boldsymbol{e}_{i_2}$	Unit direction vectors of incident light beams	
F_I	Correlation left after in-plane motion of tracer particles	
F_O	Correlation left after out-of-plane motion of tracer particles	
f	Focal length of an imaging lens	m
$f^{\#}$	Numerical aperture of an imaging lens (f/D_a)	
f_0	Frequency of laser light	Hz
f_D	Doppler frequency	Hz
f_s	Shifting frequency	Hz
f_{w_1}, f_{w_2}	Frequencies of scattered light waves	Hz
$\boldsymbol{G}$	Matrix resulting from discretizing a spatial integral	m
G	Green part of a color signal	
G_{max}	Maximum value for green signal	
g_i	Gravity vector	$m\ s^{-2}$
H	Hue-angle (in Sections 3.3, 4.2.2, and 4.2.3)	$^\circ$
H	Nozzle-to-plate distance	m
$H_{i,j}$	Expected value of hue-angle in pixel (i,j)	$^\circ$
h	Height of a horizontal plane above the impingement plate	m
h	Heat transfer coefficient	$W\ m^{-1}\ K^{-1}$
h_d	Heat transfer coefficient of draught	$W\ m^{-1}\ K^{-1}$
h_j	Heat transfer coefficient of impinging jets	$W\ m^{-1}\ K^{-1}$
$h_{i,j}$	Measured hue-angle in pixel (i,j)	$^\circ$
$\overline{h}_{\mathrm{surr}(i,j)}$	Mean hue-angle of the eight neighbors of pixel (i,j)	$^\circ$
$\tilde{h}_{\mathrm{surr}(i,j)}$	Median hue-angle of the eight neighbors of pixel (i,j)	$^\circ$
$\mathbf{I}$	Identity matrix	
I	Color intensity (only in Section 3.3.2)	
I	Current through the impingement sheet	A
$\hat{I}$	Fourier transformed image	
i, j	Integer coordinates	
i, j, k	Integer indices	
$J_{i,j}$	Jacobian matrix on grid position (i,j)	m^{-1}
K	Pressure drop coefficient	
k	Turbulent kinetic energy: $\frac{1}{2}\overline{u_i'^2}$	$m^2\ s^{-2}$
k'	$\frac{1}{2}u_i'^2$	$m^2\ s^{-2}$
L	Length of the pipe (only in Section 4.1)	m
L	Length of the impingement sheet	m
l, m	Exponents in a Nusselt correlation	
M	Image magnification factor	
m, n	Mode number	
N	(Integer) half-width of a filter kernel (only in Section 3.3.4)	
N	Total number of samples in an ensemble	

N_1, N_2, N_3	Color tristimulus (e.g. R, G, and B)	
N_k	Kinematic vorticity number	
N_I	Image density	
N_M	Total number of modes of a POD	
N_P	Total number of spatial locations of measurements	
N_T	Total number of time instants for snapshots	
$n_{undef}(x, y)$	Number of undefined temperatures at position (x, y)	
Nu	Nusselt number $(h\mathcal{D}/\lambda)$	
$\mathrm{Nu}(x, y)_i$	Nusselt number on position (x, y) in image i	
Nu_{stag}	Nusselt number in the stagnation point of an impinging jet	
Nu_{ave}	Area-averaged Nusselt number	
P_k	Production of turbulent kinetic energy	$\mathrm{m^2\ s^{-3}}$
$P_{k,normal}$	Production of turbulent kinetic energy by normal stresses	$\mathrm{m^2\ s^{-3}}$
$P_{k,shear}$	Production of turbulent kinetic energy by shear stresses	$\mathrm{m^2\ s^{-3}}$
P_{uu}	Normal production of turbulent kinetic energy by uu stress	$\mathrm{m^2\ s^{-3}}$
P_{uv}	Shear production of turbulent kinetic energy by uv stress	$\mathrm{m^2\ s^{-3}}$
P_{vv}	Normal production of turbulent kinetic energy by vv stress	$\mathrm{m^2\ s^{-3}}$
P_{ww}	Normal production of turbulent kinetic energy by ww stress	$\mathrm{m^2\ s^{-3}}$
p	Pressure in a flow	Pa
p'	Pressure fluctuations	Pa
Pr	Prandtl number (ν/a)	
Q	Second invariant of the velocity gradient tensor	$\mathrm{s^{-2}}$
q''	Heat flux	$\mathrm{W\ m^{-2}}$
q_c	Heat loss due to lateral conduction within the sheet	W
q_d	Heat loss due to draught along the sheet	W
q_e	Heat production through electrical dissipation	W
q_j	Heat flow to impinging jets	W
q_r	Heat loss due to radiation	W
R	Red part of a color signal	
R_C	Mean background correlation	
R_D	Displacement correlation peak	
R_F	Noise term due to random particle correlations	
$R_{i,j}$	Value of the correlation function at pixel (i, j)	
R_{max}	Maximum value for red signal	
r	Radial coordinate	m
Re	Reynolds number $(\mathcal{U}\mathcal{D}/\nu)$	
$\boldsymbol{S}$	Symmetric part of the velocity gradient tensor	$\mathrm{s^{-1}}$
S	Color saturation	
S_{ij}	Element i, j from $\boldsymbol{S}$	$\mathrm{s^{-1}}$
$\boldsymbol{s}$	Particle displacement vector	m
s	Magnitude of shear (in Sections 2.1.3 and 5.2.3)	$\mathrm{s^{-1}}$
s	Distance between nozzles (pitch) in the multiple jet array	m
$s_{H_{\mathrm{surr}(i,j)}}$	Hue sample standard deviation of eight pixels surrounding (i, j)	°
$s_{\mathrm{surr}(i,j)}$	Sample standard deviation of eight neighbors of vector at (i, j)	$\mathrm{m\ s^{-1}}$

T	Total time duration of measurements (only in Section 2.1.3)	s
T	Temperature	K
T^*	Non-dimensionalized temperature (T/T_∞)	
T_∞	Bulk temperature of the fluid	K
T_b	Temperature of a solid boundary	K
T_s	Temperature of the surroundings	K
T_k	Turbulent kinetic energy transport due to velocity fluctuations	$m^2\ s^{-3}$
t, t'	Time	s
t^*	Non-dimensionalized time ($t\mathcal{U}/\mathcal{D}$)	
$\boldsymbol{U}$	Three-dimensional velocity matrix ($\boldsymbol{u}(\boldsymbol{x}, t)$)	$m\ s^{-1}$
$\mathcal{U}$	Characteristic velocity scale	$m\ s^{-1}$
U_{bulk}	Bulk (or superficial) velocity of a jet	$m\ s^{-1}$
U_{CL}	Center line velocity of a jet	$m\ s^{-1}$
U_m	Maximum radial wall jet velocity	$m\ s^{-1}$
$\boldsymbol{u}(\boldsymbol{x}, t)$	Velocity vector at position $\boldsymbol{x}$ and time instant t	$m\ s^{-1}$
u, v, w	Velocity components	$m\ s^{-1}$
u_i	Velocity component in x_i-direction	$m\ s^{-1}$
u_i	i^{th} velocity sample (only in Section 3.1.4)	$m\ s^{-1}$
u_j^*	Non-dimensionalized velocity in x_j direction ($u_j/\mathcal{U}$)	
u_i'	Fluctuating part of the i^{th} velocity component	$m\ s^{-1}$
V	Domain in which flow velocities are measured (in Section 2.1.3)	m^3
V	Voltage over the impingement sheet	V
$\boldsymbol{v}$	Velocity vector	$m\ s^{-1}$
$\boldsymbol{v}_{i,j}$	Velocity vector on position (i, j)	$m\ s^{-1}$
$\tilde{\boldsymbol{v}}_{i,j}$	Median velocity vector of eight neighbors of the vector at (i, j)	$m\ s^{-1}$
v_{max}	Maximum in-plane velocity	$m\ s^{-1}$
w_i	Weighting factor of the i^{th} sample	
w_{max}	Maximum out-of-plane velocity	$m\ s^{-1}$
$\mathbf{x}$	Position vector	m
x_j	j^{th} coordinate	m
x_j^*	Non-dimensionalized j^{th} coordinate ($x_j/\mathcal{D}$)	
x_0, y_0	Precise coordinates of the correlation peak in pixels	
x_e, y_e	Coordinates of an eddy	m
x, y, z	coordinates	m

Greek symbols

Symbol	Description	Units
α	Parameter determined on the basis of a confidence interval	
$\alpha_{1...5}$	Non-dimensional fit parameters	
$\alpha, \beta, \gamma, \lambda$	Fit parameters in Equation 3.19	

β	Open area ratio of wire-mesh (only in Appendix A)	
$\gamma_{i,j}$	Smoothing filter weighting factor for pixel i, j	
ΔT	Temperature difference between metal sheet and liquid crystals	K
Δt	Time separation between two PIV images	s
Δu	Velocity difference over an interrogation area	m s^{-1}
Δx	Grid spacing	m
Δx_I	Distance between two Nusselt number peaks	m
Δz_0	Thickness of the laser sheet	m
δ	Wall jet height	m
δ_{mn}	Kronecker delta	
ε	Dissipation of turbulent kinetic energy	m^2 s^{-3}
ε	Emission coefficient	
ϵ_{ijk}	Alternating unit tensor	
η	Dynamic viscosity of a fluid	Pa s
θ	Angle between two laser beams	rad
$\mathbf{\Lambda}$	Diagonal matrix of eigenvalues λ^n	m^3 s^{-2}
λ, λ_0	Wavelength of light	m
λ_2	Second eigenvalue of $\boldsymbol{S}^2 + \mathbf{\Omega}^2$	s^{-2}
λ	Heat conductivity	W m^{-1} K^{-1}
λ^n	Eigenvalue of mode n	m^3 s^{-2}
ν	Kinematic viscosity of a fluid	m^2 s^{-1}
ν_p	Expected rate of particles passing a measurement volume	s^{-1}
Π_k	Turbulent kinetic energy transport due to pressure fluctuations	m^2 s^{-3}
ρ	Density of a fluid	kg m^{-3}
ρ_p	Density of a seeding particle	kg m^{-3}
σ	Stefan-Boltzmann constant	W m^{-2} K^{-4}
$\sigma_{\mathrm{surr}(i,j)}$	Standard deviation of eight velocity samples surrounding (i, j)	m s^{-1}
τ_l	Characteristic time scale of particle lag	s
τ	Characteristic time scale of conduction	s
$\mathbf{\Phi}$	Matrix of orthogonal spatial basis functions $\boldsymbol{\varphi}^n(\boldsymbol{x})$	m$^{-1/2}$
$\Phi(h_{i,j})$	Smoothing filter operator for the hue angle	
$\boldsymbol{\varphi}^n(\boldsymbol{x})$	Orthogonal spatial basis function of mode n on position $\boldsymbol{x}$	m$^{-1/2}$
$\boldsymbol{\omega}$	Vorticity vector	s^{-1}
ω_z	Z-component (i.e. out-of-plane) of vorticity vector	s^{-1}
ω	Vorticity magnitude	s^{-1}
$\mathbf{\Omega}$	Anti-symmetric part of the velocity gradient tensor	s^{-1}

Special operators

$\langle X \rangle$	Ensemble mean value of quantity X
δX	RMS error of quantity X

Subscripts and superscripts

LC	Referring to the liquid crystal layer
paint	Referring to the black backing paint layer
steel	Referring to the stainless steel impingement sheet
$''$	Referring to a flux

Acronyms

AU	Arbitrary Units
CCD	Charge Coupled Device
CFD	Computational Fluid Dynamics
FFT	Fast Fourier Transform
FT	Fourier Transform
FT^{-1}	Inverse Fourier Transform
HSI	Hue, Saturation, Intensity
HSV	Hue, Saturation, Value (equal to HSI)
HWA	Hot Wire Anemometry
LCT	Liquid Crystal Thermography
LDA	Laser Doppler Anemometry
NTSC	National Television Systems Committee
PIV	Particle Image Velocimetry
POD	Proper Orthogonal Decomposition
PTV	Particle Tracking Velocimetry
RGB	Red, Green, Blue
RANS	Reynolds Averaged Navier-Stokes
RMS	Root mean square
SNR	Signal-to-noise ratio
V/STOL	Vertical/Short Take-Off and Landing
WIDIM	Window Displacement Iterative Multigrid
YAG	Yttrium-Aluminum Garnet

Summary

Multiple impinging jet arrays: an experimental study on flow and heat transfer

Leonard F.G. Geers

Because of their high efficiency and their ability to provide high heat transfer rates, impinging jets are applied for rapid cooling and heating in a wide variety of industrial processes. However, the physical phenomena controlling the heat transfer from impinging jets are to a large degree unknown. The goal of the present project was to gain a better understanding of the interaction between the flow and heat transfer in impinging jet arrays.

Experiments were performed in two different configurations: a single impinging jet and multiple impinging jet arrays. LDA and PIV velocity measurements in the single jet were compared: these measurements were aimed at serving as a reference for comparison of the multiple jet features. In a hexagonal and an in-line array of jets PIV was used to provide instantaneous velocity fields over the flow area of interest, what proved to be essential for detecting some salient features of the multiple-jet dynamics. These dynamics were investigated on the basis of POD filtered snapshots of the flow. In both arrays, large scale eddies in the development zone cause the impinging jets to break up or be severely displaced in the out-of-plane direction. A horse-shoe vortex appears around the outer jets of the hexagonal array, whereas the in-line array does not show this feature. This is most likely caused by the higher pitch in the in-line configuration. On the other hand, the flow field in the in-line arrangement appears to be diagonally asymmetrical, even though the symmetry of the nozzle arrangement would imply a symmetrical flow field. This flow asymmetry causes an elliptical heat transfer pattern in the impingement zone of the center jet. The flow asymmetry was also found in numerical simulations of a similar configuration, conducted in a parallel project.

Heat transfer measurements were performed in the impingement surface for seven multiple jet arrays using LCT, which provided insight in the influence of different geometrical parameters of the arrays on the heat transfer. Additionally, a non-dimensional correlation was derived linking heat transfer to geometrical and flow parameters. Heat transfer profiles were subsequently compared to velocity and turbulence quantities just above the

impingement plate to investigate the effect of the mean flow features on the heat transfer. The apparent correlation between the Nusselt number and the normal contribution to the production of turbulent kinetic energy is coincidental: the cause of the increased Nusselt number in the impingement points of the jets is a combination of an oscillating impingement position due to large vortical structures and a very strong acceleration of the fluid from the impingement point outwards. In the impingement point the boundary layer is very thin and the temperature gradient is very steep, enabling impinging vortices to encapsulate and remove heat in an effective way.

The results presented in this thesis should aid in better understanding the role of turbulence and vortical structures in the interaction between adjacent impinging jets, and in the heat transfer from impinging jets. With the advent of a measurement technique capable of capturing instantaneous heat transfer distributions, a potential extension of the present work is a more detailed analysis of the influence of individual vortical structures on impingement heat transfer.

Samenvatting

Reeksen van meerdere impinging jets: een experimenteel onderzoek naar stroming en warmteoverdracht

Leonard F.G. Geers

Impinging jets worden toegepast voor snelle koeling of verwarming van producten in een breed scala aan industriële processen vanwege hun hoge rendement en warmteoverdrachtscapaciteit. Echter, welke fysische processen aan de warmteoverdracht van impinging jets ten grondslag liggen is momenteel nog niet geheel bekend. Het doel van dit project was een beter begrip te krijgen van de interactie tussen de stroming en de warmteoverdracht van meerdere impinging jets.

Experimenten werden uitgevoerd in twee verschillende configuraties: een enkele impinging jet en combinaties van meerdere impinging jets. LDA en PIV snelheidsmetingen in de enkele jet werden vergeleken: deze metingen gelden als referentie voor de vergelijking van kenmerken van meerdere impinging jets. In een hexagonale en een vierkante opstelling van meerdere jets werd PIV gebruikt om instantane snelheidsvelden te meten. Dit bleek essentieel voor de ontdekking van enkele opmerkelijke kenmerken van de dynamica van meerdere jets. Deze dynamica werd onderzocht gebruikmakend van POD gefilterde momentopnamen van de stroming. In beide configuraties bleken grote wervelstructuren in het overgangsgebied van de jets de oorzaak te zijn van het opbreken of verplaatsen van de jets in de richting loodrecht op het vlak van de meting. Om de buitenste jets in de hexagonale configuratie bevonden zich hoefvormige wervels, terwijl dit niet het geval was voor de vierkante configuratie. Hoogstwaarschijnlijk wordt dit veroorzaakt door de grotere afstand tussen de jets in het geval van de vierkante configuratie. Daarentegen, de stroming in de vierkante jet configuratie blijkt asymmetrisch te zijn in de diagonaal, terwijl de symmetrische rangschikking van jets een symmetrische stroming zou impliceren. Deze asymmetrische stroming veroorzaakt een elliptisch warmteoverdrachtspatroon in het inslaggebied van de centrale jet. In een parallel project werd dezelfde symmetriebreuk gevonden in numerieke simulaties in dezelfde configuratie.

Warmteoverdrachtsmetingen met behulp van LCT werden gedaan op het oppervlak waarop de jets insloegen. Deze metingen gaven inzicht in de invloed van diverse geometrische parameters van de jetconfiguraties op de warmteoverdracht. Daarnaast werd

een dimensieloze correlatie afgeleid waarmee de warmteoverdracht te berekenen is op basis van geometrische parameters en stromingseigenschappen. Profielen van de warmteoverdracht werden vergeleken met profielen van de snelheid en turbulente grootheden genomen op een positie vlak boven het oppervlak van inslag met als doel het effect van de gemiddelde stroming op de warmteoverdracht te onderzoeken. De schijnbare correlatie tussen het Nusselt getal en de normale bijdrage aan de produktie van turbulente kinetische energie berust op toeval: de toename van het Nusselt getal in de punten van inslag van de jets wordt veroorzaakt door een combinatie van een oscillerende inslagpositie door grote wervel-structuren en een zeer sterke acceleratie van het fluïdum vanuit het punt van inslag van een jet. In het inslagpunt van een jet is de grenslaag erg dun en de temperatuurgradient erg sterk, waardoor inslaande wervel zeer effectief warmte kunnen insluiten en wegvoeren.

Op basis van de hier gepresenteerde resultaten kan een beter inzicht worden verkregen in de rol van turbulentie en wervel-structuren bij de interactie tussen naburige impinging jets en bij de warmteoverdracht van impinging jets. Met de komst van een meettechniek waarmee instantaan warmteoverdrachtsmetingen kunnen worden gedaan in een vlak, kan de invloed van individuele wervels op de warmteoverdracht in impinging jets in meer detail onderzocht worden.

List of publications

Conference Proceedings

L.F.G. Geers, M.J. Tummers, G.C.J. Bart, and K. Hanjalić. LDA and PIV measurements applied to single and multiple impinging jets. In G.P. Celata, P. Di Marco, A. Goulas, and A. Mariani, editors, *Experimental Heat Transfer, Fluid Mechanics and Thermodynamics 2001*, volume 2, pages 1201–1206, September 2001.

L.F.G. Geers, M.J. Tummers, and K. Hanjalić. PIV measurements in impinging jets at a high Reynolds number. In E. Lindborg, A. Johansson, and J. Eaton, editors, *Turbulence and Shear Flow Phenomena 2*, volume 2, pages 289–294, June 2001.

L.F.G. Geers, M.J. Tummers, and K. Hanjalić. POD and structure identification in an impinging jet array using PIV (P1017). In *4th International Symposium on Particle Image Velocimetry*, September 2001.

Journals

G.C.J. Bart, A.J. van IJzerloo, L.F.G. Geers, L. Hoek, and K. Hanjalić. Heat transfer of phase-locked modulated impinging-jet arrays. *Exp. Thermal Fluid Sci.*, 26:299–304, 2002.

L.F.G. Geers, M.J. Tummers, and K. Hanjalić. Experimental investigation of impinging jet arrays. *Accepted for publication in Exp. Fluids*, 2003.

L.F.G. Geers, M.J. Tummers, and K. Hanjalić. PIV-based eduction of coherent structures in normally impinging multiple jets. *Submitted for publication.*

L.F.G. Geers, M.J. Tummers, and K. Hanjalić. Heat transfer and large scale flow structures in multiple impinging jet arrays. *Submitted for publication.*

Dankwoord

Allereerst ben ik dank verschuldigd aan Professor Hanjalić voor zijn adviezen en zijn kritische noten bij alles wat ik in de afgelopen vier-en-een-half jaar aan tekst produceerde. Het was me een waar genoegen in uw groep te mogen werken. Theo en Gerard, die mij begeleidden in de eerste twee jaar van mijn promotie, dank ik voor hun luisterend oor en wijze raad. In de laatste jaren van mijn promotie werd die rol vervuld door Mark Tummers. Mark, we hebben naast een hele goede en vruchtbare samenwerking ook enorm gelachen. Ik hoop dat dat nog even zo blijft; bedankt voor de afgelopen jaren.

Zonder een gezellige groep collega's kan niemand zijn promotie goed afronden. Ik heb altijd enorm genoten van de diversiteit aan karakters, talen en culturen, die voortvloeit uit de internationale samenstelling van de sectie Warmte en Stroming (WS). Daarom wil ik alle mensen die ik via WS heb leren kennen bedanken voor de interessante gesprekken tijdens de koffie. Een bijzondere rol werd daarin vervuld door mijn collega-AIO's Werner, Krzysztof, Bertrand en Tieying, door wie mijn Duits en Frans gestotter verbeterd werd en ik de eerste woorden Pools en Chinees sprak. Maar bovenal wil ik Luuk, mijn projectmaat, bedanken. Luuk, je hebt meer dan vier jaar tegen mijn kop aan moeten kijken en ik tegen de jouwe, maar dat heeft ons er niet van weerhouden er een gezellige tijd van te maken. We zien elkaar bij TNO!

Arjan en Tycho, 'mijn studenten', van jullie heb ik veel geleerd en jullie hopelijk ook van mij. Bedankt voor jullie inzet tijdens je afstuderen, ik vond het een gouwe tijd. Tenslotte rest mij nog de Technische Drie-eenheid van de groep te bedanken: Erwin, Rob en Bart. Zonder jullie valt er niks te experimenteren bij WS. Ik hoop dat ik nog een keer terug mag komen voor raad op het gebied van software, elektronica en wat er allemaal mis kan gaan bij een experiment....

Naast mijn promotie heb ik een heleboel nieuwe vrienden gemaakt in mijn tijd als contact-AIO en webmaster van het JM Burgerscentrum. De twee belangrijkste mensen daar waren de wetenschappelijk directeur en zijn secretaresse: Gijs en Ilse, het was me een genoegen met jullie te mogen werken. Mijn mede contact-AIO's wens ik succes bij het vervullen van hun taak en het afronden van hun proefschrift.

Mijn project werd gefinancierd door STW, TNO-TPD en Rademaker-Den Boer. Naast

een financiële bijdrage hebben zij ook in de vorm van begeleiding bijgedragen aan mijn project. Marijke, Peter-Paul, Cor, Remco, Fons, en de overige leden van de gebruikerscommissie, bedankt voor jullie centen en goede ideeën. Ze zijn goed besteed.

Tenslotte kom ik bij de mij meest dierbare mensen aan wie ik dit proefschrift opdraag: mijn ouders en mijn vrouw. Pa, ma, jullie hebben mij de aanleiding gegeven van mijn wetenschappelijke carrière. Zonder jullie was het zeker niet gelukt, want behalve jullie sponsoring was jullie stimulans erg welkom (en nodig). Bedankt voor het begrip, de wijze raad, de steun en de liefde van de afgelopen 30 jaar. En Natasja, ik heb een enorm respect voor jou. Jij bent er altijd voor mij, ook al laat je lichaam je wel eens in de steek. Ik ben jou minstens vier-en-een-half jaar schuldig. Dankjewel.

About the author

December 3, 1973	Born in Tilburg.
1986-1992	Secondary education at the St. Odulphuslyceum in Tilburg on the level Atheneum-β.
1992-1998	MSc study in Chemical Technology at the Delft University of Technology. Graduation at the Kramers Laboratorium voor Fysische Technologie on the subject *Optimization of Particle Image Velocimetry for turbulent stirred tank flow.*
1998-2003	PhD project in the Thermal and Fluids Sciences Section of the Department of Applied Sciences at the Delft University of Technology.
Since July 2003	Research Scientist Physical Protection at TNO Prins Maurits Laboratorium, Rijswijk.